Bioinspired Nanostructures for Biomedical Applications

Thesis by
Vinayak Narasimhan

In Partial Fulfillment of the Requirements for the
Degree of
Doctor of Philosophy in Medical Engineering

CALIFORNIA INSTITUTE OF TECHNOLOGY
Pasadena, California

2020
Defended April 15th, 2020

Vinayak Narasimhan
ORCID: 0000-0003-4165-402X

To my beloved grandfather in whose footsteps I hope to follow

ACKNOWLEDGEMENTS

I would like to express my sincere gratitude to my advisors Dr. Hyuck Choo and Dr. Mory Gharib. To Dr. Choo – from hosting me at Caltech during my first visit and helping me settle in to providing me with complete flexibility and ample resources over the years to pursue my own research, your guidance and mentorship have been absolutely pivotal. What I have come to appreciate the most about you is your fierce loyalty towards those in your care. To Dr. Gharib – thank you very much for providing me the support and guidance needed to see me past the finish line.

To the amazing postdocs in my group who I have had the pleasure of working with – Radwan, Shailabh, Jeong, Blaise and Daejong, you have been my co-advisors and I cannot thank you enough. This work would have been inconceivable without your vision, creativity, mentorship and selflessness. To my fellow grads Haeri and Hyunjun, we have weathered many a storm together and I am glad to have had your support and friendship throughout.

I would also like to thank my lovely friends Abbas, Amanda, Gautam, Jorge, Marcel and Magnus who have been nothing short of a second family to me. Only a band of misfits can stick together and forge a friendship for the ages. Thank you for putting up with all my endless and often controversial ranting. The local watering holes will greatly miss our patronage. *Salud*!

Not many PhD students can boast of parents who understand the ins and outs of the academic process. In my father, who walked the same corridors at Caltech as a graduate student nearly forty years before me, I have had the lifelong support and mentorship of the best professor in the world! To my wonderful mother who has sacrificed so much to ensure my happiness and well-being, I owe everything I am to you.

Finally, a big thank you to my brilliant and beautiful wife Akshita. Your unwavering support through the years has been instrumental. I have turned to you for so much secure in the knowledge that you will always be in my corner. There is so much I have learned from you that helped me navigate life in grad school. This was a joint milestone – one of many that I am sure we will successfully cross together in the years to come.

ABSTRACT

Nature boasts a myriad examples of coloration achieved purely through the physical interaction of light with nano-scale features also known as biophotonic nanostructures. From reptiles to insects, birds to flora, structural coloration has been achieved through a variety of fascinating nano-architectures that leverage different physics. Beyond structural coloration, these nanostructures are often truly multifunctional. For instance, biophotonic nanostructures can also serve as self-cleaning and bactericidal surfaces, gas and thermal sensors, waveguides and beam splitters. With the growing need for robust and compact biomedical devices, the requirement to embed multiple functionalities towards sensing, monitoring, diagnostics and therapeutics within a diminutive device footprint becomes crucial. In this regard, inspiration from the multifunctionality of biophotonic nanostructures can prove to be greatly beneficial for medical applications. Consequently, this work attempts to showcase various examples of the utilization of nanostructures inspired from biophotonic nanostructures for biomedical applications under various overlapping themes such as ophthalmic sensors, bioinspired optics and plasmonic biosensing.

This thesis is summarized in two parts. The first part (Chapters 2–4) introduces a proof-of-concept optical intraocular pressure (IOP) sensor implant and various challenges faced during its *in vivo* implementation. In Chapter 3, nanostructures inspired by light-trapping epidermal micro-/nanostructures on flower petals are proposed and embedded onto the sensor platform to improve its *in vivo* optical signal-to-noise ratio and biocompatibility. Chapter 4 covers nanostructures inspired by biophotonic nanostructures on longtail glasswing butterfly wings that improve the *in vivo* angle of acceptance and biocompatibility of the sensor.

The second part (Chapters 5 and 6) presents the use of bioinspired nanostructures in plasmonic biosensors. Chapter 5 discusses an on-chip platform consisting of bioinspired plasmonic nanostructures to detect various nucleic acid sequences of relevance in the pathogenesis of HIV-1 via plasmon-enhanced fluorescence. Chapter 6 describes the employment of bioinspired quasi-ordered nanostructuring on flexible substrates for broadband surface-enhanced Raman spectroscopy (SERS). Here, SERS-based biosensing enabled by quasi-ordering is used to detect uric acid – a biomarker of various pathologies in human tears.

I: Bioinspired nanostructures for medical implants

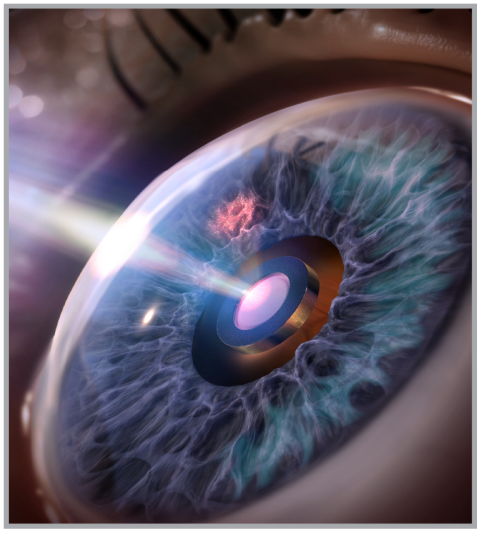

Chapter 3: Flower-petal-inspired IOP sensor implant

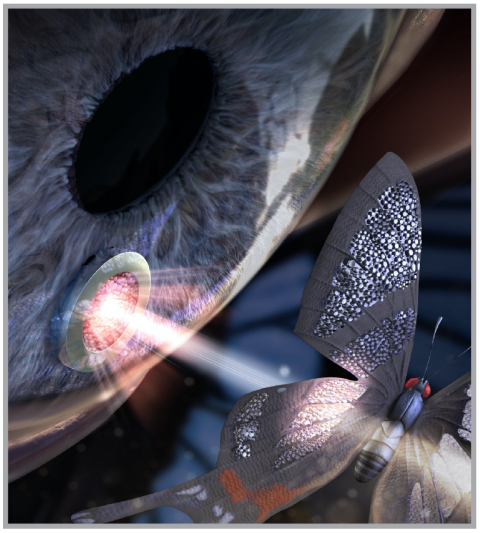

Chapter 4: Butterfly-inspired IOP sensor implant

II: Bioinspired nanostructures for plasmonic biosensors

Chapter 5: Bioinspired plasmon-enhanced fluorescence biosensor

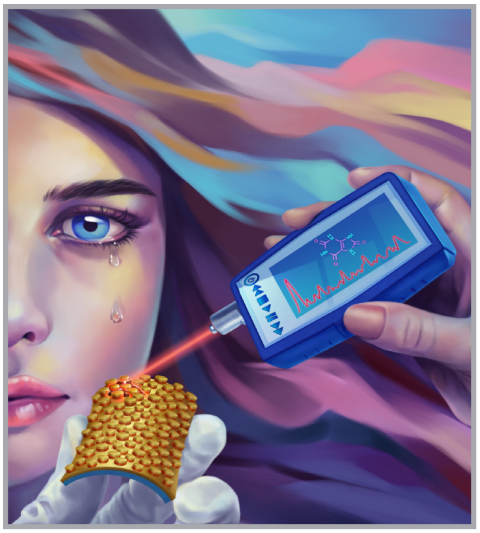

Chapter 6: Bioinspired flexible SERS biosensor

Illustrative summary of the thesis

PUBLISHED CONTENT AND CONTRIBUTIONS

Journal *** – Co-first author**

V. Narasimhan, R. H. Siddique, H. Park and H. Choo (2020). "Bioinspired disordered flexible metasurfaces for human tear analysis using broadband surface-enhanced Raman scattering." In: ***ACS Omega*** 5.22, pp. 12915–12922. DOI: 10.1021/acsomega.0c00677. (**Article featured on journal cover**).

V.N. participated in the conception of the work, performed simulations, fabrication and characterization, carried out biosensing experiments, prepared the data, and wrote the manuscript.

S. Kumar*, H. Park*, H. Cho, R. H. Siddique, **V. Narasimhan**, D. Yang and H. Choo (2020). "Overcoming evanescent field decay using 3D-tapered nanocavities for on-chip targeted molecular analysis." In: ***Nature Communications*** 11.1, pp. 1–9. DOI: 10.1038/s41467-020-16813-5.

V.N. assisted in performing the necessary fabrication, prepared the data, and participated in the writing of the manuscript.

R. H. Siddique*, S. Kumar*, **V. Narasimhan**, H. Kwon and H. Choo (2019). "Aluminum metasurface with hybrid multipolar plasmons for 1000-fold broadband visible fluorescence enhancement and multiplexed biosensing." In: ***ACS Nano*** 13.12, pp. 13775–13783. DOI: 10.1021/acsnano.9b02926. (**Article featured on journal cover**).

V.N. assisted in performing the necessary simulations, prepared the data, and participated in the writing of the manuscript.

V. Narasimhan, R. H. Siddique, M. Hoffmann, S. Kumar and H. Choo (2019). "Enhanced broadband fluorescence detection of nucleic acids using multipolar gap-plasmons on biomimetic Au metasurfaces." In: ***Nanoscale*** 11.29, pp. 13750–13757. DOI: 10.1039/C9NR03178B. (**Article featured on journal cover**).

V.N. participated in the conception of the work, performed simulations, fabrication and characterization, carried out biosensing experiments, prepared the data, and wrote the manuscript.

J. O. Lee, **V. Narasimhan**, A. Balakrishna, M. R. Smith, J. Du, D. Sretavan and H. Choo (2019). "Fabry-Pérot optical sensor and portable detector for monitoring high-resolution ocular hemodynamics." In: ***IEEE Photonics Technology Letters*** 31.6, pp. 423–426. DOI: 10.1109/LPT.2019.2896840.

V.N. participated in the conception of the work, performed the necessary fabrication and characterization, assisted in *in vivo* studies, prepared the data, and co-wrote the manuscript.

V. Narasimhan*, R. H. Siddique*, J. O. Lee, S. Kumar, B. Ndjamen, J. Du, N. Hong, D. Sretavan and H. Choo (2018). "Multifunctional biophotonic nanostructures inspired by the longtail glasswing butterfly for medical devices." In: ***Nature Nanotechnology*** 13.6, pp. 512–519. DOI: 10.1038/s41565-018-0111-5. (**Article featured on journal contents page**).

V.N. participated in the conception of the work, performed fabrication and characterization, assisted in *in vivo* studies, prepared the data, and co-wrote the manuscript.

D. Yang, S. Afroosheh, J. O. Lee, H. Cho, S. Kumar, R. H. Siddique, **V. Narasimhan**, Y-. Z. Yoon, A. T. Zayak and H. Choo (2018). "Glucose sensing using surface-enhanced raman-mode constraining." In: ***Analytical Chemistry*** 90.24, pp. 14269–14278. DOI: 10.1021/acs.analchem.8b03420. (**Article featured on journal cover**).

V.N. performed the necessary mathematical modeling, and participated in the writing of the manuscript.

D. Assumpcao, S. Kumar, **V. Narasimhan**, J. Lee and H. Choo (2018). "High-performance flexible metal-on-silicon thermocouple." In: ***Scientific Reports*** 8.1, pp. 13725-1–13725-10. DOI: 10.1038/s41598-018-32169-9.

V.N. performed the necessary fabrication, and participated in the writing of the manuscript.

J. O. Lee*, **V. Narasimhan***, J. Du, B. Ndjamen, D. Sretavan and H. Choo (2017). "Biocompatible multifunctional black-silicon for implantable intraocular pressure sensor." In: ***Advanced Healthcare Materials*** 6.4, pp. 1601356-1–1601356-7. DOI: 10.1002/adhm.201601356. (**Article featured on journal cover**).

V.N. participated in the conception of the work, performed the necessary fabrication and characterization, assisted in *in vivo* studies, prepared the data, and co-wrote the manuscript.

Conference

R. H. Siddique, **V. Narasimhan**, J. O. Lee, S. Kumar and H. Choo (2019). "Biophotonic nanostructured translational implants for remote intraocular pressure sensing." In: ***SPIE Photonics West / SPIE BiOS***, San Francisco, CA, USA, February 2–7. (**Oral presentation**).

V. Narasimhan, R. H. Siddique, J. O. Lee, S. Kumar, B. Ndjamen, J. Du, N. Hong, D. Sretavan and H. Choo (2018). "Bioinspired multifunctional nanostructures for micro-optical implants." In: ***Hilton Head Workshop***, Hilton Head, SC, USA, June 3–7. (**Oral presentation, Best Paper Award**).

V. Narasimhan, J. O. Lee, J. Du, B. Ndjamen, D. Sretavan and H. Choo (2017). "Black silicon as a multifunctional material for medical implants: first demonstrated use in in-vivo intraocular pressure sensing." In: ***Transducers***, Kaohsiung, Taiwan, June 18–22. (**Oral presentation**)

D. Magley, **V. Narasimhan** and H. Choo (2017). "Hydro-ionic microthruster for locomotion in low-Reynold's number ionic fluids." In: ***IEEE MEMS***, Las Vegas, NV, USA, January 22–26. (**Poster presentation**)

Patent applications

V. Narasimhan, R. H. Siddique, J. O. Lee and H. Choo (2018). "Intraocular pressure sensor." App. No.: **US20190133442A1**, Filed: September 5.

D. Magley, **V. Narasimhan** and H. Choo (2017). "Systems, methods and devices for electro-osmotic propulsion in a microfluidic environment." App. No.: **US20180078902A1**, Filed: September 20.

H. Choo, A. Balakrishna, O. Chen, K. H. Kim, J. Lee, **V. Narasimhan** and H. Park (2016). "System and method for measuring intraocular pressure." App. No.: **US20170164831A1**, Filed: November 29.

TABLE OF CONTENTS

LIST OF ILLUSTRATIONS

LIST OF TABLES

Chapter 1

STRUCTURAL COLORATION AND MULTIFUNCTIONAL BIOPHOTONIC NANOSTRUCTURES

1.1 Historical perspective

Our understanding of structural colors has truly evolved over the last four centuries. This has involved various degrees of experimental observations and conflicting theories that attempted to elucidate the underlying physics of structural coloration. One of the earliest observations of structural colors appeared in *Micrographia* by Hooke in 1665 [1]. Here, through 17th century microscopy, he described the brilliant colors of peacock and duck feathers that were miraculously extinguished by a drop of water. He theorized that alternating layers of thin materials that comprised the feathers and air interacted with light uniquely, thereby reflecting it. In 1704, Newton in his work *Opticks* [2], posited that the iridescent colors of the peacock feathers arose from the thin transparent parts located within them. The establishment of the electromagnetic theory by Maxwell in 1873 [3] followed by its experimental observation by Hertz in 1884 [4] paved the way for quantifying properties of light such as reflection, refraction, interference and diffraction. As a result, research on structural coloration progressed at an unprecedented scale which lead to two conflicting theories. The first theory was that of pigmentary coloration which was first proposed by Walter in 1895 [5] which attempted to attribute coloration in nature to interaction of light with chemical pigments. The second theory of structural coloration proposed by Rayleigh in 1917 [6] hypothesized that coloration originated purely from interaction of light with physical topology.

1.2 Mechanisms of coloration

Pigmentary colors

Pigmentary colors primarily originate from chemical pigments that absorb a specific bandwidth of light while reflecting the rest. This form of coloration is responsible for most of the green, yellow, red, brown and black colors found on butterfly wings, bird feathers, flower petals and leaves. The absorption bands of pigments correspond with the energy required by absorbed incident

photons to excite electrons in pigment molecules to reach higher energy levels. Figure 1.1 illustrates this concept. In nature, a combination of pigmentary and structural colors can be found to exist simultaneously.

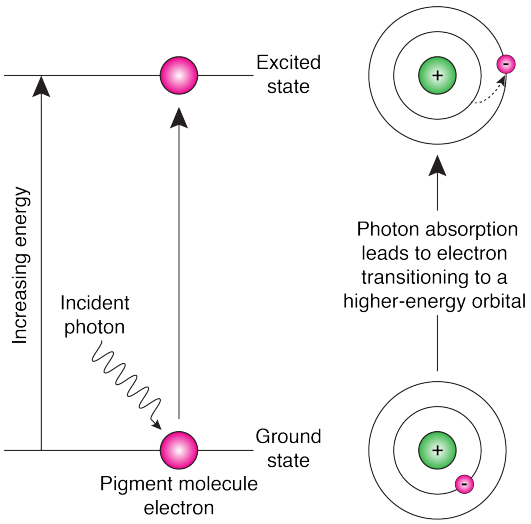

Figure 1.1: The physical process behind pigmentary coloration. Pigment molecules absorb incident photons and the energy imparted by this process excites an electron from the ground state to an excited state. Only incident photons of energies meeting the band-gap between the excited and ground states are absorbed leading to selective absorption and coloration.

In nature, a combination of pigmentary and structural colors can be found to exist simultaneously. For instance, the relative contribution of the two is elegantly shown in Figure 1.2 [7]. Here, different types of Budgerigar (*Melopsittacus undulates*) feathers were spectroscopically analyzed before (solid lines) and after (dashed lines) yellow pigment extraction. It is apparent that pigment concentration has an impact on the relative change of the reflectance profile indicating that the coloration is due to the interplay between pigments and surface topology.

Structural colors

Unlike pigments which leverages narrow-band or broad-band absorption of light to impart coloration, structural coloration is caused by the purely physical interaction of light with various types of spatial inhomogeneity. Structural colors are often brilliant and in many cases iridescent as opposed to pigmentary colors that appear dull and weak regardless of viewing angle. It is generally believed that structural coloration originates from the five following fundamental optical processes or a combination of them: (1) thin-film and multilayer in-

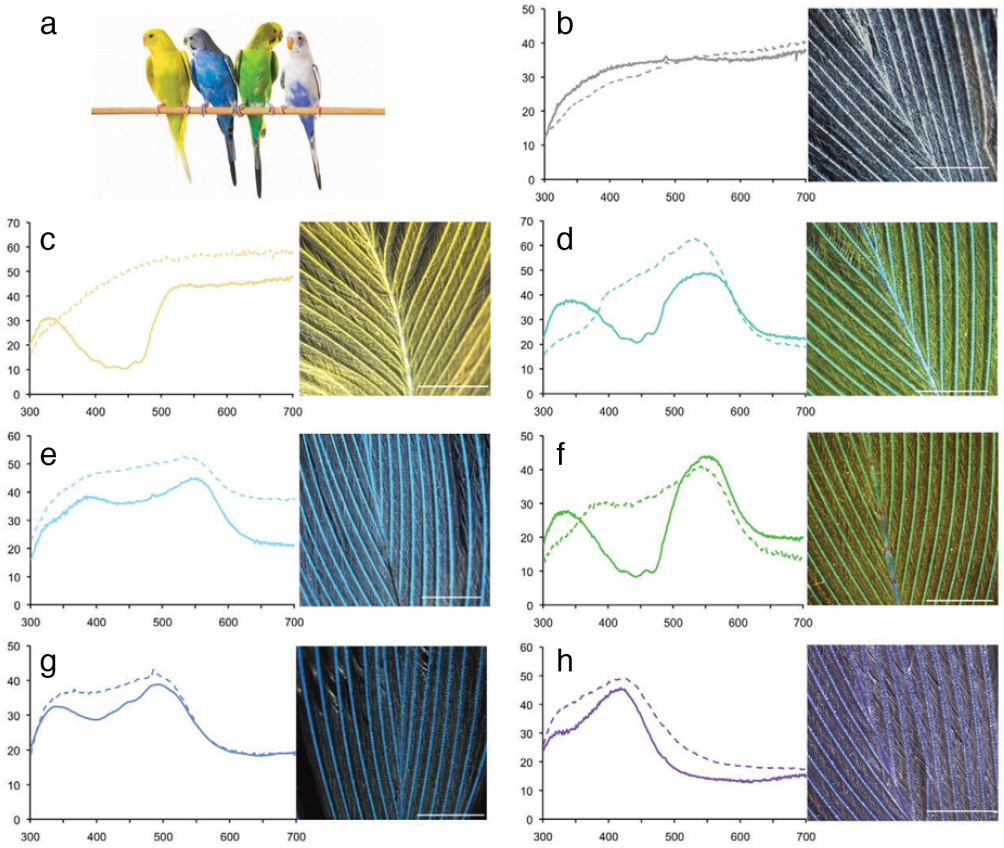

Figure 1.2: Various colored feathers of budgerigars (*M. undulates*) with their reflection spectra measured before (solid line) and after (dashed line) yellow pigment extraction. The difference in coloration before and after extraction is a function of relative distribution of pigmentary and structurally-mediated colors. Image reproduced with permission from [7].

terference, (2) anti-reflection, (3) diffraction gratings, (4) light scattering, and (5) photonic crystals. While, these five categories represent coloration brought about by different physical mechanisms, geometry and spatial distribution of photonic nanostructures also influence coloration. In this context, biophotonic nanostructures can be further categorized as: (1) periodic/ordered, (2) quasi-/short-range ordered, (3) random/disordered.

1.3 Classification of biophotonic nanostructures by distribution

Periodic nanostructures

Periodic nanostructures typically consist of ordered networks of structures much like a crystalline lattice. Periodicity or order can exist in one-, two-,

and three-dimensions as in the case of photonic crystals. Nanostructural distributions in nature are not perfectly ordered. However, they exist over areas that are infinitely larger than wavelengths of light that they interact with. As a result, this interaction can be modeled similar to that of perfectly ordered nanostructures. Examples of 1D periodic nanostructures include Christmas tree-like nanostructures along the cross-section of ridges on the wings of the Morpho butterfly (*Morpho rhetenor*). Nano-holes in an approximate hexagonal lattice on the wings of the black butterfly (*Pachliopta aristolochiae*) are examples of 2D periodic nanostructures as they have two periodic directions. These are shown in Figure 1.3.

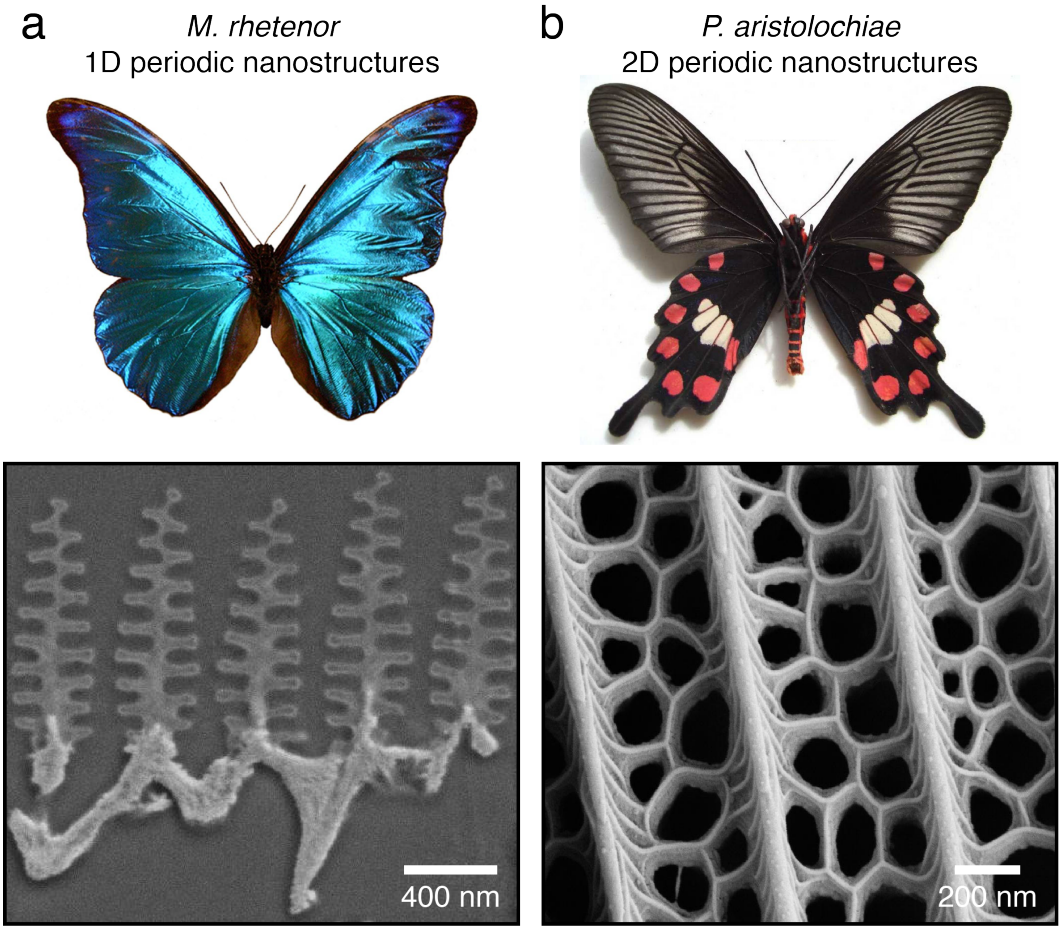

Figure 1.3: Periodic nanostructures in nature. (a) 1D and (b) 2D periodic nanostructures on the wings of the Morpho (*M. rhetenor*) and black (*P. aristolochiae*) butterflies. Image adapted in part with permission from: [8–10]

Quasi-ordered nanostructures

This class of nanostructures sits in between periodic and random nanostructures. A qualitative way of visualizing quasi-ordered or short-range ordered nanostructures is that while they appear disordered in larger length-scales, a regular or predictable periodicity exists over shorter length-scales such as between one or two adjacent nanostructures. Often in nature, this periodicity is isotropic and can be observed by characteristic ring-like patterns in the Fourier space. Because of this isotropy in the k-space, colors produced in this fashion are non-iridescent and do not vary with viewing angle as light effectively interacts with nanostructures with the same periodicity in all directions. Such nanostructures can produce coherent light scattering as shown in Figure 1.4 [11].

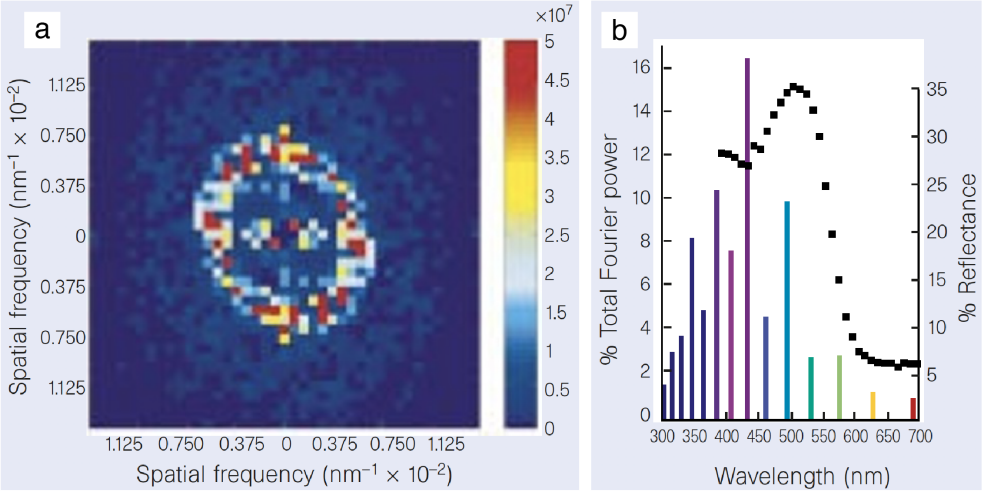

Figure 1.4: Quasi-ordered nanostructures in nature. (a) Pioneering work on blue avian feather barbs revealed a quasi-ordered nanostructure distribution with a characteristic ring-like pattern in the Fourier space. (b) The observed reflectance spectrum of the feather barb is overlaid with the measured 2D Fourier power spectrum. Image reproduced with permission from: [11].

Random nanostructures

Typically, random nanostructures diffuse all wavelengths equally which leads to a white coloration. In nature, random distributions often exist in conjunction with periodic distributions. The interplay bit with coherence brought about by periodicity and incoherence brought about by randomness results in broadband omnidirectional optical properties. An example of this in nature is

the glasswing butterfly (*Greta oto*) wings which consist of short-range ordered nanostructures with a random height distribution as shown in Figure 1.5 [12]. This random height distribution broadens effective refractive index n_{eff} of the system (discussed in greater detail in Section 1.4) which is greatly significant in obtaining omnidirectional broadband anti-reflectivity [12].

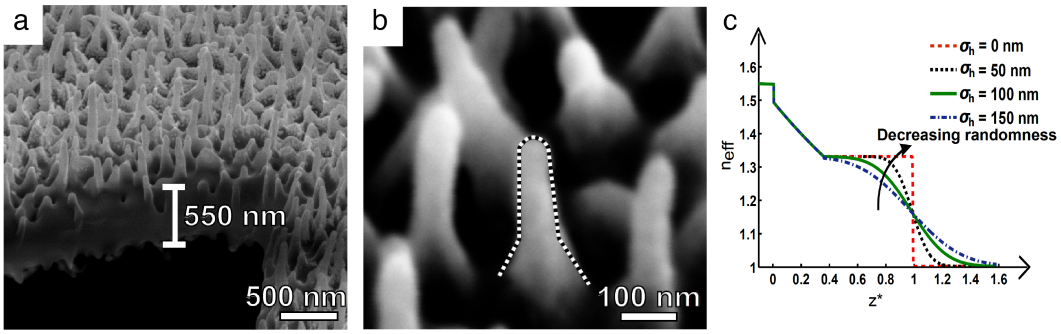

Figure 1.5: Random nanostructures in nature. (a, b) Nanostructures on glasswing butterfly (*G. oto*) wings that have a random height distribution spatially. (c) This randomness smoothens the effective refractive index n_{eff} profile which greatly improves anti-reflectivity. Image reproduced with permission from: [12].

1.4 Optical processes involved in structural coloration

Thin-film and multilayer interference

Some of the most popular examples of structural colors are attributed to the reflection, refraction, and transmission of light at the interface of two dielectric media with different refractive indices n_1 and n_2. As shown in Figure 1.6, light incident at this interface at an angle of θ_1 with respect to the normal of the interface is reflected obeying the condition $\theta_r = -\theta_1$. The refracted light propagates into the second medium at an angle of θ_2 given by Snell's law:

$$n_1 \sin\theta_1 = n_2 \sin\theta_2. \tag{1.1}$$

The reflectance and transmittance at each interface depend on the polarization of light. The two orthogonal linear polarization states in this case are referred to as p- and s-polarization. P-polarized (transverse magnetic, TM) light has its electric field vector parallel to the plane of incidence, while s-polarized (transverse electric, TE) light has its electric field vector perpendicular to the plane of incidence. The amplitude reflectance and transmittance coefficients r_s, t_s, r_p, and t_p for each case are given by Fresnel's equations:

$$r_s = \frac{n_1 \cos\theta_1 - n_2 \cos\theta_2}{n_1 \cos\theta_1 + n_2 \cos\theta_2} \tag{1.2}$$

$$t_s = \frac{2n_1 \cos\theta_1}{n_1 \cos\theta_1 + n_2 \cos\theta_2} \tag{1.3}$$

$$r_p = \frac{n_1 \cos\theta_2 - n_2 \cos\theta_1}{n_1 \cos\theta_2 + n_2 \cos\theta_1} \tag{1.4}$$

$$t_p = \frac{2n_1 \cos\theta_1}{n_1 \cos\theta_2 + n_2 \cos\theta_1}. \tag{1.5}$$

The resultant reflectance R and transmittance T for different combinations of light polarizations as well as for unpolarized light are given by:

$$R_{s,p} = |r_{s,p}|^2 \tag{1.6}$$

$$R = \frac{R_s + R_p}{2} \tag{1.7}$$

$$T_{s,p} = \frac{n_2 \cos\theta_2}{n_1 \cos\theta_1} |t_{s,p}|^2 \tag{1.8}$$

$$T = \frac{T_s + T_p}{2}. \tag{1.9}$$

The above equations hold only for pure dielectric media with no absorption. As a result, due to conservation of energy, $R + T = 1$.

For a multilayer system or a stack of multiple alternating thin films of refractive index n_1 and n_2, the same calculation has to be performed at each interface iteratively. This is illustrated in Figure 1.7. Here, light constructively interferes if the optical path length differences are an integer multiple of the wavelength or $m\lambda$, where m is a positive integer and λ is the wavelength of light at which this condition is met. Similarly, light destructively interferes if the optical path length differences are a half-integer multiple of the wavelength or $(m - \frac{1}{2})\lambda$.

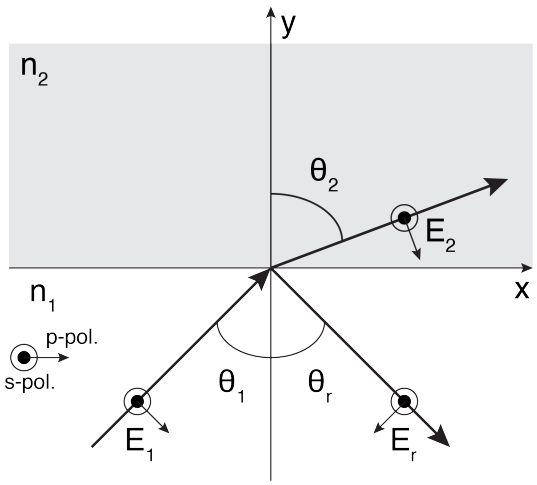

Figure 1.6: Incidence, reflection, and refraction of s- and p-polarized light at an interface of two media with differing refractive indices n_1 and n_2. E_1, E_r, and E_2 represent the electric field vectors of the incident, reflected, and refracted light, respectively.

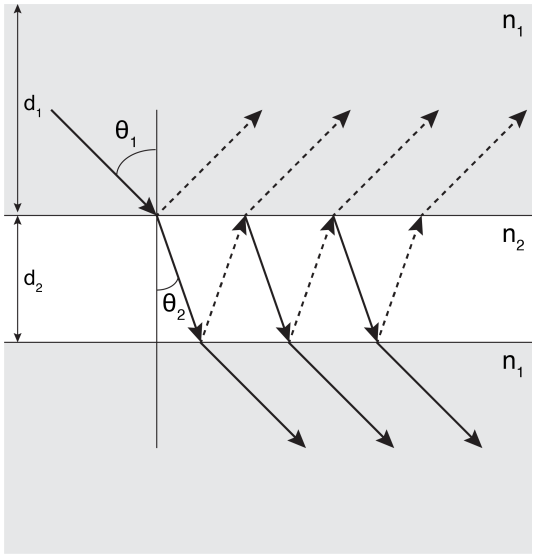

Figure 1.7: The phenomenon of multilayer interference occurring over two alternating thin-film media with differing refractive indices n_1 and n_2.

The relationship between the optical path length and the conditions for interference in each case can be obtained in accordance with Snell's law.

Constructive interference:

$$m\lambda = 2 \cdot n_1 d_1 \cos\theta_1 + n_2 d_2 \cos\theta_2; \tag{1.10}$$

Destructive interference:

$$m - 12\lambda = 2 \cdot n_1 d_1 \cos\theta_1 + n_2 d_2 \cos\theta_2 \tag{1.11}$$

where d_1 and d_2 are the thicknesses of the two alternating layers. The effective reflectance and transmittance for the multilayer system can be computed through solving the Maxwell's equations with matching boundary conditions at each interface followed by the application of the transfer matrix model. Briefly, the amplitude reflection and transmission coefficients ρ and τ can be computed at normal incidence as

$$\rho = \frac{\eta_o - Y}{\eta_o + Y} \tag{1.12}$$

$$\tau = \frac{2\eta_o}{\eta_o + Y} \tag{1.13}$$

where $\eta_o = \sqrt{\frac{\varepsilon_o}{\mu_o}}$ is the surface admittance of the incident medium which is usually free-space with a permittivity and permeability of ε_o and μ_o, respectively. Y is the surface admittance of the thin film stack and the substrate given by

$$Y = \frac{H_T}{E_T} \tag{1.14}$$

$$\begin{bmatrix} E_T \\ H_T \end{bmatrix} = \prod_{j=1}^{q} \begin{bmatrix} \cos\delta_j & \frac{i\sin\delta_j}{y_j} \\ iy_j \sin\delta_j & \cos\delta_j \end{bmatrix} \times \begin{bmatrix} 1 \\ y_{sub} \end{bmatrix} \tag{1.15}$$

where

- E_T and H_T are the normalized total tangential electric and magnetic fields, respectively, at the input surface
- $\delta_j = 2\pi n_j - ik_j \frac{d_j}{\lambda}$ is the phase thickness of layer j
- $n_j - ik_j$ and d_j are the complex refractive index and the physical thickness of the layer j
- y_j is the characteristic admittance of layer j

– q is the number of layers where the q^{th} layer is adjacent to the substrate

– y_{sub} is the characteristic admittance of the substrate.

Finally, the reflectance and transmittance from the stack are given by

$$R = \rho\rho^* = \frac{\eta_1 - Y}{\eta_1 + Y}\frac{\eta_1 - Y}{\eta_1 + Y}^* \tag{1.16}$$

$$T = \frac{4\eta_1 \Re Y}{\eta_1 + Y \eta_1 + Y^*}. \tag{1.17}$$

At oblique angles of incidence, the effect of polarization must be considered. The expressions for ρ, τ, R, and T hold when the admittance is replaced by the tilted admittance $y_j \cos\theta_j$ for s-polarized light and $y_j \cos\theta_j$ for p-polarized light where θ_j is the angle of incidence at the interface of layer j and $j + 1$. Therefore, the reflectance of a multilayer system primarily depends upon the number of layers, the refractive index contrast of the individual layers, the layer thickness, and the angle of incidence. Its dependence on angle of incidence lends to multilayers their metallic, iridescent appearance.

The wings of various species of the Morpho butterfly and fruit of the marble berry (*Pollia condensata*) are fantastic examples of naturally occurring brilliant iridescent colors brought about by thin-film and multilayer interference. Figure 1.3 highlights the Christmas tree-like nanostructures along the cross-section of ridges on the wings of the *M. rhetenor* butterfly. These nanostructures form alternating layers of air and chitin in a multilayer stack. Similarly, as shown in Figure 1.8, the cell walls of the *P. condensata* fruit form a periodic multilayer envelope with nanofibrils oriented in a helical stack that gives rise to polarization-dependent iridescent coloration [13].

Anti-reflection

Anti-reflection is another fascinating consequence of destructive interference in reflection. Broadband and omnidirectional anti-reflection properties have been achieved by omnidirectional biophotonic nanostructures. In butterflies, chitin nanostructures form air-chitin interfaces from which reflection is governed by Fresnel's equations (equations 1.2–1.5). Due to the subwavelength nature of these nanostructures, each interface can be approximated as a thin film with

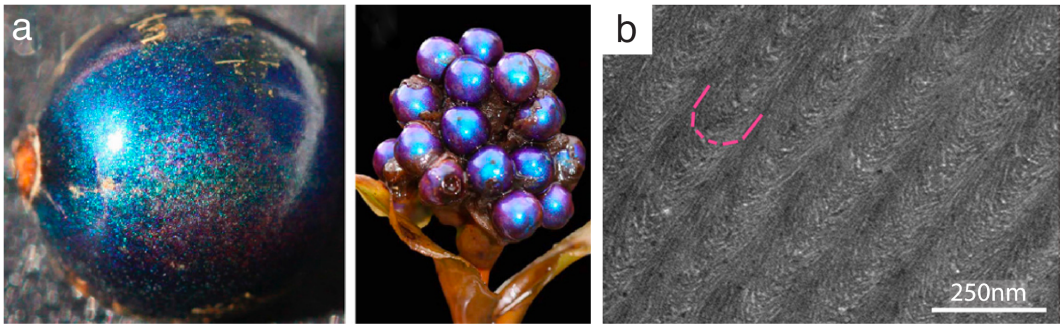

Figure 1.8: Multilayer interference in nature. (a) The fruit of the marble berry (*P. condensata*). (b) The cell walls of the fruit consist of a multilayer stack. The arrangement of nanofibrils is indicated by red lines. Image reproduced with permission from: [13].

an effective refractive index n_{eff} using Maxwell-Garnett model or the effective medium theory [12]

$$n_{\text{eff}}{}^2 = n_{\text{chitin}}{}^2 \frac{2\left(1 - f_{\text{air}}\right) n_{\text{chitin}}{}^2 + \left(1 + 2f_{\text{air}}\right) n_{\text{air}}{}^2}{\left(2 + f_{\text{air}}\right) n_{\text{chitin}}{}^2 + \left(1 - f_{\text{air}}\right) n_{\text{air}}{}^2} \tag{1.18}$$

where n_{chitin} ($n_{\text{chitin}} \approx 1.57$ without absorption) and n_{air} ($n_{\text{air}} = 1$) are the refractive indices of air and chitin respectively while $f_{\text{air}} = 1 - f_{\text{chitin}}$ is the volume fraction of air as a function of height z for a given cross section. For example, as shown in Figure 1.9, the fair for anti-reflective moth eye nanostructures of height h can be mathematically modeled as [12],

$$f_{air} = 1 - \begin{cases} 1 & z < 0 \\ \frac{\pi}{2\sqrt{3}}\left(1 - \frac{z}{h}\right) & 0 \leq z \leq h. \\ 0 & z > h \end{cases} \tag{1.19}$$

Due to the variation of f_{air} as a function of z, n_{eff} also varies as a refractive index gradient as a function of z. As a result, infinitesimal variations in n_{eff} between adjacent layers leads to negligible reflection at each interface as per equations 1.2 and 1.4 since $n_1 \approx n_2$ and $\theta_1 \approx \theta_2$. A simplified version of this concept is illustrated in Figure 1.10.

Like moth eye nanostructures, another truly remarkable example of anti-reflectivity in nature is showcased by the omnidirectional transparency of the glasswing butterfly (*G. oto*) wings (Figure 1.11) [15]. This property is ren-

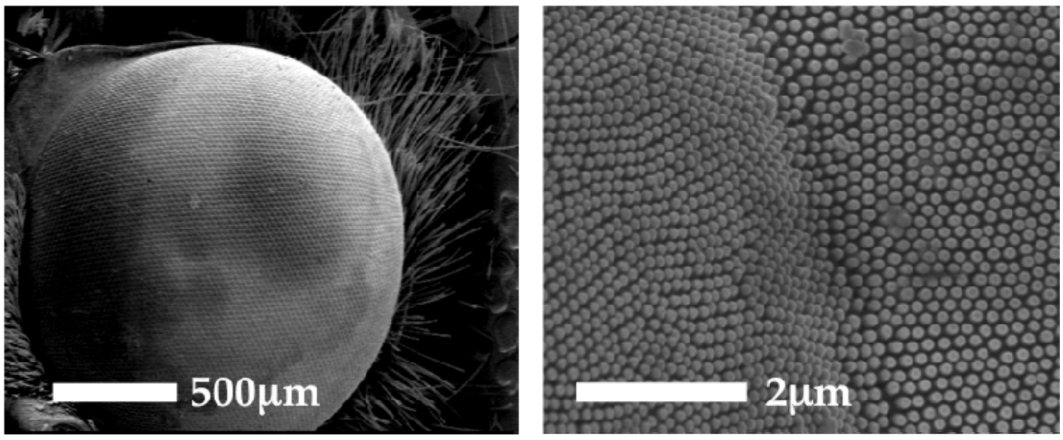

Figure 1.9: SEM images of the moth eye consisting of hexagonally-packed anti-reflective nanostructures. Image reproduced with permission from: [14].

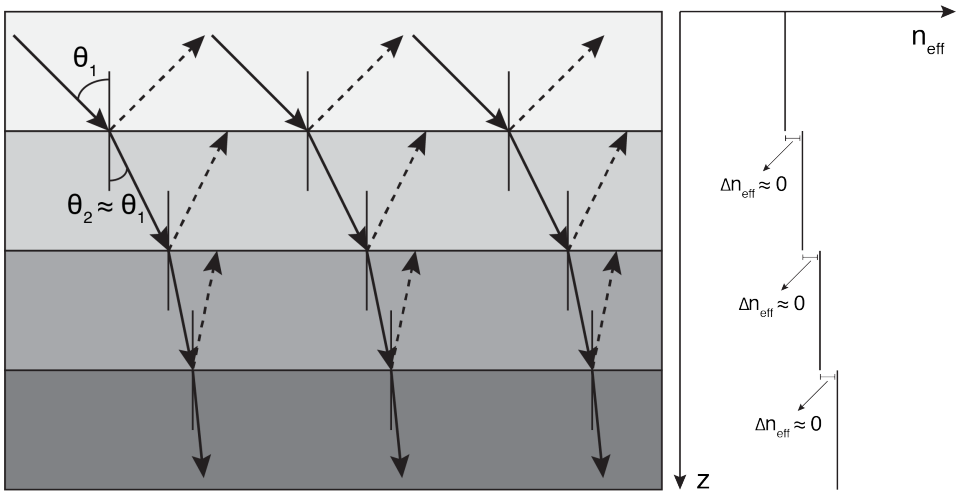

Figure 1.10: The phenomenon of anti-reflectivity occurring over a thin-film stack of media with infinitesimally increasing effective refractive index n_{eff}.

dered by subwavelength nanopillars present on both sides of the dorsal and ventral wing [12].

Diffraction gratings

Diffraction gratings separate different wavelengths of light using periodic structures either in reflection or transmission. The periodic structures modulate the amplitude and/or phase of an incident light wave causing an interference in the output wave that appears as characteristic diffraction patterns. Based on the Rayleigh-Sommerfeld integral and Fraunhofer approximation, the far-field diffraction pattern can be obtained from the Fourier transform of the phase modulation of an incident plane wave assuming the grating periodicity is larger

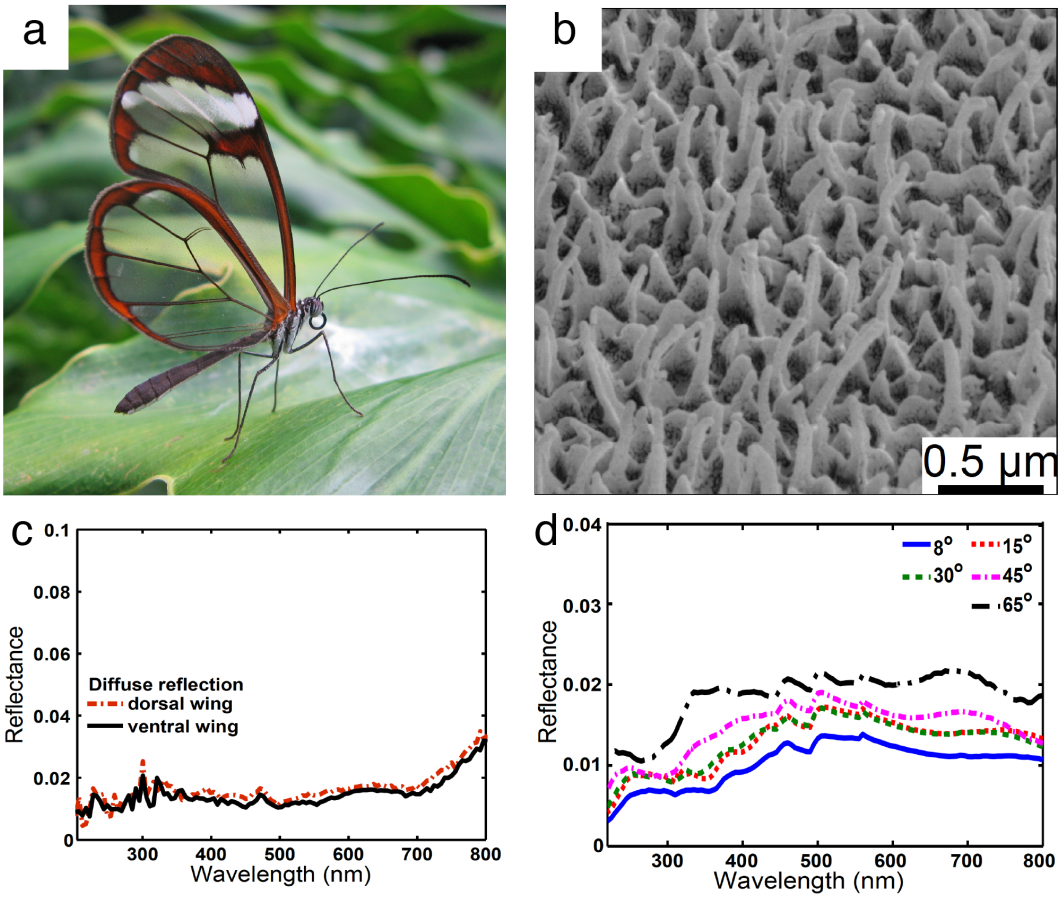

Figure 1.11: Anti-reflection in nature. (a) The glasswing butterfly (*G. oto*) with transparent anti-reflective wings. (b) Quasi-ordered nanostructures of random heights on both sides of the dorsal and ventral wing. (c) The wing has a diffuse reflectance of less than 2%. (d) The reflectance is also omnidirectional. Image reproduced in part with permission from: [12, 15].

than the wavelength of the light. For a diffraction grating of periodicity a, the diffraction pattern corresponds to discrete directions of light propagation also referred to as orders. The generalized diffraction equation for a reflective grating can be written as

$$a\sin\theta_m + \sin\theta_i = m\lambda \qquad m = 0, \pm 1, \pm 2 \ldots \tag{1.20}$$

where θ_i and θ_m are the incident and diffracted angles, m is the order, and λ is the wavelength at which the diffraction condition is met. This is illustrated in Figure 1.12. From the above relationship, it is apparent that the 0th order corresponds to purely specular reflection or $\theta_m = -\theta_i$ and contains no diffrac-

tion pattern due to its λ independence. Due to their dependence on θ_i, colors from diffraction gratings are also iridescent in nature.

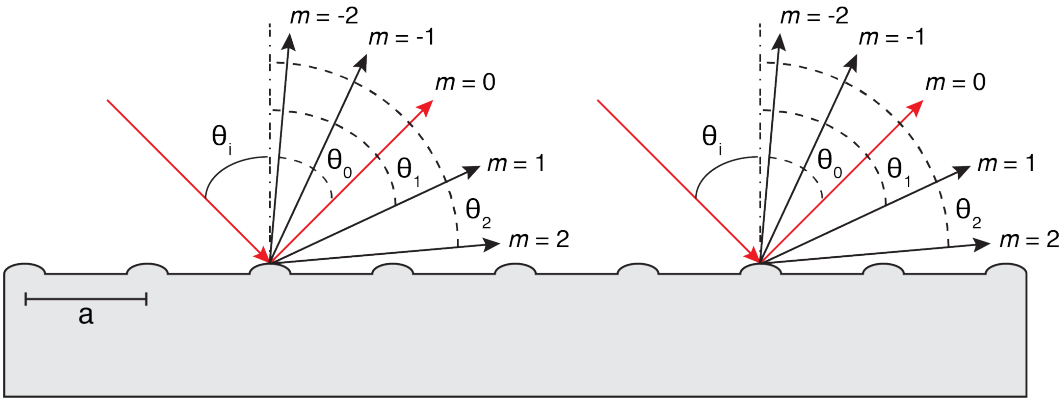

Figure 1.12: Schematic of a reflective grating with periodicity a. The different diffraction modes m with corresponding diffracted angles are shown.

Examples of diffraction grating-based iridescent coloration can be observed on various hibiscus and tulip flowers. For example, *Hibiscus trionum* flowers typically have white petals with an iridescent pigmented patch at the base. The base, which is another example of colors rendered by a combination of pigments and structures appear blue, green, and yellow depending upon the incident angle [16]. This is shown in Figures 1.13a–c. Similar grating structures are also clearly observable on *Tulipa kolpakowskiana*. However, unlike the *H. trionum* whose iridescence is visible to the human eye, the same is only evident in *T. kolpakowskiana* when the pigmentary and structural colors are separated [16]. This could be attributed to the relative pigment concentrations. Figures 1.13d–g show images of an epoxy cast of the *H. trionum* with striations slightly larger than the wavelength of visible light much like those seen on compact discs (CDs) [16].

Light scattering

Light scattering is another important source of structural coloration. Light scattering by particles considerably smaller than the wavelength of light is called Rayleigh scattering. Rayleigh scattering, whose intensity $I \propto \lambda^{-4}$ has a strong wavelength dependence, is an omnidirectional and incoherent process. In other words, the scattering intensity is uniform in all directions and scattered light originating from individual scatterers do not interfere. This is because the particles being considerably smaller than the wavelength of light ($d \leq \frac{\lambda}{10}$) generate negligible phase differences. For example, the origin of the

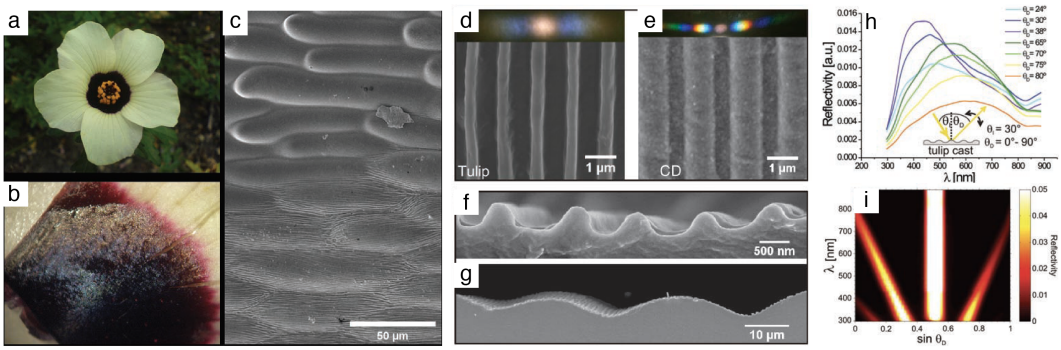

Figure 1.13: Diffraction in nature. (a-c) Diffraction gratings observable on the base of the *H. trionum* flowers. (d, f) A cast made from *T. kolpakowskiana* flowers reveals a grating structure much like those on (e, g) compact discs. (h) The iridescence of coloration from the grating structures on *T. kolpakowskiana* casts is clearly observable as reflectivity from the surface is angle-dependent. (i) The zeroth, first, and second order modes from the cast gratings is shown. The zeroth order mode is purely specular and wavelength-independent. Image reproduced with permission from: [16].

blue sky is explained by Rayleigh scattering as blue light due to its shorter wavelength is scattered considerably more through this phenomenon. When the size of the particle or scatterer is comparable or larger than the wavelength of light, the regime of Mie scattering becomes prominent. This form of scattering is directional in that particles scatter light forward considerably more than in the backward direction. This is because owing to the larger sizes of the particles, light is scattered primarily by reflection, refraction, and diffraction. As the particle sizes become larger than the wavelength of light, the scattered light is only weakly dependent on the wavelength. Like Rayleigh scattering, the Mie scattering model is also typically incoherent because individual Mie scatterers in a system are spatially incoherent or randomly distributed.

In nature, however, coherent scattering is what predominantly occurs due to a certain order or spatial periodicity among individual scatterers. Due to a periodic spatial variation in refractive index, predictable phase relationships among light waves scattered by different scatterers occur, thereby reinforcing a limited set of wavelengths. Unlike incoherent scattering, coherent scattering from periodic structures can produce iridescent colors. In this regard, multilayer interference, diffraction, and Bragg scattering are all examples of iridescent coherent scattering.

Research over the last decade has revealed a new class of quasi-ordered nanos-

tructures that can produce non-iridescent or angle-invariant coloration through coherent scattering alone [17]. This form of ordering is covered in greater detail in Chapters 4 and 6.

A classic example of such coherent scattering in nature is found on the violet and blue feather barbs of many birds [18]. Previously confused with incoherent Rayleigh or Tyndall scattering, recent work has conclusively shown that this form of coloration is brought about by coherent scattering due to quasi-ordered vacuoles in spongy keratin located in the medullary layers of bird feathers [18]. This is shown in Figure 1.14 for scarlet macaw (*Ara macao*) blue feather barbs.

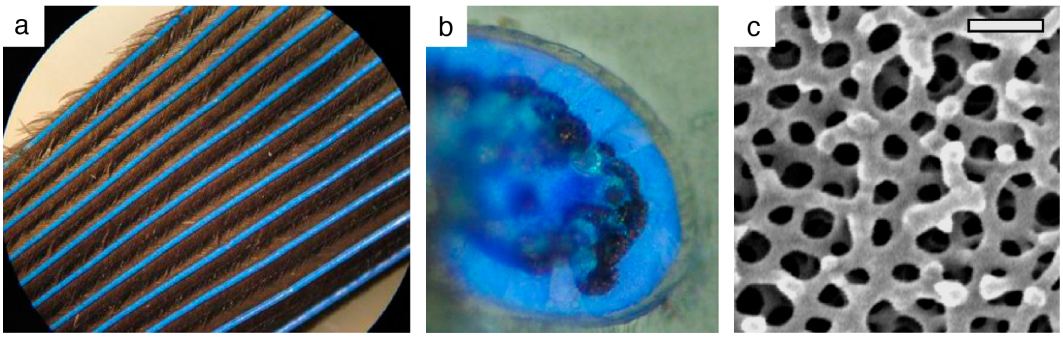

Figure 1.14: Scattering in nature. (a-b) The blue feather barbs of the *A. macao*. (c) Quasi-ordered vacuoles in the spongy keratin located in the medullary layers of the feather barbs coherently scatter violet and blue light to produce non-iridescent coloration. Image reproduced with permission from: [18].

Photonic crystals

Photonic crystals are formed by periodic or quasi-ordered structures composed of two or more media with different refractive indices. As shown in Figure 1.15, photonic crystals can exist in one-, two-, and three-dimensions [19, 20]. From Figure 1.15, it is also clear that multilayer interference stacks and diffraction gratings are examples of one-dimensional photonic crystals. Similarly, the light scattering vacuoles in spongy keratin located on bird feather barbs is an example of quasi-ordered three-dimensional photonic crystals. The main property of photonic crystals is their band-gap. Their optical structure mediates the motion of photons similar to how ionic lattices affect electrons. Akin to semiconductors which possess band-gaps or energy barriers between the top of the valence band and the bottom of the conduction band, which is essentially a forbidden zone for electrons due to a lack of electronic states, photonic crystal

band-gaps act as forbidden zones for photons of certain wavelengths. It is this band-gap property that lends coloration for photonic crystal structures.

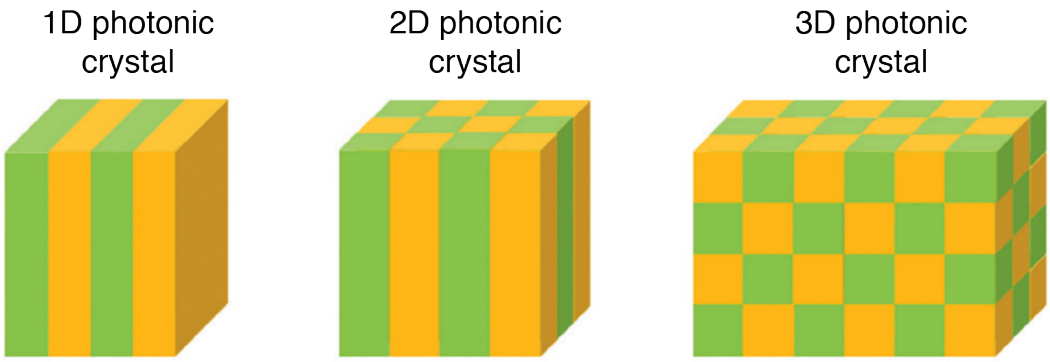

Figure 1.15: Illustrations of 1-, 2- and 3-D photonic crystal structures. Image reproduced with permission from: [20].

In nature, examples of tunable photonic crystal structures that result in active color modulation exist. This can be achieved through alterations in the physical geometry of the structures. The skin of the panther chameleon (*Furcifer pardalis*), which can modulate its skin color from blue or green to yellow or orange, contains iridophore cells with guanine crystals of differing size, shapes, and orientation [21]. As shown in Figure 1.16, this architecture is analogous to a periodic two-dimensional photonic crystal. It was observed that the distance between guanine crystals or the periodicity of the photonic crystal was on average 30% smaller in the resting state where the skin appears blue or green compared to the excited state where the skin appears yellow or orange [21].

1.5 Objectives and outline

Beyond structural coloration, biophotonic nanostructures are truly multifunctional [22, 23]. A rich body of literature has documented the utilization of such nanostructures as self-cleaning surfaces [24], bactericidal surfaces [25], gas sensors [26], thermal sensors [27], waveguides and beam splitters [28], and solar cells [29], to name a few. Figure 1.17 summarizes some of this work. With the ever-increasing need for robust biomedical devices to support various bodily functions, the requirement to incorporate multiple functionalities within sensing packages with small footprints becomes incumbent [23]. In this regard, the multifunctionality of biophotonic nanostructures may prove to be of great benefit for various biomedical applications such as *in vivo* sensing,

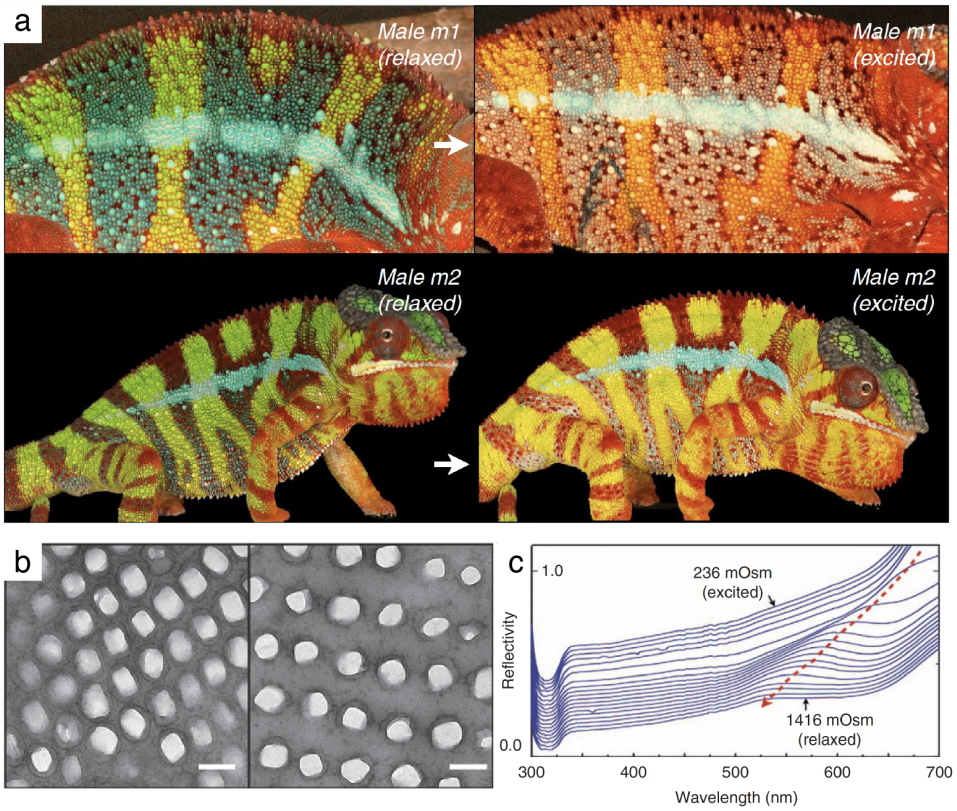

Figure 1.16: Photonic crystals in nature. (a) The panther chameleon (*F. pardalis*) that can change its skin color from green to orange when transitioning from a relaxed to an excited state. (b) 2-D periodic photonic crystal structures found on the skin. The periodicity of these structures is altered between the relaxed (left) and excited (right) states. (c) Measured reflectivity of the skin during the transition. Image reproduced with permission granted under Creative Commons CC BY License from: [21].

imaging, and stimulation. While various efforts have demonstrated engineered analogs of biophotonic nanostructures mimicking the functionalities of their natural counterparts, the use of such synthetic nanostructures in biomedicine remains largely unexplored.

The objective of this work is to therefore present various instances of the effective utilization of multifunctional nanostructures inspired from biophotonic nanostructures for medical applications. Figure 1.18 summarizes the confluence of various research themes presented here.

In the introductory chapter presented so far, various biophotonic nanostructures are broadly categorized, their multifunctionality beyond structural coloration is described, and a need for bioinspired multifunctional nanostructures

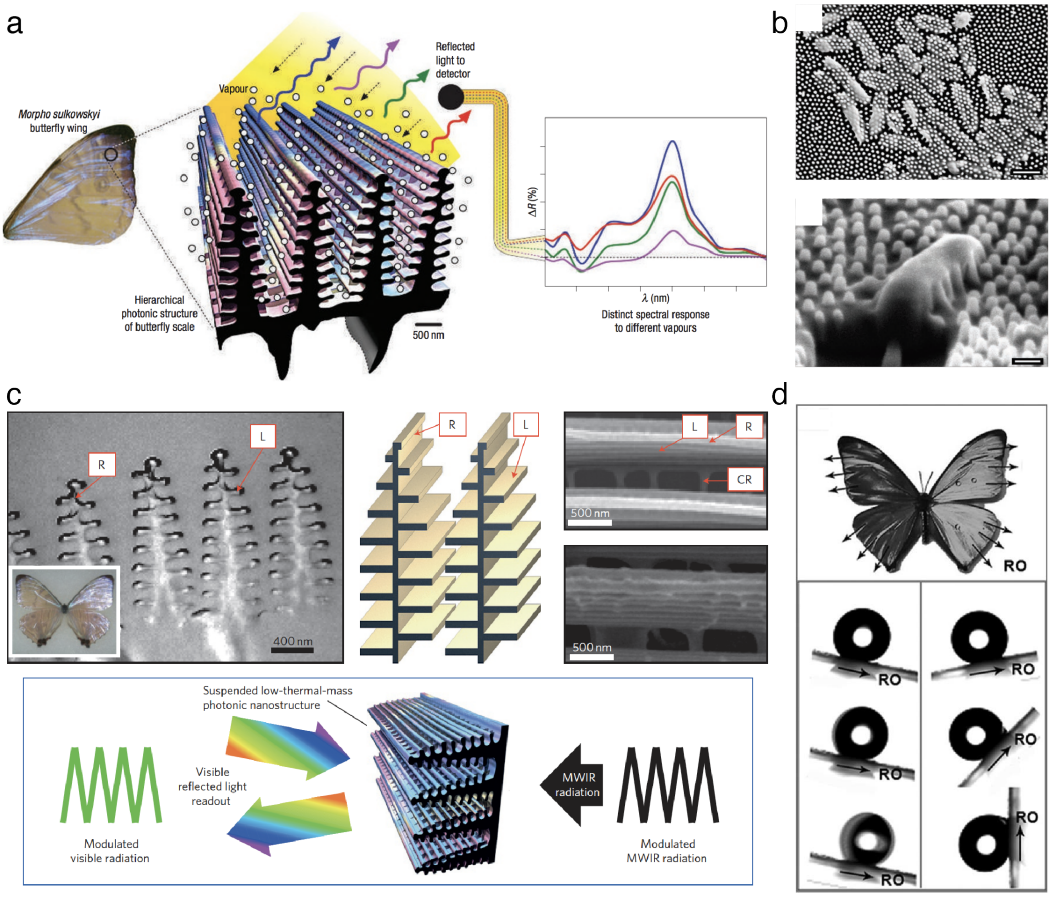

Figure 1.17: Multifunctionality of biophotonic nanostructures. (a) Wings of the *Morpho sulkowskyi* butterfly used for vapor sensing. Image reproduced with permission from: [26]. (b) Bactericidal activity of *Psaltoda claripennis* wings. Image reproduced with permission from: [25]. (c) Doped *M. sulkowskyi* scales used for infrared imaging. Image reproduced with permission from: [27]. (d) Self-cleaning properties of *Morpho aega* wings. Image reproduced with permission from: [24].

in biomedicine is motivated. Chapter 2 introduces glaucoma and a proof-of-concept passive optically-driven intraocular pressure (IOP) sensor implant. Chapters 3 and 4 present challenges faced during *in vivo* implementation of the IOP implant and how bioinspired nanostructures mitigated those challenges. Specifically, Chapter 3 covers the engineering, characterization, and *in vivo* testing of synthetic nanostructures embedded onto the IOP sensor platform inspired by light-trapping epidermal micro-/nanostructures on flower petals. These nanostructures improve the optical signal-to-noise ratio (SNR) of the device by absorbing background bias and also improve the *in vivo* biophysical properties of the device. Chapter 4 first deals with the in-depth study of the

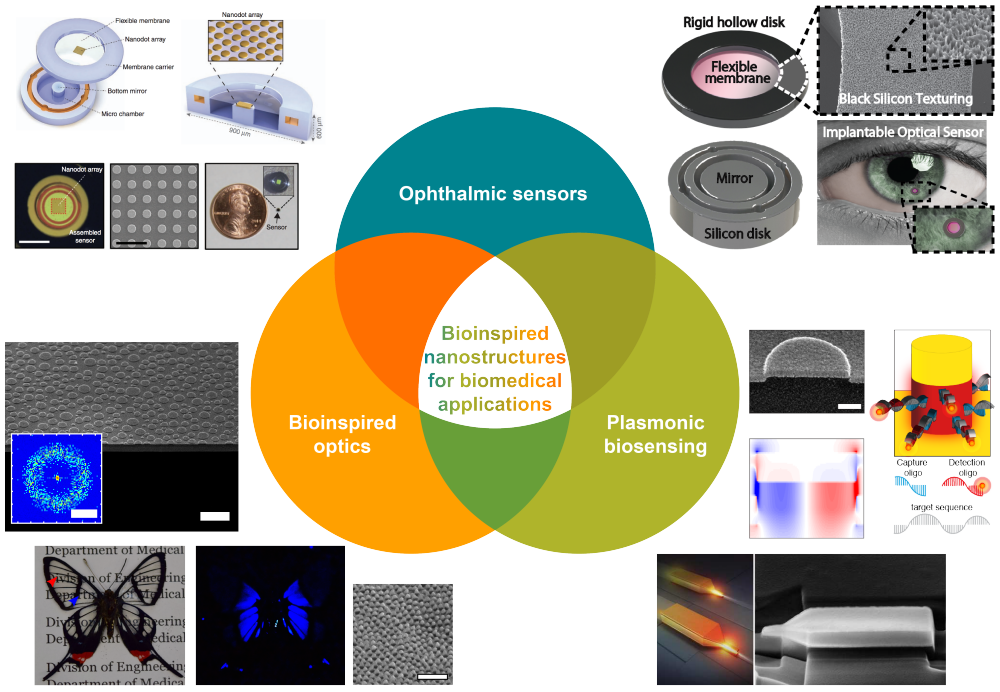

Figure 1.18: The objective of this work is to present various instances of the utilization biophotonic nanostructures for biomedical sensing applications. The research themes covered here broadly span three categories – ophthalmic sensors, plasmonic biosensing, and bioinspired optics.

optical and biophysical properties of longtail glasswing butterfly (*Chorinea faunus*) wings. Next, a subset of these properties are incorporated onto the IOP sensor platform to enhance the *in vivo* angle of acceptance and biocompatibility, thereby greatly improving usability and longevity. Chapters 5 and 6 present optical on-chip diagnostics platforms consisting of bioinspired tunable plasmonic nanostructures fabricated through a simple and scalable biomimetic technique. In Chapter 5, we discuss how these nanostructures enable the rapid multiplexed sensing of various nucleic acid sequences such as oligonucleotides, single-stranded DNA (ssDNA), and messenger RNA (mRNA) from the lysate of live cell cultures. Here, the underlying physics that enables broadband enhancement of optical signal from on-chip-bound low-concentration nucleic acid bio-analytes is elucidated through rigorous simulations and experimentation following which a useful application of the platform is demonstrated. Chapter 6 presents a flexible variant of similar bioinspired nanostructures used for label-free near-infrared (NIR) surface-enhanced Raman scattering (SERS) biosensing of uric acid from whole human tears. Here, the beneficial effect of bioinspired quasi-order (discussed in Section 1.3) towards broadband SERS

enhancement is covered. Finally, Chapter 7 offers concluding remarks and presents the future outlook of this research.

References

[1] Robert Hooke. *Micrographia: or, Some physiological descriptions of minute bodies made by magnifying glasses*. London: J. Martyn and J. Allestry, 1665.

[2] Isaac Newton. *Opticks: or, A treatise of the reflections, refractions, inflections and colours of light*. London: S. Smith and B. Walford, first edition, 1704.

[3] James Clerk Maxwell. *A treatise on electricity and magnetism*. Oxford : Clarendon Press, first edition, 1873. ISBN 9780511709333. doi: 10.1017/CBO9780511709333.

[4] Heinrich Hertz. *On the relation between Maxwell's fundamental electromagnetic equations and the fundamental equations of the opposing electromagnetics*. London: Macmillan, first edition, 1884.

[5] Bernhard Walter. *Die Oberflächen- oder Schiller-Farben*. Braunschweig: F. Vieweg und Sohn, first edition, 1895.

[6] Lord Rayleigh. On the reflection of light from a regularly stratified medium. *Proceedings of the Royal Society of London. Series A*, 93(655): 565–577, 1917. doi: 10.1098/rspa.1917.0040.

[7] Liliana D'Alba, Leah Kieffer, and Matthew D. Shawkey. Relative contributions of pigments and biophotonic nanostructures to natural color production: A case study in budgerigar (*Melopsittacus undulatus*) feathers. *The Journal of Experimental Biology*, 215(8):1272–1277, 2012. doi: 10.1242/jeb.064907.

[8] Kathryn Knight. Making *Morpho* butterflies blue. *Journal of Experimental Biology*, 219(24):3823–3824, 2016. doi: 10.1242/jeb.153825.

[9] Radwanul Hasan Siddique. *Structural colors of butterflies: Analysis and fabrication of bio-inspired nanophotonic surfaces*. PhD thesis, Karlsruhe Institute of Technology (KIT), February 2016.

[10] `https://en.butterflycorner.net/Pachliopta-aristolochiae-Common-Rose.532.0.html`, 2019 (Accessed: Oct 28, 2019).

[11] Richard O. Prum, Rodolfo H. Torres, Scott Williamson, and Jan Dyck. Coherent light scattering by blue feather barbs. *Nature*, 396(6706):28–29, 1998. doi: 10.1038/23838.

[12] Radwanul Hasan Siddique, Guillaume Gomard, and Hendrik Holscher. The role of random nanostructures for the omnidirectional anti-reflection properties of the glasswing butterfly. *Nature Communications*, 6(1):1–8, 2015. doi: 10.1038/ncomms7909.

[13] Silvia Vignolini, Paula J. Rudall, Alice V. Rowland, Alison Reed, Edwige Moyroud, Robert B. Faden, Jeremy J. Baumberg, Beverley J. Glover, and Ullrich Steiner. Pointillist structural color in *Pollia* fruit. *Proceedings of the National Academy of Sciences*, 109(39):15712–15715, 2012. doi: 10.1073/pnas.1210105109.

[14] Federico Lora Gonzalez and Michael J. Gordon. Bio-inspired, sub-wavelength surface structures for ultra-broadband, omni-directional anti-reflection in the mid and far IR. *Optics Express*, 22(11):12808–12816, 2014. doi: 10.1364/OE.22.012808.

[15] `https://en.wikipedia.org/wiki/Greta_oto`, 2019 (Accessed: Oct 28, 2019).

[16] Heather M. Whitney, Mathias Kolle, Piers Andrew, Lars Chittka, Ullrich Steiner, and Beverley J. Glover. Floral iridescence, produced by diffractive optics, acts as a cue for animal pollinators. *Science*, 323(5910):130–133, 2009. doi: 10.1126/science.1166256.

[17] Richard O. Prum, Tim Quinn, and Rodolfo H. Torres. Anatomically diverse butterfly scales all produce structural colours by coherent scattering. *Journal of Experimental Biology*, 209(4):748–765, 2006. doi: 10.1242/jeb.02051.

[18] Haiwei Yin, Biqin Dong, Xiaohan Liu, Tianrong Zhan, Lei Shi, Jian Zi, and Eli Yablonovitch. Amorphous diamond-structured photonic crystal in the feather barbs of the scarlet macaw. *Proceedings of the National Academy of Sciences*, 109(27):10798–10801, 2012. doi: 10.1073/pnas.1204383109.

[19] John D. Joannopoulos, Steven G. Johnson, Joshua N. Winn, and Robert D. Meade. *Photonic crystals: Molding the flow of light*. Princeton University Press, second edition, 2011. ISBN 9780691037448. doi: 10.2307/j.ctvcm4gz9.

[20] Junshi Liu, Mengnan Yao, and Liang Shen. Third generation photovoltaic cells based on photonic crystals. *Journal of Materials Chemistry C*, 7: 3121–3145, 2019. doi: 10.1039/C8TC05461D.

[21] Jérémie Teyssier, Suzanne V. Saenko, Dirk van der Marel, and Michel C. Milinkovitch. Photonic crystals cause active colour change in chameleons. *Nature Communications*, 6(1):1–7, 2015. doi: 10.1038/ncomms7368.

[22] Shichao Niu, Bo Li, Zhengzhi Mu, Meng Yang, Junqiu Zhang, Zhiwu Han, and Luquan Ren. Excellent structure-based multifunction of *Morpho* butterfly wings: A review. *Journal of Bionic Engineering*, 12(2):170–189, 2015. doi: 10.1016/S1672-6529(14)60111-6.

[23] Vinayak Narasimhan, Radwanul Hasan Siddique, Jeong Oen Lee, Shailabh Kumar, Blaise Ndjamen, Juan Du, Natalie Wong, David Sretavan, and Hyuck Choo. Multifunctional biophotonic nanostructures inspired by the longtail glasswing butterfly for medical devices. *Nature Nanotechnology*, 13(6):512–519, 2018. doi: 10.1038/s41565-018-0111-5.

[24] Yongmei Zheng, Xuefeng Gao, and Lei Jiang. Directional adhesion of superhydrophobic butterfly wings. *Soft Matter*, 3(2):178–182, 2007. doi: 10.1039/B612667G.

[25] Elena P. Ivanova, Jafar Hasan, Hayden K. Webb, Vi Khanh Truong, Gregory S. Watson, Jolanta A. Watson, Vladimir A. Baulin, Sergey Pogodin, James Y. Wang, Mark J. Tobin, Christian Löbbe, and Russell J. Crawford. Natural bactericidal surfaces: Mechanical rupture of *Pseudomonas aeruginosa* cells by cicada wings. *Small*, 8(16):2489–2494, 2012. doi: 10.1002/smll.201200528.

[26] Radislav A. Potyrailo, Helen T. Ghiradella, Alexei Vertiatchikh, Katharine Dovidenko, James R. Cournoyer, and Eric Olson. *Morpho* butterfly wing scales demonstrate highly selective vapour response. *Nature Photonics*, 1(2):123–128, 2007. doi: 10.1038/nphoton.2007.2.

[27] Andrew D. Pris, Yogen Utturkar, Cheryl Surman, William G. Morris, Alexey Vert, Sergiy Zalyubovskiy, Tao Deng, Helen T. Ghiradella, and Radislav A. Potyrailo. Towards high-speed imaging of infrared photons with bio-inspired nanoarchitectures. *Nature Photonics*, 6(3):195–200, 2012. doi: 10.1038/nphoton.2011.355.

[28] Jingyun Huang, Xudong Wang, and Zhong Lin Wang. Controlled replication of butterfly wings for achieving tunable photonic properties. *Nano Letters*, 6(10):2325–2331, 2006. doi: 10.1021/nl061851t.

[29] Radwanul H. Siddique, Yidenekachew J. Donie, Guillaume Gomard, Sisir Yalamanchili, Tsvetelina Merdzhanova, Uli Lemmer, and Hendrik Hölscher. Bioinspired phase-separated disordered nanostructures for thin photovoltaic absorbers. *Science Advances*, 3(10):1–11, 2017. doi: 10.1126/sciadv.1700232.

Chapter 2

GLAUCOMA AND INTRAOCULAR PRESSURE SENSING

2.1 Introduction to glaucoma

Today, glaucoma is a leading cause of irreversible blindness [1, 2]. Around 70 million people world-wide suffer from glaucoma [1]. It is estimated that over 3 million Americans have glaucoma, but have not been formally diagnosed [3]. Glaucoma is an umbrella term for a variety of related ocular pathologies. There are two major types of glaucoma – primary open-angle and angle-closure (or closed-angle) glaucoma.

Primary open-angle is the most common type of glaucoma and is chronic in nature. Normally, the eye produces a fluid called the aqueous humor which originates from the ciliary body. It then travels through the posterior chamber (the region between the iris and the lens), through the pupil into the anterior chamber (the region between the iris and the cornea). It is then drained out through a mesh-like network called the trabecular meshwork. The aqueous humor largely consists of water (98% water) with amino acids and electrolytes. The aqueous humor has various functions, chief amongst which are (1) maintaining the intraocular pressure (IOP) or the hydrostatic pressure inside the eye and (2) providing nutrition for the avascular regions of the eye such as the posterior cornea, trabecular meshwork, lens, and anterior vitreous. In a diseased state, the aqueous humor drainage pathway is either partially or completely blocked leading to fluid build-up within the eye. This, in turn, elevates the IOP which leads to damage of the optic nerve fibers located at the back of the eye. Initial symptoms include tunnel vision which could lead to permanent visual loss if the progression of the disease is inadequately monitored. Angle-closure is an acute form of glaucoma where the iridocorneal angle is significantly narrowed by the iris which leads to blockage of the drainage pathway. The mechanism of the disease progression in both cases is shown in Figure 2.1.

Barring some sub-categories of glaucoma, a major risk factor associated with the disease in general is elevation in IOP [5]. It is posited that both nocturnal and diurnal spikes in IOP are a major contributing factor towards the damage

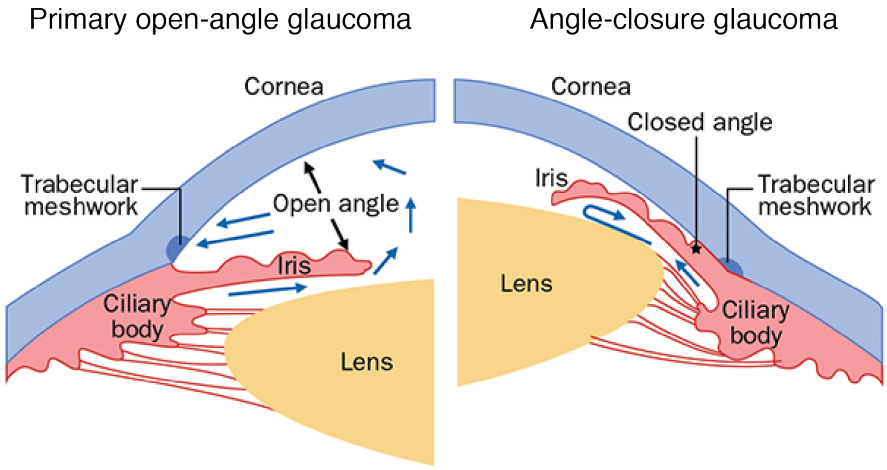

Figure 2.1: The mechanism of the disease progression in primary open-angle and angle-closure glaucoma [4].

of the optic nerve fiber. Furthermore, IOP can also be influenced by patient activity, diet, and other factors that are not well understood [6–9]. Therefore, the monitoring of IOP in an accurate and high-throughput fashion becomes crucial to not only better understand the progression of glaucoma, but to also inform the timely administration of IOP lowering treatment modalities.

2.2 Current IOP measurement techniques

As shown in Figure 2.2, current gold-standard techniques for IOP measurement include Goldmann, air-puff, rebound, and dynamic contour tonometry, amongst others. However, they are indirect measurement techniques that are heavily influenced by factors such as the corneal biomechanics [10]. They are also typically bulky and expensive pieces of equipment that require trained staff such as technicians to operate [11]. As a result, patient IOP 'snapshots' are recorded a few times annually during visits to the clinic. These measurements are extremely inadequate due to the fact that IOP varies at much shorter time-scales such as hours and days. Both wearable and implantable solutions for continual monitoring of IOP have been developed with technologies such as SENSIMED Triggerfish® [12] and Implandata EYEMATE® [13] being notable examples. These approaches are based on RF systems that telemetrically power and communicate with the devices. They are limited by very short readout distances and cannot be arbitrarily miniaturized due to the dependence of interrogation and readout signals on distances and size [14, 15]. As a result, *in vivo* measurements have only been obtained by large RF-based

devices that are 0.5 – 1 cm in diameter [16–18]. Furthermore, the practical use of such technology is limited by the need for sophisticated detection systems such as vector-network analyzers (VNAs) [19].

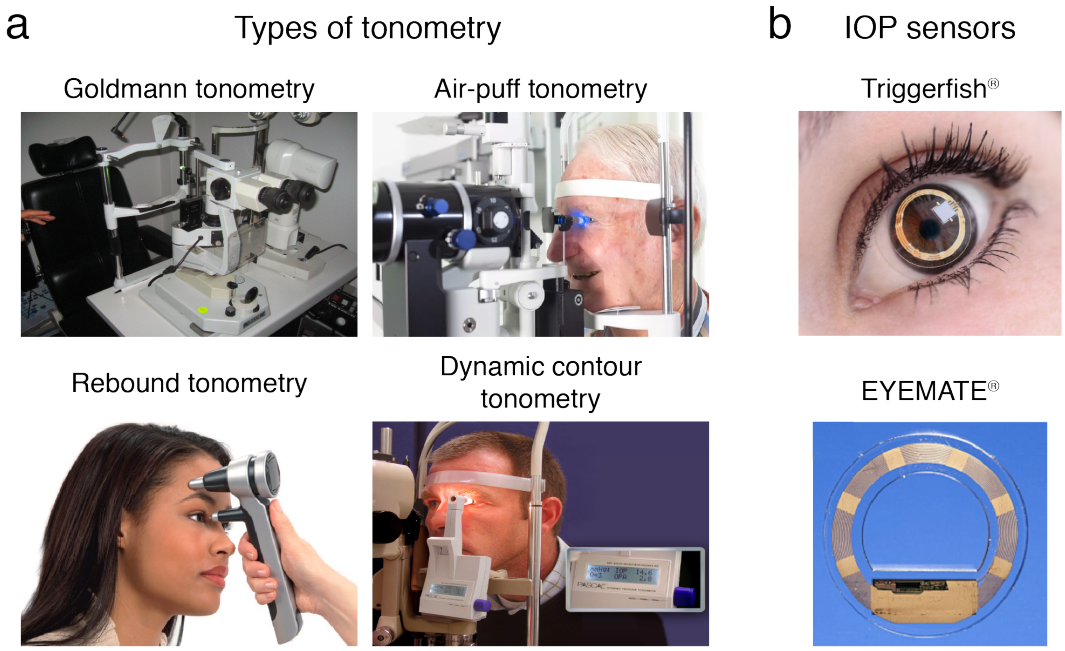

Figure 2.2: Current IOP measurement solutions. (a) Different types of tonometry routinely used in clinics for IOP measurements [20–22]. (b) Notable IOP sensors include contact lens-based devices such as the Triggerfish® and implants such as the EYEMATE® [12, 13].

2.3 IOP implant

Working principle

To enable accurate high-throughput and real-time IOP monitoring, this section reports the development of a highly-miniaturized (sub-mm) IOP sensor implant. The sensor is passive (i.e. requires no battery for operation), interrogated and read out purely through broadband near-infrared (NIR) light. It consists of two parts: (1) a deformable silicon nitride (Si_3N_4) membrane that is suspended over (2) a reflective silicon (Si) mirror. The two parts are separated by a carefully engineered microscale recess and are sealed together to form a Fabry-Perot (FP) cavity or an optical resonator. Under ambient pressure changes, the membrane deforms, thereby changing the gap-size of the FP cavity. This change in gap-size induces a wavelength-shift in the optical resonance of the cavity which is in turn used to discern the ambient pressure change. A schematic of the device working principle is shown in Figure 2.3.

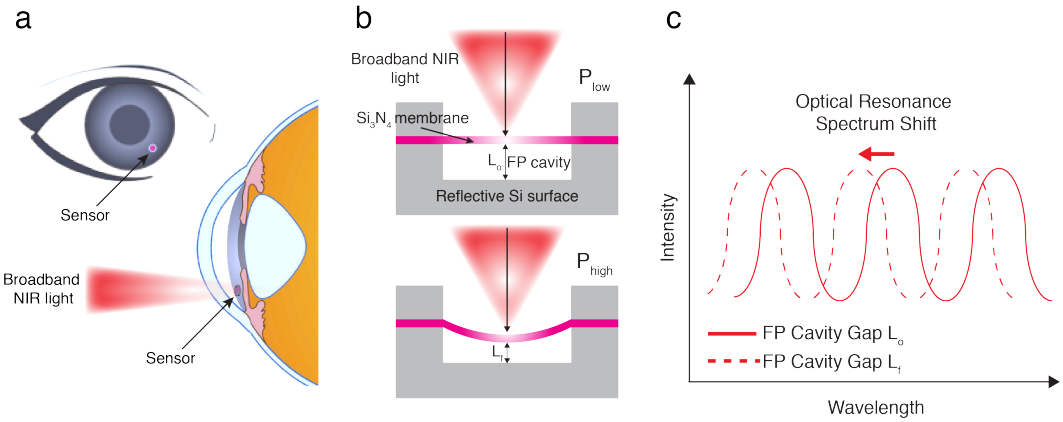

Figure 2.3: IOP sensor implant working principle. (a) Schematic of the IOP sensor implant. (b,c) Implant working principle. Change from a pressure state of P_{low} to P_{high} changes the FP cavity gap-size from L_o to L_f which blue-shifts its optical resonance.

The FP cavity operates on the principle of interference which is described in Section 1.4. Similar to equation 1.10, the optical path difference or phase-shift undergone by light interacting with the cavity is an integer multiple of λ,

$$\phi = \frac{2\pi d}{\lambda} \tag{2.1}$$

where d is the gap-size. The intensity of the transmitted light I_{out} as a function of the incident light I_{in} can be written as [23]

$$I_{\text{out}} = I_{\text{in}} \frac{1 - R^2}{1 - R^2 + 4R \sin \phi} \tag{2.2}$$

where R is the reflectivity of the membrane and mirror surfaces (assumed to be the same in this relationship). The transmittance T from the cavity can be expressed as $T = \frac{I_{\text{out}}}{I_{\text{in}}}$.

Two standard performance parameters of FP cavities are typically tuned: (1) the full-width-at-half-maximum (FWHM or γ) and (2) the free spectral range (FSR). The FWHM essentially measures the bandwidth of the signal at half the intensity while the FSR is peak-to-peak distance. Another parameter that is often reported is the finesse which is simply $\frac{FSR}{\gamma}$. These parameters are illustrated in Figure 2.4a. By altering the R and d of the cavity, the γ and FSR can be altered. Figure 2.4b shows the theoretical resonance profile of cavities with R of 0.1, 0.5, and 0.9 for a fixed d of 10 μm. Similarly, Figure

2.4c shows the profile of cavities with d of 2.5 μm, 5 μm, and 10 μm for a fixed R of 0.1.

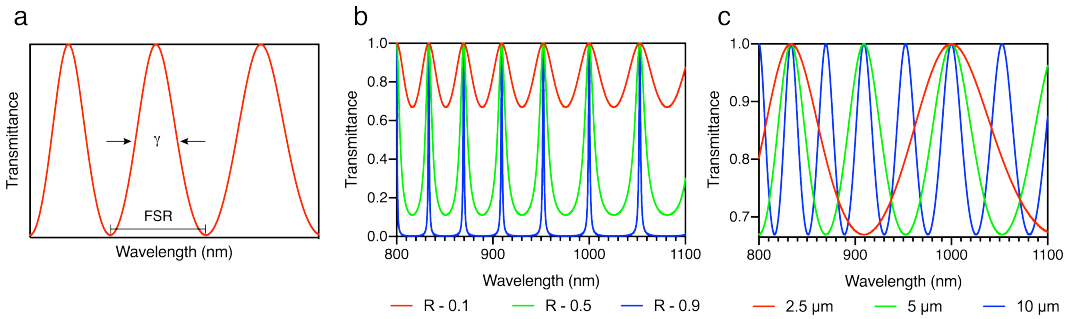

Figure 2.4: FP cavity parameters. (a) Typical parameters to consider when designing FP cavities. Dependence of the theoretical resonance profile on (b) surface reflectance R and (c) cavity gap-size d.

Device fabrication

The device is batch-fabricated through traditional IC fabrication processes at a wafer-scale. The fabrication process flow is illustrated in Figure 2.5. The membrane and mirror substrates are fabricated separately and are then brought together using a chip-to-chip bonding technique using UV-curable medical grade epoxy. The process flow for each of the two parts is as follows:

Top substrate (or membrane):

T1. Starting with a double-side polished 300 μm-thick Si wafer, a 2 μm thermal oxide (SiO_2), and a 400 nm low pressure chemical vapor deposition (LPCVD) Si_3N_4 layers are deposited on both sides.

T2. A combination of reactive ion etching (RIE) and buffered oxide etch (BOE) is conducted on the top-side of the wafer to strip away the Si_3N_4 and SiO_2 thin-films respectively. Following this, a photolithography step and a 300 nm-thick Al_2O_3 hard mask E-beam evaporation step is carried out.

T3. Deep reactive ion etching (DRIE) is performed to punch through the bulk of the wafer to reach the back-side SiO_2 layer.

T4. The back-side SiO_2 layer as well as the hard mask is removed with a single BOE step.

T5. A back-side alignment, photolithography and RIE step is performed to etch Si_3N_4 selectively and release individual membrane chips that are between 600 – 800 μm in diameter.

Bottom substrate (or mirror):

B1. Start with a double-side polished 300 μm-thick Si wafer.

B2. Top-side photolithography is performed and a pseudo Bosch (p-Bosch) process is carried out to etch shallow trenches on the order of 5 – 10 μm on the top-side of the wafer. These trenches define the gap-size of the FP cavity.

B3. A second alignment, photolithography and hard mask evaporation step (300 nm Al_2O_3) are performed.

B4. DRIE is performed to punch through the bulk of the wafer to punch out individual mirror chips that are between 600 – 800 μm in diameter.

B5. BOE is performed to remove the hard mask.

Benchtop characterization

Seminal work on the sensor implant was carried out by Lee *et al.* [24]. The sensor is detected using a custom-built NIR microscope as shown in Figure 2.6a. A 20x objective (Plan, Apo, Infinity Corrected, Long Working Distance, Mitutotyo, Kawasaki, Japan) with a numerical aperture (NA) of 0.42 was used to image and focus on the Si_3N_4 membrane. The image of the sensor was captured using a USB camera (STC-MB133USB, Sentech Co., Atsugi, Japan). A micrometer-precision XYZ-stage (PT3, Thorlabs Inc., Newton, NJ, USA) is used to adjust the field of view. The interrogating light is delivered from a broadband light source (OSL1 High-Intensity Fiber Light Source, Thorlabs Inc., Newton, NJ, USA) through a polarizer, a dichroic beam splitter (pass: NIR; reflect: VIS), a quarter wave plate, the microscope objective, and finally to the sensor. The reflection from the sensor is collected through the same optical path and relayed to an off-the-shelf, commercially available mini VIS-NIR spectrometer (Maya 2000 Pro, 780 nm-1200 nm, resolution of 0.22 nm, Ocean Optics, Dunedin, FL, USA). Readout is performed at a distance of 3-5 cm.

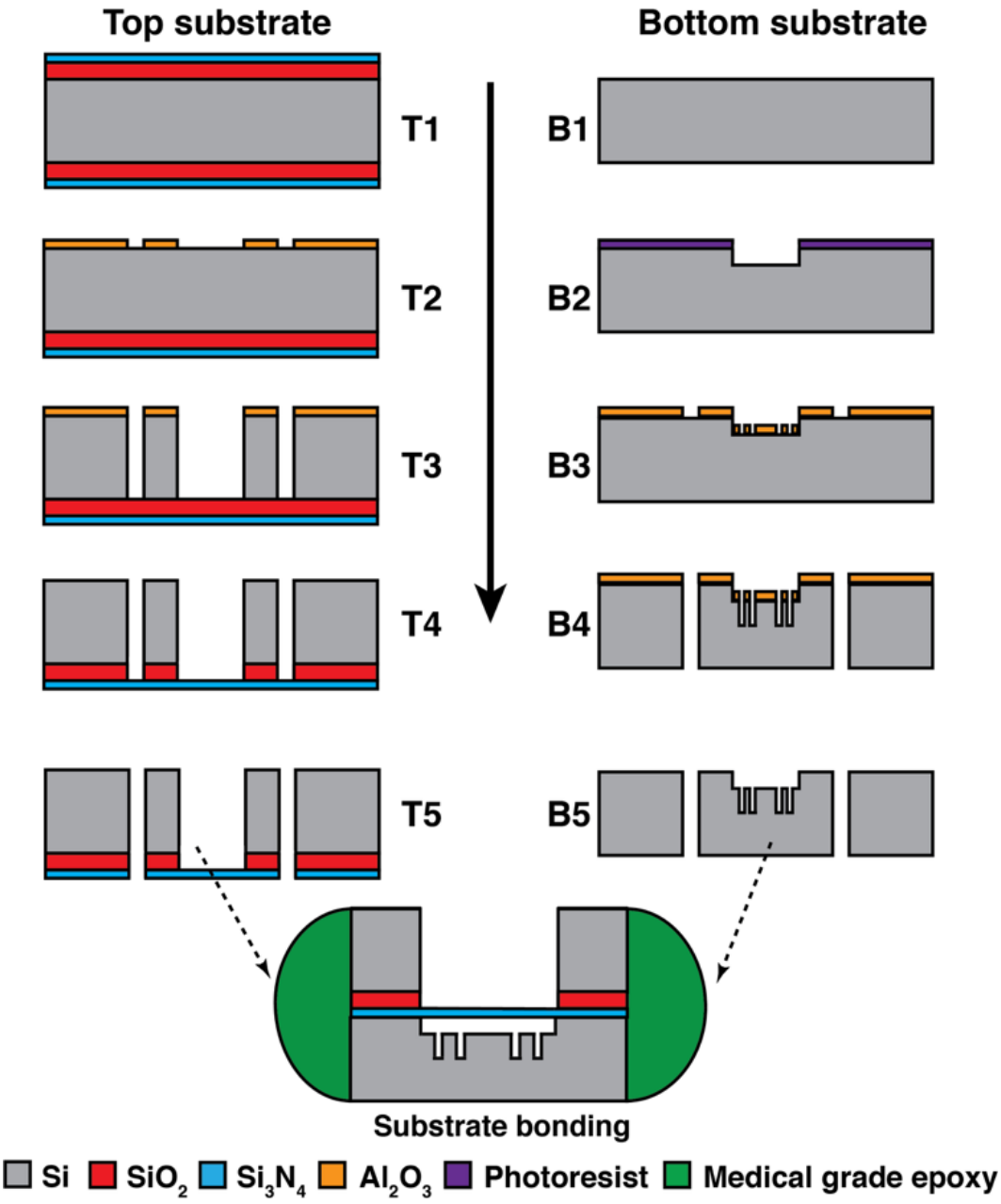

Figure 2.5: Fabrication process flow of the IOP sensor implant.

Sensor characterization is performed in a controlled pressure chamber as shown in Figure 2.6a which is essentially a water column and a programmable syringe pump (NE 1000, ABC Scientific, CA, USA). The system is also integrated with a digital reference pressure gauge (1210 Pressure Sensor, TE Connectivity Ltd., Schaffhausen, Switzerland). The pressure is ramped from 0 to 40 mmHg in steps of 0.05 or 0.1 mmHg and the corresponding spectra captured from each pressure state is mapped against the reference pressure gauge to develop

characteristic curves from each sensor as shown in Figure 2.6b and c [24].

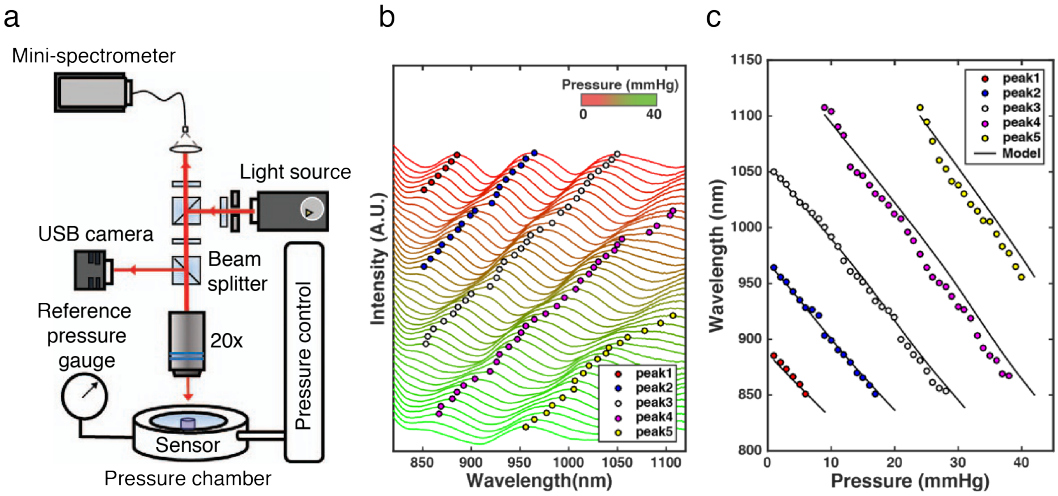

Figure 2.6: IOP sensor implant benchtop characterization. (a) The custom-built NIR microscope setup used to interrogate and readout from the IOP sensor implant. (b) A characteristic set of spectra captured from the sensor when induced to a pressure ramp from 0 to 40 mmHg. The peak locations of each spectrum is captured using a MATLAB script. (c) The peak locations are tracked with the reference pressure gauge to obtain characteristic curves for each sensor. Image reproduced with permission granted under Creative Commons Attribution 4.0 International License from: [24].

Implantation and in vivo demonstration

For all *in vivo* work, New Zealand White rabbits (females 2.5-3.2 kg in weight) are used. Two modes of implantation are considered. The first method reported by Lee *et al.* delivers the IOP sensor implant mounted on an intraocular lens (IOL) [24]. The second method delivers the sensor mounted on silicone haptics. The latter being the one primarily used for this work is discussed here. For implantation, following pre-surgical preparation and sedation, a 2.8-mm corneal incision is made and ophthalmic viscosurgical device (OVD) is injected into the anterior chamber. The sensor with silicone haptics is folded onto itself and introduced into the anterior chamber through the corneal incision. The haptics were allowed to unfold spontaneously and positioned into the iridocorneal angles for fixation. The OVD is then removed by irrigation, and a 10-0 suture is placed to close the incision as needed. Cefazolin antibiotic is applied sub-conjunctivally and a neomyxin / dexamethasone ointment is applied to the eye. The rabbit is then removed from anesthesia and allowed to revive before being returned to the housing area.

Preliminary *in vivo* work showed great promise in monitoring IOP in a high-throughput fashion with a sampling rate of 10 Hz as shown in Figure 2.7e. The device displayed an average *in vivo* IOP error that was within the 2-mmHg error range of rebound tonometry (TonoVet, Icare, Vanda, Finland) measurements taken concurrently. IOP spikes induced artificially by intravitreal injections were effectively tracked by the device as shown in 2.7f. Furthermore, long-term monitoring of IOP over 4.5 months was also reported [24].

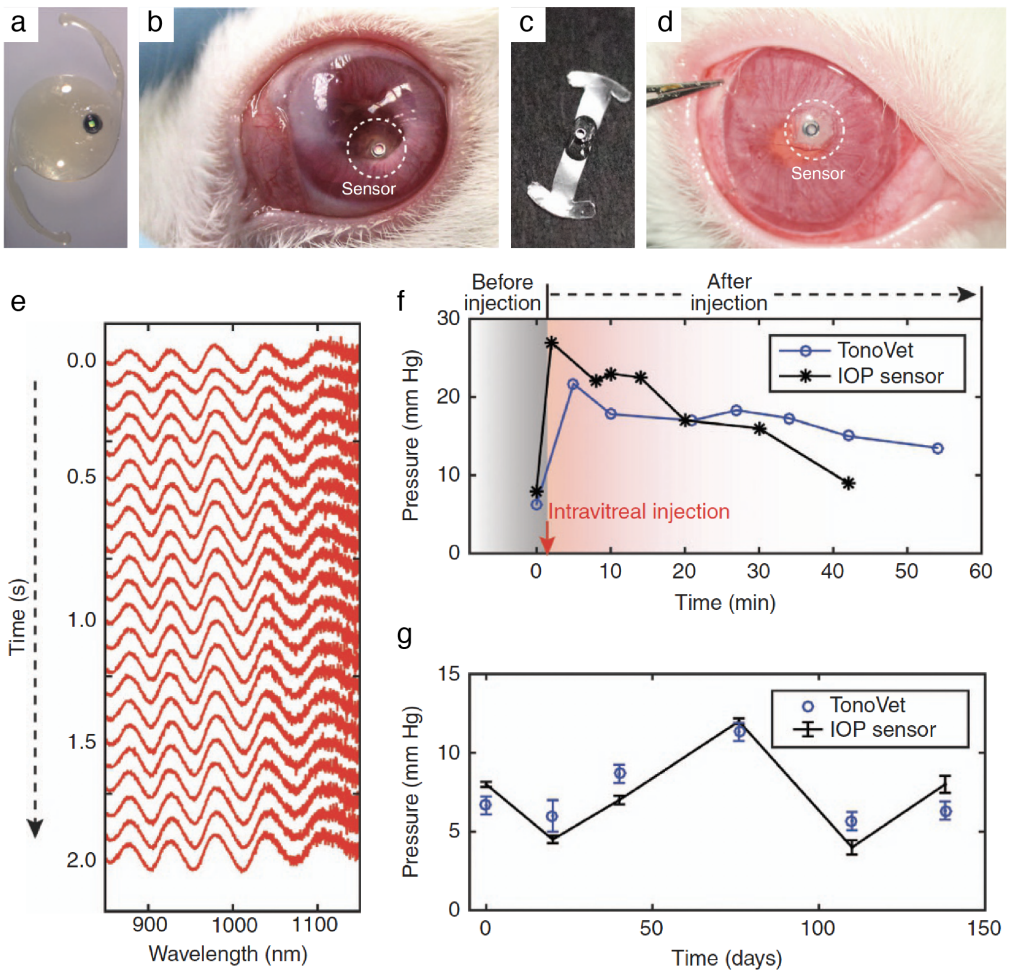

Figure 2.7: Implantation method (a,b) using IOLs and (c,d) silicone haptics. (e) A series of spectra obtained over 2 seconds at a sampling rate of 10 Hz. (f) Tracking of artificial IOP spikes induced by an intravitreal injection in conjunction with measurements taken using rebound tonometry. (g) IOP snapshots taken over 4.5 months in good agreement with rebound tonometry. Image reproduced with permission granted under Creative Commons Attribution 4.0 International License from: [24].

References

[1] Harry A. Quigley and Aimee T. Broman. The number of people with glaucoma worldwide in 2010 and 2020. *British Journal of Ophthalmology*, 90(3):262–267, 2006. doi: 10.1136/bjo.2005.081224.

[2] Yih Chung Tham, Xiang Li, Tien Y. Wong, Harry A. Quigley, Tin Aung, and Ching Yu Cheng. Global prevalence of glaucoma and projections of glaucoma burden through 2040: A systematic review and meta-analysis. *Ophthalmology*, 121(11):2081–2090, 2014. doi: 10.1016/j.ophtha.2014.05.013.

[3] The Eye Diseases Prevalence Research Group. Prevalence of open-angle glaucoma among adults in the United States. *Archives of Ophthalmology*, 122(4):532–538, 2004. doi: 10.1001/archopht.122.4.532.

[4] `https://www.opticianonline.net/cet-archive/129`, 2019 (Accessed: Oct 28, 2019).

[5] Anders Heijl, M. Cristina Leske, Bo Bengtsson, Leslie Hyman, Boel Bengtsson, and Mohamed Hussein. Reduction of intraocular pressure and glaucoma progression results from the early manifest glaucoma trial. *Archives of Ophthalmology*, 120(10):1268–1279, 2002. doi: 10.1001/archopht.120.10.1268.

[6] Stefan De Smedt, Andre Mermoud, and Corinne Schnyder. 24-hour intraocular pressure fluctuation monitoring using an ocular telemetry sensor: Tolerability and functionality in healthy subjects. *Journal of Glaucoma*, 21(8):539–544, 2012. doi: 10.1097/IJG.0b013e31821dac43.

[7] John H. K. Liu, Randy P. Bouligny, Daniel F. Kripke, and Robert N. Weinreb. Nocturnal elevation of intraocular pressure is detectable in the sitting position. *Investigative Ophthalmology and Visual Science*, 44(10):4439–4442, 2003. doi: 10.1167/iovs.03-0349.

[8] John H. K. Liu, Xiaoyan Zhang, Daniel F. Kripke, and Robert N. Weinreb. Twenty-four-hour intraocular pressure pattern associated with early glaucomatous changes. *Investigative Ophthalmology and Visual Science*, 44(4):1586–1590, 2003. doi: 10.1167/iovs.02-0666.

[9] Melike Pekmezci, Sidney T. Chang, Bradley S. Wilson, Mae O. Gordon, and Anjali M. Bhorade. Effect of measurement order between right and left eyes on intraocular pressure measurement. *Archives of Ophthalmology*, 129(3):276–281, 2011. doi: 10.1001/archophthalmol.2011.33.

[10] Etsuo Chihara. Assessment of true intraocular pressure: The gap between theory and practical data. *Survey of Ophthalmology*, 53(3):203–218, 2008. doi: 10.1016/j.survophthal.2008.02.005.

[11] Jeong Oen Lee, Vinayak Narasimhan, Ashwin Balakrishna, Marcus R. Smith, Juan Du, David Sretavan, and Hyuck Choo. Fabry-Pérot optical sensor and portable detector for monitoring high-resolution ocular hemodynamics. *IEEE Photonics Technology Letters*, 31(6):423–426, 2019. doi: 10.1109/LPT.2019.2896840.

[12] `https://www.sensimed.ch/sensimed-triggerfish/`, 2019 (Accessed: Oct 31, 2019).

[13] `https://www.implandata.com/EN/eyemate.html`, 2019 (Accessed: Oct 31, 2019).

[14] Cagdas Varel, Yi Chun Shih, Brian P Otis, Tueng S Shen, and Karl F Bohringer. A wireless intraocular pressure monitoring device with a solder-filled microchannel antenna. *Journal of Micromechanics and Microengineering*, 24(4):045012–1– 045012–8, 2014. doi: 10.1088/0960-1317/24/4/045012.

[15] Po Jui Chen, Damien C. Rodger, Saloomeh Saati, Mark S. Humayun, and Yu Chong Tai. Microfabricated implantable parylene-based wireless passive intraocular pressure sensors. *Journal of Microelectromechanical Systems*, 17(6):1342–1351, 2008. doi: 10.1109/JMEMS.2008.2004945.

[16] Cheol In Jang, Kyeong Sik Shin, Mi Jeung Kim, Kwang Seok Yun, Ki Ho Park, Ji Yoon Kang, and Soo Hyun Lee. Effects of inner materials on the sensitivity and phase depth of wireless inductive pressure sensors for monitoring intraocular pressure. *Applied Physics Letters*, 108(10):103701–1–103701–5, 2016. doi: 10.1063/1.4943136.

[17] Girish Chitnis, Teimour Maleki, Brian Samuels, Louis B. Cantor, and Babak Ziaie. A minimally invasive implantable wireless pressure sensor for continuous IOP monitoring. *IEEE Transactions on Biomedical Engineering*, 60(1):250–256, 2013. doi: 10.1109/TBME.2012.2205248.

[18] Samir Melki, Amir Todani, and George Cherfan. An implantable intraocular pressure transducer: Initial safety outcomes. *JAMA Ophthalmology*, 132(10):1221–1225, 2014. doi: 10.1001/jamaophthalmol.2014.1739.

[19] Mahmoud H. Ouda, Muhammad Arsalan, Loic Marnat, Atif Shamim, and Khaled N. Salama. 5.2-GHz RF power harvester in 0.18-um CMOS for implantable intraocular pressure monitoring. *IEEE Transactions on Microwave Theory and Techniques*, 61(5):2177–2184, 2013. doi: 10.1109/TMTT.2013.2255621.

[20] `https://en.wikipedia.org/wiki/Ocular_tonometry`, 2019 (Accessed: Oct 31, 2019).

[21] `https://www.verywellhealth.com/air-puff-test-3421804`, 2019 (Accessed: Oct 31, 2019).

[22] https://www.icare-usa.com/, 2019 (Accessed: Oct 31, 2019).

[23] Nikolai V. Tkachenko. *Optical spectroscopy*. Amsterdam: Elsevier Science, first edition, 2006. ISBN 978-0-444-52126-2. doi: 10.1016/B978-0-444-52126-2.X5024-2.

[24] Jeong Oen Lee, Haeri Park, Juan Du, Ashwin Balakrishna, Oliver Chen, David Sretavan, and Hyuck Choo. A microscale optical implant for continuous in vivo monitoring of intraocular pressure. *Microsystems and Nanoengineering*, 3(1):17057–1–17057–9, 2017. doi: 10.1038/micronano.2017.57.

Chapter 3

MULTIFUNCTIONAL BLACK-SILICON FOR IOP SENSING

This chapter was adapted from:

J. O. Lee*, **V. Narasimhan***, J. Du, B. Ndjamen, D. Sretavan and H. Choo (2017). "Biocompatible multifunctional black-silicon for implantable intraocular pressure sensor." In: ***Advanced Healthcare Materials*** 6.4, pp. 1601356-1–1601356-7. DOI: 10.1002/adhm.201601356. [*co-first authors]

Abstract

Burgeoning research on implantable medical microdevices has been actively driving the development of multifunctional biomaterials to improve device performance and reliability. Black-silicon (b-Si) or nanograss, a textured silicon (Si) surface with micro- and nanoscale high aspect-ratio topologies, is known to possess highly useful surface properties and has been used in a myriad of applications such as in light-absorbing antireflection layers in photovoltaics and surface-enhanced Raman scattering, bonding layers in microelectromechanical systems, liquid-guiding layers in microfluidics, and bioinspired/mimetic functional surfaces. In this work, we demonstrated the use of b-Si as an antireflection and antibiofouling layer on an optically probed implantable intraocular pressure (IOP) sensor and significantly improved its optical performance and long-term *in vivo* biocompatibility and reliability. The b-Si enabled IOP monitoring at 12 cm on fully awake rabbits, the largest readout distance reported to our knowledge, and demonstrated remarkable antifouling properties analogous to biological nanostructures found in nature, preventing encapsulating tissue growth on the implant. To our knowledge, this is the first *in vivo* demonstrated use of b-Si as a multifunctional biomaterial on an implantable medical sensor.

3.1 Introduction

Continual monitoring of *in vivo* IOP was successfully shown using developed implant reported in Chapter 2. Detection was performed using a custom-built NIR microscopy setup [1]. However, as shown in Figure 3.1a, this required sedation of the animal under study as well as fixation of the animal eye for consistent readouts. Furthermore, the performance of the detection setup was limited by a short readout distance of 2–3 cm. A more practical IOP-sensing approach demands for the adaptation of easy-to-use readout systems such as the slit-lamp which is a ubiquitous ophthalmic microscope. Routinely used in ocular inspections, the slit-lamp is used by clinicians to examine both the anterior and posterior segments of the eye. By adapting the slit-lamp as the detector for the IOP sensor, the device can be made more accessible to clinicians. Furthermore, the slit-lamp can be operated at much longer readout distances than the custom-built NIR microscope on un-anesthesized animals. However, with increase in readout distance, the field-of-view is also expanded which inevitably increases background noise detection. The noise reflected from the cornea, lens, iris, or aqueous humor is not significant because of their low reflectivities, about 3% or smaller [2]. However, the inactive region of the sensor is a highly reflective Si surface and is coaxially aligned with the detector (Figure 1b), generating strong background noise and degrading the signal-to-noise ratio (SNR) of the sensor [3].

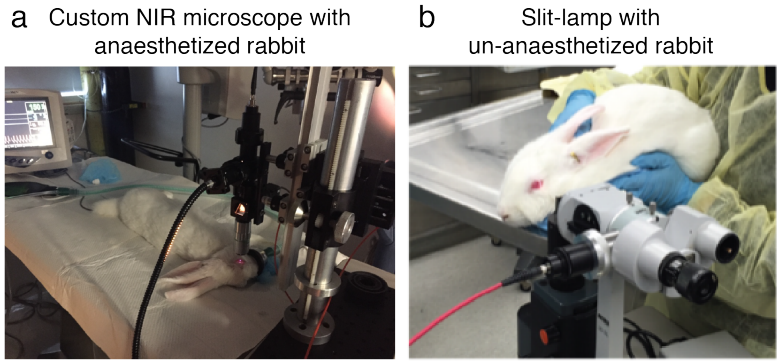

Figure 3.1: IOP sensor implant detection techniques. (a) Previous *in vivo* IOP measurements using the custom-built NIR microscope required sedation of the animal and was limited by short readout distances. (b) Using the slit-lamp as a detector for the device would require no sedation and offer large readout distances.

Plant surfaces such as leaves and petals posses micro-/nanostructures on their

epidermal cell that are not only anti-reflective in nature, but they also redirect and trap incoming light [4, 5]. These effects lead to strong absorption effects that are utilized by plants in low-light environments to enhance and sustain metabolic processes such as photosynthesis. Such light-trapping properties have been employed in useful applications. For instance, as shown in Figure 3.2, structures replicated from the *Rosa* 'El Toro' flower were used as effective light harvesting elements for photovoltaics [6].

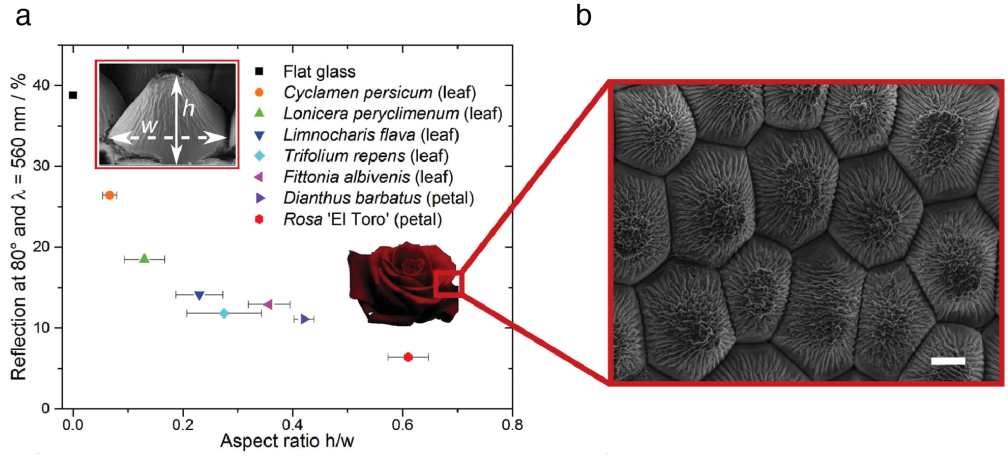

Figure 3.2: Light-trapping micro-/nanostructures in plants. (a) The reflection at an incident angle = 80° of various leaf and petal replicas at a wavelength of 560 nm. The reflection observed lowers with increasing aspect ratio. Additionally, the reflection from the petal of the *Rosa* 'El Toro' flower is below 10%. (b) Top-view SEM image of the light trapping microstructures on the *Rosa* 'El Toro' petal. Image reproduced with permission from: [6].

In this Chapter, similar light-trapping micro-/nanostructures are directly grown on the highly reflective Si surface on the inactive region of the IOP sensor. These structures are dubbed black-silicon (b-Si) or nanograss. B-Si is known to possess highly useful surface properties and has been used in a myriad of applications such as in light-absorbing antireflection layers in photovoltaics and surface-enhanced Raman scattering [7, 8], bonding layers in microelectromechanical systems [9], liquid-guiding layers in microfluidics [10, 11], and bioinspired/mimetic functional surfaces [12].

In order to suppress the background noise, antireflective b-Si was integrated on the inactive region of the sensor as shown in Figure 3.3. The b-Si effectively scatters incoming light and significantly increases its absorption. This enabled IOP monitoring at 12 cm on fully awake rabbits using the slit-lamp as a detector. Furthermore, the b-Si demonstrated antifouling properties thereby

preventing encapsulating tissue growth on the implant. To date, this is the first *in vivo* demonstrated use of b-Si as a multifunctional biomaterial on an implantable medical sensor.

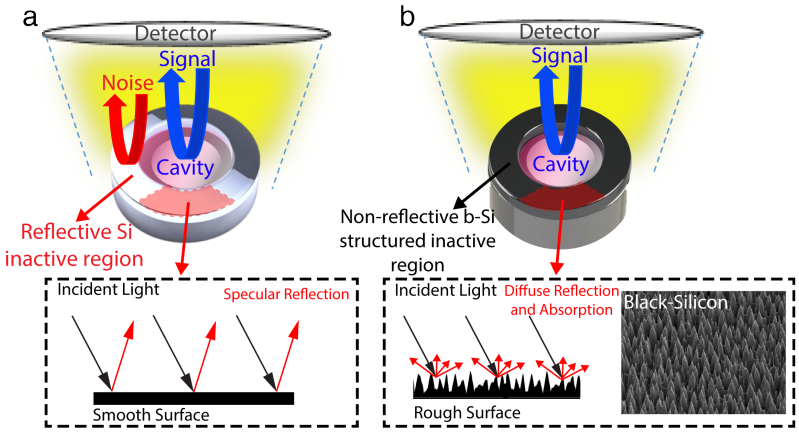

Figure 3.3: Background noise suppression on IOP sensor by b-Si. (a) Si-only sensor consisting of an active core cavity and a reflective peripheral inactive region. Reflection arises from both the cavity (shown in blue) and the Si (shown in red). b) A sensor with integrated b-Si on the inactive hollow disk. Only the reflection from the core cavity is captured. The inset is an SEM image of the b-Si grown on the inactive region.

3.2 B-Si growth and integration

A room-temperature wafer-scale b-Si process was developed using a mixed-mode plasma etch, which did not require an expensive cryogenic setup or a time-consuming cooling process (Figure 3.4) [13]. Specific process parameters are reported in the Methods Section 3.6. As shown in Figure 3.4b and c, by varying the process conditions, b-Si nanostructures were successfully optimized to obtain the antireflection properties in the wavelength range of interest. Much like in Figure 3.2, increasing the process duration increases the aspect-ratio of the b-Si nanostructures thereby lowering the relative reflectivity. Integrating the b-Si on the inactive region lowered reflectivity down to 10% of a polished Si surface and produced 3.5% absolute reflectivity.

The b-Si growth was then seamlessly integrated with the existing IOP sensor fabrication process as shown in Figures 3.5 and 3.6.

The integration ensured that the existing IOP sensor fabrication process flow as reported in Section 2.3 remained largely the same with some changes introduced to the membrane fabrication. The mirror fabrication and chip-to-chip

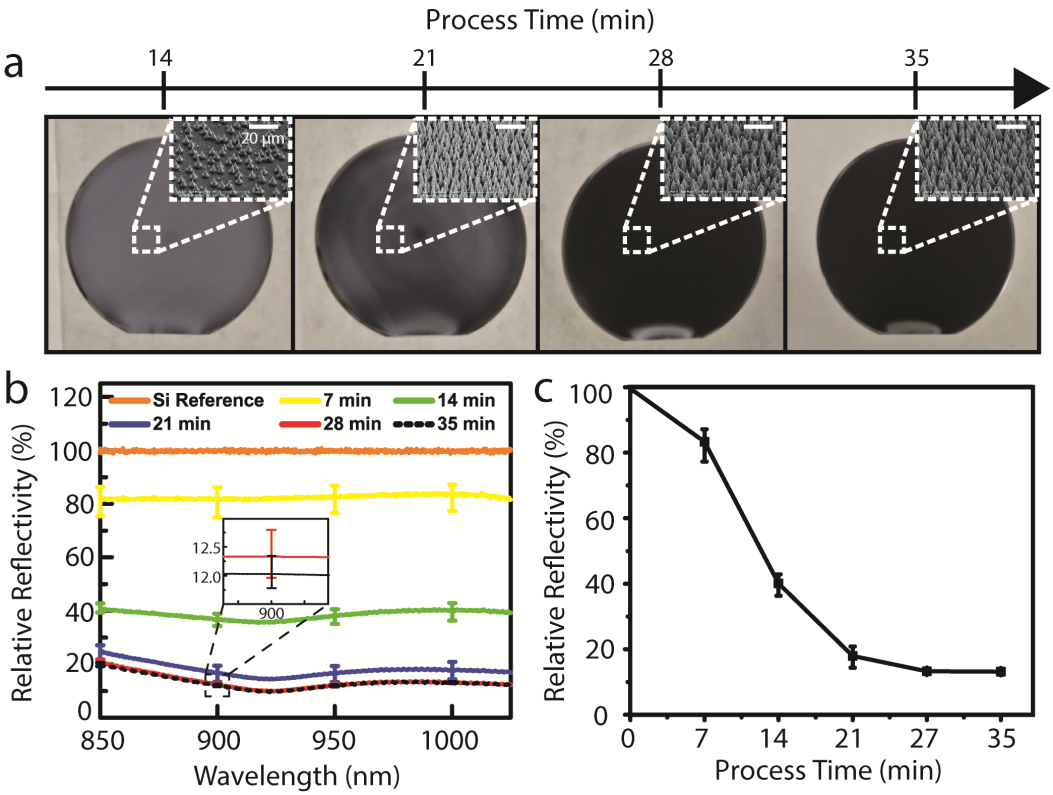

Figure 3.4: B-Si process development. (a) Wafer-scale b-Si process performed on 6 in. wafers (insets: SEM images taken at 45°; scale: 20 μm). (b) Relative reflectivity of b-Si surface versus the wavelength range of interest for five different process durations (5-point measurements). The inset shows a zoomed-in image of the error bars for 28 and 35 min process times. Increasing process times increase aspect-ratios and lower reflectivity. (c) Wavelength-averaged relative reflectivity versus process time.

bonding step remained the same as before. The new b-Si integrated membrane fabrication process flow is detailed below:

B-Si integrated top substrate (or membrane):

T1. Starting with a double side polished 300 μm-thick Si wafer, a 2 μm thermal oxide (SiO_2) and a 400 nm low pressure chemical vapor deposition (LPCVD) Si_3N_4 layers are deposited on both sides.

T2. A combination of reactive ion etching (RIE) and buffered oxide etch (BOE) is conducted on the top-side of the wafer to strip away the Si_3N_4 and SiO_2 thin-films, respectively. Following this, a photolithography step and a 300 nm-thick Al_2O_3 hard mask E-beam evaporation step is carried out.

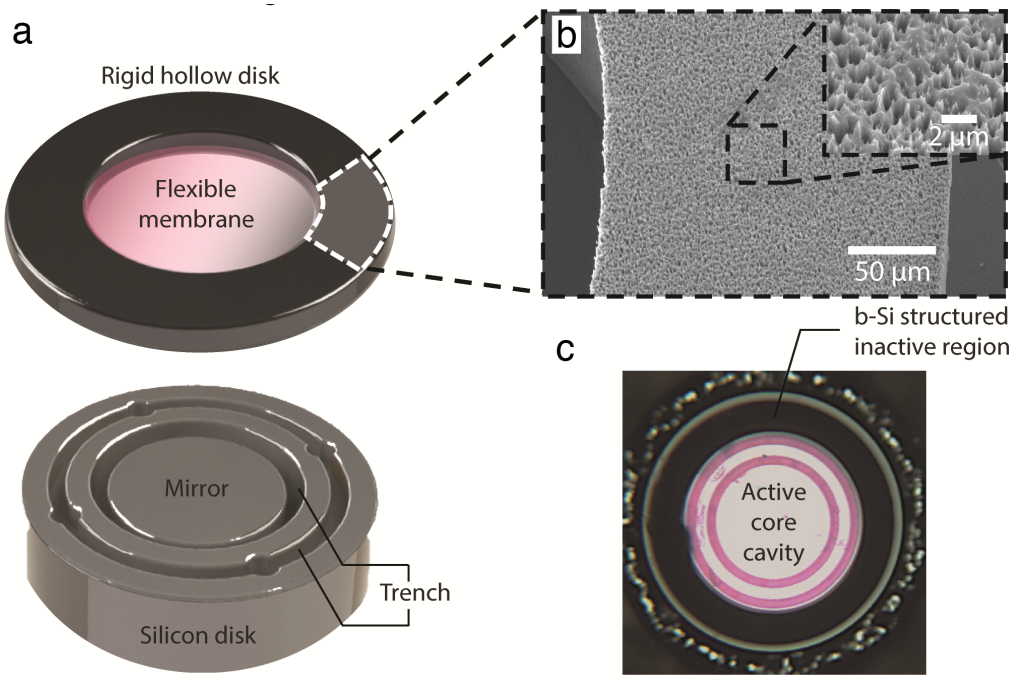

Figure 3.5: B-Si IOP sensor integration. (a) B-Si-textured inactive region on the top and a Si mirror on the bottom. (b) SEM image of the b-Si-textured inactive region. Scale bar: 50 μm. Inset: magnified SEM image of the b-Si surface. Scale: 2 μm. (c) A photograph of an assembled IOP sensor with the b-Si-integrated inactive region.

T3. Deep reactive ion etching (DRIE) is performed to punch through the bulk of the wafer to reach the back-side SiO_2 layer.

T4. Unlike the original IOP fabrication process, SiO_2 layer in this case is only partially removed by the BOE step while the hard mask is completely removed. This is because the SiO_2 will act as a protective layer over the Si_3N_4 during the subsequent b-Si growth step.

T5. Wafer-scale b-Si growth process is performed. The process specifications are detailed in the Methods Section 3.6.

T6. A second BOE is performed to remove any remaining SiO_2.

T7. A back-side alignment, photolithography and RIE step is performed to etch Si_3N_4 selectively and release individual b-Si integrated membrane chips that are between 600–800 μm in diameter.

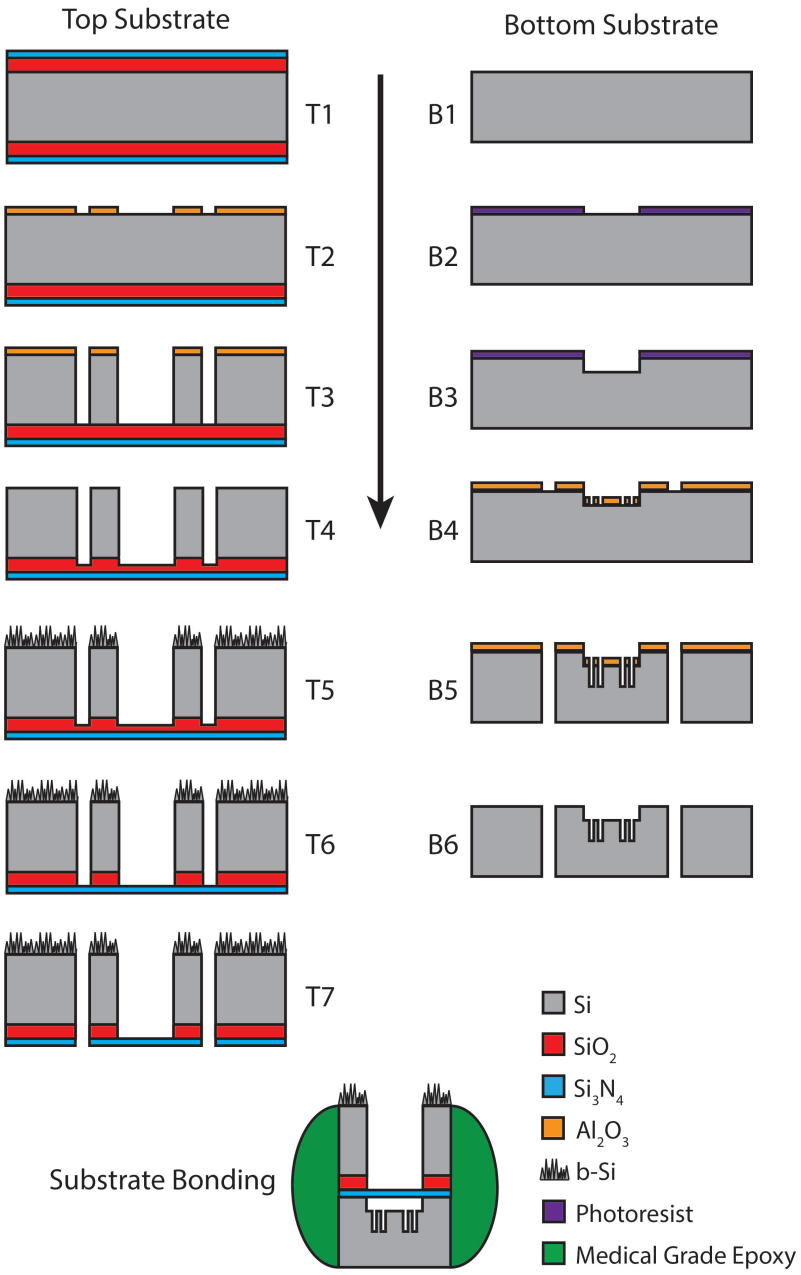

Figure 3.6: B-Si integrated IOP sensor fabrication process flow.

3.3 B-Si integrated IOP sensor characterization

To characterize the performance of the b-Si integrated IOP sensor, IOP sensing performance of b-Si-integrated and Si-only IOP sensors with identical dimensions were examined using the custom-built NIR microscope and a slit-lamp (Figure 3.7a). First, signals were captured from the 600 μm-wide active core cavities of the sensors, excluding the inactive regions, using a microscope (20x objective) at a readout distance of 3 cm. The resonance spectra from the two

sensors were almost identical and of good quality (Figure 3.7b). The outer envelope of the captured spectrum is determined by the black-body radiation of the tungsten light source, NIR filters in the detector, and the thickness of Si_3N_4 membrane, while higher frequency peaks and valleys inside the envelop are determined by the optical cavity with an air gap between the Si_3N_4 membrane and the Si substrate. Next, when the slit-lamp was used as the detector for the two sensors, the increased field-of-view (2×2 mm^2) included the active core cavity of the sensors and the surrounding inactive region. While the quality of resonance spectra captured from the b-Si sensor was hardly influenced by the inclusion of the surrounding regions, the SNR of the resonance spectra captured from the Si-only sensor decreased by 71%, below 10 dB, due to the highly reflective inactive region of the sensor (Figure 3.7c). The slit-lamp used for this purpose is shown in Figure 3.7d. A mini-spectrometer and a CCD camera were connected onto the two slit-lamp expansion ports allowing spectra to be captured at 12 cm.

Next, using the pressure-controlled test chamber reported previously in Section 2.3 (range: 0–40 mmHg, step size: 0.5 mmHg) interfaced with a digital pressure gauge and applying the slit-lamp measurement conditions, the IOP measurement accuracy was determined. When compared to the digital pressure gauge, measurements using the Si-only sensor showed considerable fluctuations (Figure 3.8a): the root-mean-square error (RMSE) and the peak-to-peak fluctuation were 1.96 and 8 mmHg, respectively (Figure 3.8b). In contrast, measurements using the b-Si sensor exhibited an RMSE of 0.58 mmHg and peak-to-peak variation less than ± 2 mmHg over the entire pressure range (Figure 3.8c and d), which would satisfy the clinically accepted error range of ± 2 mmHg [14].

3.4 B-Si integrated IOP sensor in vivo demonstration

For *in vivo* tests using the modified slit-lamp as the readout system as shown in Figures 3.9a and 3.9c, each sensor was individually mounted on a thin, flexible silicone strip and implanted into the anterior chambers of two New Zealand rabbits (Figures 3.9b and 3.9d). All IOP measurements were performed on fully awake rabbits.

For each IOP measurement, the top 30 highest SNR spectra from a set of continuously captured 600–1800 spectra (measurement time: 1–3 min, resolution

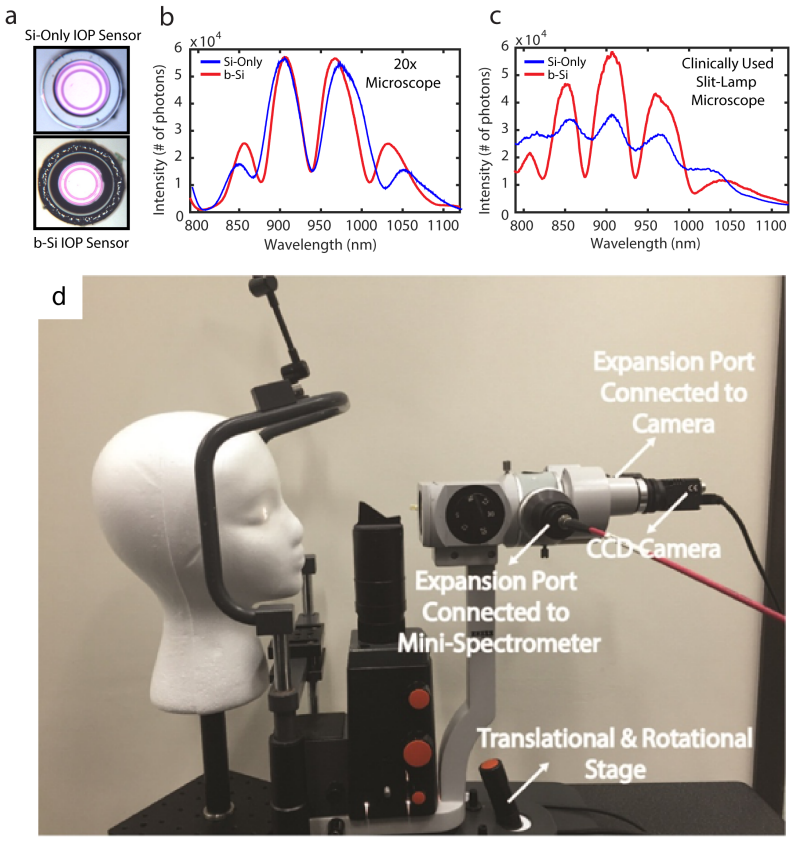

Figure 3.7: B-Si and Si-only IOP sensor characterization. (a) Fabricated Si-only (top) and b-Si (bottom) sensors. (b) Spectral measurements using the custom-built NIR microscope with a 20x objective lens (field-of-view: 800 × 800 μm^2; working distance: 3 cm). (c) Spectral measurements using a slit-lamp (field-of-view: 2 × 2 mm^2; working distance: 12 cm). (d) Photograph of a slit-lamp readout setup with a spectrometer and a CCD camera connected to the slit-lamp expansion ports.

bandwidth: 10 Hz) were averaged to improve accuracy. The resonance spectra of the b-Si sensor shown in Figure 3.10a fluctuated less than ±1 nm (Figures 3.10c and d), and the corresponding IOP was 7.3 mmHg. In contrast, it was impossible to identify peak-and-valley locations from the resonance spectra of the Si-only sensor and calculate the IOP (Figure 3.10b). For reference, b-Si sensor measurements were compared with those made using tonometry (TonoVet, ±2 mmHg accuracy) for three months (Figure 3.10e). The IOP measurements using the b-Si sensor generally paralleled the tonometer read-outs, however the average standard deviation of the b-Si-sensor measurements was much smaller, 0.48 mmHg versus 1.45 mmHg for the tonometer measurements. In addition, the b-Si sensor showed no sign of performance degradation,

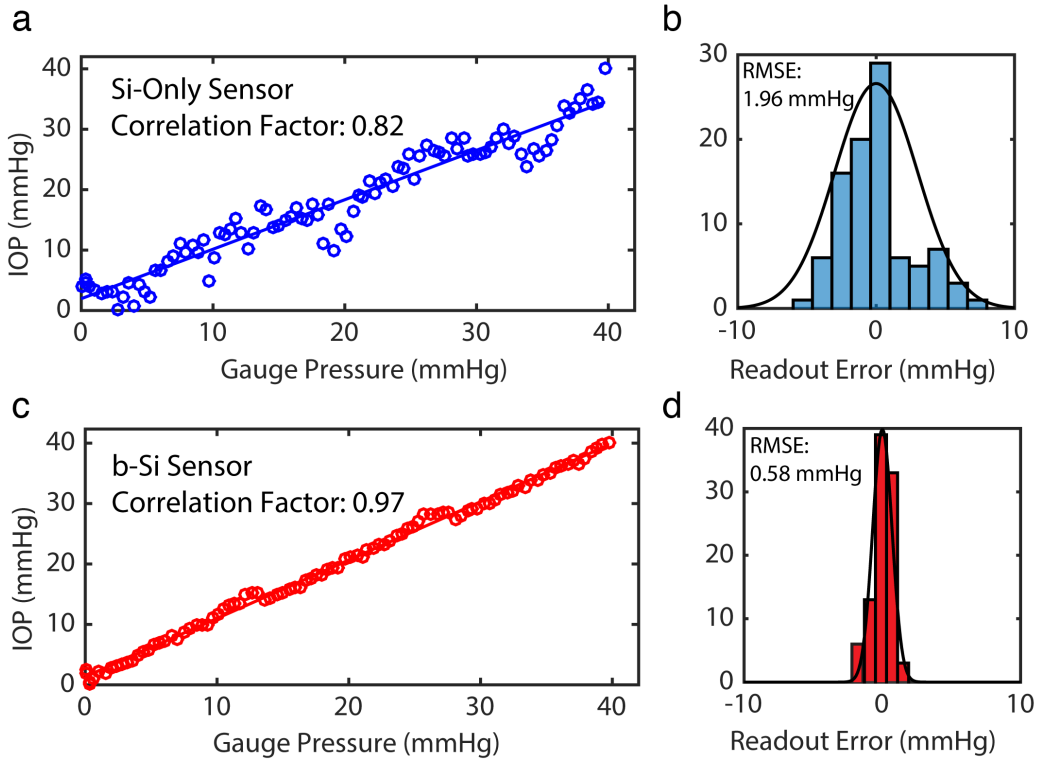

Figure 3.8: B-Si and Si-only IOP sensor characterization. (a) IOP measurements using the Si-only sensor. (b) Readout-error distribution of the Si sensor. (c) IOP measurements using the b-Si sensor. (d) Readout-error distribution of the b-Si sensor.

constantly maintaining an SNR over 10 dB for three months (Figure 3.10f).

To investigate the extent of surface fouling and its influence on the sensor reliability, Si-only and b-Si IOP sensors that had been implanted for more than six months were harvested. Confocal immunofluorescence microscopy was performed on the sensors to determine cell and tissue viability at the time of extraction. The amount of F-actin present in the cytoskeleton of eukaryotes was used as an indicator of cellular processes and health, and provided evidence to predict cell and tissue encapsulation of the implant [15]. The extracted sensors were counterstained using DAPI 405 (cell nucleus marker), Phalloidin 555 (cell F-actin marker), and CD62L 488 (L-selectin inflammation marker) and scanned from the surface of the inactive region down to the top of the Si_3N_4 membrane along the z-axis (step: 2.5 μm, scan range: 300 μm, Zeiss LSM 880, 10x EPI objective).

Figure 3.11 presents the results of the z-stack imaging performed on the Si-only and b-Si sensors, respectively, and illustrates the extent of tissue growth.

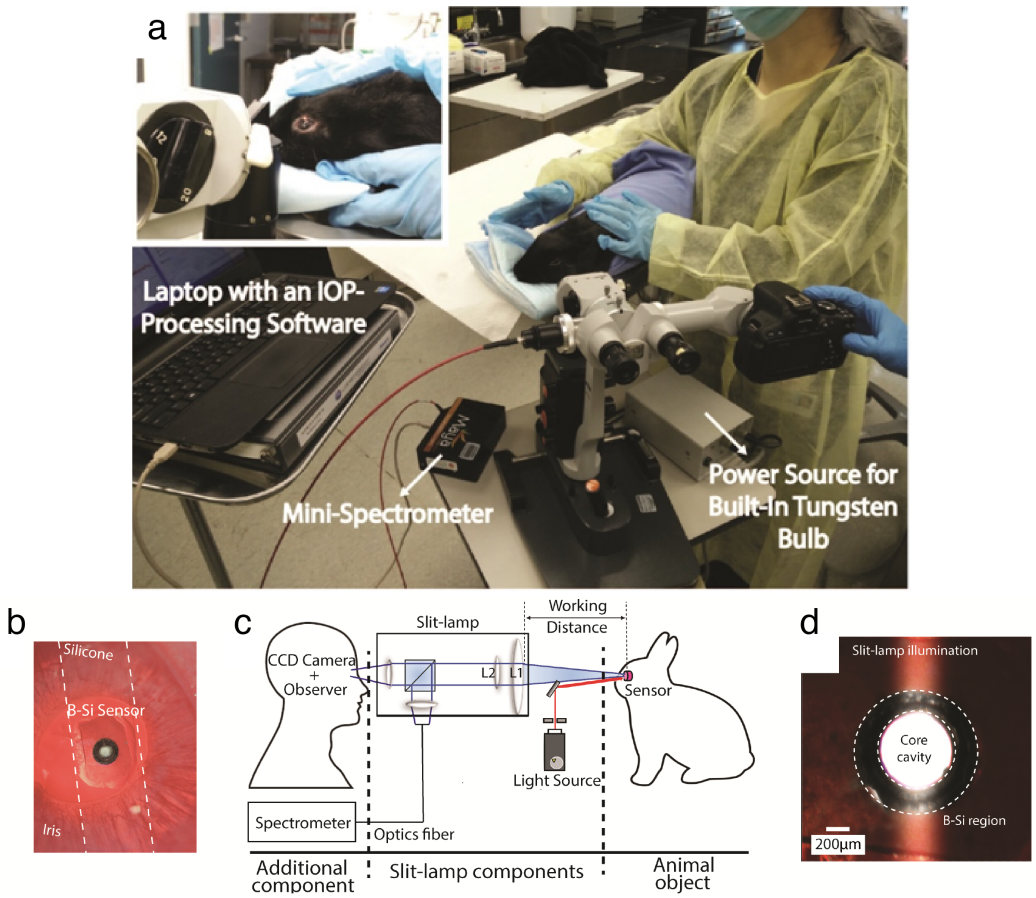

Figure 3.9: B-Si IOP sensor *in vivo* implantation. (a) Photograph of the slit-lamp being used for *in vivo* IOP measurements on an awake rabbit. The inset shows slit-lamp illumination in the rabbit's eye. (b) A photo of the b-Si sensor implanted inside a rabbit eye using a flexible silicone strip. (c) Schematic of the modified slit-lamp readout system used *in vivo*. (d) A photo of the illuminated sensor in the rabbit eye taken using a slit-lamp at 30x magnification.

On the Si-only sensor, the cells extended from the inactive region onto the active (Si_3N_4 membrane surface) region, covering about 62% of the active area, and contained large F-actin filaments, which implied the adherent cells were growing healthily at the time of extraction. This is highly undesirable because dense tissue growth would ultimately block the optical pathway of the sensor and alter its mechanical properties. In addition, imaging with CD62L 488 indicated several instances of inflammation within a tight cluster of cells covering the Si_3N_4 membrane (Figure 3.12).

In contrast, the b-Si sensor showed almost no sign of tissue growth or discernible onset of encapsulation. Only 5% of the active region was covered by tissue and some nonspecific binding of fluorophores were seen on the b-Si

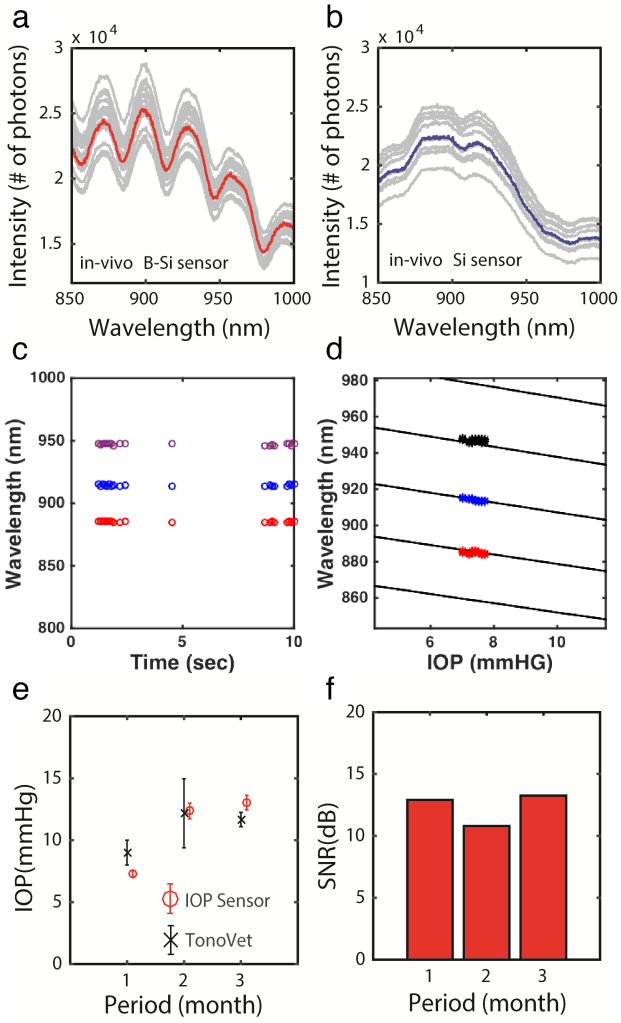

Figure 3.10: Top 30 highest-SNR *in vivo* spectra (gray curves) selected out of 600–1800 measurements from (a) the b-Si sensor and (b) Si-only sensor, captured at one month following the implantation. Corresponding means: red (b-Si sensor) and blue (Si-only sensor) curves. (c) Fluctuations of the major peaks during the 10-sec *in vivo* measurement. Only the top 30 highest SNR spectra were selected and plotted. The spectral fluctuation in the peak locations is within ±1 nm. (d) The corresponding IOP for the spectrum was 7.3 mmHg and the peak-to-peak fluctuation was less than 0.4 mmHg. (e) IOP measurements using the b-Si sensor and a TonoVet. (f) SNRs of the b-Si sensor over three months.

surface in the form of a partial ring. The surface-area ratio of Phalloidin 555 to DAPI 405 was 3.3 for the b-Si sensor, approximately four times smaller than the Si-only sensor (13.3). This indicates that most of the cells on the b-Si sensor were unhealthy and F-actin deficient, experiencing depolymerization whereby filamentous F-actin disassociates into its globular G-actin form

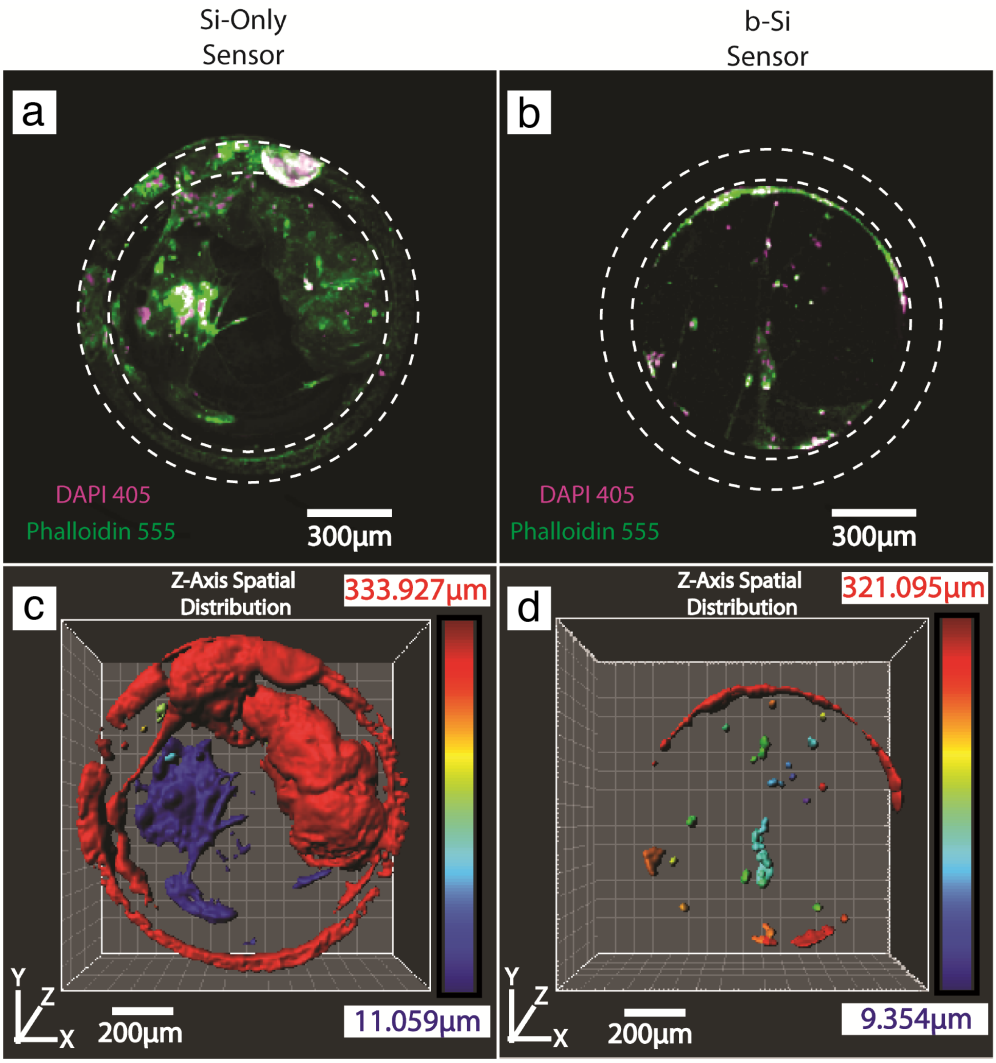

Figure 3.11: 3D-confocal z-stack images (Zeiss LSM-880 confocal microscope) of (a) the Si-only sensor and (b) the b-Si sensor harvested more than six months after implantation (DAPI: purple channel, nucleus; Phalloidin: green channel, F-actin; step size: 2.5 μm; scan range: 300 μm). 3D reconstruction (Imaris, Bitplane Inc.) showing the spatial distributions of tissues adherent on (c) the Si-only sensor and (d) the b-Si sensor. The color bar indicates the vertical location of the tissue along the z-axis, with blue indicating the top of the Si_3N_4 membrane.

[16, 17]. This leads to degeneration and thus deters any further growth or encapsulation.

The highly nonuniform surface of b-Si is postulated to prevent cell adhesion and therefore inhibit tissue-encapsulation of the implant. Furthermore, no instances of inflammation were observed on the b-Si sensor (Figure 3.12), which

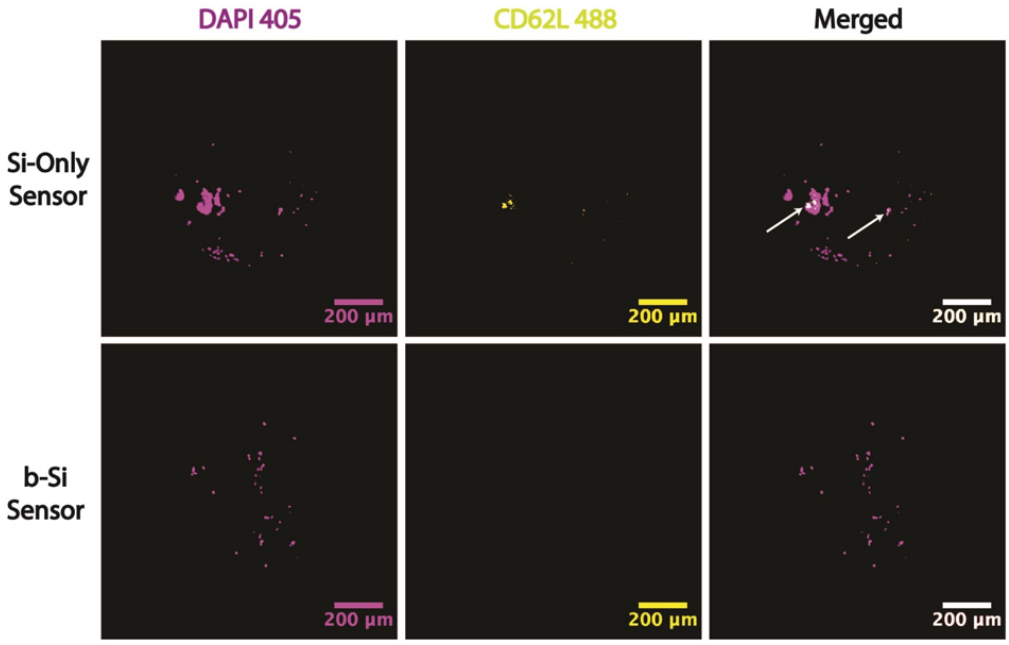

Figure 3.12: Immune response comparison that indicates the presence of potential inflammation in the Si-only sensor. The CD62L 488 marker is overlapped with DAPI 405 to ascertain the location of immune cells. Multiple instances of inflammation were observed in the case of the Si-only sensor (indicated with white arrows). No inflammation was detected in the b-Si sensor.

correlates with the recent findings indicating the biocompatibility of b-Si surfaces in the presence of eukaryotes [18]. Further studies are required to better understand the biophysical interaction of b-Si within the ocular environment and its antifouling properties for implant applications in general.

3.5 Conclusion

To conclude, using b-Si as a multifunctional material on an IOP-sensing medical implant significantly improved the sensor performance and reliability. The b-Si was fabricated using a newly developed room-temperature process, which seamlessly integrated with the fabrication steps of the implantable IOP sensors. The antireflective properties of b-Si reduced the background noise of the sensor and allowed adaption of a slit-lamp, the most commonly used clinical ophthalmic microscope, as a readout system during *in vivo* IOP monitoring. B-Si effectively suppressed tissue growth on the surface of the implant over a six-month period, promising significantly improved long-term reliability of the implant. The demonstrated improvement in both performance and reliability enabled *in vivo* studies on fully awake rabbits for six months, providing

positive indications of the possibility of realizing our IOP-sensing approach for everyday use. Further miniaturization of the sensor and improvement of the sensor-securing mechanism inside the eye will greatly simplify the insertion procedure and enhance patient comfort. Furthermore, additional studies will be conducted in the future to elucidate the underlying mechanisms of the presented work and the long-term effect of b-Si inside the eye, which will ultimately allow us to demonstrate the full potential of b-Si as a multifunctional biomaterial for medical implants.

3.6 Materials and methods

B-Si fabrication at room temperature

A reactive-ion-etching process (Oxford Instruments System 100 ICP 380) was used to fabricate the wafer-scale b-Si surface. The process chamber was maintained at 20^{o}C, while the flow rates of SF_6 and O_2 gas were set at 47 and 44 sccm, respectively. The etching process was conducted in multiple steps to tune the reflectivity (Figure 3.4a). Integration of the b-Si process into the IOP-sensor fabrication is shown in Figure 3.6.

Characterization of the b-Si IOP sensor

Two measurement setups were used: (1) a custom-built NIR optical microscope equipped with a CCD camera (ThorLabs), a broadband light source (Ocean Optics HL-2000), and a spectrometer (Ocean Optics Maya2000 Pro-NIR); and (2) a slit-lamp integrated with a CCD (Thorlabs) and a spectrometer (Ocean Optics Maya2000 Pro-NIR) using two of the slit-lamp's expansion ports. For slit-lamp measurements, the spectra were collected using the built-in tungsten bulb and optics (L1, L2, and a beam splitter, wherein L2 is configurable to four different magnifications (5x, 8x, 10x, and 30x), Figure 3.9c).

To calculate IOPs, an in-house-developed program was used to identify and convert the locations of the peaks and valleys in a captured spectrum into the corresponding size of the cavity gap and external pressure [19]. The reference pressures inside the test chamber were obtained using a commercial digital pressure gauge (1210 Pressure Sensor, TE Connectivity Ltd.) with $\pm$0.1 mmHg accuracy.

Continuous in vivo IOP monitoring in un-anesthetized rabbits

Surgical procedures detailed in Section 2.3 were followed. Briefly, each IOP sensor was mounted on a 200 μm wide and 2.5 mm long flexible I-shaped silicone strip and inserted into the anterior chamber of the rabbit eye through a 2 mm corneal incision. The sensor mounted strip was positioned over the iris and the crystal lens and secured against the inner walls of the cornea.

In vivo measurements were performed using a modified slit-lamp. Using the built-in eye piece or the CCD camera, the sensor was located by setting L2 at its lowest magnification. The optical alignment between the sensor and the detection system was easily accomplished using the built-in transnational stage of the slit-lamp (4 degrees of freedom, 3 transnational, and 1 rotational). The L2 magnification was then increased to 30x and the active region of the sensor occupied $\approx$ 9.6% of the field-of-view. A single spectrum required 100 ms to capture.

Sensor retrieval and staining

Upon retrieval, the sensors were rinsed in sterile 1x PBS/0.02% NaN_3. They were then incubated in 4% PFA for at least 30 min at room temperature (RT) overnight (O/N) or longer at 4^{o}C. Next, a quenching step was performed where the sensors were rinsed in sterile 1x PBS three times gently shaken for 5 mins each time. The sensors were then incubated in freshly prepared 1xPBS/0.02% NaN_3/50 mM NH_4Cl (quenching buffer) for 10 min at RT. The sensors were then rinsed in sterile 1x PBS/0.02% NaN_3 three times gently shaken for 5 mins each time. Next, a blocking step was performed where the sensors were incubated in 1x PBS/0.02% NaN_3/2% BSA/0.25% TritonX100 (blocking buffer) at 4^{o}C with gentle shaking O/N. Next, the sensors were stained by incubating them in 1 mL blocking buffer/DAPI 405 1:2000/CD62L 488 1:500/Phalloidin 555 1:1000 (staining reagent) at RT with shaking for 1 hr. They were then incubated in the staining reagent at 4^{o}C O/N. The sensors were then prepared for imaging by first being transferred into the blocking buffer. Next, they were washed in the blocking buffer three times followed by incubating in blocking buffer at 4^{o}C O/N. Finally, the sensors were rinsed in sterile 1x PBS/0.02% NaN_3 three times gently shaken for 5 mins each time and were soaked in the same reagent for imaging.

Confocal immunofluorescence microscopy and analyses

Surface area measurements (DAPI 405 and Phalloidin 555) and inflammatory response (CD62L 488) were determined over the core cavity regions of the sensors using ImageJ, an open-source image-processing program. Inflammatory response assessment was conducted by studying the overlap between DAPI 405 and CD62L 488.

References

[1] Jeong Oen Lee, Haeri Park, Juan Du, Ashwin Balakrishna, Oliver Chen, David Sretavan, and Hyuck Choo. A microscale optical implant for continuous in vivo monitoring of intraocular pressure. *Microsystems and Nanoengineering*, 3(1):17057–1–17057–9, 2017. doi: 10.1038/micronano.2017.57.

[2] Eugene Hecht. *Optics*. New York: Pearson, fifth edition, 2016. ISBN 9780133979091.

[3] Jeong O. Lee, Vinayak Narasimhan, Juan Du, Blaise Ndjamen, David Sretavan, and Hyuck Choo. Biocompatible multifunctional black-silicon for implantable intraocular pressure sensor. *Advanced Healthcare Materials*, 6(4):1601356–1–1601356–7, 2017. doi: 10.1002/adhm.201601356.

[4] H. L. Gorton and T. C. Vogelmann. Effects of epidermal cell shape and pigmentation on optical properties of *Antirrhinum* petals at visible and ultraviolet wavelengths. *Plant Physiology*, 112(3):879–888, 1996. doi: 10.1104/pp.112.3.879.

[5] Dimitrios Gkikas, Apostolos Argiropoulos, and Sophia Rhizopoulou. Epidermal focusing of light and modelling of reflectance in floral-petals with conically shaped epidermal cells. *Flora - Morphology, Distribution, Functional Ecology of Plants*, 212(1):38–45, 2015. doi: 10.1016/j.flora.2015.02.005.

[6] Ruben Hünig, Adrian Mertens, Moritz Stephan, Alexander Schulz, Benjamin Richter, Michael Hetterich, Michael Powalla, Uli Lemmer, Alexander Colsmann, and Guillaume Gomard. Flower power: Exploiting plants epidermal structures for enhanced light harvesting in thin-film solar cells. *Advanced Optical Materials*, 4(10):1487–1493, 2016. doi: 10.1002/adom.201600046.

[7] Martin Otto, Matthias Kroll, Thomas Käsebier, Seung Mo Lee, Matti Putkonen, Roland Salzer, Paul T. Miclea, and Ralf B. Wehrspohn. Conformal transparent conducting oxides on black silicon. *Advanced Materials*, 22(44):5035–5038, 2010. doi: 10.1002/adma.201002515.

[8] Jinsu Yoo, Gwonjong Yu, and Junsin Yi. Large-area multicrystalline silicon solar cell fabrication using reactive ion etching (RIE). *Solar Energy Materials and Solar Cells*, 95(1):2–6, 2011. doi: 10.1016/j.solmat.2010.03.029.

[9] M. Stubenrauch, M. Fischer, C. Kremin, M. Hoffmann, and J. Muller. Bonding of silicon with filled and unfilled polymers based on black silicon. *Micro and Nano Letters*, 2(1):6–8, 2007. doi: 10.1049/mnl:20065064.

[10] C. Dorrer and J. Ruhe. Wetting of silicon nanograss: From superhydrophilic to superhydrophobic surfaces. *Advanced Materials*, 29(1):159–163, 2007. doi: 10.1002/adma.200701140.

[11] Marios Barberoglou, Vassilia Zorba, Alexios Pagozidis, Costas Fotakis, and Emmanuel Stratakis. Electrowetting properties of micro/nanostructured black silicon. *Langmuir*, 26(15):13007–130014, 2010. doi: 10.1021/la101138u.

[12] Elena P. Ivanova, Jafar Hasan, Hayden K. Webb, Gediminas Gervinskas, Saulius Juodkazis, Vi Khanh Truong, Alex H.F. Wu, Robert N. Lamb, Vladimir A. Baulin, Gregory S. Watson, Jolanta A. Watson, David E. Mainwaring, and Russell J. Crawford. Bactericidal activity of black silicon. *Nature Communications*, 4(1):2838–1–2838–7, 2013. doi: 10.1038/ncomms3838.

[13] Maria Gaudig, Jens Hirsch, Norbert Bernhard, and Ralf B. Wehrspohn. Properties of black silicon obtained at room-temperature by different plasma modes. *Journal of Vacuum Science and Technology A*, 33(5): 05E132–1– 05E132–8, 2015. doi: 10.1116/1.4929540.

[14] Antti Kontiola and Paivi Puska. Measuring intraocular pressure with the Pulsair 3000 and rebound tonometers in elderly patients without an anesthetic. *Graefes Archive for Clinical and Experimental Ophthalmology*, 242(1):3–7, 2004. doi: 10.1007/s00417-003-0671-3.

[15] Roberto Dominguez and Kenneth C. Holmes. Actin structure and function. *Annual Review of Biophysics*, 40(1):169–186, 2011. doi: 10.1146/annurev-biophys-042910-155359.

[16] Thomas D. Pollard and John A. Cooper. Actin, a central player in cell shape and movement. *Science*, 326(5957):1208–1212, 2009. doi: 10.1126/science.1175862.

[17] Kenneth C. Holmes. Actin in a twist. *Nature*, 457(7228):389–390, 2009. doi: 10.1038/457389a.

[18] Vy T. H. Pham, Vi Khanh Truong, Anna Orlowska, Shahram Ghanaati, Mike Barbeck, Patrick Booms, Alex J. Fulcher, Chris M. Bhadra, Ricardas Buividas, Vladimir Baulin, C. James Kirkpatrick, Pauline Doran, David E. Mainwaring, Saulius Juodkazis, Russell J. Crawford, and Elena P. Ivanova. Race for the surface: Eukaryotic cells can win. *ACS Applied Materials and Interfaces*, 8(34):22025–22031, 2016. doi: 10.1021/acsami.6b06415.

[19] G.C. Hill, R. Melamud, F.E. Declercq, A.A. Davenport, I.H. Chan, P.G. Hartwell, and B.L. Pruitt. SU-8 MEMS Fabry-Pérot pressure sensor. *Sensors and Actuators A*, 138(1):52–62, 2007. doi: 10.1016/j.sna.2007.04.047.

Chapter 4

MULTIFUNCTIONAL SILICON-NITRIDE BIOINSPIRED NANOSTRUCTURES FOR IOP SENSING

This chapter was adapted from:

V. Narasimhan*, R. H. Siddique*, J. O. Lee, S. Kumar, B. Ndjamen, J. Du, N. Hong, D. Sretavan and H. Choo (2018). "Multifunctional biophotonic nanostructures inspired by the longtail glasswing butterfly for medical devices." In: ***Nature Nanotechnology*** 13.6, pp. 512–519. DOI: 10.1038/s41565-018-0111-5. [*co-first authors]

Abstract

Numerous living organisms possess biophotonic nanostructures that provide coloration and other diverse functions for survival. While such structures have been actively studied and replicated in the laboratory, it remains unclear whether they can be used for biomedical applications. Here, we show a transparent photonic nanostructure inspired by the longtail glasswing butterfly (*Chorinea faunus*) and demonstrate its use in intraocular pressure (IOP) sensors *in vivo*. We exploit the phase separation between two immiscible polymers (poly(methyl methacrylate) and polystyrene) to form nanostructured features on top of a Si_3N_4 substrate. The membrane thus formed shows good angle-independent white-light transmission, strong hydrophilicity and anti-biofouling properties, which prevent adhesion of proteins, bacteria and eukaryotic cells. We then developed a microscale implantable IOP sensor using our photonic membrane as an optomechanical sensing element. Finally, we performed *in vivo* testing on New Zealand white rabbits, which showed that our device reduces the mean IOP measurement variation compared with conventional rebound tonometry without signs of inflammation.

4.1 Introduction

This chapter presents further engineering efforts on the IOP sensor implant platform to greatly improve *in vivo* performance. Two specific improvements

to the platform are discussed here, the first of which is optical. As described in Section 2.3, the FP-based IOP sensor works on the principle of interference which is an angle-dependent property (see Section 1.4). In other words, the signal from the FP cavity changes as a function of incident angle. When light incidence occurs at an oblique angle $\alpha \neq 0$ ($\alpha = 0$ at normal incidence), the equation for the resonance profile (equation 2.2) can be rewritten with $d = h\cos\alpha - \sin^2\alpha$ where h is the gap-size [1]. As a result, changes in incident angle change the optical path length traversed by light within the cavity, thereby generating shifts in the resonance profile. This is shown in Figure 4.1.

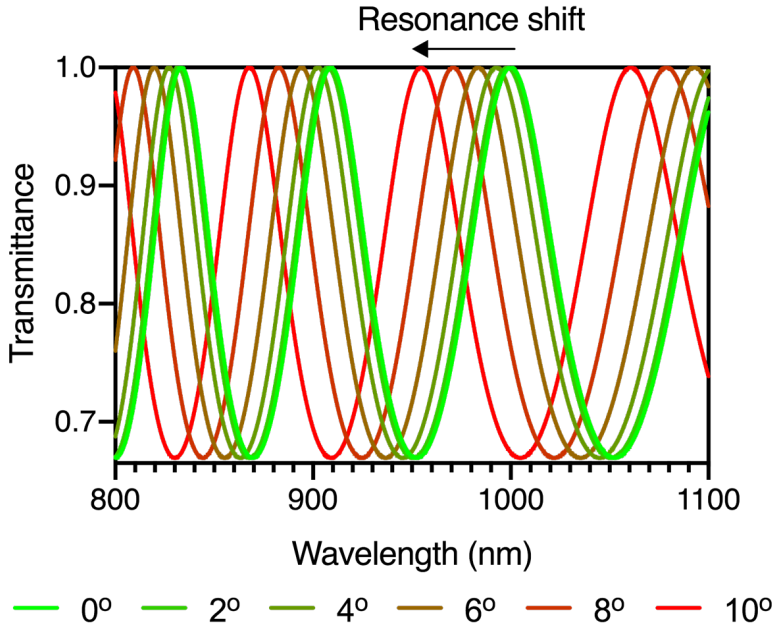

Figure 4.1: Dependence of the FP cavity resonance profile on the angle of incidence. The spectrum blue-shifts with increasing angle where 0° corresponds normal incidence.

Since shifts in resonance of the FP-based sensor is the mode of detection used to discern changes in ambient IOP, *in vivo* performance of the device was often hindered by sensor/detector optical alignment issues. Not only were erroneous pressures detected as a result of undesirable resonance-shifts due to changes in sensor/detector alignment, but also loss in signal due to limitations imposed by the numerical aperture (NA) of the collection optics of the detector. In other words, beyond a certain sensor/detector angle, the maximum acceptance angle of the detector is exceeded which results in loss of signal. These issues are illustrated in Figure 4.2a.

The second issue observed during *in vivo* work was that of biofouling. Often due to acute inflammation post surgery, the active regions of the device, specifically the Si_3N_4 membrane of the device would be fouled. Tissue, being scattering in nature, occludes the optical pathway of light being used to interrogate and readout from the device leading to loss of signal and reduced *in vivo* longevity. This issue is illustrated in Figure 4.2b.

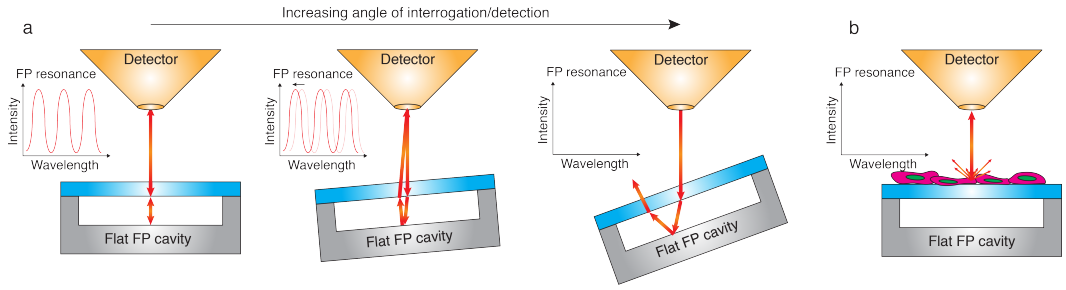

Figure 4.2: Challenges faced during *in vivo* implementation of IOP sensor. (a) With increasing angle of interrogation/detection, erroneous shifts in the resonance profile of the sensor are first observed. When the angle of interrogation/detection becomes larger than the collection angle of the objective lens of the detector, a loss of signal is observed. (b) Cell adhesion and proliferation on the Si_3N_4 membrane of the device leads to loss of signal.

In this chapter, inspiration is sought from the multifunctional biophotonic nanostructures found on the transparent wings of the longtail glasswing butterfly (*C. faunus*) to advance the versatility of the IOP sensor implant whose practical use is limited by the angle dependency of sensing and readout processes as well as short- and long-term biofouling. The surface and optical properties of the short-range-ordered nanostructures found on *C. faunus* wings are characterized in detail, which could overcome the aforementioned shortcomings of the IOP sensor. The study reveals that *C. faunus* relies on relatively moderate-aspect-ratio (aspect ratio ≈ 1) chitin nanostructures to produce (1) transparency that is a unique combination of wavelength-selective anti-reflection and angle-independent transmission resulting from isotropic Mie scattering, and (2) antifouling properties through disruption of cellular growth similar to that observed on high-aspect-ratio (aspect ratio > 1) structures found in nature [2, 3]. Drawing inspiration from the *C. faunus* nanostructures, low-aspect-ratio (aspect ratio < 1) bioinspired nanostructures were created on freestanding Si_3N_4-membranes using a highly scalable phase-separation-based polymer-assembly process. Unlike previous high-aspect-ratio bio-inspired nanostructures replicating anti-reflection [2–4], the pseudo-periodic arrangement and

dimensions of nanostructures were engineered to control isotropic scattering and enhance omnidirectional optical transmission, which could benefit sensing and readout processes of the IOP sensor. In addition, improving on the anti-biofouling properties of high- and moderate-aspect-ratio nanostructures that typically rely on physical cell lysis [2, 3, 5], low-aspect-ratio nanostructures were engineered to generate strong nanostructure-mediated hydrophilicity and an anti-adhesion barrier for proteins and cellular fouling without inducing cell lysis and inflammation. These enhancements are illustrated in Figure 4.3.

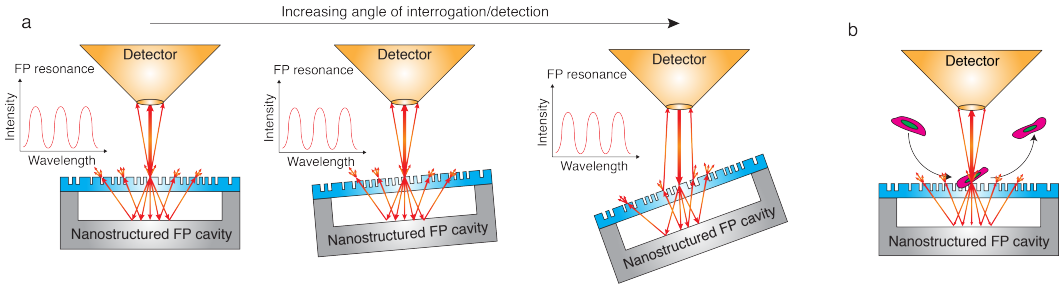

Figure 4.3: Sensor *in vivo* performance improvement using bioinspired nanostructures. (a) Enhanced optical properties rendered by multifunctional bioinspired nanostructures on the Si_3N_4 membrane make the sensor more angle-independent and improve the acceptance angle of the device. (b) The same nanostructures also mediate the adhesion of host cells, thereby improving the *in vivo* lifetime of the device.

4.2 Multifunctional nanostructures of C. faunus

Wing characterization

The *C. faunus* (Figure 4.4a) butterfly belongs to the Riodinidae family found in South America. *C. faunus* wings are distinct from most other transparent wings in nature [4, 6, 7]. They have a rare combination of two transparent regions that transmit light differently: basal transparent areas close to the thorax (indicated by a blue arrow in Figure 4.4a); and postdiscal transparent areas further away from the thorax (red arrow in Figure 4.4a) of both the forewing and hindwing. High-resolution atomic force microscopy (AFM) and scanning electron microscopy (SEM) of the postdiscal transparent area reveals dome-shaped nanopillars with moderate aspect ratios (1.090 ± 0.041; Figures 4.4b and c) compared with other natural transparent wings with higher aspect ratios (> 1) [2, 6, 8]. Interestingly, the basal transparent area is composed of similarly shaped nanostructures at a lower density (Figure 4.4d). Two-dimensional fast Fourier transforms (2D-FFT) of the SEM images showed

ring-shaped distributions (insets of Figures 4.4c and d), which confirmed their short-range-ordered arrangements [6, 9]. The finite diameters of the rings in k-space quantified the average periods of the nanostructures as 140–180 nm and 200–300 nm for the postdiscal and basal areas, respectively.

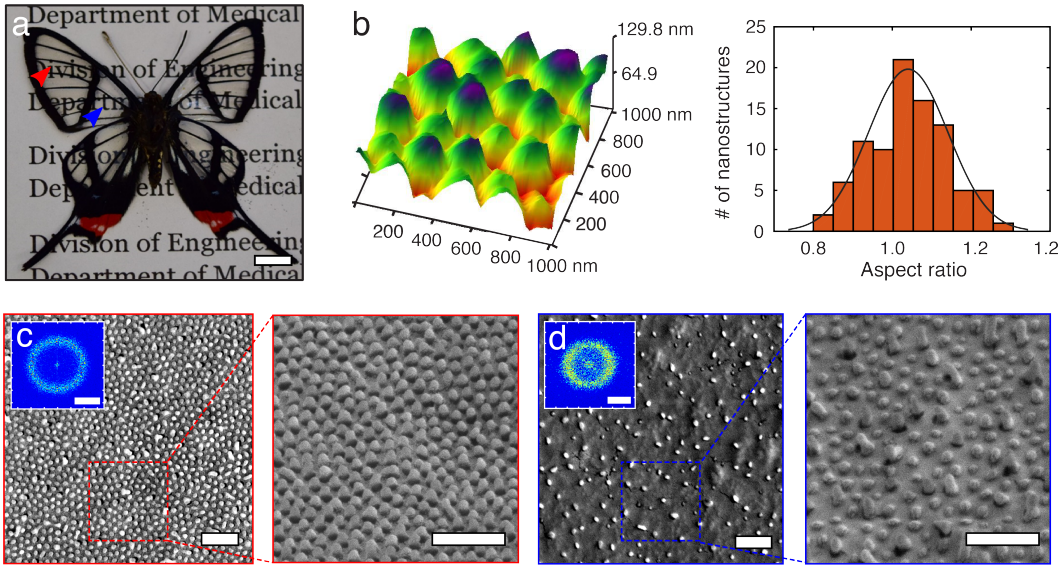

Figure 4.4: *C. faunus* butterfly wing characterization. (a) Photo of a *C. faunus* butterfly under visible light. The red and blue arrowheads indicate the postdiscal and basal areas, respectively. Scale bar: 1 cm. (b) AFM and statistical analysis of the aspect ratio (height over base diameter) of nanostructures on the *C. faunus* wing. An average aspect ratio of 1.090 ± 0.041 is estimated by fitting a Gaussian profile. SEM images of the (c) densely packed postdiscal area (d) and sparsely located basal area dome-shaped nanostructures. Insets: 2D Fourier transform of the corresponding nanostructures. Scale bars: 1 μm (inset: 2 μm^{-1}).

Wing optical properties

The zone-dependent variation in average interstructural periods on the *C. faunus* wing plays an important role in the extent of light scattering on the wing. The postdiscal area with an average period below 200 nm remains scattering-free and anti-reflective in the visible–near-infrared (VIS–NIR) regime. The transparency of the postdiscal area can be well-explained by effective medium theory and a transfer matrix model similar to other anti-reflective subwavelength nanostructures found in nature considering the low absorption of chitin [6, 10]. The subwavelength nanodome-shaped structures of the postdiscal area induces a refractive index with a linear gradient from

1 for air to 1.56 [11] for the chitin membrane, and effectively reduces surface reflection [6, 10]. Nanodome-shaped structures of the postdiscal area are hexagonally arranged and hence, a hexagonal unit cell was considered with an area of $A_{\text{hex}} = \frac{\sqrt{3}}{2}d^2$ where d is the center-to-center distance between adjacent nanodomes. The radius of the nanodome at height z was provided by $r(z) = r_0\sqrt{1-\frac{z}{h}}$, where h is the height of the nanodomes, and r_0 is the base radius that is equal to $\frac{d}{2}$. Consequently, the postdiscal nanodome area at height z is given by $A_{\text{PD}}(z) = \pi r_0^2\left(1-\frac{z}{h}\right)$, and the volume fraction of chitin as a function of actual height is given by

$$f_{\text{PD}} = \begin{cases} 1 & z < 0 \\ \frac{\pi}{2\sqrt{3}}\left(1-\frac{z}{h}\right) & 0 \le z \le h \\ 0 & z > h \end{cases} \tag{4.1}$$

which is identical to equation 1.19. The base of the nanodomes was defined to include the origin of the z-axis at its center. The remaining fraction of air is given by $f_{\text{air}} = 1 - f_{\text{PD}}$. After determining the volume fraction, the effective refractive index can be calculated for any z using the well-known Maxwell-Garnett model. Then, the optical admittance and the corresponding reflection (R) and transmission (T) spectra of the stacked thin layers can be calculated using a characteristic matrix method [10].

The basal area with an average period exceeding 200 nm comparable to light wavelengths shows forward narrow-angle scattering due to more sparsely located, moderate-aspect-ratio, low-index nanostructures [12, 13]. In other words, the transparency occurs due to non-resonant forward Mie scattering from low index chitin ($n_{\text{chitin}} = 1.56$) nanostructures that can be calculated by rigorously solving the Maxwell's equations [12, 13].

In order to compare the simulated transmission spectra of postdiscal and basal areas with experimental spectra, the membrane absorption and light reflections from its backside were considered assuming the wing membrane was surrounded by nanostructures on both sides. Considering the thickness of the wing membrane l (500 nm) and absorption coefficient $\alpha = 4\pi\kappa\lambda$ where $\kappa = 0.008 \pm 0.001$, the extinction coefficient considered here for the chitin, the final transmittance (T_F) can be calculated by [6]

$$T_F = \frac{T^2 e^{-\alpha l}}{1 - R^2 e^{-2\alpha l}}. \tag{4.2}$$

The simulated transmission spectra of both postdiscal and basal areas are plotted in Figure 4.5 along with the experimental outcomes, showing good agreement.

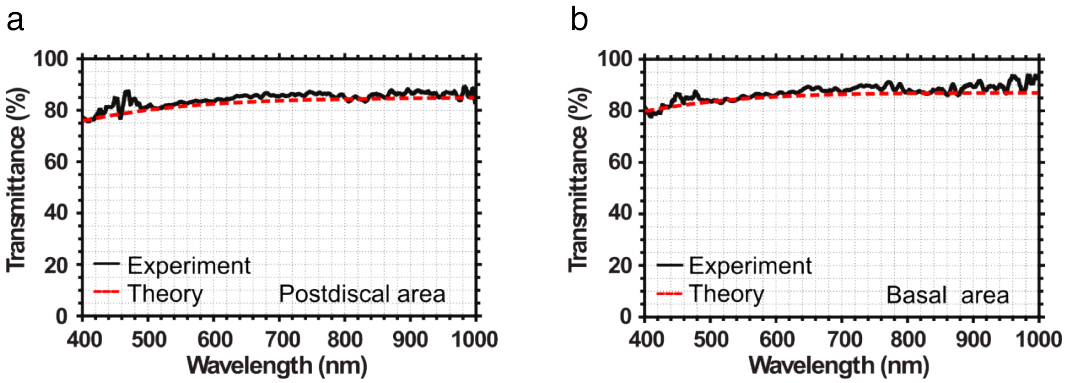

Figure 4.5: Comparisons of simulated and experimentally measured total transmittance spectra of the (a) postdiscal and (b) basal areas. Simulation results are in accord with the experimental outcomes, confirming the discussed physics for the transparency observed in the *C. faunus* butterfly wings.

To selectively characterize the scattering behavior of the basal area, FDTD simulations performed on both groups of nanostructures at a wavelength of 420 nm produced matching results that confirmed the scattering mechanism of the basal area (Figure 4.6). Though the same structural height and diameter for both groups were used in the simulations, the nanostructures with a 150 nm period (similar to the postdiscal area) did not alter the transmitted field (Figure 4.6a), whereas nanostructures with a 300 nm period (similar to the basal area) showed forward scattering of the transmitted light (Figure 4.6b). The scattering phenomenon of the basal region is moreover confirmed by the difference observed between the specular transmittance and total transmittance in the VIS–NIR range shown in Figures 4.7a and b.

To further analyze the transmissive scattering properties of both areas, angle-resolved scattering spectroscopy was performed in the VIS range varying both the incident and detection angles (Figures 4.7c and d). Having almost identical specular and diffuse transmissions in the VIS–NIR range (Figure 4.7a), the postdiscal area exhibited specular transmittance with a low scattering angle of $\pm 3^{\circ}$ (Figure 4.7c). Contrastingly, the basal area scattered light in the forward

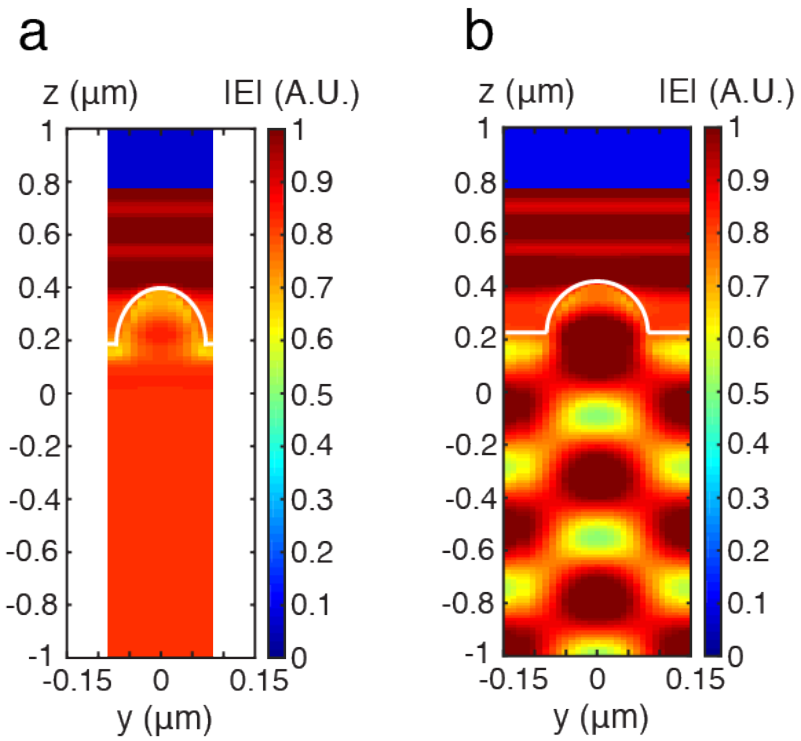

Figure 4.6: Finite-difference time-domain simulations of the near-field scattering profile for (a) the postdiscal area (cell periodicity: 150 nm) and (b) basal area (cell periodicity: 300 nm) at a wavelength of 420 nm.

direction with scattering angles up to $\pm 12^{o}$ and showed negligible changes with incident angle variation, demonstrating its potentially very useful angle-independent scattering property (Figure 4.7d). This scattering property could ameliorate the difficulty of detecting optical signals at wide angles, a commonly observed challenge among many light-based devices [14] such as implantable IOP sensors [15].

The angle-independent scattering properties of the basal area as found in Figure 4.7d are directly correlated to the isotropic spatial frequency of the short-range-ordered nanostructures. For example, if we consider light with an incident wave vector $\mathbf{k_i}$ being scattered to a wave vector $\mathbf{k_s}$, the difference between $\mathbf{k_i}$ and $\mathbf{k_s}$ can be provided by the spatial frequency $\mathbf{k_b}$ of the structure, i.e. $\mathbf{k_s} - \mathbf{k_i} = \mathbf{k_b}$ [9]. Due to the isotropic nature of the spatial frequency $\mathbf{k_b}$ (see the FFT inset in Figure 4.4d), the $\mathbf{k_s} - \mathbf{k_i}$ will remain the same irrespective of the incident angle, thereby improving the angle-independent scattering properties.

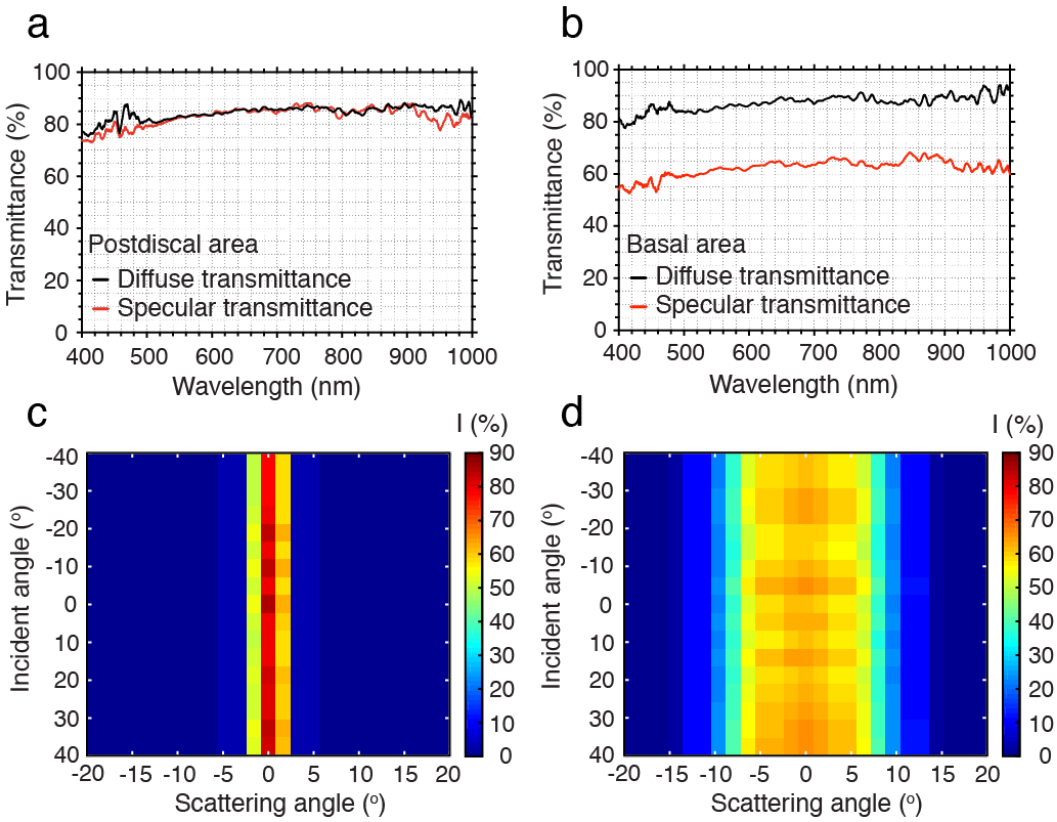

Figure 4.7: *C. faunus* wing scattering. (a) Measured diffuse and specular transmittance of the postdiscal area; difference in spectra within the experimental uncertainty. (b) Measured diffuse and specular transmittance of the basal area showing a 20% difference in transmittance and a noticeable scattering property. The forward scattering of (c) postdiscal and (d) basal areas were recorded for a range of incident angles varying from -20 to 20° at a wavelength of 420 nm. The measurements depict different degrees of the haze effect for the postdiscal (low in haze) and basal (high in haze) areas. The postdiscal area exhibits specular transmittance with a low scattering angle of ±3°. Conversely, the basal area scatters light in a forward direction with a much wider scattering angle of ±12°.

Biological significance

To elucidate the biological significance of the dual nano-structural basis for transparency of the *C. faunus* wing, the wings were illuminated under ultraviolet (UV) light and corresponding images were captured using a camera (Figure 4.8a). No UV signature in the postdiscal areas was observed, whereas the basal areas showed violet-coloured reflectance under UV illumination (Figure 4.8a). The short-range-ordered nanostructures with subwavelength periods in the postdiscal areas exhibited minimal scattering and high transparency in

the UV-VIS light. However, similar nanostructures in the basal areas with larger inter-structural spacing comparable to the light wavelength generated backscattering in the UV range. The short-range order of the nanostructures in the spatial arrangement introduces a phase correlation in the backscattered light, leading to a coherent reflection peak in the UV regime as shown in Figure 4.8b. The characteristic length scale of the nanostructures generates such strong backward scattering of light within a narrow frequency range [16]. In general, for any wave vector of $\mathbf{k} > \frac{\mathbf{k_b}}{2}$, short-range structural order introduces a phase correlation of light scattered by adjacent particles [17]. $\mathbf{k_b}$ ranges between 0.021 nm^{-1} and 0.032 nm^{-1} in the 2D FFT calculation of the basal area and hence $\frac{\mathbf{k_b}}{2}$ corresponds to the frequencies in the blue spectrum. Therefore, a coherent backscattered peak should appear in the frequencies higher than the blue spectrum, i. e. in the UV regime, which agrees with the experimental outcome.

Butterflies are known to use the UV regime as a key spectral range for mating signals [18–20], and the nanostructures with larger spacing in the basal area may play an important role in this regard. The UV signature with a peak at a wavelength of 345 nm is confirmed by the optical spectra shown in Figure 4.8b of the basal area. The total reflection of postdiscal area is remarkably low over the whole UV–VIS regime. In order to confirm that the UV reflection of the basal area is structure-based, we removed the structural effect by soaking the wing in bromoform ($n_{\text{bromoform}}$ = 1.57) to match the refractive index of the inter-structural space to that of the nanostructures. After soaking, we repeated the reflection measurement and observed no reflection from the basal region confirming the structural origin of the reflection property (Figure 4.8c).

4.3 Development of bio-inspired nanostructured membranes

Membrane fabrication

Inspired by the nanostructures on the basal area of *C. faunus* wings, we implemented short-range-ordered nanostructures on Si_3N_4-membranes (Figure 4.9) by utilizing a highly scalable bottom-up fabrication process based on polymer phase separation [21]. Si_3N_4 was chosen for its ease of fabrication on Si and proven performance as an optically transparent and mechanically robust free-standing membrane in microdevices as well as for its intrinsic hydrophilicity, which is crucial to the antifouling property of the nanostructures as discussed in more detail later [22, 23].

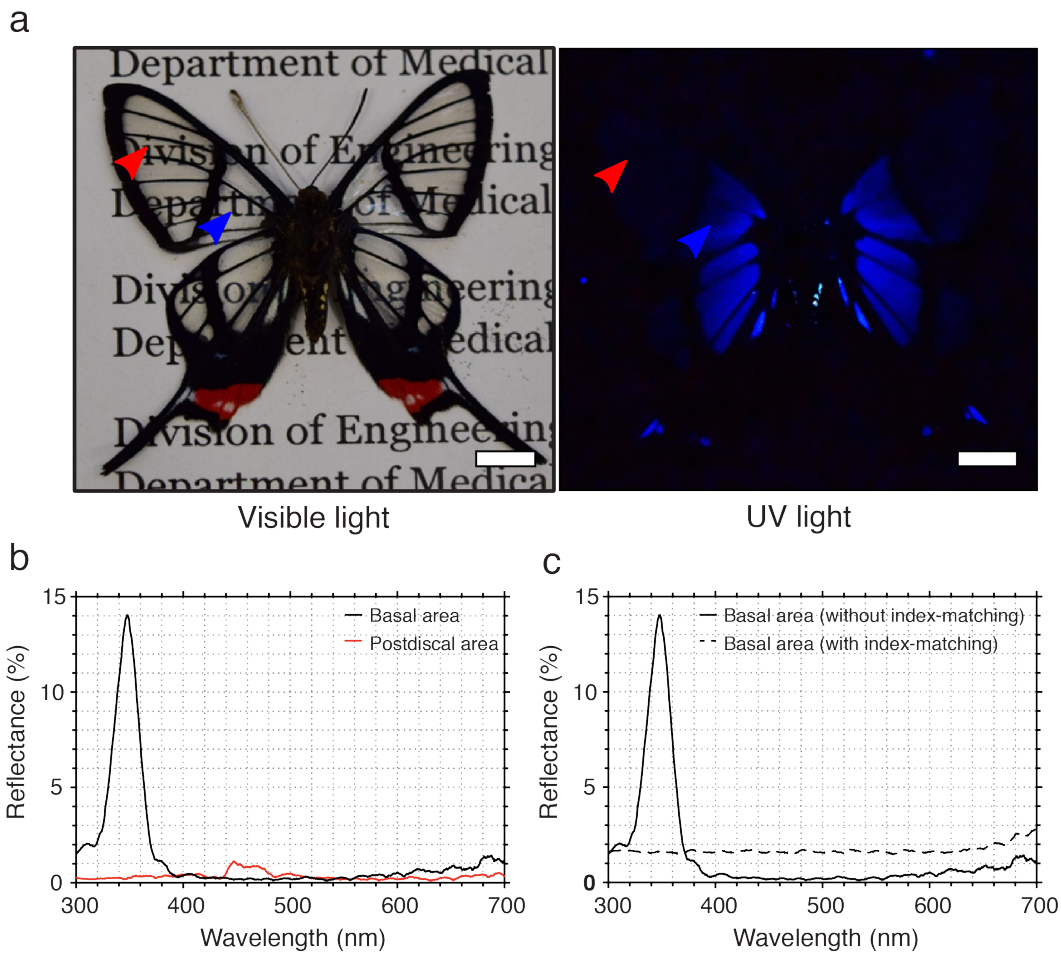

Figure 4.8: Selective UV reflection of *C. faunus* wings. (a) Photos of a *C. faunus* butterfly under visible and UV light. The red and blue arrows indicate the postdiscal and basal areas. (b) The UV signature of the basal area is clearly visible while the reflection from the postdiscal area is negligible confirming the violet-colored reflectance under UV illumination of the basal area. (c) The UV-VIS reflection spectra were obtained when soaking the wing in an index-matching liquid (bromoform, $n = 1.57$) to cancel out the structural contribution. In this case, no reflectance was observed under UV illumination from the basal area confirming the structural origin of this unique UV signature.

The membrane was fabricated as follows:

1. Spin-coating of a blend solution of PMMA and PS in MEK on $Si_3N_4/SiO_2/Si/SiO_2/Si_3N_4$ wafer.

2. Phase separation of the polymers.

3. Selective development of the PS.

4. Al_2O_3 hard mask formation using evaporation and lift-off processes.
5. Nanopillar-pattern transfer onto Si_3N_4 using plasma etch.
6. Release of the nanostructured Si_3N_4-membrane using backside optical lithography and reactive ion etching.

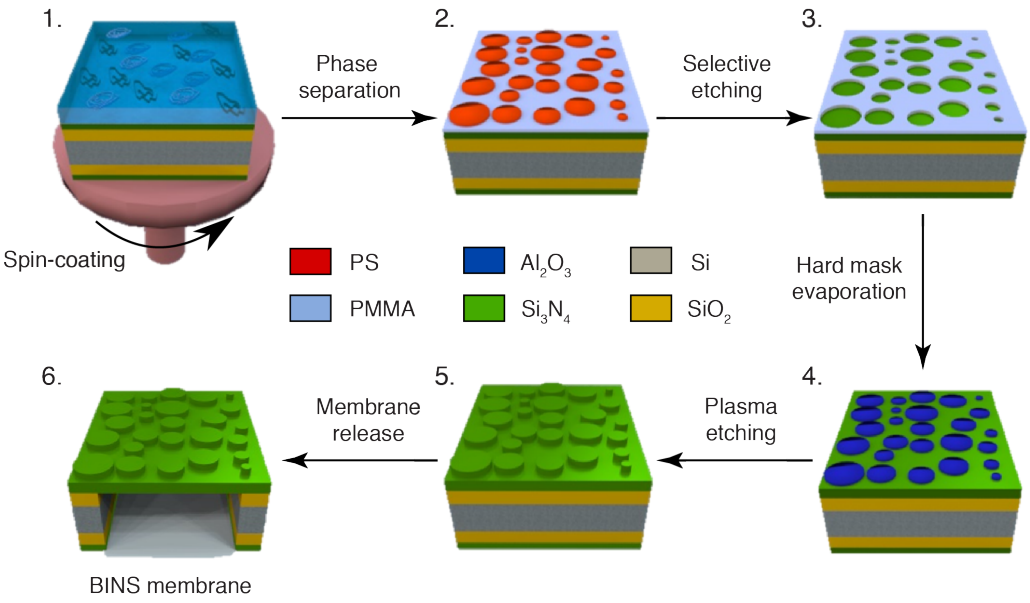

Figure 4.9: Fabrication flow of the bio-inspired nanostructured Si_3N_4-membrane.

Aspect-ratio optimization of the nanostructures

We created disk-shaped nanostructures with aspect ratios ranging from 0.15 to 0.90 and performed parametric studies to determine optical and anti-biofouling properties (Figure 4.10).

An antifouling approach relying on physical lysis may damage tissues and cells that come in contact with the implant, which may not be suitable for some medical uses. The aspect-ratio of the nanostructures was kept below 1 to rely on the hydrophilicity of the nanostructured Si_3N_4 surfaces to promote antifouling through anti-adhesion instead of through physical lysis. A literature survey on this phenomenon (summarized in Table 4.1) reveals that the aspect-ratio of 1 or greater will cause physically induced lysis on both naturally occurring and synthetic nanostructured surfaces.

With this background in mind, the nanostructure topography was optimized to an average aspect-ratio of 0.45 and a flat disk-shaped top. This aspect-ratio

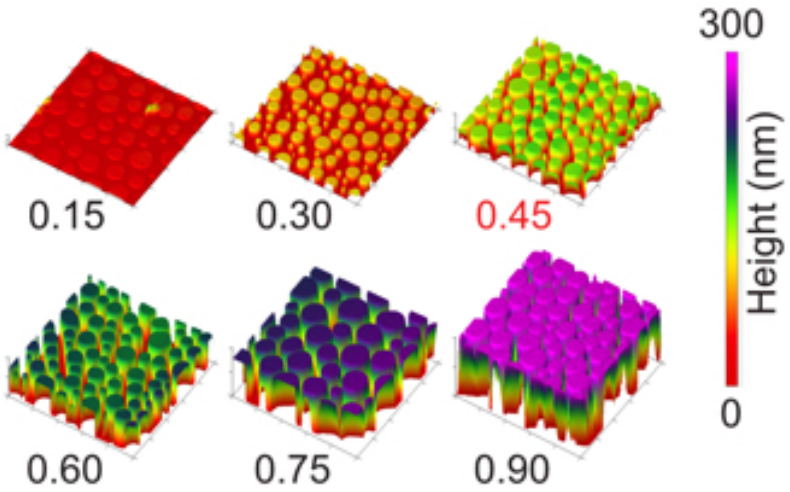

Figure 4.10: 3D AFM images of nanostructured Si_3N_4 templates with aspect-ratios ranging from 0.15 to 0.90. The aspect-ratio chosen for the nanostructured Si_3N_4-membrane and sensor is highlighted in red.

was chosen because there was no significant statistical difference in the anti-adhesion properties between nanostructured Si_3N_4 surfaces with an aspect-ratio of 0.45 and those with an aspect-ratio ranging from 0.45 to 0.9 (see Section 4.3: Biophysical properties of the nanostructures).

Furthermore, optical simulations indicate that increasing the aspect-ratio broadens the resonance peak of the nanostructured Si_3N_4 (Figure 4.11). The flat Si_3N_4-membrane produces a ballistic (specular) transmission peak due to the phase delay introduced by the thin membrane that causes light interference. The integration of nanostructures on the Si_3N_4-membrane broadens the total transmission-peak profile due to the combination of ballistic (due to the thin membrane) and scattered transmission (due to the nanostructures) [30].

Optimized bioinspired nanostructures

The SEM image of the nanostructured Si_3N_4-membrane is shown in Figure 4.12. The 2D fast Fourier transform of the SEM image shown in the inset indicates a short-range order with a mean period of 445 $\pm$ 60 nm, similar to the periodicity of the basal area.

The contact angle on the surface of the nanostructured Si_3N_4-membrane was 17^o, suggesting an increase in hydrophilicity compared to 38^o measured on flat Si_3N_4 without nanostructures (Figure 4.13).

We characterized the optical properties of the nanostructured Si_3N_4-membrane

Structure Type	Material/ Species	Aspect Ratio	Surface Wetting Properties		Cell Type Tested		Incubation Time		Comments
			Surface Type	Contact Angle (o)	Prokaryotes	Eukaryotes	Prokaryotes	Eukaryotes	
Synthetic	Silicon Nitride	0.15 - 0.9	Hydrophilic	22 - 13	*E. coli*	HeLa cells	4 hrs	1, 2, 3 days	Sharp drop in prokaryote and eukaryote adhesion with structuring *.
	PMMA	1.53	Hydrophobic	114	*P. aeruginosa*	C2C12 myoblasts	4, 8 hrs	7 days	Fair bactericidal activity. However, eukaryotes killed [3].
	PDMS	-	Hydrophilic	66	*E. coli, S. aureus*	Human fibroblasts	1, 2 days	4 hrs	Considerable bactericidal activity. Proliferation of eukaryotes [24].
	PMMA	1.39 - 3.0	Hydrophilic	-	*E. coli*	-	3, 18, 24 hrs	-	Adhesion density similar for all samples tested. Bactericidal activity increased with aspect ratio [25].
	Titanium	3.0 - 4.0	Hydrophilic	41.4	*E. coli, S. aureus*	HMSC, PBMC	1, 3 hrs	2 days	Bactericidal activity shown only against gram-negative *E. coli*. Additionally, proliferation of HMSC and PBMC observed [26].
	Black Silicon	7.14 - 10.0	Hydrophobic	95.65	*P. aeruginosa, S. aureus, B. subtilis*	COS-7	3, 18, 24, 30 hrs	1, 3, 7 days	Considerable bactericidal activity [2, 27]. Proliferation of eukaryotes [27].
Natural	*A. spectabile*	0.88	Hydrophobic	95.65	*P. fluorescens*	-	30 min	-	Minimal bactericidal activity. No eukaryotes tested [28].
	C. faunus	1	Hydrophobic	85.16, 105.42	*E. coli*	HeLa cells	4 hrs	1, 2, 3 days	Cell lysis and minimal cell adhesion in prokaryotes and eukaryotes *.
	C. aguila	1.15	Hydrophobic	113.2	*P. fluorescens*	-	30 min	-	Minimal bactericidal activity. No eukaryotes tested [28].
	M. intermedia	1.55	Hydrophobic	135.5	*P. fluorescens*	-	30 min	-	Considerable bactericidal activity. No eukaryotes tested [28].
	P. claripennis	2.0 - 3.33	Super-hydrophobic	147 - 172	*P. aeruginosa*	-	1 hr	-	Extensively studied. Considerable bactericidal activity. No eukaryotes tested [8, 29].
	D. bipunctata	2.67 - 8.0	Super-hydrophobic	153	*P. aeruginosa, S. aureus, B. subtilis*	-	3, 18, 24, 30 hrs	-	Considerable bactericidal activity. No eukaryotes tested [2].

Table 4.1: Summary of the literature survey on biophysical properties of synthetic and naturally occurring nanopillars. Butterfly species and materials discussed or utilized in this work are highlighted and marked as * in the comments section.

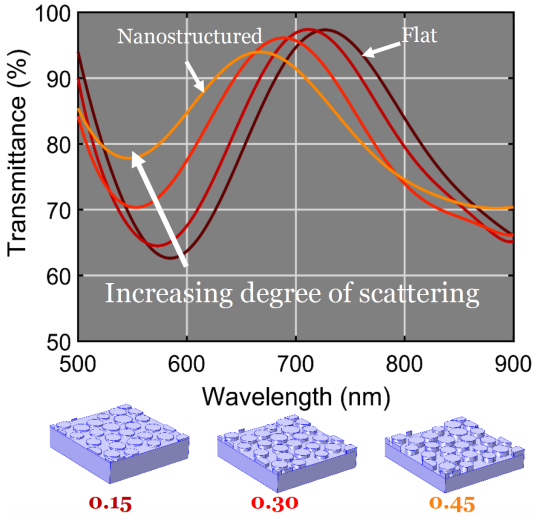

Figure 4.11: By gradually increasing the aspect ratio (height) of the nanostructures from 0 (i.e. flat membrane) to 0.45 in an FEM simulator using the exact geometry of the fabricated samples, a gradual increase in the total transmission is observed.

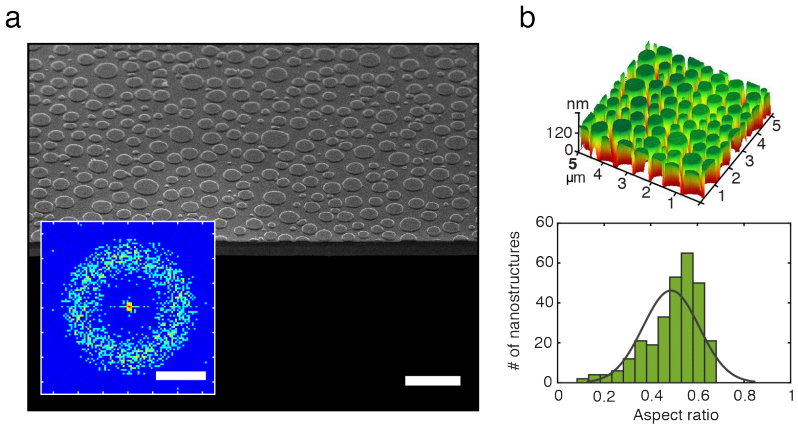

Figure 4.12: Optimized bioinspired nanostructured free-standing Si_3N_4-membrane. (a) SEM image of the nanostructures on the Si_3N_4-membrane and corresponding ring-shaped 2D Fourier power spectrum shown inset. Scale bars: 0.5 μm, inset 1.25 μm^{-1}. (b) 3D AFM image of the nanostructured Si3N4-membrane and nanostructure aspect ratio of 0.450 $\pm$ 0.065 approximated with a Gaussian fit.

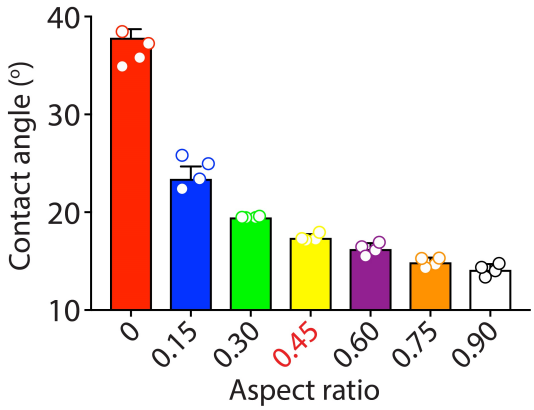

Figure 4.13: The wetting properties of nanostructured Si_3N_4 templates with aspect-ratios ranging from 0.15 to 0.90 ($n = 4$ measurements). Unmodified flat Si_3N_4 (aspect-ratio = 0) is moderately hydrophilic. Through structuring, the hydrophobicity of nanostructured Si_3N_4 increased. The aspect-ratio chosen for the nanostructured Si_3N_4-membrane and sensor is highlighted in red.

using angle-resolved transmission spectroscopy in the VIS–NIR range and compared the results to a flat Si_3N_4-membrane without nanostructures (Figure 4.14). Using the nanostructures, the angle independence of the Si_3N_4-membrane transmission was improved by 50%. 3D simulation of the fabricated structures further confirms the improved angle independent transmittance. This angle-independent transmission results from the isotropic nature of the

forward scattering property caused by the short-range-ordered nanostructures, which is independent of the incident angle (Figure 4.7d). As the total transmission is a combination of ballistic (specular) transmission through the thin membrane and scattered transmission caused by the nanostructures [30], the angle-independent property of the scattered component decreases the overall angle dependence of the total transmission.

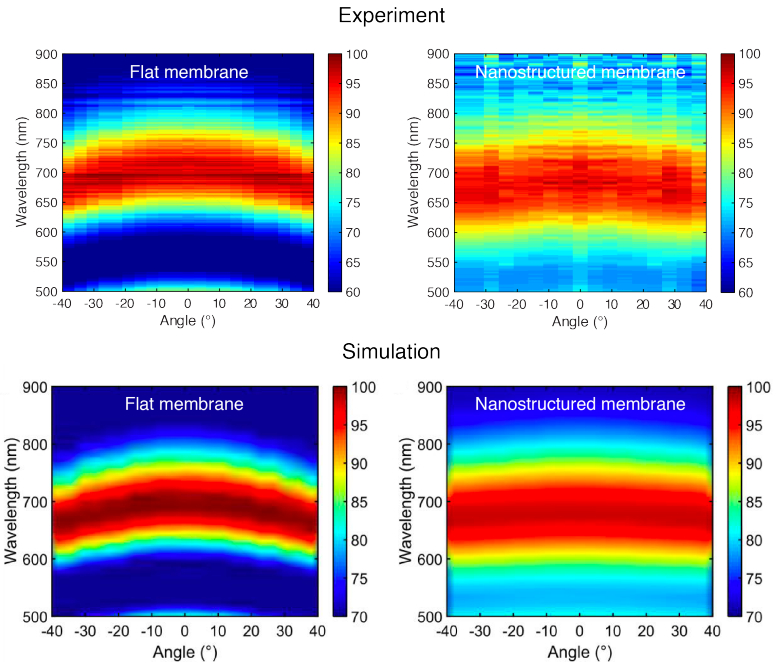

Figure 4.14: Experimentally obtained angle-resolved total transmittance of flat Si_3N_4-membrane showing a transmission peak around 705 nm due to the light interference introduced by the thin membrane with its peak blue-shifted 30 nm at 40° incident angle due to the angle-dependent nature of the coherent interference process, which agrees with analytical thin-film modeling. Experimentally obtained angle-resolved total transmittance of nanostructured Si_3N_4-membrane, showing significant reduction in angle-dependence. The integration of nanostructures on the Si_3N_4-membrane broadens the total transmission-peak profile, moves its center from 705 to 685 nm, and limits the magnitude of the peak shift to 15 nm at 40°, compared with 30 nm for a flat Si_3N_4-membrane.

Biophysical properties of the nanostructures

In vitro testing compared the adhesion of representative proteins, prokaryotes and eukaryotes on nanostructured and flat Si_3N_4 surfaces with lysine-coated glass slides as positive controls. Flat Si_3N_4 is moderately hydrophilic (contact angle: 35–40°) and known to vigorously promote cell adhesion and

proliferation due to increased adsorption of proteins when compared to more hydrophilic surfaces (contact angle: $< 20^{o}$) [31, 32]. Hence, we further increased the hydrophilicity of the Si_3N_4 surface by varying the aspect ratios of the nanostructures from 0.15 to 0.90 and systematically controlled surface hydrophilicity (Figure 4.13). Once strong hydrophilicity is achieved (contact angle: $< 20^{o}$), a nanostructure-mediated aqueous barrier forms on the surface and limits protein adsorption and cell adhesion to provide an anti-adhesion property (Figures 4.15c,d and 4.17d,e) [33–35].

We initially investigated the surface adhesion of two representative proteins: fluorescent-labeled bovine serum albumin for its cardinal role in blood–material interactions [36] and high non-specific binding affinity to the surfaces of biomaterials [37]; and streptavidin for its specific binding affinity to Si_3N_4 surfaces [38]. Fluorescence intensity-based quantification of the adhesion force (Figure 4.15) demonstrated adhesion on flat Si_3N_4 surfaces was three and two times greater than nanostructured Si_3N_4 surfaces for albumin and streptavidin, respectively.

We then quantified bacterial adhesion using *Escherichia coli* transformed with the green fluorescent protein (Figure 4.16a). In addition to being a popular prokaryotic model, *E. coli* was chosen for its pathogenic potential to cause Gram-negative and often antibiotic-resistant infections on and around implants [39, 40]. Bacteria on each surface were quantified through a measure of fluorescence-intensity measurements (Figure 4.16b) and colony-forming units (CFU) (Figure 4.16c). Both results indicated significantly lower bacterial adhesion on the nanostructured surface compared to flat Si_3N_4. Additionally, the SEM image of individual bacterial cells on the nanostructured surface shows no disruption to their shape, indicating no physical lysis (Figure 4.16d).

The HeLa cell line was chosen as a representative eukaryote for its proven robustness, aggressive growth rate and adherent nature, which prompts its frequent usage in adhesion and cytotoxicity assays [41, 42]. After 72 h, the adherent cell density on the flat Si_3N_4 was eight times greater than that on the nanostructured Si_3N_4 surface (Figures 4.17a, b). Next, a mortality ratio, the number of dead cells to the number of living cells, was computed for each surface every 24 h over a 72-h period. The difference in the mortality ratios of the two surfaces after 72 h was not statistically significant (Figure 4.17c), which suggested the nanostructured surfaces inhibited eukaryote adhesion and

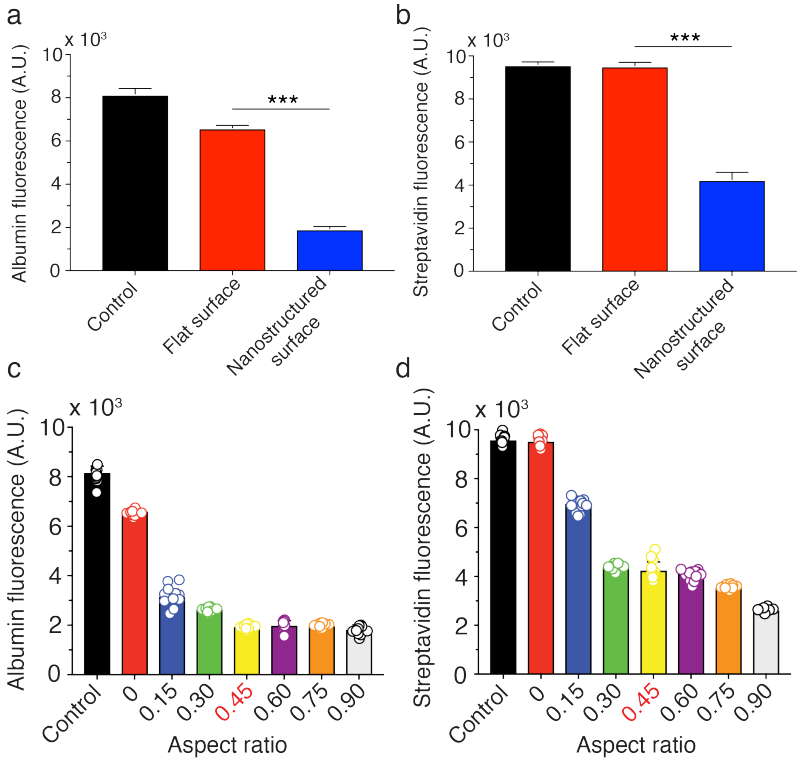

Figure 4.15: Adhesion force characterized using fluorescence-intensity microscopy for (a) bovine serum albumin and (b) streptavidin on positive control, flat Si_3N_4 and nanostructured Si_3N_4 surfaces. Nanostructured Si_3N_4 surfaces show significant reduction in albumin and streptavidin adhesion relative to the control and flat Si_3N_4 ($^{***}P < 0.001$, one-way ANOVA with post-hoc Tukey test, error bars show s.d., $n = 12$ representative images). (c,d) Nanostructured Si_3N_4 templates with different aspect-ratios (0 – 0.90) were studied. In both cases, a sharp decline in protein adhesion was observed upon structuring the Si_3N_4 (aspect-ratio ≥ 0.15). The protein adhesion on the flat Si_3N_4 (aspect-ratio $= 0$) was comparable to that of the positive control. The aspect-ratio of 0.45 chosen for use with an IOP-sensing implant is highlighted in red.

proliferation without inducing cell death.

These results highlight the advantage of the anti-biofouling approach based on strong hydrophilicity and anti-adhesion properties. High- or moderate-aspect-ratio nanostructures either with tapered sharp tips or dome-shaped tips as in *C. faunus* display potent geometry-dependent bactericidal properties that induce large stresses and deformation on cell walls regardless of their surface chemical composition [29] and actively promote autogenous lysis when placed in contact with mammalian cells [43]. Such anti-biofouling approaches relying on physical lysis could undesirably damage tissues surrounding implants

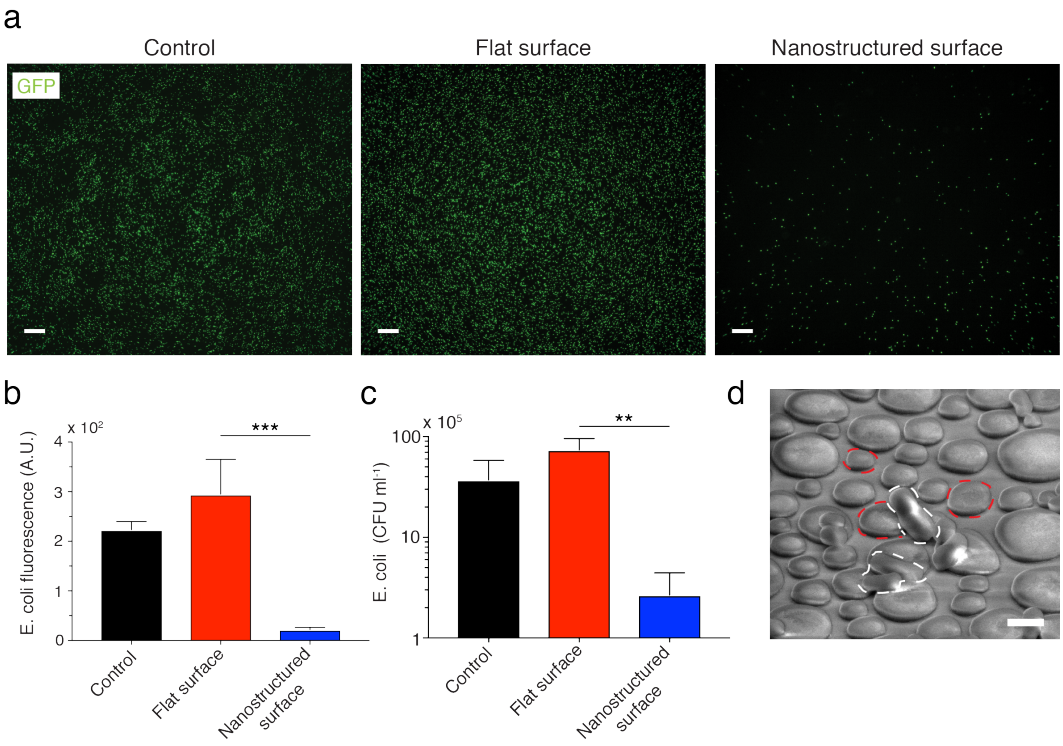

Figure 4.16: *In vitro* prokaryotic adhesion studies using *E. coli*. (a) Fluorescent micrographs of positive control, flat Si_3N_4, and nanostructured Si_3N_4 surfaces incubated for 4 hours in *E. coli* cultures transformed with green fluorescent protein (GFP)-expressing pFluoroGreen^{TM} plasmid. Minimal bacterial adhesion is observed on the nanostructured Si_3N_4 surface compared to the flat Si_3N_4 and control surfaces. Scale bars: 100 μm. (b) The average *E. coli* fluorescence intensity observed on the nanostructured Si_3N_4 surface was considerably lower than the flat Si_3N_4 surface ($^{***}P \leq 0.001$, one-way ANOVA with post-hoc Tukey test, s.d., $n = 5$ representative images). Adjustments were made for multiple comparisons. (c) The number of adherent CFUs of *E. Coli* on the nanostructured Si_3N_4 surface was significantly lower than that on the flat Si_3N_4 surface ($^{**}P < 0.01$, one-way ANOVA with post-hoc Tukey test, error bars show s.d., $n = 3$ agar plates). d) The nanostructures (circled in red) do not disrupt the shape of the cells (circled in white) and therefore do not induce physical lysis as seen in high aspect-ratio structures. Here, antifouling is achieved through anti-adhesion. Scale bar: 1 μm.

and elicit inflammation. Table 4.1 shows that physical lysis occurs on either natural or synthetic nanostructured surfaces if the aspect ratio of the nanostructures is one or greater. Hence, by keeping the aspect ratio of the nanostructures at 0.45, the anti-adhesion property was leveraged to prevent biofouling without causing any physical lysis. Additionally, the hydrophilic-

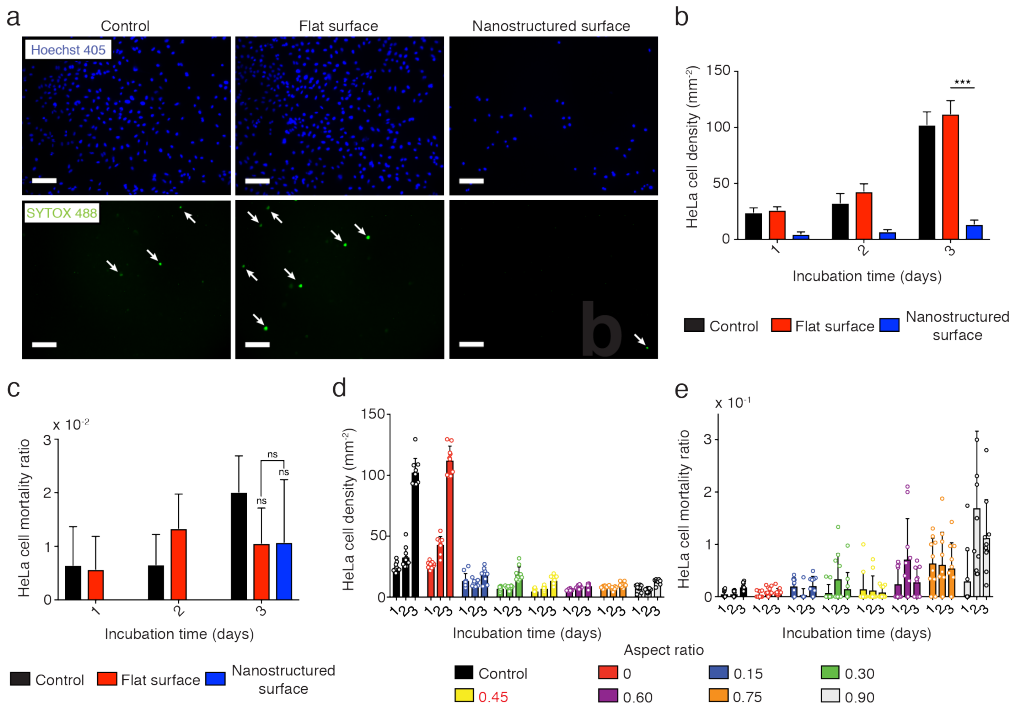

Figure 4.17: *In vitro* eukaryotic adhesion studies using HeLa cells. (a) Fluorescent micrographs of a positive control, flat Si_3N_4 and nanostructured Si_3N_4 incubated for 72 h in HeLa cell cultures labeled with cell-permeable nucleic acid markers Hoechst 405 (upper panels) and SYTOX Green (lower panels) indicating the anti-adhesive properties of nanostructured Si_3N_4. The arrows in the micrographs indicate dead cells. Scale bars: 100 μm. (b) Adherent HeLa cell density on the nanostructured Si_3N_4 surface was significantly lower than on the positive control and the flat Si_3N_4 surface (***$P < 0.001$, two-way ANOVA with Bonferroni's multiple comparisons test, error bars show s.d., n = 10 representative images). (c) Statistically similar mortality ratios (measured as the ratio of the number of dead cells to living cells) displayed by the control, flat Si_3N_4, and nanostructured Si_3N_4 surfaces after 72 hours ($P > 0.05$, ns: not significant, two-way ANOVA with Bonferroni's multiple comparisons test, s.d., n = 8 representative images). (d) HeLa live cell density was computed over 72 hours at 24-hour intervals using 10 representative fields-of-view captured through wide-field epifluorescence microscopy. A sharp reduction in adherent live cell density was observed upon structuring Si_3N_4 with nanostructures (n = 10 representative images). (e) HeLa cell viability was quantified as the ratio between the number of dead to living cells per field-of-view using 10 representative fields-of-view captured through widefield epifluorescence microscopy (n = 10 representative images). Higher rates of physically induced lysis were observed with increased nanostructured Si_3N_4 aspect-ratios. The aspect-ratio of 0.45 chosen to implement the nanostructured Si_3N_4-membrane for the IOP-sensing implant is highlighted in red.

ity of the nanostructured surface originates from surface topology, which may provide better long-term reliability over chemical-treatment methods.

Antifouling properties explained

We describe in this section our findings on the improved biocompatibility of the nanostructures: the nanostructures resist protein adhesion as well as prokaryotic and mammalian eukaryotic biofouling due to the surface hydrophilicity and nanostructured topology. To reach our conclusion, we have performed extensive literature study on the mechanisms behind the adhesion of plasma proteins, prokaryotes, and eukaryotes on the surface of implanted biomaterials; and also carried out a comprehensive set of experimental measurements and theoretical analysis performed on the nanostructured surfaces.

The adsorption behavior of a protein onto a surface is a complex process, which is influenced by the nature of the protein as well as the properties of the surface, and it may involve several steps such as protein association-disassociation, change in conformation, denaturation, and charge interaction between neighboring proteins [44–46]. As a result, there is a huge variation among underlying antibiofouling mechanisms and resulting outcomes of surfaces that have been proposed to control biofouling [47–49]. In the case of the nanostructured Si_3N_4 surface presented in this manuscript, our results indicate that the high degree of wettability (or hydrophilicity) acts in concert with the nanostructured surface topology to produce improved biocompatibility. We discuss this behavior of the substrate by considering energy barriers in the following paragraphs.

Let us consider attachment of a protein to a surface first. The reaction can be represented as

$$PL + SL \leftrightarrow PS \tag{4.3}$$

where protein molecules in an aqueous media or liquid (PL) are interacting with a surface submerged in liquid (SL) and leading to adsorption of protein molecules on the surface represented as PS. The effective free energy change for this reaction can be represented as ΔG_{PS}, which is dependent on the interfacial free energies of protein-liquid (γ_{PL}), protein-surface (γ_{PS}), and surface-liquid (γ_{SL}) [50]. This can be shown as [51]

$$\Delta G_{PS} = \gamma_{PS} - (\gamma_{PL} + \gamma_{SL}) \,. \tag{4.4}$$

For improved biocompatibility and reduced adsorption, the net energy change for the process should be positive, i.e. $\Delta G_{PS} > 0$, and a higher value of ΔG_{PS} would imply an unstable protein-surface interaction or a higher resistance to biofouling due to easy detachment. The interfacial free energies are dependent on the interactions between (1) the substrate surface and the liquid media (governed by the wettability of the surface); (2) the protein molecules and the liquid media (governed by the structure and distribution of hydrophobic/hydrophilic residues on the proteins); and (3) the protein molecules and the surface (dependent on both of the above factors). Normally proteins hide their hydrophobic residues away from water while their charged, polar amino-acid side-chains are exposed to water [52, 53]. As a result, charges on the proteins will also influence protein-protein interactions, which can lead to an aggregation of proteins in solution.

Noticeably hydrophilic surfaces such as nanostructures improve the affiliation between the surface and water molecules by lowering ΔG_{SL}, which is favorable for improved biocompatibility. If the protein has a higher degree of hydrophobic residues or behavior, ΔG_{PS} will be higher, which is favorable, but ΔG_{PL} will also be higher, which is unfavorable. Decrease in hydrophobicity of the protein will result in both lowering the ΔG_{PS} (unfavorable) and ΔG_{PL} (favorable). Changes in protein conformation during the surface adsorption process can also occur [44, 45], changing the interfacial free energy (ΔG_{PS}).

The surface-energy analysis indicates that in the case of the nanostructured Si_3N_4 surface, the increased hydrophilicity of the substrate also increases the energy barrier for protein adsorption on the surface. That is to say, there is a larger energy barrier to the replacement of water molecules in contact with the nanostructured Si_3N_4 surface (measured contact angle: 17^o) with proteins as compared to a mildly hydrophilic surface such as flat Si_3N_4 (measured contact angle: 38^o). However, it is important to keep in mind that the degree of resistance to protein adsorption also depends on factors such as the structure, sequence, and nature of resultant charges on the protein molecules.

Previously, hydrophilic surfaces, which effectively bind water molecules and prevent protein adsorption, have been utilized for improved biocompatibility

such as immobilized PEG-based films [54, 55] and self-assembled monolayers (SAMs) [56, 57]. However, the protein resistance of these surfaces decay over time due to factors such as auto-oxidation resulting in the formation of more nonpolar and less hydrophilic functional groups such as aldehydes and ethers [58]. Additionally, these surfaces are susceptible to physical defects and therefore are not suitable for long-term usage [33, 59]. The noticeable hydrophilicity of the nanostructured Si_3N_4 surface results from the physical topology of the surface and is expected to show much better long-term reliability than chemical coatings.

To isolate the contribution from the improved hydrophilicity to the deterrence of protein adhesion, we plasma-treated flat Si_3N_4 surfaces (Figure 4.18a) and compared them with non-treated flat Si_3N_4 surfaces. Decrease in protein adsorption as a function of increasing surface wettability becomes evident when comparing the results obtained for plasma treated and non-plasma treated substrates, as shown in Figure 4.18b. After 2 hours of incubation, the extent of protein adhesion on the plasma-treated Si_3N_4 and nanostructured Si_3N_4 surfaces are almost the same. This could be attributed to the dominance of the antifouling contribution from the hydrophilicity as the length-scale of the nanotopology of the nanostructured Si_3N_4 surface is over an order of magnitude greater than the size of proteins, implying that the nanoscale geometry effect is possibly negligible. However, after 24 hours, the nanostructured Si_3N_4 surface displays the lowest contact angle and the greatest resistance to protein adsorption while the non-permanent plasma-treated surface loses its hydrophilicity and its contact angle returns to a value close to that of a non-treated flat Si_3N_4 surface (Figure 4.18a).

When considering the case of cellular adhesion to surfaces, we can consider the following reaction:

$$CL + SL \leftrightarrow CS \tag{4.5}$$

where cells in an aqueous media or liquid (CL) are interacting with a surface submerged in liquid (SL) and leading to adsorption of cellular molecules on the surface represented as CS. The free energy change can be expressed as

$$\Delta G_{CS} = \gamma_{CS} - (\gamma_{CL} + \gamma_{SL})\,. \tag{4.6}$$

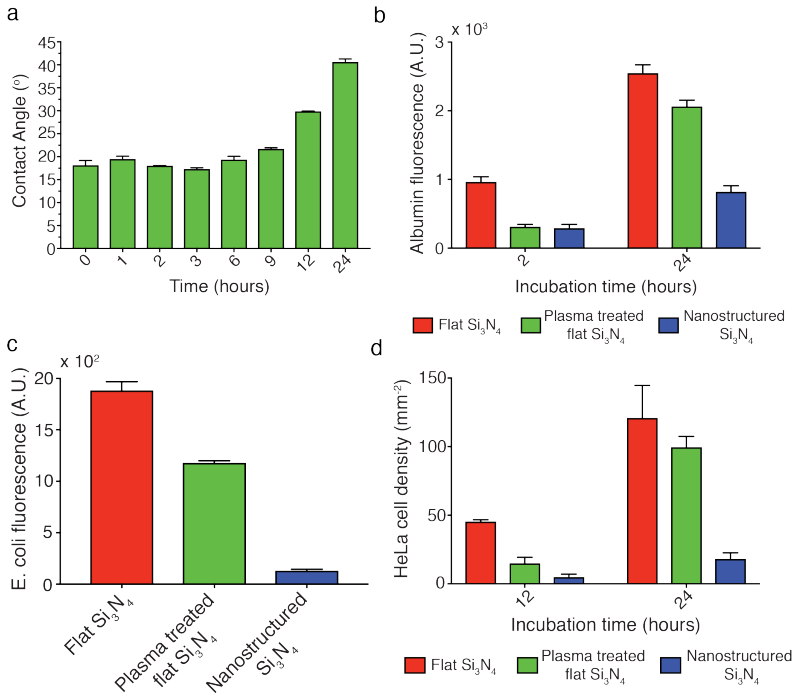

Figure 4.18: Hydrophilicity-mediated protein anti-adhesion. (a) Contact angle vs. time elapsed after plasma treatment: flat Si_3N_4 surfaces were plasma-oxidized in order to lower their contact angles to values comparable to the nanostructured Si_3N_4 surface (n = 2 measurements). Plasma oxidation produced non-permanent enhanced hydrophilicity that dissipates in 24 hours. (b) Bovine serum albumin (BSA) adhesion measured as a function of fluorescence intensity on untreated flat, plasma treated flat Si_3N_4 and nanostructured Si_3N_4 surfaces: in case of protein anti-adhesion, hydrophilicity plays a greater role than the nanotopology of the nanostructures (n = 12 representative images). (c) *E. coli* adhesion measured as a function of fluorescence intensity after 4 hours of incubation (n = 3 representative images). (d) HeLa cell density measured after 12 hours and 24 hours (n = 5 representative images). For cells, nanotopology plays a greater role as indicated by greater adhesion resistance offered by the nanostructured Si_3N_4 surface over the plasma treated Si_3N_4 surface of a similar contact angle.

The effect of surface wettability on the free energies in this case is also very similar to that of proteins. Improved hydrophilicity of the surface implies that γ_{SL} will be lower, which increases the barrier for displacement of water molecules on the surface by cells and is favorable for improving biocompatibility. The degree of improvement will once again be dependent on the other two terms (γ_{CS} and γ_{CL}), which are dependent on the nature of charges on the cells and their apparent hydrophilicity or hydrophobicity (discussed in further

detail by Liu *et al.*) [51]. Indeed, it has been shown that increase in surface hydrophobicity (contact angle change from 15° to 100°) correlated directly with increase in surface adsorption of bacteria, algal spores, and eukaryotic cells [31, 32, 60, 61]. Our results (Figure 4.18c,d) show that there is a significant decrease in cellular adhesion upon increasing the hydrophilicity of flat Si_3N_4 surfaces through plasma oxidation, which agrees with the surface wettability model.

The second important contribution towards improved biocompatibility for the nanostructured Si_3N_4 surface originates from the nanostructured surface topology. Being in the same length-scale or more typically an order of magnitude smaller than cells, nanotopology plays a greater role in biofouling resistance against bacteria and mammalian cells (Figures 4.18c, d). Various reports have claimed that structured surfaces reduce biofouling as compared to flat substrates [49, 60, 61]. Two primary cases can be considered when cells are interacting with patterned substrates. The first case is when cells can elongate to increase their interaction with the surface and fill the gaps between nanostructures [62]. This cellular elongation directly leads to an increase in surface tension along the cell membrane and has been modeled by Pogodin *et al.* assuming a planar piece of membrane [29]. The increase in interfacial surface energy is described by [29]

$$\Delta\gamma_{CS} = \frac{\varepsilon\eta_0 d\sigma}{1+\alpha r} \tag{4.7}$$

where η_0 represents the surface density of adsorption sites on the membrane; ε represents energy gained per unit of adsorption site; αr represents the local degree of cell membrane stretching at point r; and $d\sigma$ is the elemental surface area. The integration is performed over the total contact area between the cell membrane and the nanostructured surface. For high-aspect-ratio structures such as the nanopillars (diameter 160 nm, height 200 nm) described by Pogodin *et al.*, stretching of the membrane can eventually lead to rupture and cell lysis. For low-aspect-ratio nanostructures with an average diameter of 345 nm and height of 150 nm, our experimental results have not shown any signs of cell lysis (Figures 4.16d and 4.17c-e), indicating that while membrane elongation is likely increasing γ_{CS} in equation 4.6 and improving biocompatibility of the substrate, cell membranes are not rupturing.

The second possible case occurs when the cell membrane does not elongate to fill the gaps in the nanopatterned substrate. It has been shown that this situation leads to a reduction in adhesion points between the substrate and cells [63], leading to poor adhesion of cells on patterned surfaces as compared to a flat surface and consequently easier detachment. Therefore, nanotopology-driven outcomes such as membrane deformation or reduction in adhesion points contribute towards destabilizing the interaction between the cell membrane and substrate, improving resistance to cellular adsorption. Our results demonstrate that nanostructured Si_3N_4 surface shows a drastic decrease in both prokaryotic and mammalian cellular adhesion as compared to a flat substrate (with or without plasma treatment) due to the increased contribution from the nanotopology (Figures 4.18c, d). This is evident from the fact that greater cell adhesion resistance is offered by the nanostructured Si_3N_4 surface over the plasma-treated Si_3N_4 surface of a similar contact angle.

To summarize, based on evidences found in literatures and results obtained from our experiments, we have analyzed the underlying mechanism that produced the much improved biocompatibility of the nanostructured substrate: it is the combination of (a) much-improved, nanopattern-based, hydrophilicity that increases the energy barrier for protein and cellular adhesion on the substrate; and (b) nanostructured surface topology, which reduces the energy barrier for detachment of cells from the surface and destabilizes cellular adhesion to the substrate.

4.4 Use of nanostructures in intraocular pressure sensing

To demonstrate a medical application for multifunctional nanostructures, we used the nanostructured Si_3N_4-membrane as an opto-mechanical sensing element in a microscale implantable IOP sensor (previously described in Chapter 2), which is a hermetically sealed, pressure-sensitive, Fabry–Pérot resonator. A flat-surfaced or nanostructured flexible Si_3N_4-membrane forms the top surface of the Fabry–Pérot resonator and a mirror-like rigid Si forms the bottom surface. The sensor is optimized in the NIR range for minimum absorption in tissue and water. If the ambient pressure or IOP changes, the membrane will deflect accordingly, and the resulting shift in the resonance wavelength will be captured remotely in reflection (Figures 2.3, 2.6 and 4.19a).

Optical characterization of the bioinspired nanostructured IOP sensor

To study the dependence on readout angle, we compared the measurements from a nanostructured and a flat-surfaced IOP sensor at 1 atm (Figures 4.19b-d). The flat-surfaced sensor produced a maximum resonance shift of 16 nm at an incident angle of 12^o (Figure 4.19b). By contrast, the nanostructured sensor produced shifts of 2 nm at 12^o and 5 nm at 30^o. Decay in the intensity of reflected resonance was also measured as a function of the incident angle (Figure 4.19c). For the flat-surfaced sensor, the intensity decayed to zero when the incident angle reached 12^o while the signal from the nanostructured sensor remained detectable until 30^o. The IOP measurement error of the flat-surfaced sensor reached 4.59 mmHg at 12^o (Figure 4.19d), which is approximately 46% of the physiological IOP range observed in humans (10–20 mmHg) and exceeds the $\pm$1.2 mmHg error range of existing clinical tonometers (http://www. icaretonometer.com/, http://www.reichert.com/). On the other hand, the IOP-measurement error of the nanostructured sensor was 0.07 and 0.92 mmHg at 12^o and 28^o, respectively. These results highlight the wide-angle performance of the nanostructured sensor. The nanostructured sensor showed excellent linearity (correlation factor: $\sim$1.00) over the clinical range of interest from 0 to 32 mmHg when tested in a pressure-controlled chamber interfaced with a digital pressure gauge (Figure 4.19e). The maximum readout error was 0.26 mmHg, approximately four times lower than that of the flat surfaced sensor (1 mmHg).

In vivo performance of the bioinspired nanostructured IOP sensor

A nanostructured and a flat-surfaced sensor were implanted individually inside the anterior chambers of two New Zealand white rabbits to investigate *in vivo* optical performance and biocompatibility (Figure 4.20a). To examine the stability of sensor measurements, the shift $\Delta\lambda$ of the most prominent peak in each spectrum of the set was computed with respect to the mean of the set (Figure 4.20b). The s.d. of $\Delta\lambda$ of the nanostructured sensor was 0.6 nm as opposed to 1.3 nm observed for the flat-surfaced sensor (Figure 4.20c). Additionally, the s.d. of IOP measurements produced using the nanostructured sensor was 0.23 mmHg as opposed to 0.64 and 1.97 mmHg calculated from measurements concurrently obtained using the flat-surfaced sensor and tonometry, respectively (Figure 4.20d). The angle independence enhanced

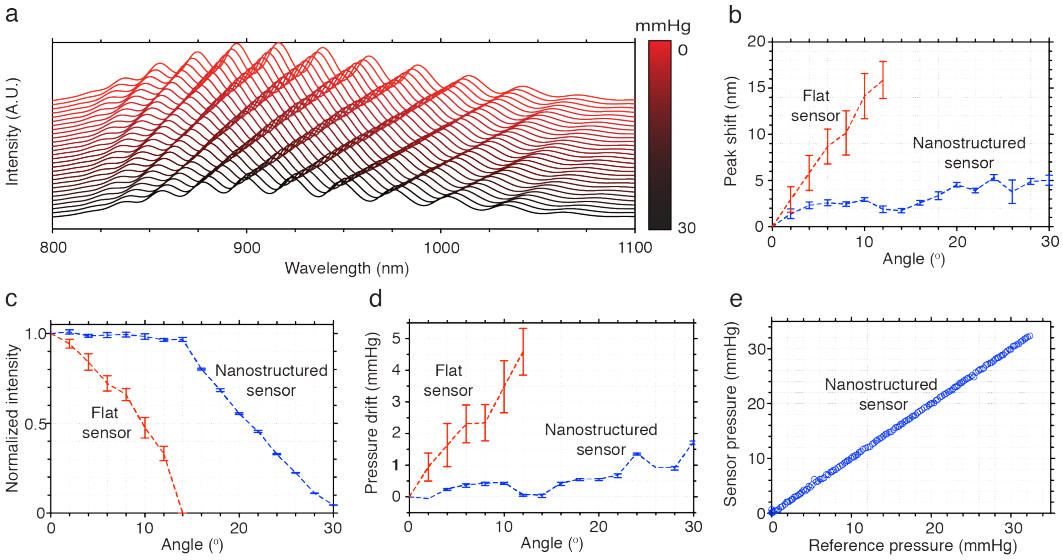

Figure 4.19: Bioinspired nanostructured IOP sensor benchtop characterization. (a) Resonance shifts of the sensor Fabry–Pérot cavity measured in reflection as a function of the IOP. (b) Peak shift in the reflected resonance spectra as a function of incident angles (n = 3 measurements). Considerably smaller magnitudes of peak shifts are observed in the nanostructured sensor, indicating its angle-independent property. (c) Intensity, taken as a measure of peak-to-valley contrast of the most prominent peak and valley of the resonance profile and normalized with respect to the measurement taken at a 0^{o} angle of incidence. The nanostructured sensor displays negligible loss of intensity up to 14^{o} (n = 3 measurements). (d) Pressure drift error induced by increasing the angle of incidence. The nanostructured sensor displays negligible pressure drifts even at large angles of incidence (n = 3 measurements). (e) Nanostructured sensor tested from 0–32 mmHg in a pressure-controlled chamber interfaced with a digital pressure gauge used as a reference. Error bars show the s.d. about the mean.

by the nanostructure integration improved the stability and accuracy of the optical measurements against potential error sources such as respiratory movements, subtle eye motions, and detector misalignment. Furthermore, indirect IOP measurement techniques, such as tonometry, are influenced by various factors such as corneal thickness, curvature and biomechanics and are in general more error-prone compared with direct IOP measurement techniques such as implantable sensors [15, 64].

Both sensors were retrieved after one month of implantation to quantify cell growth on the surface and to assess biocompatibility. We used confocal fluorescence microscopy to determine the extent of tissue growth and cellular viability

at the time of retrieval. DAPI was used to localize all constituent cells while phalloidin, which selectively binds to actin, was used as an indicator of cellular processes and health [65]. Additionally, matrix metalloproteinases-2 (MMP-2) was used as an indicator of inflammation for its role in various inflammatory and repair processes [66].

Figures 4.20e, f show top views of the z-stacked multi-channel immunofluorescence images of the flat-surfaced and the nanostructured sensors, respectively. Approximately 59% of the flat-surfaced sensor was covered by tissue, and the presence of a vast filamentous F-actin network (Figure 4.20e, in green) indicates healthy tissue growth at the time of extraction. Additionally, MMP-2 (Figure 4.20e, in red) was observed over the membrane of the flat-surfaced sensor, which could have triggered the extensive cell migration towards this region. In comparison, approximately 5% of the nanostructured surface was covered by tissue, which was a 12-fold improvement over the flat-surfaced sensor, and there was no detectable MMP-2 signal, suggesting the cell signalling and migration patterns present on the flat-surfaced sensor were absent on the nanostructured sensor. This indicates no inflammation occurred post-implantation and highlights the promising role of the nanostructures towards significantly improving *in vivo* biocompatibility of medical implants.

4.5 Conclusion

Inspired by the short-range-ordered nanostructures found on the wings of the transparent longtail glasswing butterfly (*C. faunus*), we engineered biophotonic nanostructures optimized for use in medical implants. By tuning key physical dimensions of the nanostructures, we engineered structurally induced scattering that expands optical readout angle and improves antifouling with suppressed inflammation suitable for IOP-sensing implants. In glaucoma, accurate IOP monitoring is the only mainstay of disease diagnosis and management [64], and optical sensing approaches for IOP monitoring have been promising in terms of miniaturization, energy efficiency, and frequency of monitoring [15]; however, they also require improvement in readout angle and biocompatibility for practical use. Integration of the nanostructures on an IOP-sensing implant significantly expanded its detection range while reducing threefold the mean *in vivo* IOP error. Further, the nanostructures effectively suppressed biofouling and inflammation 12-fold, resulting in a highly practical implant for long-term IOP monitoring. Further development of our bio-

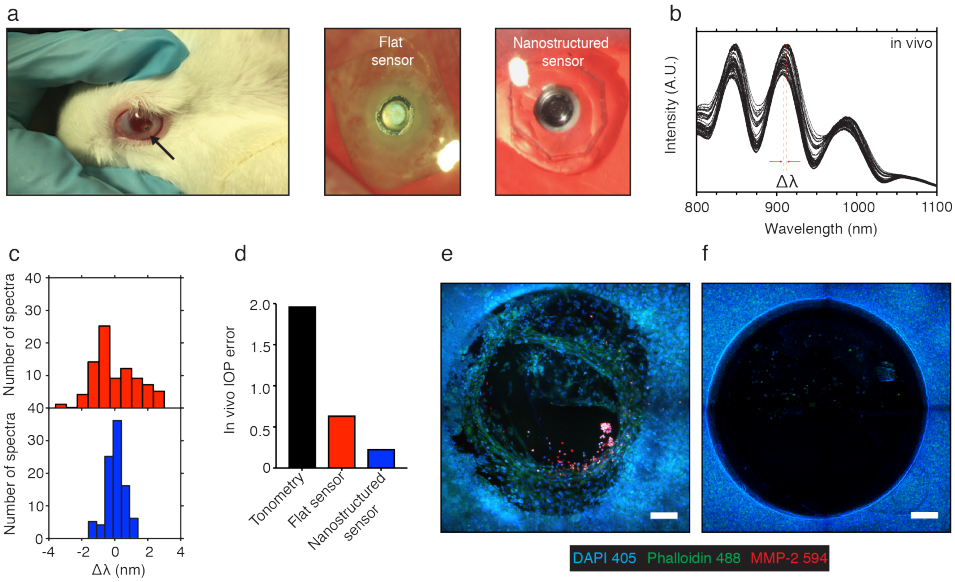

Figure 4.20: Bioinspired nanostructured IOP sensor *in vivo* studies. (a) A flat-surfaced and a nanostructured sensor were each implanted in the anterior chamber (indicated by the black arrow) of two living New Zealand white rabbits for a period of one month. The flat-surfaced sensor appears hazy compared with the nanostructured sensor due to dense tissue growth on the sensor surface indicating significant biofouling after one month of implantation. (b) Spectra with the highest signal-to-noise ratio collected from continual IOP measurements taken over 60-s intervals with an integration time of 10 ms per spectrum. The variation in the position of the resonance spectra that occurred during a single set of measurements is indicated as $\Delta\lambda$ (n = 95 spectra). (c) Histograms showing the numbers of spectra at specific $\Delta\lambda$ relative to the mean wavelength for the flat (s.d. = 1.3 nm) and nanostructured (s.d. = 0.6 nm) sensors, respectively (n = 95 spectra). (d) Standard deviation of *in vivo* IOP measurements made using the flat (s.d. = 0.64 mmHg, n = 95 spectra) and nanostructured (s.d. = 0.23 mmHg, n = 95 spectra) sensors compared with a traditional rebound tonometry reading (s.d. = 1.97 mmHg, n = 12 measurements). (e) Three-channel immunofluorescence confocal microscopy image (z-stack) of the flat Si_3N_4 sensor after one month of *in vivo* study. Several signs of inflammation (shown in red) over the flat Si_3N_4-membrane of the sensor have elicited a foreign body reaction by means of a vast cellular migration process. Healthy tissue growth with a vast F-actin network is observed over the flat Si_3N_4-membrane. (DAPI: cell nucleus marker, blue; phalloidin: cell F-actin marker, green; and MMP-2: matrix metalloproteinases marker, red.) (f) Immunofluorescence image of a nanostructured sensor after one month *in vivo* study. Considerably reduced tissue adhesion over the nanostructured Si_3N_4-membrane (the circular region) indicating the contribution of nanostructures to *in vivo* antifouling through anti-adhesion. Scale bars: 100 μm.

inspired work, including continuous IOP monitoring using mobile devices with integration of features such as memory-based tracking, will improve glaucoma treatment outcomes and lower the risk of visual impairment and blindness. With these promising results, we envisage that numerous medical technologies and devices will benefit greatly from the multifunctionality of biophotonic nanostructures.

4.6 Materials and methods

High-resolution imaging

Dried wings of *C. faunus* were coated with a 15 nm gold layer (Lesker Labline E-beam Evaporator, Kurt J. Lesker Company, USA) before examination by scanning electron microscopy (SEM) (FEI Nova 200 NanoLab Dualbeam, USA) operated at 5 kV.

Topographical analysis

ImageJ (https://imagej.nih.gov/ij/), a public domain and Java-based image processing program tool, was used to perform the statistical analysis of the nanostructure size on the wing membrane and fabricated the nanostructured Si_3N_4 samples. The images were turned into binary black and white images under a specific threshold value. Subsequently, the diameters and areas of the nanostructures were computed. The 2-D Fourier power spectra were obtained from SEM images and calculated with a fast Fourier transform algorithm in MATLAB.

Optical simulations

The thin film simulations of flat Si_3N_4-membrane and the postdiscal area were calculated analytically using MATLAB [6]. The developed multilayer thin-film calculator is based on matching the boundary conditions for Maxwell's equations. Calculations were first done for individual polarizations and by taking the average afterwards to consider the unpolarized light ($TE + TM2$) condition.

The optical properties of the basal area nanostructures were numerically simulated with the 2D finite-difference time-domain software (Lumerical Solutions Inc., Canada). The transmittance of the nanostructured membrane were numerically simulated with the 3D finite element method (FEM) (COMSOL Multiphysics, USA). In order to simulate exact optical properties of the fabri-

cated nanostructured samples, the measured 3D patterning profile was directly imported by SEM in the simulated model. Periodic boundary conditions in the lateral directions (x and y) were applied for the calculations. An incoming plane wave impinging the structures under normal and oblique incidence was used and all calculations were performed with a spatial resolution of 5 nm. In the simulation process, the boundary conditions of the electromagnetic fields in the vertical (z) direction were set on the perfect matching layer (PML) for the model. The total transmittance was calculated for individual geometries for unpolarized light ($TE + TM2$) at normal and oblique incident angles by integrating the near-zone scattered power (Poynting vector) over a surface before the bottom PML and afterward normalizing with incident intensity.

Optical spectroscopic analysis

Specular transmission and scattering spectra of the *C. faunus* wings were measured using a custom-built optical goniometric setup. A stabilized Tungsten-Halogen light source (SLS201, ThorLabs, USA) was collimated to form a 500 μm wide parallel incident beam that illuminates the sample at a fixed angle. The specular transmission and forward scattered light was detected at fixed and different angles, respectively, with an angular resolution of 2^{o} and coupled into an optical fiber connected to the spectrometer (Flame, Ocean Optics, USA). All measurements were recorded with an unpolarized light.

The diffuse transmittance measurements were performed using a custom-built motorized integrating-sphere apparatus with a monochromator coupled tunable (λ = 450-900 nm) supercontinuum laser (Fianium) and a Si photodetector. All measurements were recorded with unpolarized light. The samples were placed in the middle of the integrating sphere using a vise-type center-mount and the sample holder was rotated around the vertical axis for angle-resolved measurements. Transmission measurements were normalized to that of the uncovered area of the underlying glass slide.

Phase-separation through polymer blends and nanostructure texturing

Poly (methyl methacrylate) (PMMA, M_w = 9.59 kg/mol, Polymer Standards Service GmbH, Germany) and polystyrene (PS, M_w = 19.1 kg/mol, Polymer Standards Service GmbH, Germany) were dissolved in methyl ethyl ketone (MEK, Sigma-Aldrich Co. LLC, USA) with a mass ratio of 65% and 35%.

The concentration of the solutions was kept fixed to 25 mg/ml. Solutions were spin-coated on the substrates with a speed of 3500 rpm and acceleration of 2000 rpm/s for 30 seconds. Relative humidity was maintained between 40% and 50% during the spin-coating. The de-mixing of the blend components out of the smooth surface occurred during spin-coating itself due to the difference in relative solubilities of PS and PMMA in MEK [21]. When the sample begins to spin, water condensation begins at humidity levels above 35%. A layer of water-rich solution is formed at the air solution interface due to the difference in evaporation rate between water and MEK. Water starts to condense from the air into the solution because of the evaporation of MEK, which decreases the temperature on top below the dew point. Because of the high water concentration, a 3-dimensional phase separation occurs between PS/MEK and PMMA/MEK/water. The PS molecules start to precipitate before they reach the middle of the solvent. With the further evaporation of MEK, the PS/MEK, and PMMA/MEK/water phases reach the same height and when the film is completely dried, a purely lateral morphology is formed and the PS islands end with an ellipsoidal shape. The samples were then rinsed in cyclohexane for 2 minutes and dried in a stream of N_2 to remove the PS islands. Using the PMMA layer as a template, a 30 nm Al_2O_3 hard masking layer was deposited via e-beam evaporation (CHA Industries Mark 40). After lift-off, the Si_3N_4 was textured through RIE (Oxford PlasmaLab 100 ICP380) resulting in the nanostructured surface.

Nanostructured membrane and sensor fabrication

The fabrication process flow of the nanostructured membrane and IOP sensor is provided in Figure 4.21. The sensor consists of two parts (top and bottom) that were individually batch-fabricated and bonded together using a medical grade epoxy to produce a hermetically sealed miniaturized Fabry-Perot (FP) cavity. (T1) The top substrate fabrication begins with 2 μm-thick silicon dioxide (SiO_2) and 400 nm thick silicon nitride (Si_3N_4) layers deposited on the top and bottom surfaces of a double-side polished (DSP) Si wafer (thickness: 300 μm) using thermal oxidation and low pressure chemical vapor deposition (LPCVD), respectively. (T2) The Si_3N_4 and SiO_2 layers on the top surface of the wafer were completely removed using reactive ion etching (RIE) (Plasmalab System 100 RIE/ICP, Oxford Instruments, Inc.) and buffered oxide etch (BOE). Next, a 300 nm-thick aluminum oxide (Al_2O_3) layer was de-

posited using an e-beam evaporator (FC-1800 E-Beam Evaporator, Temescal) and patterned the surface using photolithography and BOE. (T3) Using the patterned Al_2O_3 layer as a hard mask, the wafer was etched using a Bosch process (Plasmalab System 100 RIE/ICP, Oxford Instruments, Inc.) down to the SiO_2 etch stop at the bottom surface of the wafer. (T4) The SiO_2 layer was removed through BOE to create freestanding Si_3N_4-membranes. The phase-separation process described in the previous section was used to structure the Si_3N_4-membrane. (T5) Individual nanostructured membranes were released from the substrate through photolithography and RIE from the backside. (B1) The bottom substrate fabrication begins with a double-side-polished Si wafer (thickness: 300 μm). (B2) Using a photoresist mask, a precisely controlled 4 μm recess was created through RIE to generate the FP cavity gap. (B3) Next, a 300 nm-thick aluminum oxide (Al_2O_3) layer was deposited using an e-beam evaporator, and then patterned. (B4) Using a single Bosch process, concentric shallow trenches and a deep trench were etched. The shallow trenches were created to serve as reservoirs during the epoxy bonding process to prevent any of the adhesive from overflowing into the FP cavity. The deep trenches were created for the easy separation of bottom chips (bottom parts of the sensors) from the wafer. (B5) The Al_2O_3 masking layer was removed in BOE. Finally, a medical grade epoxy was applied along the sides of the top nanostructured membrane chip and the bottom chip to create a hermetically sealed FP sensor implant.

Nanostructured sensor characterization

The sensors were placed on a tilt stage, which allows for variation of the incident angle, and were probed by a 20x objective lens interfaced with an NIR light source (HL-2000, Ocean Optics), a mini-spectrometer (Maya200 Pro), Ocean Optics), and a CCD camera (Thorlabs, Inc). For linearity measurements, the sensors were placed in a custom-build pressure-controlled chamber. The hydrostatic pressure was between 0 to 30 mmHg and increased at steps of 0.2 mmHg. The output from the sensors were referenced against a digital pressure gauge (1210 Pressure Sensor, TE Connectivity Ltd.) with an accuracy of $\pm 0.5\%$. An in-house IOP detection algorithm on MATLAB was used to rapidly calculate the IOP based on the peak locations of the captured reflection spectra.

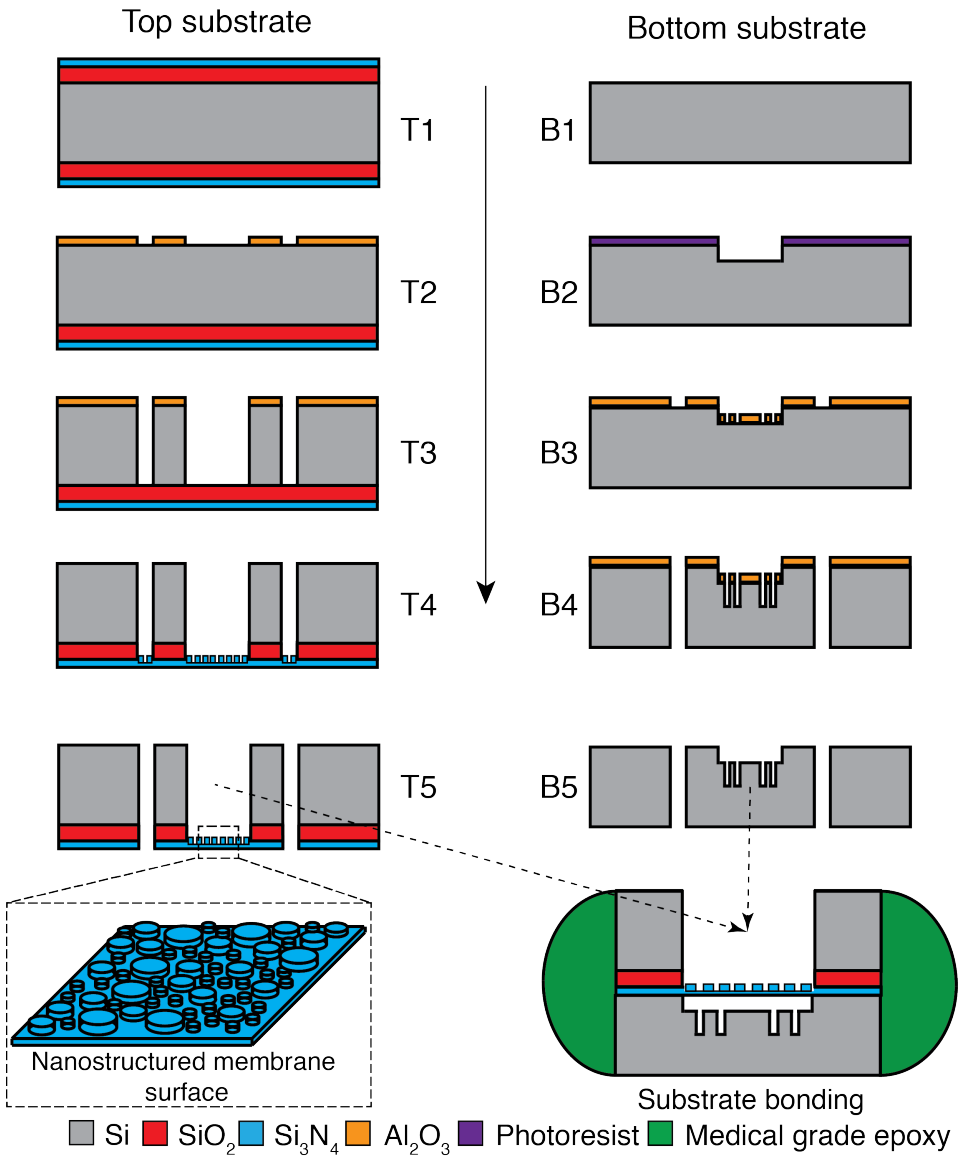

Figure 4.21: Fabrication process flow of the nanostructured IOP sensor. The top and bottom substrates are separately fabricated and later assembled together.

Protein adhesion assay

Fluorescently labeled bovine serum albumin (BSA) (A13100, Thermo Fisher Scientific Inc., Waltham, MA, USA) protein with molecular weight of 66 kDa and streptavidin (S21375, Thermo Fisher Scientific Inc., Waltham, MA, USA) were used for the protein adsorption studies of the control, flat Si_3N_4, and nanostructured Si_3N_4 samples with different aspect-ratio. The BSA and streptavidin were dissolved separately in phosphate buffered saline (PBS, 10 mM, pH 7.4) to a concentration of 2 mM. The substrates were rinsed with PBS to

rehydrate the surfaces. All the sample substrates were then immersed in both protein solutions separately and were incubated at 4°C for 24 h. The samples were then removed from the protein solutions, gently washed three times with PBS, and rinsed once with deionized water to remove the PBS salt. Surface protein adsorption was imaged using a Hamamatsu ORCA-Flash4.0 V2 Digital CMOS camera on a Nikon Eclipse 80i fluorescence microscope with a 10x objective. ImageJ (https://imagej.nih.gov/ij/) was used to quantify the protein adsorption data on 12 different imaging areas from each sample. All images were converted into binary images with a fixed threshold to enable sample comparison.

Prokaryote adhesion assay

A culture of chemically competent *E. coli* was transformed with the green fluorescent protein (GFP) expressing and ampicillin-resistant plasmid pFluoroGreen^{TM} (Edvotek) followed by plating on selective agar for overnight (O/N) incubation at 37°C. The bacteria were then inoculated in fresh lysogeny broth (LB) with 100 μg/mL ampicillin and isopropyl-β-D-thiogalactopyranoside (IPTG) and incubated O/N at 37°C under gentle shaking (250 rpm). Upon recovery, the bacteria were diluted in fresh LB to an OD600 – 0.25. Two sets of autoclaved substrates consisting of a positive control, a flat Si_3N_4, and a nanostructured Si_3N_4 were incubated with 2 mL of the bacterial culture. The sets were used for fluorescence imaging and colony-forming unit (CFU) counts. After 4-hour incubation under gentle shaking (100 rpm), the substrates were washed with 1x PBS and placed in a sonication bath for 15 minutes. The substrates for fluorescence intensity measurements were analyzed using a wide-field epifluorescence microscope (10x objective, Leica DMI 600, Leica AG). For CFU counts, a 10^{-5} serial dilution was performed for the control and flat Si_3N_4 while a 10^{-4} serial dilution was performed for the nanostructured Si_3N_4.

Eukaryote adhesion assay

Three sets of autoclaved substrates consisting of a positive control, flat Si_3N_4, and nanostructured Si_3N_4 were incubated in complete Dulbecco's modified Eagle's medium (DMEM) (10% fetal bovine serum (FBS) and 1% 100x penicillin/streptomycin) at 37°C and 5% CO_2 for 30 minutes. The medium was then aspirated followed by re-addition of fresh complete DMEM. HeLa cells at a fixed concentration of 250,000 mL^{-1} were seeded on each substrate and

measurements were collected at 24-hour time point measurements, three in total. At each 24-hour time point, one set of substrates were incubated in a staining reagent consisting of fresh complete FluoroBrite DMEM (10% FBS, 1% 100x penicillin/streptomycin, 1:1000 Hoechst 33342, and 1:1000 SYTOX green) at 37°C and 5% CO_2 for 15 minutes. Hoechst 33342 (excitation/emission 350/461 nm) and SYTOX Green (excitation/emission 554/567 nm) probes were used to stain the nuclei of adherent HeLa cells on the surfaces under test for live imaging. Hoechst 33342 is nonspecific of either dead or live cells and provides an estimate of total adherent cell density, whereas SYTOX Green is impermeant into live cells and functions as an indicator of cell death. The co-localization of the two nucleic acid markers was used to ascertain viability ratios (dead/live) for each surface. For the total adherent cell density measurement, 10 representative fields-of-view were obtained through wide-field epifluorescence microscopy (10x objective, 2 mm diameter of field area, Leica AG) by scanning a fixed 2 cm x 2 cm substrate of each surface. Using a fixed field area and the representative images, an average adherent cell density (count/mm^2) was obtained for each surface. An estimate of viability was computed as an average ratio of number of dead cells and live cells per field-of-view taken over 10 representative fields-of-view. The co-localization of the two labels yielded the number of dead cells per representative field-of-view. The number of live cells was obtained by subtracting the number of dead cells from the total cell count tagged by Hoechst 33342 alone. The ImageJ/FIJI software (NIH) was used to perform all required measurements.

In vivo IOP measurements

The sensors, mounted on silicone haptics, were folded and inserted into the anterior chamber through a 2.8-mm corneal incision. Upon spontaneous unfolding, the haptics were positioned into the iridocorneal angles. A custom-built hand-held detection system was used for the *in vivo* IOP measurements from the nanostructured IOP sensor. The system was interfaced with a high-resolution NIR mini-spectrometer (Maya200 Pro, Ocean Optics) and a portable Tungsten halogen light source (HL-2000, Ocean Optics). To obtain a single IOP measurement, spectra were captured for a 60-seconds period with an integration time of 10 ms per spectrum, resulting in 6000 spectra. Many of these measurements are influenced by naturally induced respiratory and subtle eye motions of the rabbits, which cause the angle of incidence to deviate

from normal and increase readout errors. Hence, 100 representative reflection spectra with the highest signal-to-noise ratio (SNR) were chosen out of 6000 spectra and used to calculate the IOP. An in-house IOP detection algorithm on MATLAB was used to rapidly calculate the IOP based on the peak locations of the captured reflection spectra. Rebound tonometry was performed using a handheld off-the-shelf system (TonoVet, Icare, Finland).

Confocal immunofluorescence microscopy sample preparation

Once harvested, the sensors were rinsed in 1x PBS with 0.02% NaN_3 and incubated in 4% paraformaldehyde (PFA) for 30 minutes at room temperature (RT) followed by O/N incubation at 4°C. Then, the sensors were rinsed in 1x PBS with 0.02% NaN_3 followed by incubation in freshly prepared quenching buffer (1x PBS with 0.02% NaN_3 and 50 mM NH_4Cl) for 15 minutes at RT. Following quenching, the sensors were rinsed again in 1x PBS with 0.02% NaN_3. The sensors were then incubated in blocking buffer (1x PBS with 0.02% NaN_3, 2% BSA and 0.25% TritonTM X-100) O/N at RT with gentle shaking (20 rpm). For staining, the sensors were incubated in 1 mL staining reagent containing blocking buffer with 1:1000 DAPI 405 (cell nucleus marker), 1:500 Phalloidin 488 (cell F-actin marker), and 1:500 MMP-2 594 (matrix metalloproteinases marker)) O/N at RT with gentle shaking (20 rpm) followed by 37°C for 1 hour. Following staining, the sensors were washed in blocking buffer several times followed by incubation O/N at RT with gentle shaking (20 rpm). All confocal imaging was performed with the sensors fully immersed in blocking buffer to retain the morphology of the tissue.

Confocal immunofluorescence microscopy and analyses

Imaging for *in vivo* biocompatibility analysis was performed using a laser scanning confocal microscope (LSM 880 with Airyscan, Carl Zeiss AG). Z-stack images (step size: 2.5 μm, range: 500 μm) were captured using a 25x EPI objective with immersion oil, and controlled by Zeiss ZEN 2.1 software. A 2x2 tiling with 10% overlap section of each sensor field of view was captured and then stitched together using an imaging software (Zeiss ZEN, Carl Zeiss AG). All subsequent image analyses were performed with ImageJ/FIJI software.

References

[1] Nikolai V. Tkachenko. *Optical spectroscopy*. Amsterdam: Elsevier Science, first edition, 2006. ISBN 978-0-444-52126-2. doi: 10.1016/B978-0-444-52126-2.X5024-2.

[2] Elena P. Ivanova, Jafar Hasan, Hayden K. Webb, Gediminas Gervinskas, Saulius Juodkazis, Vi Khanh Truong, Alex H.F. Wu, Robert N. Lamb, Vladimir A. Baulin, Gregory S. Watson, Jolanta A. Watson, David E. Mainwaring, and Russell J. Crawford. Bactericidal activity of black silicon. *Nature Communications*, 4(1):2838–1–2838–7, 2013. doi: 10.1038/ncomms3838.

[3] Sohee Kim, Une Teak Jung, Soo Kyoung Kim, Joon Hee Lee, Hak Soo Choi, Chang Seok Kim, and Myung Yung Jeong. Nanostructured multifunctional surface with antireflective and antimicrobial characteristics. *ACS Applied Materials and Interfaces*, 7(1):326–331, 2015. doi: 10.1021/am506254r.

[4] Yi Fan Huang, Yi Jun Jen, Li Chyong Chen, Kuei Hsien Chen, and Surojit Chattopadhyay. Design for approaching cicada-wing reflectance in low- and high-index biomimetic nanostructures. *ACS Nano*, 9(1):301–311, 2015. doi: 10.1021/nn506401h.

[5] Jafar Hasan, Russell J. Crawford, and Elena P. Ivanova. Antibacterial surfaces: the quest for a new generation of biomaterials. *Trends in Biotechnology*, 31(5):295–304, 2013. doi: 10.1016/j.tibtech.2013.01.017.

[6] Radwanul Hasan Siddique, Guillaume Gomard, and Hendrik Holscher. The role of random nanostructures for the omnidirectional anti-reflection properties of the glasswing butterfly. *Nature Communications*, 6(1):1–8, 2015. doi: 10.1038/ncomms7909.

[7] Ian R. Hooper, Peter Vukusic, and Robin J. Wootton. Detailed optical study of the transparent wing membranes of the dragonfly *Aeshna cyanea*. *Optics Express*, 14(11):4891–4897, 2006. doi: 10.1364/oe.14.004891.

[8] Elena P. Ivanova, Jafar Hasan, Hayden K. Webb, Vi Khanh Truong, Gregory S. Watson, Jolanta A. Watson, Vladimir A. Baulin, Sergey Pogodin, James Y. Wang, Mark J. Tobin, Christian Löbbe, and Russell J. Crawford. Natural bactericidal surfaces: Mechanical rupture of *Pseudomonas aeruginosa* cells by cicada wings. *Small*, 8(16):2489–2494, 2018. doi: 10.1002/smll.201200528.

[9] Heeso Noh, Seng Fatt Liew, Vinodkumar Saranathan, Simon G. J. Mochrie, Richard O. Prum, Eric R. Dufresne, and Hui Cao. How non-iridescent colors are generated by quasi-ordered structures of bird feath-

ers. *Advanced Materials*, 22(26–27):2871–2880, 2010. doi: 10.1002/adma.200903699.

[10] Hemant Kumar Raut, V. Anand Ganesh, A. Sreekumaran Nair, and Seeram Ramakrishna. Anti-reflective coatings: A critical, in-depth review. *Energy and Environmental Science*, 4(10):3779–3804, 2011. doi: 10.1039/C1EE01297E.

[11] Peter Vukusic, John R. Sambles, Christopher R. Lawrence, and Robin J. Wootton. Quantified interference and diffraction in single *Morpho* butterfly scales. *Proceedings of the Royal Society B*, 266(1427):1403–1411, 1999. doi: 10.1098/rspb.1999.0794.

[12] Hendrik Christoffel van de Hulst. Light scattering by small particles. *Physics Today*, 10(12):28–30, 1957. doi: 10.1063/1.3060205.

[13] Tural Khudiyev, Ersin Huseyinoglu, and Mehmet Bayindir. Non-resonant Mie scattering: Emergent optical properties of core-shell polymer nanowires. *Scientific Reports*, 4(4607):1–10, 2014. doi: 10.1038/srep04607.

[14] David D. Nolte. Review of centrifugal microfluidic and bio-optical disks. *Review of Scientific Instruments*, 80(10):101101–1–101101–22, 2009. doi: 10.1063/1.3236681.

[15] Jeong Oen Lee, Haeri Park, Juan Du, Ashwin Balakrishna, Oliver Chen, David Sretavan, and Hyuck Choo. A microscale optical implant for continuous in vivo monitoring of intraocular pressure. *Microsystems and Nanoengineering*, 3(1):17057–1–17057–9, 2017. doi: 10.1038/micronano.2017.57.

[16] Richard O. Prum, Rodolfo H. Torres, Scott Williamson, and Jan Dyck. Coherent light scattering by blue feather barbs. *Nature*, 396(6706):28–29, 1998. doi: 10.1038/23838.

[17] Seng F. Liew, Jason Forster, Heeso Noh, Carl F. Schreck, Vinodkumar Saranathan, X. Lu, Lin Yang, Richard O. Prum, Corey S. O'Hern, Eric R. Dufresne, and Hui Cao. Short-range order and near-field effects on optical scattering and structural coloration. *Optics Express*, 19(9):8208–8217, 2011. doi: 10.1364/OE.19.008208.

[18] Randi S. Papke, Darrell J. Kemp, and Ronald L. Rutowski. Multimodal signalling: Structural ultraviolet reflectance predicts male mating success better than pheromones in the butterfly *Colias eurytheme* L. (Pieridae). *Animal Behaviour*, 73(1):47–54, 2007. doi: 10.1016/j.anbehav.2006.07.004.

[19] Darrell J. Kemp. Female mating biases for bright ultraviolet iridescence in the butterfly eurema hecabe (pieridae). *Behavioral Ecology*, 19(1):1–8, 2008. doi: 10.1093/beheco/arm094.

[20] Natalia Dushkina, Sema Erten, and Akhlesh Lakhtakia. Coloration and structure of the wings of *Chorinea sylphina* bates. *Journal of the Lepidopterists Society*, 71(1):1–11, 2017. doi: 10.18473/lepi.v71i1.a2.

[21] Cheng Huang, Markus Moosmann, Jiehong Jin, Tobias Heiler, Stefan Walheim, and Thomas Schimmel. Polymer blend lithography: A versatile method to fabricate nanopatterned self-assembled monolayers. *Beilstein Journal of Nanotechnology*, 3(1):620–628, 2012. doi: 10.3762/bjnano.3.71.

[22] Gabriela Voskerician, Matthew S. Shive, Rebecca S. Shawgo, Horst von Recum, James M. Anderson, Michael J. Cima, and Robert Langer. Biocompatibility and biofouling of MEMS drug delivery devices. *Biomaterials*, 24(11):1959–1967, 2003. doi: 10.1016/S0142-9612(02)00565-3.

[23] A. Neumann, T. Reske, M. Held, K. Jahnke, C. Ragoss, and H. R. Maier. Comparative investigation of the biocompatibility of various silicon nitride ceramic qualities in vitro. *Journal of Materials Science: Materials in Medicine*, 15(10):1135–1140, 2004. doi: 10.1023/B:JMSM.0000046396.14073.92.

[24] Luting Liu, Batur Ercan, Linlin Sun, Katherine S. Ziemer, and Thomas J. Webster. Understanding the role of polymer surface nanoscale topography on inhibiting bacteria adhesion and growth. *ACS Biomaterials Science and Engineering*, 2(1):122–130, 2016. doi: 10.1021/acsbiomaterials.5b00431.

[25] Mary Nora Dickson, Elena I. Liang, Luis A. Rodriguez, Nicolas Vollereaux, and Albert F. Yee. Nanopatterned polymer surfaces with bactericidal properties. *Biointerphases*, 10(2):021010–1–021010–8, 2015. doi: 10.1116/1.4922157.

[26] Christina Sengstock, Michael Lopian, Yahya Motemani, Anna Borgmann, Chinmay Khare, Pio John S. Buenconsejo, Thomas A. Schildhauer, Alfred Ludwig, and Manfred Koller. Structure-related antibacterial activity of a titanium nanostructured surface fabricated by glancing angle sputter deposition. *Nanotechnology*, 25(19):1–11, 2014. doi: 10.1088/0957-4484/25/19/195101.

[27] Vy T. H. Pham, Vi Khanh Truong, Anna Orlowska, Shahram Ghanaati, Mike Barbeck, Patrick Booms, Alex J. Fulcher, Chris M. Bhadra, Ricardas Buividas, Vladimir Baulin, C. James Kirkpatrick, Pauline Doran, David E. Mainwaring, Saulius Juodkazis, Russell J. Crawford, and Elena P. Ivanova. Race for the surface: Eukaryotic cells can win. *ACS Applied Materials and Interfaces*, 8(34):22025–22031, 2016. doi: 10.1021/acsami.6b06415.

[28] Susan M. Kelleher, Oliver Habimana, Jenny Lawlera, Bronagh O Reilly, Stephen Daniels, Eoin Casey, and Aidan Cowley. Cicada wing surface topography: An investigation into the bactericidal properties of nanostructural features. *ACS Applied Materials and Interfaces*, 8(24):14966–14974, 2016. doi: 10.1021/acsami.5b08309.

[29] Sergey Pogodin, Jafar Hasan, Vladimir A. Baulin, Hayden K. Webb, Vi Khanh Truong, The Hong Phong Nguyen, Veselin Boshkovik, Christopher J. Fluke, Gregory S. Watson, Jolanta A. Watson, Russell J. Crawford, and Elena P. Ivanova. Biophysical model of bacterial cell interactions with nanopatterned cicada wing surfaces. *Biophysical Journal*, 104 (4):835–840, 2013. doi: 10.1016/j.bpj.2012.12.046.

[30] Mikhail F. Limonov and Richard De La Rue. *Optical properties of photonic structures: Interplay of order and disorder*. Boca Raton: CRC Press, first edition, 2012. ISBN 9780429105210. doi: 10.1201/b12175.

[31] Jin Ho Lee, Sang Jin Lee, Gilson Khang, and Hai Bang Lee. The effect of fluid shear stress on endothelial cell adhesiveness to polymer surfaces with wettability gradient. *Journal of Colloid and Interface Science*, 230 (1):84–90, 2000. doi: 10.1006/jcis.2000.7080.

[32] Jin Ho Lee and Hai Bang Lee. A wettability gradient as a tool to study protein adsorption and cell adhesion on polymer surfaces. *Journal of Biomaterials Science, Polymer Edition*, 4(5):467–81, 1993. doi: 10.1163/156856293X00131.

[33] Indrani Banerjee, Ravindra C. Pangule, and Ravi S. Kane. Antifouling coatings: Recent developments in the design of surfaces that prevent fouling by proteins, bacteria, and marine organisms. *Advanced Materials*, 23 (6):690–718, 2011. doi: 10.1002/adma.201001215.

[34] Changsheng Peng, Shaoxian Song, and Tomlinson Fort. Study of hydration layers near a hydrophilic surface in water through AFM imaging. *Surface and Interface Analysis*, 38(5):975–980, 2006. doi: doi.org/10.1002/sia.2368.

[35] Gregory D. Bixler and Bharat Bhushan. Biofouling: Lessons from nature. *Philosophical Transactions of the Royal Society A*, 370(1967):2381–2417, 2012. doi: 10.1098/rsta.2011.0502.

[36] Daniel C Leslie, Anna Waterhouse, Julia B Berthet, Thomas M Valentin, Alexander L Watters, Abhishek Jain, Philseok Kim, Benjamin D Hatton, Arthur Nedder, Kathryn Donovan, Elana H Super, Caitlin Howell, Christopher P Johnson, Thy L Vu, Dana E Bolgen, Sami Rifai, Anne R Hansen, Michael Aizenberg, Michael Super, Joanna Aizenberg, and Donald E Ingber. A bioinspired omniphobic surface coating on medical de-

vices prevents thrombosis and biofouling. *Nature Biotechnology*, 32(11): 1134–1140, 2014. doi: 10.1038/nbt.3020.

[37] Yuehuei H. An and Richard J. Friedman. Concise review of mechanisms of bacterial adhesion to biomaterial surfaces. *Journal of Biomedical Materials Research*, 43(3):1998, 2002. doi: 10.1002/(sici)1097-4636(199823)43:3<338::aid-jbm16>3.0.co;2-b.

[38] Peng Wu, Paul Hogrebe, and David W. Grainger. DNA and protein microarray printing on silicon nitride waveguide surfaces. *Biosensors and Bioelectronics*, 21(7):1252–1263, 2006. doi: 10.1016/j.bios.2005.05.010.

[39] Lise Cremet, Stephane Corvec, Pascale Bemer, Laurent Bret, Cecile Lebrund, Beatrice Lesimple, Anne-Francoise Miegeville, Alain Reynaud, Didier Lepelletier, and Nathalie Caroff. Orthopaedic-implant infections by *Escherichia coli*: Molecular and phenotypic analysis of the causative strains. *Journal of Infection*, 64(2):169–175, 2012. doi: 10.1016/j.jinf.2011.11.010.

[40] Evan M. Hetrick and Mark H. Schoenfisch. Reducing implant-related infections: Active release strategies. *Chemical Society Reviews*, 35(9): 780–789, 2006. doi: 10.1039/b515219b.

[41] Jens Friedrichs, Jonne Helenius, and Daniel J Muller. Quantifying cellular adhesion to extracellular matrix components by single-cell force spectroscopy. *Nature Protocols*, 5(7):1353–1361, 2010. doi: 10.1038/nprot.2010.89.

[42] Hsin-Hou Chang, Po-Kong Chen, Guan-Ling Lin, Chun-Jen Wang, Chih-Hsien Liao, Yu-Cheng Hsiao, Jing-Hua Dong, and Der-Shan Sun. Cell adhesion as a novel approach to determining the cellular binding motif on the severe acute respiratory syndrome coronavirus spike protein. *Journal of Virological Methods*, 201(1):1–6, 2014. doi: 10.1016/j.jviromet.2014.01.022.

[43] Vy T. H. Pham, Vi Khanh Truong, David E. Mainwaring, Yachong Guo, Vladimir A. Baulin, Mohammad Al Kobaisi, Gediminas Gervinskas, Saulius Juodkazis, Wendy R. Zeng, Pauline P. Doran, Russell J. Crawford, and Elena P. Ivanova. Nanotopography as a trigger for the microscale, autogenous and passive lysis of erythrocytes. *Journal of Materials Chemistry B*, 2(19):2819–2826, 2014. doi: 10.1039/C4TB00239C.

[44] Jos Buijs and Vladimir Hlady. Adsorption kinetics, conformation, and mobility of the growth hormone and lysozyme on solid surfaces, studied with TIRF. *Journal of Colloid and Interface Science*, 190(1):171–181, 1997. doi: 10.1006/jcis.1997.4876.

[45] Paul Roach, David Farrar, and Carole C. Perry. Interpretation of protein adsorption: Surface-induced conformational changes. *Journal of the American Chemical Society*, 127(22):8168–8173, 2005. doi: 10.1021/ja042898o.

[46] Christian F. Wertz and Maria M. Santore. Adsorption and relaxation kinetics of albumin and fibrinogen on hydrophobic surfaces: Single-species and competitive behavior. *Langmuir*, 15(26):8884–8894, 1999. doi: 10.1021/la990089q.

[47] Jan Genzer and Kirill Efimenko. Recent developments in superhydrophobic surfaces and their relevance to marine fouling: A review. *Biofouling*, 22(5):339–360, 2006. doi: 10.1080/08927010600980223.

[48] Li-Chong Xu and Christopher A. Siedlecki. Effects of surface wettability and contact time on protein adhesion to biomaterial surfaces. *Biomaterials*, 28(22):3273–3283, 2007. doi: 10.1016/j.biomaterials.2007.03.032.

[49] Michelle L. Carman, Thomas G. Estes, Adam W. Feinberg, James F. Schumacher, Wade Wilkerson, Leslie H. Wilson, Maureen E. Callow, James A. Callow, and Anthony B. Brennan. Engineered antifouling microtopographies–correlating wettability with cell attachment. *Biofouling*, 22(1):11–21, 2006. doi: 10.1080/08927010500484854.

[50] Marco Morra. *Water in biomaterials surface science*. Chichester: John Wiley and Sons, 1 edition, 2001. ISBN 978-0-471-49041-8. URL `https://www.wiley.com/en-us/Water+in+Biomaterials+Surface+Science-p-9780471490418`.

[51] Yu Liu, Shu-Fang Yang, Yong Li, Hui Xu, Lei Qin, and Joo-Hwa Tay. The influence of cell and substratum surface hydrophobicities on microbial attachment. *Journal of Biotechnology*, 110(3):251–256, 2004. doi: 10.1016/j.jbiotec.2004.02.012.

[52] George D Rose, Ari R. Geselowitz, Glenn J. Lesser, Richard H. Lee, and Micheal H. Zehfus. Hydrophobicity of amino acid residues in globular proteins. *Science*, 229(4716):834–838, 1985. doi: 10.1126/science.4023714.

[53] Ken A. Dill. Dominant forces in protein folding. *Biochemistry*, 29(31): 7133–7155, 1990. doi: 10.1021/bi00483a001.

[54] Nan Xia, Collin J. May, Sally L. McArthur, and David G. Castner. Time-of-flight secondary ion mass spectrometry analysis of conformational changes in adsorbed protein films. *Langmuir*, 18(10):4090–4097, 2002. doi: 10.1021/la020022u.

[55] Jane P. Bearinger, Samuel Terrettaz, Rolf Michel, Nicola Tirelli, Horst Vogel, Marcus Textor, and Jeffrey A. Hubbell. Chemisorbed poly(propylene

sulphide)-based copolymers resist biomolecular interactions. *Nature Materials*, 2(4):259–264, 2003. doi: 10.1038/nmat851.

[56] Kevin L. Prime and George M. Whitesides. Self-assembled organic monolayers: model systems for studying adsorption of proteins at surfaces. *Science*, 252(5009):1164–1167, 1991. doi: 10.1126/science.252.5009.1164.

[57] Kevin L. Prime and George M. Whitesides. Adsorption of proteins onto surfaces containing endattached oligo(ethylene oxide): A model system using self-assembled monolayers. *Journal of the American Chemical Society*, 115(23):10714–10721, 1993. doi: 10.1021/ja00076a032.

[58] Angus Hucknall, Srinath Rangarajan, and Ashutosh Chilkoti. In pursuit of zero: Polymer brushes that resist the adsorption of proteins. *Advanced Materials*, 21(23):2441–2446, 2009. doi: 10.1002/adma.200900383.

[59] Hongwei Ma, Jinho Hyun, Phillip Stiller, and Ashutosh Chilkoti. 'non-fouling' oligo(ethylene glycol)-functionalized polymer brushes synthesized by surface-initiated atom transfer radical polymerization. *Advanced Materials*, 16(4):338–341, 2004. doi: 10.1002/adma.200305830.

[60] Maureen E. Callow, J. A. Callow, Linnea K. Ista, Sarah E. Coleman, Aleece C. Nolasco, and Gabriel P. Lopez. Use of self-assembled monolayers of different wettabilities to study surface selection and primary adhesion processes of green algal (*Enteromorpha*) zoospores. *Applied and Environmental Microbiology*, 66(8):3249–3254, 2000. doi: 10.1128/aem.66.8.3249-3254.2000.

[61] Kenneth M. Wiencek and Madilyn Fletcher. Bacterial adhesion to hydroxyl-and methyl-terminated alkanethiol self-assembled monolayers. *Journal of Bacteriology*, 177(8):1959–1966, 1995. doi: 10.1128/jb.177.8.1959-1966.1995.

[62] Theo G. van Kooten and Andreas F. von Recum. Cell adhesion to textured silicone surfaces: The influence of time of adhesion and texture on focal contact and fibronectin fibril formation. *Tissue Engineering*, 5(3):223–240, 2007. doi: 10.1089/ten.1999.5.223.

[63] Marco Arnold, Elisabetta Ada Cavalcanti-Adam, Roman Glass, Jacques Blummel, Wolfgang Eck, Martin Kantlehner, Horst Kessler, and Joachim P. Spatz. Activation of integrin function by nanopatterned adhesive interfaces. *ChemPhysChem*, 5(3):383–388, 2004. doi: 10.1002/cphc.200301014.

[64] Robert N. Weinreb, Tin Aung, and Felipe A. Medeiros. The pathophysiology and treatment of glaucoma: A review. *JAMA*, 311(18):1901–11, 2014. doi: 10.1001/jama.2014.3192.

[65] Roberto Dominguez and Kenneth C. Holmes. Actin structure and function. *Annual Review of Biophysics*, 40(1):169–186, 2011. doi: 10.1146/annurev-biophys-042910-155359.

[66] William C. Parks, Carole L. Wilson, and Yolanda S. Lopez-Boado. Matrix metalloproteinases as modulators of inflammation and innate immunity. *Nature Reviews Immunology*, 4(8):617–29, 2004. doi: 10.1038/nri1418.

Chapter 5

BIOINSPIRED NANOSTRUCTURES FOR PLASMON-ENHANCED FLUORESCENCE

This chapter was adapted from:

V. Narasimhan, R. H. Siddique, M. Hoffmann, S. Kumar and H. Choo (2019). "Enhanced broadband fluorescence detection of nucleic acids using multipolar gap-plasmons on biomimetic Au metasurfaces." In: ***Nanoscale*** 11.29, pp. 13750–13757. DOI: 10.1039/C9NR03178B.

Abstract

Recent studies on metal–insulator–metal-based plasmonic antennas have shown that emitters could couple with higher-order gap-plasmon modes in sub-10-nm gaps to overcome quenching. However, these gaps are often physically inaccessible for functionalization and are not scalably manufacturable. Here, using a simple biomimetic batch-fabrication, a plasmonic metasurface is created consisting of closely-coupled nanodisks and nanoholes in a metal–insulator–metal arrangement. The quadrupolar mode of this system exhibits strong broadband resonance in the visible-near-infrared regime with minimal absorptive losses and effectively suppresses quenching, making it highly suitable for broadband plasmon-enhanced fluorescence. Functionalizing the accessible insulator nanogap, analytes are selectively immobilized onto the plasmonic hotspot enabling highly-localized detection. Sensing the streptavidin-biotin complex, a 91-, 288-, 403-, and 501-fold fluorescence enhancement is observed for Alexa Fluor 555, 647, 750, and 790, respectively. Finally, the detection of single-stranded DNA (*gag*, *CD4* and *CCR5*) analogues of genes studied in the pathogenesis of HIV-1 between 10 pM–10 μM concentrations and then *CD4* mRNA in the lysate of transiently-transfected cells with a 5.4-fold increase in fluorescence intensity relative to an untransfected control is demonstrated. This outcome promises the use of biomimetic Au metasurfaces as platforms for robust detection of low-abundance nucleic acids.

5.1 Introduction

Optical field-enhancing plasmonic environments that influence the decay lifetimes of quantum emitters were first proposed theoretically by Purcell [1] and demonstrated experimentally in various efforts [2, 3]. Through sub-wavelength light confinement, plasmonic nanostructures greatly increase the intensity of localized electromagnetic fields, thereby enhancing excitation characteristics of emitters proximal to them [4]. However, emitters within 10 nm from the nanostructures couple to non-radiative, dark higher-order plasmonic modes, and the energy is dissipated through non-radiative channels that lead to rapid quenching of the far-field emission [5, 6]. Recent research of plasmonic nanogaps has revealed that emitters can effectively couple with hybridized higher-order gap-plasmon modes to overcome quenching effects [7–9] Modes that are otherwise dark in isolated nanostructures such as nanoparticles become highly radiative in plasmonic nanogaps [9] Furthermore, increased electric field lifetimes and reduced radiative losses supported by higher-order plasmonic modes can greatly benefit applications such as plasmon-enhanced fluorescence [10]. However, while recent literature has demonstrated nano-architectures capable of overcoming quenching, their use in applications such as multiplexed biosensing remains largely unexplored. This could be attributed to diminutive surface areas of the hotspots or physical inaccessibility of nanogaps for functionalization as well as challenges involved in reliably reproducing nanoscale gaps, especially in large scale, batch fabrication [11].

In this work, using a simple three-step biomimetic fabrication process, we have created a highly scalable plasmonic metasurface (MS) consisting of a short-range ordered array of closely coupled gold (Au) nanodisks on nanoholes separated by a 5 nm silica (SiO_2) nanogap with a large accessible hotspot surface area for biosensing. This metal-insulator-metal metasurface (MIM-MS) configuration whose geometry can be tuned by adjusting process parameters was found to efficiently scatter from the visible to the near-infrared (VIS-NIR) range. Furthermore, the SiO_2 nanogap can be selectively functionalized to bind molecules of interest presenting an advantage over conventional Au nanostructures [12]. Our in-depth study of an individual MIM scatterer reveals that the higher-order quadrupolar mode ($l = 2$) of this architecture is radiant, and emitters can effectively couple into this mode, resulting in enhanced quantum emissions. Furthermore, we have experimentally verified the suppression of quenching and broadband fluorescence enhancement of the $l = 2$ mode res-

onance in the VIS-NIR regime for quantum emitters within 10 nm from the nanogap, and consequently, the broad resonance profile of the $l = 2$ mode resonance can support plasmon-enhanced fluorescence when compared to isolated nanostructures favoring multiplexed biosensing using different fluorophores on the same platform.

In our experiments, we have utilized oligonucleotide-based biosensing that is now of great interest [13, 14] These single-stranded DNA (ssDNA) or RNA are often less than 5 nm in size when folded, and they can be placed within the regime of strong quenching [15]. By suppressing quenching, we demonstrate robust biosensing of nucleic acid sequences of various sizes at concentrations comparable to the resolution of commercial RNA quantitation assays [16]. Through fluorescent hybridization, ssDNA analogues of the human immunodeficiency virus type 1 (HIV-1) receptor genes *CD4* and *CCR5*, as well as the HIV-1 gene *gag*, were detected. Finally, the *CD4* mRNA was detected in the lysate of transiently-transfected cells demonstrating the versatility and specificity of the MIM-MS as a quantitative biosensor.

5.2 MIM-MS fabrication

The MIM-MS was fabricated using a simple three-step process, as illustrated in Figure 5.1a. The first step involves a biomimetic phase-separation technique analogous to the processes that form biophotonic nanostructures on the wings and scales of birds and insects [17]. It has been posited that in nature, these nanostructures are self-assembled through a phase separation of biopolymers in the amphiphilic phospholipid bilayer of scale cells, followed by chitin deposition in the extracellular space [17]. Here, we rely on the phase separation of a synthetic polymer blend of polystyrene (PS) and polymethyl methacrylate (PMMA) co-dissolved in methyl ethyl ketone (MEK) under spin-coating [18–20]. Due to differences in polarity and solubility of PS and PMMA along with varying evaporation rates of MEK and water, under specific humidity conditions, the PS/ PMMA/MEK system undergoes a lateral phase separation which results in densely packed circular islands of PS in a matrix of PMMA. Next, through selective dissolution of PMMA in acetic acid, we create isolated pillars of PS. Finally, we directionally evaporated SiO_2 and Au to form the plasmonic MIM-MS as shown in the scanning electron microscopy (SEM) image in Figure 5.1b. The atomic force microscopy (AFM) profiling of the surface reveals a highly uniform structural height (Figure 5.1c). Furthermore,

we were able to achieve MIM nanogaps of 5 nm through this simple and highly scalable process (Figure 5.1d).

5.3 Single MIM structure simulation

To better elucidate the resonance profile of the MIM-MS, we simulated the scattering response of a single MIM structure. A schematic of the structure is shown in Figure 5.2a. As explained by mode hybridization theory, strong coupling between the two metal layers (in this case a disk and hole) with a sandwiched insulator in-between them results in strong field confinement that leads to strong scattering in the far-field (Figure 5.2a) [21]. First, to determine the gap-plasmon modes of the single MIM structure, we performed three-dimensional (3D) finite-difference-time-domain (FDTD) simulations to obtain the scattering cross section in the VIS-NIR regime between 500–2500 nm. By varying the diameter of structure, we observe the origination of the first-order (l = 1) and subsequently, the second-order (l = 2) gap-mode as seen in Figure 5.2b. The l = 1 mode for larger structures (diameter: 200–500 nm) is in the mid-IR and is therefore inaccessible for most fluorescence-based applications. However, being in the VIS-NIR regime, the l = 2 mode could potentially be utilized for fluorescence enhancement. Further analysis of the structure's scattering profile in the VIS-NIR regime between 300–800 nm is shown in Figure 5.2c. The field profiles of the three gap-modes as shown in Figure 5.2d indicate that l = 1, 2, and 3 corresponding to longitudinal dipolar, quadrupolar, and hexapolar anti-bonding bright modes, respectively.

The resonance profile of the l = 2 mode is broader for larger MIM structures compared to the l = 1 mode for smaller structures. The full width at half maximum (FWHM) of the l = 2 mode for the 300 nm (FWHM $\approx$ 96 nm), 400 nm (FWHM $\approx$ 157 nm), and 500 nm (FWHM $\approx$ 197 nm) structures were 1.5, 2.4, and 3 times, respectively, that of the l = 1 mode for the 100 nm structure (FWHM $\approx$ 66 nm). Additionally, smaller structures display considerably more absorption than scattering (Figure 5.3) [22, 23]. However, a large scattering cross-section is desirable for applications based on light-scattering microscopy such as plasmon-enhanced fluorescence-based biosensing [24]. Figure 5.2e compares the ratio of the scattering and absorption components of the extinction ($C_{\mathrm{scat}}/C_{\mathrm{abs}}$) for the l = 1 mode of smaller MIM structures with the l = 2 mode of larger MIM structures for fluorophores used in this work. The $C_{\mathrm{scat}}/C_{\mathrm{abs}}$ ratio is an order of magnitude larger in the case of the latter. However, as

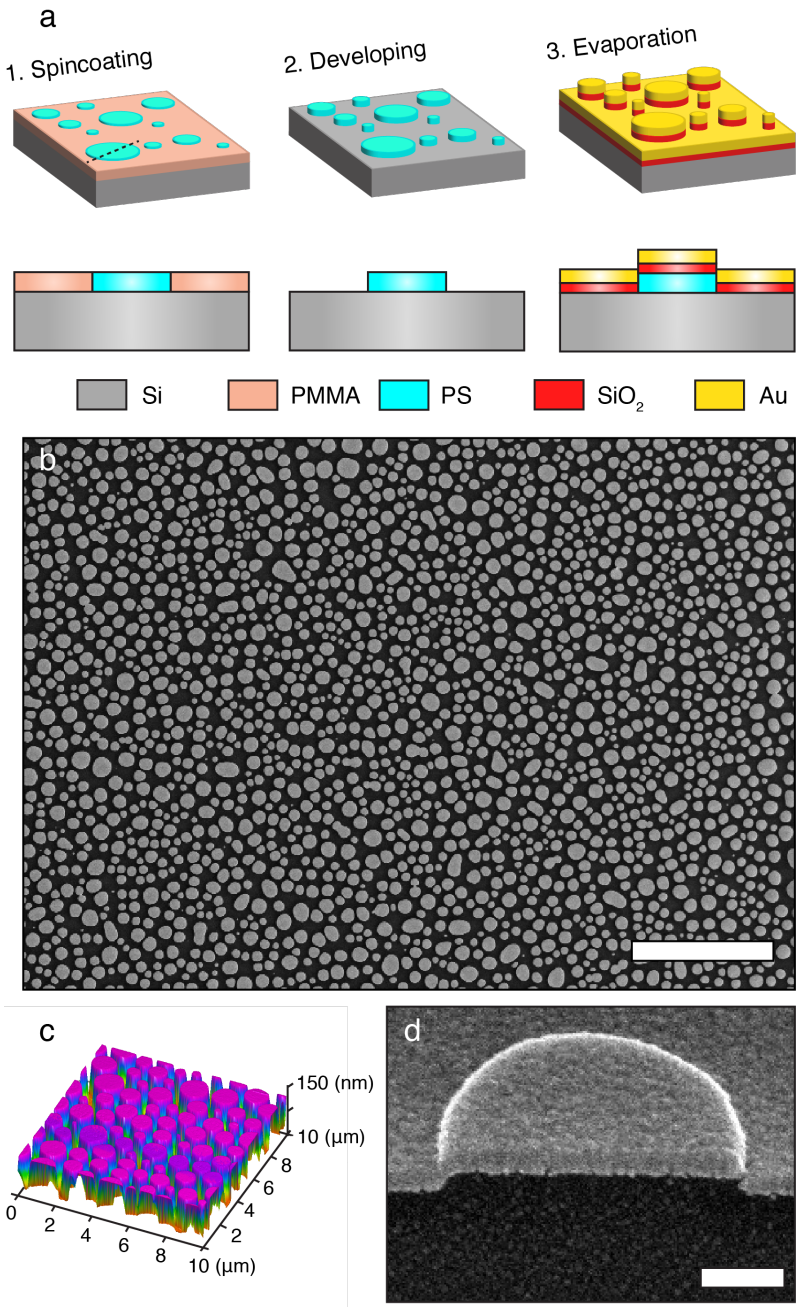

Figure 5.1: Fabrication and characterization of the MIM-MS. (a) Fabrication of the MIM-MS through a simple three-step biomimetic phase separation fabrication process. Cross-sectional view is shown as indicated by the dotted line. (b) Top view SEM image of the metasurface showing circular/ellipsoidal MIM pillars. Scale: 10 μm. (c) 3D AFM image of a 10 $\times$ 10 μm area of the MIM-MS which shows a high degree of height uniformity. (d) A cross-sectional SEM image of an individual MIM scatterer with a clearly visible 5 nm nanogap. Scale: 200 nm.

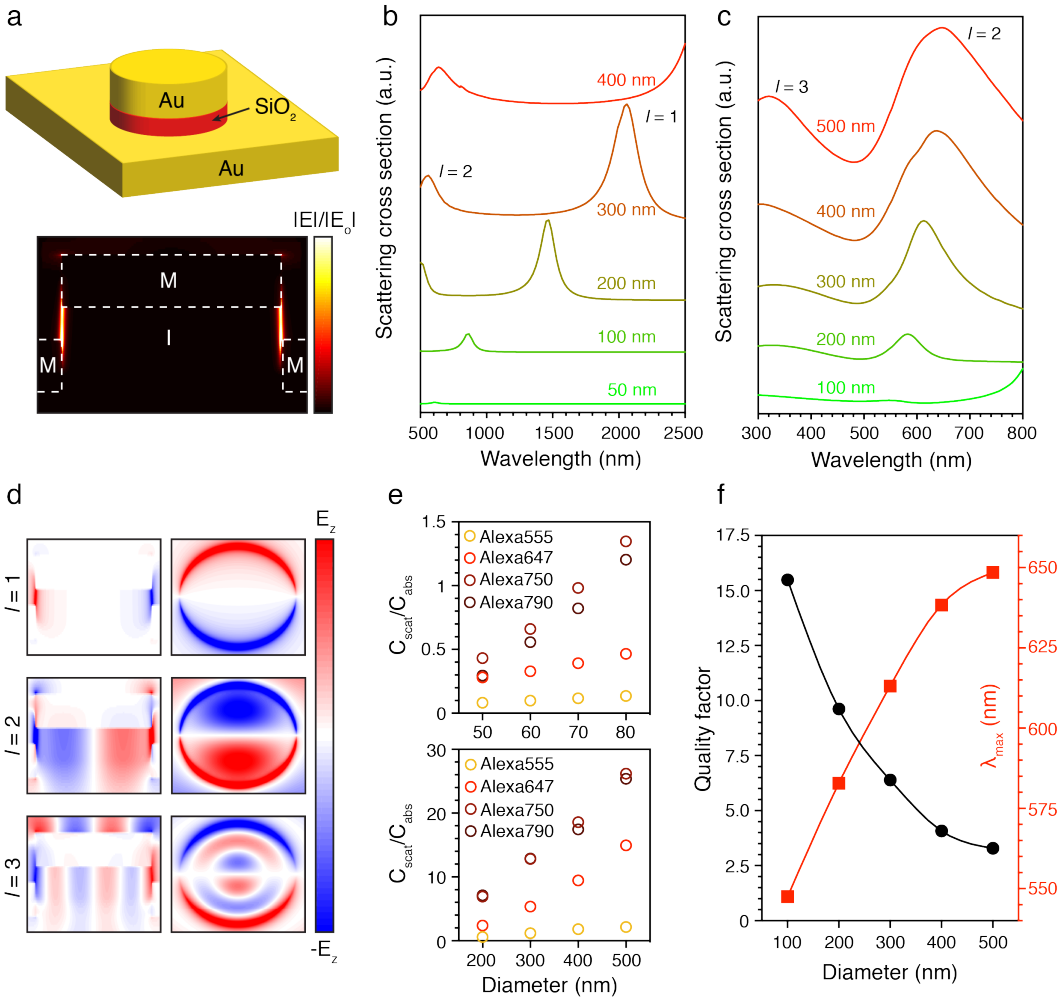

Figure 5.2: Single MIM structure simulations. (a) A schematic of the MIM configuration consisting of an Au nanodisk closely coupled with an Au nanohole separated by an SiO_2 nanogap. (b) Scattering cross section of a single MIM scatterer for different diameters from 50 nm to 400 nm. The first-order (l = 1) and second-order (l = 2) gap modes are both radiant. (c) Scattering cross sections of the second-order (l = 2) and third-order (l = 3) modes of single MIM scatterers in the VIS-NIR regime. (d) The field profile of the nanogap shows the presence of a dipolar (l = 1), quadrupolar (l = 2), and hexapolar (l = 3) anti-bonding bright gap modes. (e) The ratio of the scattering and absorption components of the extinction $C_{\mathrm{scat}}/C_{\mathrm{abs}}$ for the l = 1 mode of small MIM scatterers (top) compared with that of the l = 2 mode of larger MIM scatterers (bottom). (f) The quality factor (black) and plasmon resonance wavelength (red) for the l = 2 mode of larger MIM scatterers.

shown in Figure 5.2f, increasing the MIM structure diameter also lowers the quality factor of the plasmon resonance. Therefore, using a geometry that is between 200–400 nm in diameter would be optimal for plasmon-enhanced

fluorescence as it supports broadband resonance with a high $C_{\text{scat}}/C_{\text{abs}}$ ratio without sacrificing on the quality factor.

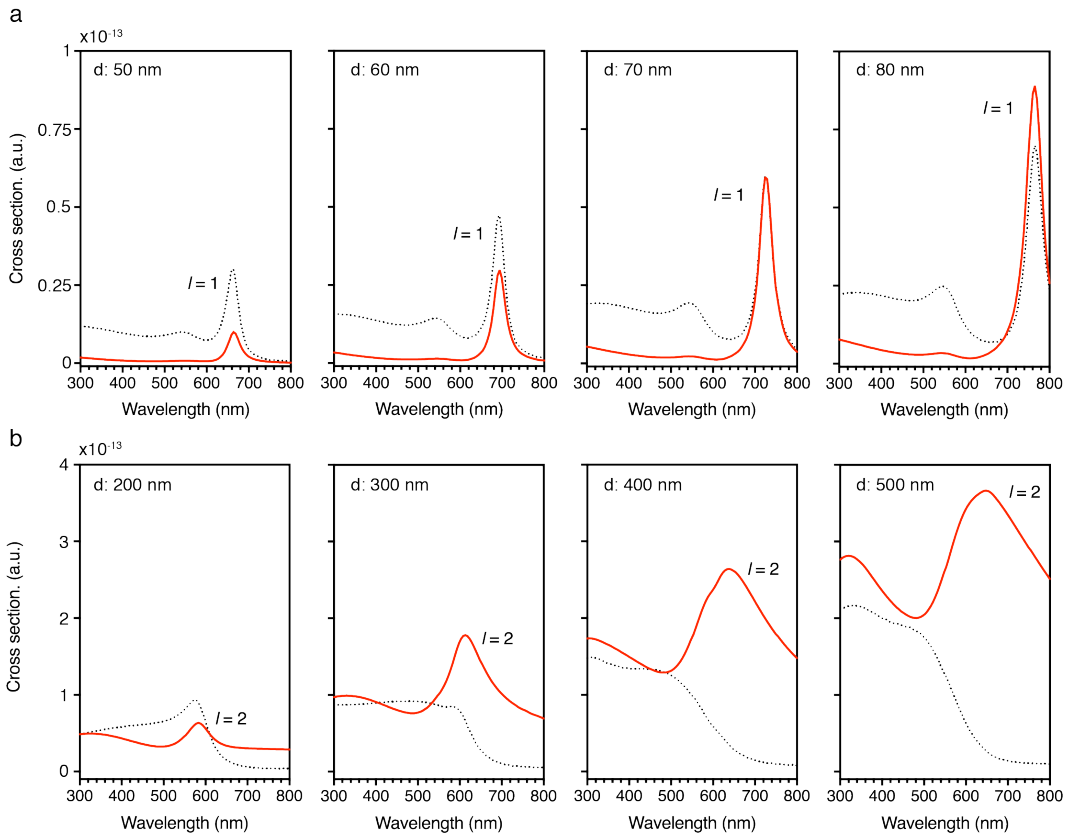

Figure 5.3: The absorption (dotted black) and scattering (solid red) cross sections in the Vis-NIR regime of (a) the $l = 1$ dipolar mode of smaller MIM structures with diameters from 50 - 80 nm and (b) the $l = 2$ quadrupolar mode of larger MIM structures with diameters from 200 - 500 nm. The ratio of the scattering to absorption cross section is considerably higher for the $l = 2$ mode compared to the $l = 1$ mode.

5.4 MIM-MS optical simulation and characterization

By varying the relative mass ratios of the PS and PMMA, we realized MIM-MS of structurally-induced varying coloration with a high chromaticity. Green, orange, and red surfaces were generated (Figure 5.4a) by controlling the average size of the MIM scatterers in the distribution with mean diameters being 195 nm, 340 nm, and 645 nm, respectively (Figure 5.4b). Using an optical micro-spectroscopic setup in dark-field (DF) mode, the scattering spectral response of each of the three plasmonic metasurfaces was obtained. Matching their macroscopic appearance, the metasurfaces displayed scattering res-

onances with maximas at 555 nm, 636 nm, and 792 nm as shown in Figure 5.4c.

3D FDTD simulations were performed on a 4 μm by 4 μm spatial array of MIM scatterers matching the size and spatial periodicity of the fabricated samples (Figure 5.4d). The FDTD simulation results confirm similar resonance profiles as the DF measurements indicating the presence of highly-radiant higher order modes that scatter strongly to the far-field (Figure 5.4e).

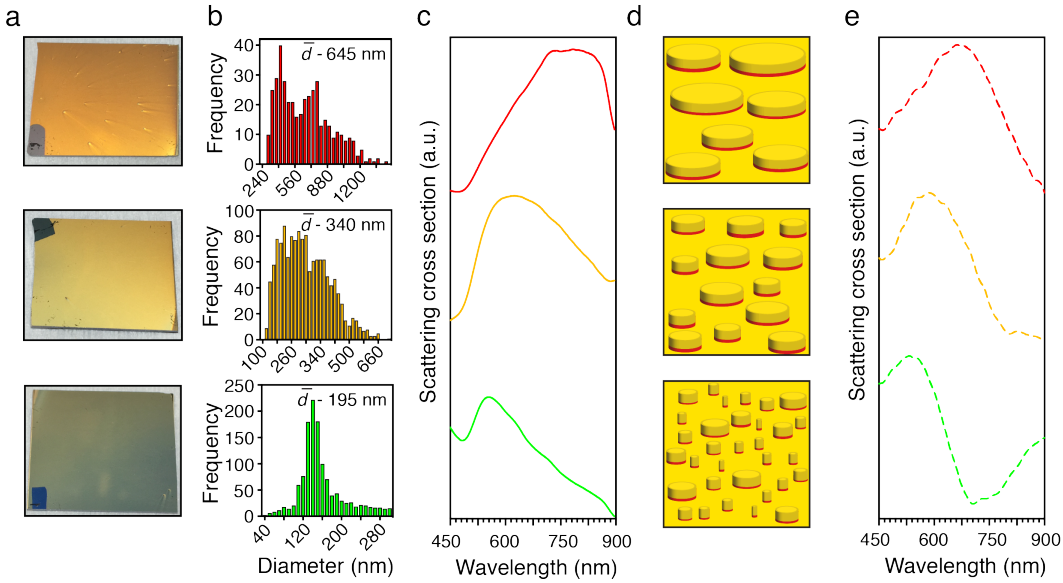

Figure 5.4: MIM-MS optical simulation and characterization. (a) Stable and tunable structurally-induced coloration with high chromaticity is obtained using the biomimetic fabrication technique. (b) MIM-MS with a mean diameter of 195 nm, 340 nm, and 645 nm resulted in green, yellow, and red structural colors, respectively. (c) The far-field scattering profile of the three MIM-MS measured through DF microscopy shows resonance profiles with maximas at 555 nm, 636 nm, and 732 nm, respectively. (d), (e) 3D FDTD simulations of a 4 μm x 4 μm array of the MIM-MS matching the geometry of the three fabricated samples shows a good correlation with the experimentally measured scattering results.

Leveraging the tunable quadrupolar resonant mode of the MIM-MS, we experimentally demonstrate broadband multiplexed fluorescence enhancement by sensing the streptavidin-biotin complex. We chose the geometry with a mean diameter of 340 nm (orange sample as shown in Figure 5.4) due to its broadband scattering response centered at 636 nm, making it ideal for the 550–850 nm wavelength range. The MIM-MS were designed with SiO_2 as the

insulator layer as it can be easily functionalized with a silane (–SH) group to bind with analytes of interest at the plasmonic hotspot.

The streptavidin–biotin complex plays a crucial role in numerous laboratory methods for the detection of low-concentration proteins and nucleic acids [25]. For instance, streptavidin conjugates bind strongly to biotinylated probes such as secondary antibodies to improve the signals from molecules expressed in low concentrations in whole samples [26]. By further enhancing the signal from the conjugated reporters through broadband plasmon-enhanced fluorescence, the detection limit of analytes at low concentrations can be greatly improved.

First, we functionalized the metasurface with silane-polyethylene glycol-biotin (SH-PEG-biotin) and detected different fluorescent conjugates of the protein streptavidin. The fluorescent conjugates used were Alexa Fluor 555 (AF555, excitation (ex)/emission (em) – 555/580 nm), Alexa Fluor 647 (AF647, ex/em – 650/665 nm), Alexa Fluor 750 (AF750, ex/em – 749/775 nm), and Alexa Fluor 790 (AF790, ex/em – 784/814 nm). The schematic of the experiment is shown in Figure 5.5a. The plasmon-enhanced fluorescence from a multiplexed assay consisting of all the aforementioned streptavidin conjugates is shown in Figure 5.5b. The ring-shaped distribution corresponding to plasmonic hotspots of individual MIM scatterers is clearly visible.

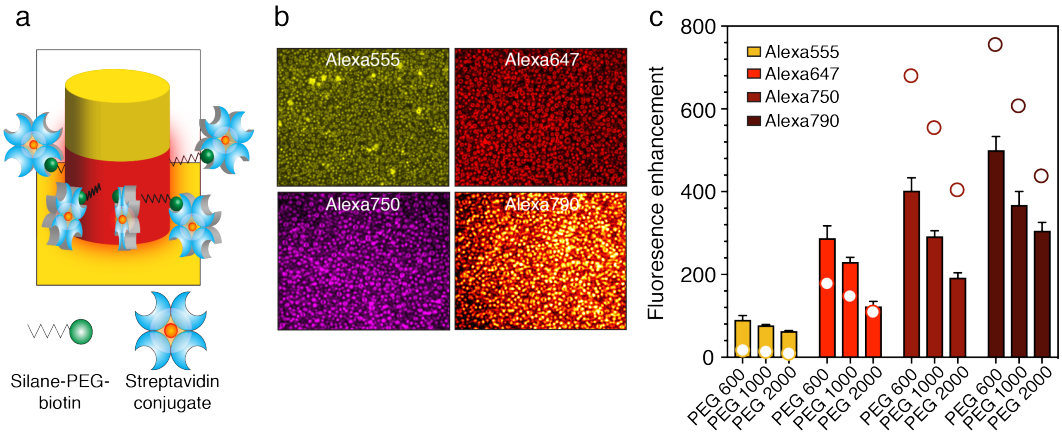

Figure 5.5: Broadband fluorescence enhancement using MIM-MS. (a) A schematic of the selective streptavidin–biotin detection. (b) Multiplexed biosensing of streptavidin conjugated with AF555, AF647, AF750, and AF790 fluorophores. (c) Broadband fluorescence enhancement relative to a glass control for different streptavidin conjugates with varying PEG lengths. The numerical enhancement factor for each case computed through FDTD is plotted as dots.

Next, by varying the PEG molecular weight from 600 Da – 2000 Da, we adjusted the chain length and consequently the distance of the fluorophores from the hotspot between 7 nm – 11 nm [27]. The distance was estimated by summing the chain length of the PEG and the size of a streptavidin tetramer [28]. We then measured the fluorescence intensity for each sample and normalized it relative to a control glass sample prepared under the same conditions. As the PEG length was shortened, the observed fluorescence enhancement for each fluorophore relative to the corresponding control increased (Figure 5.5c). In all cases, a fixed concentration of the silane-PEG-biotin and streptavidin were used. For PEG 600, enhancement factors of 91-, 288-, 403-, and 501-fold were observed for AF555, AF647, AF750, and AF790, respectively. To further test the suppression of quenching, we directly bound AF647 to the SiO_2 layer (i.e. emitter distance $\approx$ 0 nm). This was achieved through silanization of the SiO_2 layer with (3-aminopropyl)triethoxysilane (APTES) and subsequent labeling of the free primary amine ($-NH_2$) end with the N-hydroxysuccinimide (NHS) ester of AF647. An enhancement factor of 586-fold was obtained in this case, indicating strong suppression of quenching. All the experimental results were in good agreement with enhancement factors that were numerically computed using FDTD (Figures 5.5c and 5.6). We also modeled the radiative and nonradiative decay rates associated with quantum emitters placed at various distances from a single MIM scatterer (Figure 5.7) and compared them with those of an isolated nanostructure (Figure 5.8). The first-order dipolar mode of the isolated nanostructure quenches the emitter as it moves closer to the structure while the MIM scatterer effectively suppresses quenching.

5.5 Plasmon-enhanced fluorescence-based biosensing

To demonstrate the utility of the MIM-MS as a biosensor, we targeted the detection of the HIV-1 *gag*, *CD4*, and *CCR5* genes popularly studied in the pathogenesis of HIV-1. They encode the Gag, CD4, and CCR5 proteins respectively. Gag is a structural polyprotein that is essential for virion assembly as it forms the capsid that encapsulates the viral genome HIV-1 [30]. Gag is routinely used as a marker for the detection of HIV-1-infected cells [31] and the quantification of HIV-1 virion production [32]. CD4 is primarily expressed on CD4+ T-lymphocytes and functions as co-receptor to the T-cell receptor during antigen presentation [33]. CCR5 is a G-protein-coupled receptor (GPCR) found on the surface of various immune cells, including T lym-

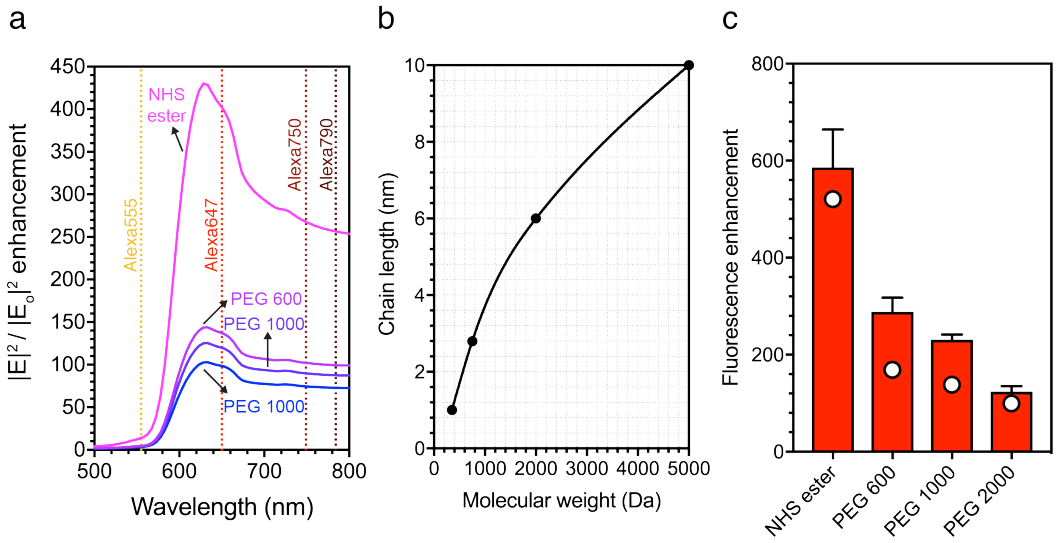

Figure 5.6: Experimental verification of suppression of fluorescence quenching. (a) Normalized $|E|^2$ enhancement computed through FDTD experienced by emitters at various distances from the plasmonic hotspot of an MIM structure of diameter 340 nm. The diameter corresponds to the mean diameter of the samples used in this work. Dotted lines correspond to the excitation maxima of each fluorophore used in the study. NHS ester corresponds to a distance of 0 nm while (b) PEG 600, PEG 1000, and PEG 2000 correspond to distances of 0, 7, 8.75, and 11 nm, respectively [27] (c) Fluorescence enhancement factor of Alexa Fluor 647 at various distances from the plasmonic hotspot of the MIM-MS. Numerically computed enhancement factors for the same distances are plotted as dots.

phocytes, macrophages, and dendritic cells [33]. HIV-1 predominantly infects CD4+ T-lymphocytes through interactions with CD4 and a co-receptor, which during early infection is almost exclusively CCR5 [34]. Therefore, a threshold level of CD4 and CCR5 receptors is required to support the infection [35, 36]. While CD4 is abundantly expressed on CD4+ T-cells, its expression fluctuates on macrophages [37] and CD34+ hematopoietic stem cells [38] making them also potentially susceptible to HIV-1 infection. Moreover, CCR5 expression is highly variable on different subsets of immune cells and depends on the cell maturation state [35]. Consequently, studying the expression of HIV-1 *gag*, *CD4*, and *CCR5* in parallel through selective capture and quantification could provide important information about the interplay of HIV-1 receptor expression levels and susceptibility to infection.

To selectively immobilize and detect the *gag*, *CD4*, and *CCR5* nucleic acids on the MIM-MS, we utilized DNA/RNA hybridization reactions in a sandwich

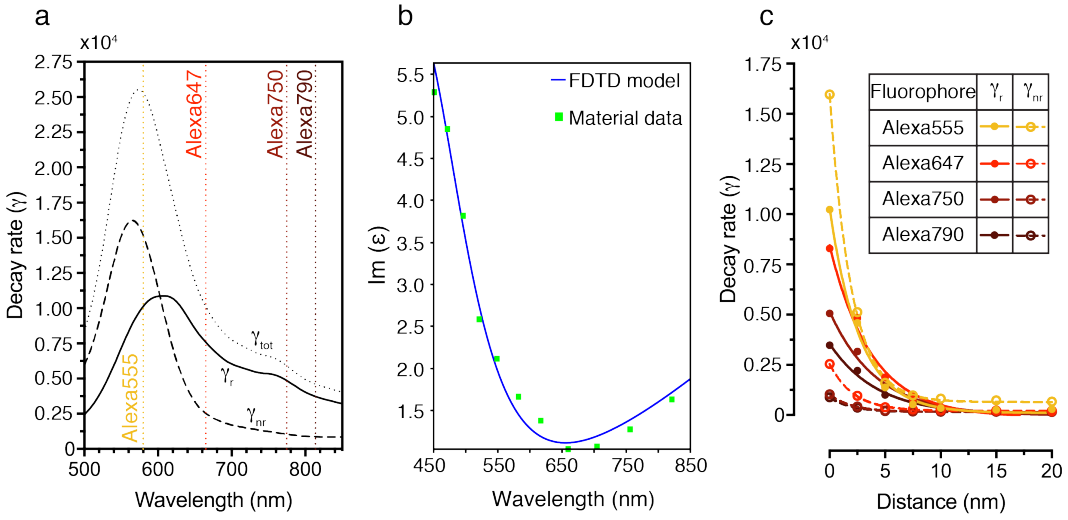

Figure 5.7: Simulation of the decay rates of different fluorophores. (a) The radiative (γ_r, solid), nonradiative (γ_{nr}, dashed) and total (γ_{tot}, dotted) decay rates versus wavelength at an emitter distance of 0 nm from an MIM structure of diameter 340 nm computed through FDTD. The vertical dotted lines correspond to the emission maxima of the fluorophores used in the study. The peak position of γ_r correlates well with the plasmon resonance wavelength of the $l = 2$ mode of the structure. (b) High absorption for wavelengths less than 500 nm which corresponds to losses through nonradiative channels is due to high intrinsic material losses [29]. (c) γ_r and γ_{nr} versus distance for the fluorophores used in the study.

assay format. The target nucleic acid would first be immobilized on the plasmonic hotspot by means of a capture oligonucleotide, and then detected with a fluorescently-labeled detection oligonucleotide (Figure 5.9a). To test the sandwich assay, we selected the first 100 base pairs (bp) of the coding strand in the target complementary DNA (cDNA) sequences. Then, using a nucleic acid analysis software (NUPACK) to avoid secondary structure formations, we selected the binding sites for the complementary capture and detection oligos (Figure 5.10) [39]. Following hybridization, the detection oligo conjugated with AF555 (*gag*), AF647 (*CD4*), and AF750 (*CCR5*) at the 5'-end is bound to the target sequence. Figure 5.9b shows multiplexed detection of *gag*, *CD4*, and *CCR5* 100 bp ssDNA sequences at a concentration of 100 nM.

For the remainder of the study, the *CD4* gene was chosen as a representative to study the MIM-MS biosensing specificity in more detail. Figures 5.9c and 5.11 show capture and detection of the *CD4* 100 bp ssDNA from a concentration of 10 pM to 10 μM. Overcoming quenching, we also demonstrate the sensing of

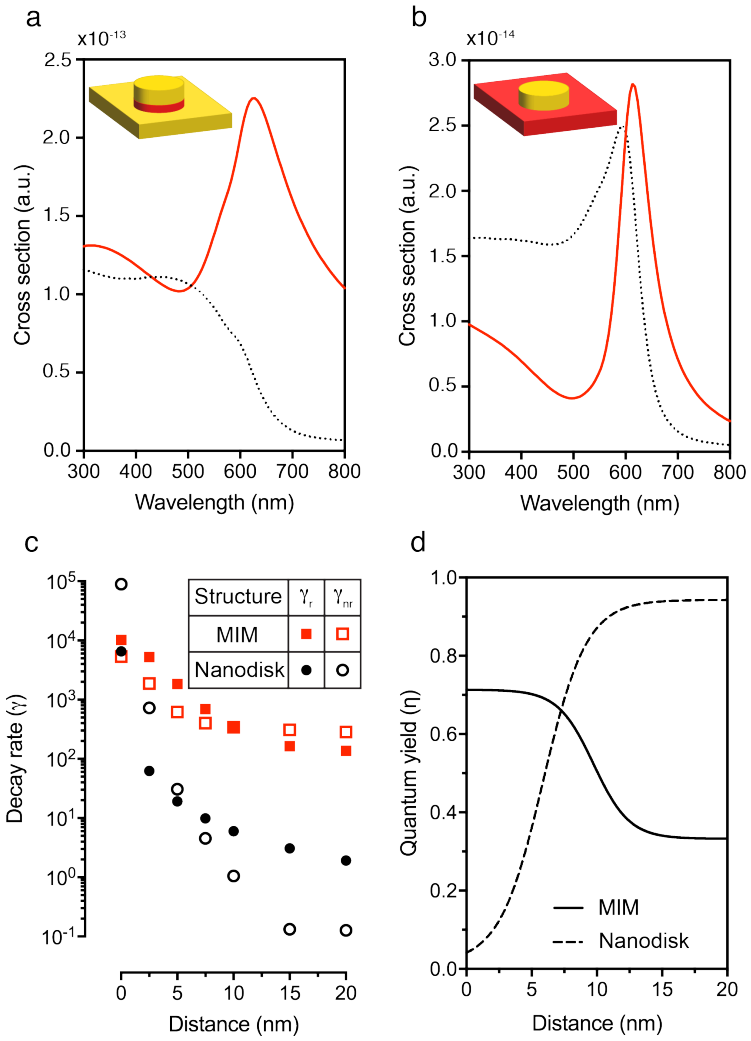

Figure 5.8: The absorption (dotted black) and scattering (solid red) cross sections of (a) a 340 nm MIM structure and (b) a 100 nm nanodisk with a matching plasmon resonance computed through FDTD. The resonance of the nanodisk is considerably narrower. (c) The γ_r and γ_{nr} for the MIM structure and nanodisk at various distances computed through FDTD. In most cases, the γ_r for the MIM structure is orders of magnitude greater than the nanodisk. (d) The structurally-induced quantum yield η for an emitter with an intrinsic quantum yield of unity ($\eta_o = 1$) for various distances computed through FDTD. The nanodisk quenches the emitter for distances < 10 nm while the MIM structure suppresses quenching.

just the detection oligo (20 bp) at concentrations as low as 10 pM (Figure 5.12). Next, an ssDNA analogue of the fulllength *CD4* cDNA coding strand (1377 bp) was generated through a two-step PCR protocol and diluted to working concentrations of 10, 60, and 125 nM in a hybridization buffer. To demonstrate sequence capture specificity, chimeric *CCR5-CD4* ssDNA molecules containing

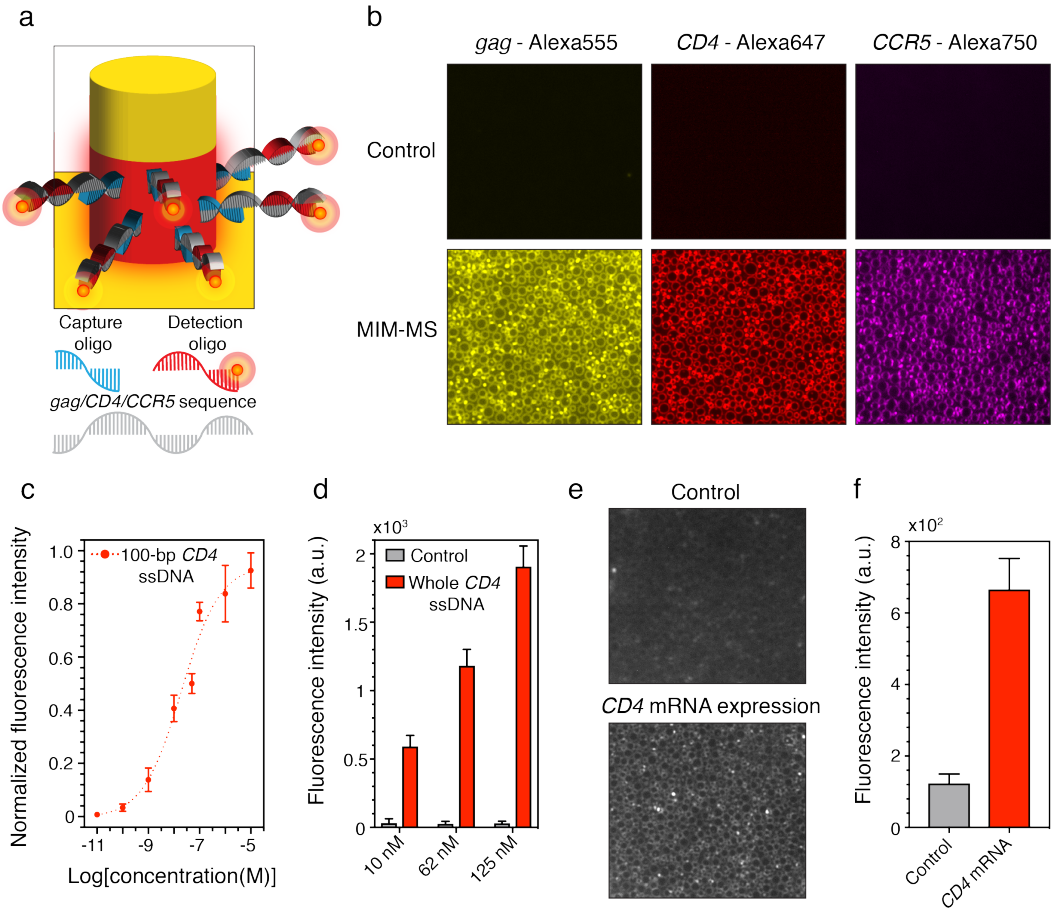

Figure 5.9: Practical biosensing using the MIM-MS. (a) A schematic of the selective nucleic acid sequence detection assay. (b) Multiplexed detection of 100 bp *gag*, *CD4*, and *CCR5* sequences on MIM-MS with detection oligos conjugated with AF555, AF647, and AF790 compared to glass controls treated with the same conditions. (c) Normalized fluorescence intensity for the 100 bp *CD4* sequence captured at concentrations ranging from 10 pM - 10 μM. (d) Fluorescence intensity of a ssDNA analogue of the whole *CD4* gene captured and detected at concentrations of 10, 62, and 125 nM. In comparison, the negative control shows negligible change in fluorescence. (e) Fluorescent micrographs of the functionalized MIM-MS for the lysate of untransfected (control) and transfected cell cultures. (f) The sample overexpressing *CD4* mRNA displays a 5.4-fold higher average fluorescence intensity compared to the untransfected control.

bases 1–56 of the *CCR5* cDNA and bases 57–1377 of the *CD4* cDNA were used as a control. This particular region of the *CD4* cDNA was replaced because the capture and detection oligos were designed to bind to bases 1–20 and 36–56, respectively (Figure 5.10). While the fluorescence intensity from the MIM-MS containing the *CCR5-CD4* ssDNA control remained comparable to the

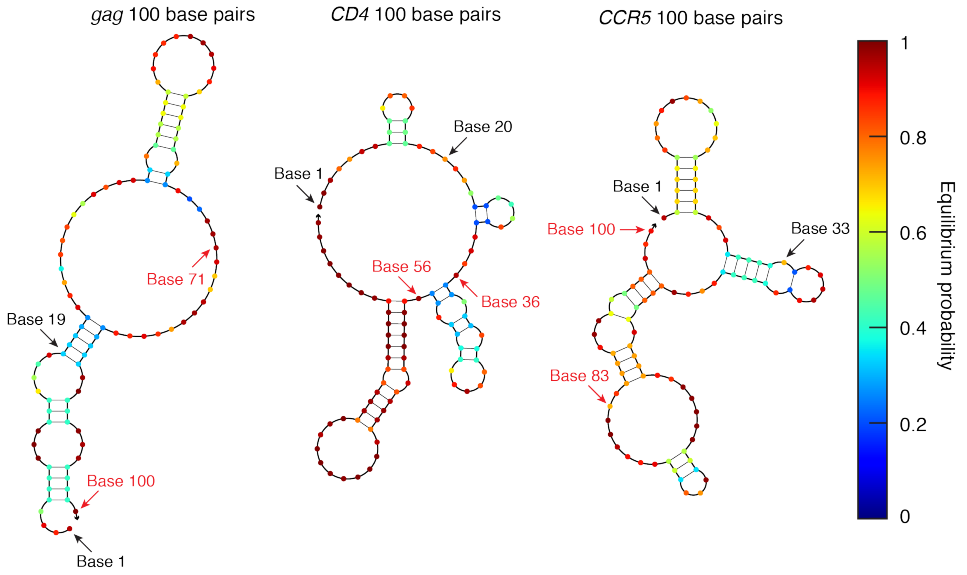

Figure 5.10: The design of capture and detection oligonucleotides using NUPACK [39]. The base sequence range indicated in black (*gag*: bases 1 – 19, *CD4*: bases 1 – 20 and *CCR5*: bases 1 – 33) and red (*gag*: bases 71 – 100, *CD4*: bases 36 – 56 and *CCR5*: bases 83 – 100) correspond to the location of binding of the capture and detection oligos respectively. Regions with a high probability of secondary structure formation were avoided.

background signal for all three concentrations, the intensity for the full-length *CD4* ssDNA samples scaled by 1.9- and 2.6-fold for 60 and 125 nM compared to 10 nM (Figure 5.9d). This indicates high specificity and scalability of the sandwich assay using the MIM-MS towards the detection of full-length nucleic acid molecules.

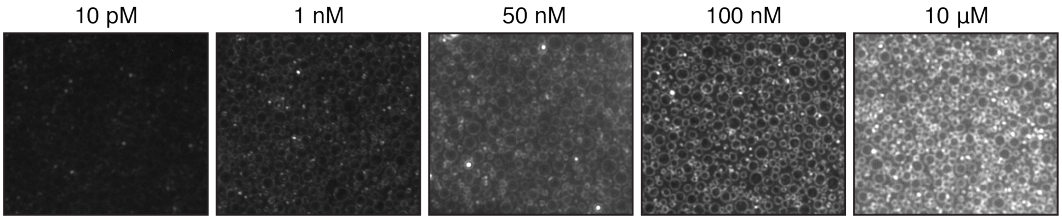

Figure 5.11: Fluorescence micrographs of 100-bp *CD4* sequence captured and detected from a concentration of 10 pM to 10 μM.

Finally, we tested if our MIM-MS sandwich assay protocol could specifically detect *CD4* mRNA molecules in total RNA samples derived from Expi293 cells. Total RNA was isolated from the lysate of Expi293 control cells and cells transiently transfected to overexpress *CD4*. Initially, cell surface expression levels of the *CD4* protein were verified using flow cytometry (Figure

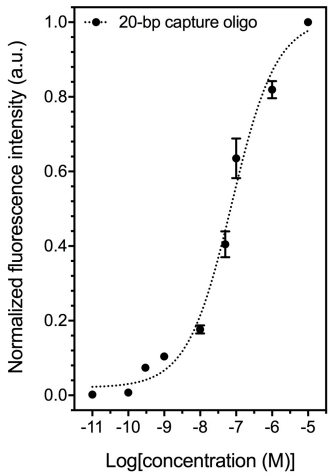

Figure 5.12: Normalized fluorescence intensity for the 20-bp *CD4* capture oligo conjugated with AF647. The biosensing of such a small sequence is enabled by the suppression of quenching by the quadrupolar mode of the MIM-MS.

5.13). Although mRNA only represents a small fraction of total RNA [40], and thousands of genes are expressed simultaneously in mammalian cells [41], the MIM-MS sandwich assay was able to specifically detect full-length *CD4* mRNA molecules in the total RNA sample of the transfected cells. Compared to the control cells, the sample derived from the transfected cells displayed a 5.4-fold increase in fluorescence (Figures 5.9e and f). In a similar fashion, multiple genes of varying concentrations could be simultaneously isolated, detected, and quantified using this approach, making it a highly versatile platform for studying nucleic acids.

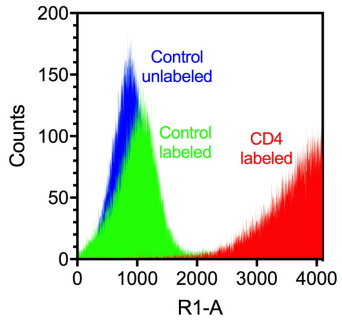

Figure 5.13: Flow cytometry histogram indicating high expression of CD4 glycoprotein on the surface of transfected Expi293 cells (red) in comparison to untransfected, but labeled Expi293 cells (green) and untransfected, unlabeled Expi293 cells (blue).

5.6 Conclusion

In summary, using a three-step biomimetic fabrication process, we have developed a highly scalable MIM-MS that consists of a dense array of closely-coupled Au nanodisks and nanoholes separated by 5 nm SiO_2 nanogaps. The higher-order quadrupolar gap mode of this configuration is highly radiant in the VIS-NIR regime, displays negligible absorptive losses, and suppresses quenching, making it highly suitable for supporting plasmon-enhanced fluorescence. The nanogaps can be engineered to have sufficiently large usable surface areas which can be physically accessed and functionalized for biosensing applications. Utilizing these benefits, we conducted the multiplexed, substrate-enhanced biosensing of proteins (streptavidin–biotin complex) and nucleic acid sequences (*gag*, *CD4* and *CCR5*) of varying sizes (and therefore varying proximity to the plasmonic hotspot) and demonstrated the versatility of the MIM-MS in a practical application.

5.7 Materials and methods

Biomimetic phase-separation through polymer blends

Poly(methyl methacrylate) (PMMA, M_w = 9590, Polymer Standards Service GmbH, Germany) and polystyrene (PS, M_w = 19100, Polymer Standards Service GmbH, Germany) were dissolved in methyl ethyl ketone (MEK, Sigma-Aldrich, USA) with mass ratios of 75%:25%, 65%:35%, and 55%:45% to fabricate the three samples with mean diameters of 195 nm, 340 nm, and 645 nm, respectively. The solution concentrations were 20 mg mL^{-1}. Solutions were spin-coated at a spin-speed of 3500 rpm and acceleration of 2000 rpm s^{-1} for 30 s. Relative humidity was maintained between 40–50% during the spincoating. The de-mixing of the blend components occurs during spin coating due to the difference in relative solubility of PS and PMMA in MEK [18, 19]. First, water condensation begins at humidity levels above 35% forming a water-rich layer at the air/solution interface due to the difference in evaporation rate between water and MEK. Water starts to condense from the air into the solution because of the evaporation of MEK decreasing the temperature on the top below the dew point. Due to the high water concentration, a 3D phase separation occurs between PS/MEK and PMMA/MEK/water. Upon drying, a purely lateral morphology is formed with ellipsoidal PS islands in a PMMA matrix. The samples were then rinsed in acetic acid for 2 min and dried in a stream of N_2 to remove the PMMA matrix leaving behind the PS islands.

High-resolution imaging and statistical analysis of the MIM-MS

High-resolution SEM imaging was performed on the MIM-MS samples using a Nova 200 Nanolab Dualbeam microscope (FEI, USA) at 5 kV while AFM imaging was performed using a Bruker Dimension ICON AFM (Bruker, Germany) using a 100 μm long monolithic silicon cantilever (BudgetSensors) under ambient laboratory conditions using tapping mode with a resonance frequency of about 350 kHz. ImageJ (National Institutes of Health, USA), a public-domain and Java-based image processing tool was used for the statistical analysis of the MIM-MS surface. Every pixel in the acquired SEM images were converted to black or white based on a thresholding condition that was obtained by calculating the mean intensity value of all pixels of the image. Following this, the diameter distribution of the MIM scatterers was determined.

Optical simulations of the MIM-MS

Optical simulations of a single MIM scatterer as well as the MIM-MS as a whole were performed using a 3D finite-difference time-domain software (Lumerical Solutions, Canada). A combination of periodic and perfect matching layer (PML) boundary conditions along with a total-field scattered-field (TFSF) source was used. The absorption cross section was obtained in the total field region inside the TFSF source while the scattering cross section was obtained in the scattered field region outside the TFSF source. For the quantum yield simulations, a dipole source was placed at various distances from the plasmonic hotspot. The radiative and total decay rates were measured as a function of the amount of radiation leaving the system and the total power injected by the dipole source respectively. These measurements were made by means of a transmission box placed around the structure and the dipole source. The quantum yield q of the emitter in the presence of the MIM scatterer was then computed as $q = \frac{\gamma_r}{\gamma_r+\gamma_{nr}+\gamma_{abs}}$ where γ_r and γ_{nr} are the radiative and non-radiative decay rates while γ_{abs} corresponds to absorptive losses. Finally, the enhancement factor was computed as $EF = \frac{q}{q_o} \times \frac{|E|^2}{|E_o|^2}$ where q_o is the intrinsic quantum yield of the fluorophore and $\frac{|E|^2}{|E_o|^2}$ is the normalized electric-field enhancement at the location of the emitter due to the MIM scatterer.

Optical spectroscopic analysis of the MIM-MS

A customized optical microscope operating in dark-field (DF) mode was used for the micro-spectroscopic investigation of the fabricated MIM-MS samples. A

halogen lamp was used as a light source using a 100x objective with a numerical aperture of $NA = 0.90$. The scattered light was collected in a confocal configuration and analyzed using a spectrometer (AvaSpec-ULS2048x64-USB2). A 400 μm core optical fiber was used to obtain a spatial resolution of 20 μm to characterize the scattering of the MIM-MS.

Streptavidin–biotin complex assay preparation

Lyophilized SH-PEG-biotin of varying PEG lengths (Nanocs, Inc., USA) were dissolved in 90% ethanol at concentrations greater than 10 mg mL^{-1}. Then, the solution was added to the MIM-MS and glass slide control surfaces for a 2 h incubation at room temperature (RT). The samples were then washed in deionized (DI) water for 30 min. Streptavidin conjugates (ThermoFisher Scientific, USA) at a working concentration of 0.5 mg mL^{-1} in phosphate-buffered saline (PBS) were added to the MIM-MS surface for a 1 h incubation at RT. Following this, the samples were washed again in DI water for 30 min and prepared for imaging.

NHS ester assay preparation

First, the MIM-MS and glass slide control samples were incubated for 1 h in 4% APTES (Sigma-Aldrich, USA) dissolved in acetone. After washing in acetone, the NHS ester of AF647 (ThermoFisher Scientific, USA) at a concentration of 2 mg mL^{-1} in dimethyl sulfoxide (Sigma-Aldrich, USA) was added to the substrate for 3 h. Following this, the samples were washed in DI water for 30 min and prepared for imaging.

SsDNA and mRNA hybridization

The capture oligo was bound to the MIM-MS through the crosslinking of two primary -NH_2 groups. The capture oligo was designed with an -NH_2 group at the 3'-end. The SiO_2 insulator layer of the MIM-MS was functionalized with APTES. The two primary –NH_2 groups on the APTES functionalization and the capture oligo are linked by means of a water soluble crosslinker (bis(sulfosuccinimidyl)suberate) (BS3). Once the capture oligo was bound to the SiO_2 layer, the ssDNA/mRNA target molecules diluted to the working concentration in a hybridization buffer (Molecular Technologies, USA) were dispensed on the substrate. First, the MIM-MS samples were incubated for 1 h in 4% APTES (Sigma-Aldrich, USA) dissolved in acetone. After washing

in acetone, BS3 (Sigma-Aldrich, USA) dissolved at a 50x molar excess to the capture oligo concentration in a coupling buffer (100 mM sodium phosphate, 0.15 M sodium chloride, pH 7.2) was added to the MIM-MS samples for 15 min. Next, the capture oligo (Integrated DNA Technologies, Inc., USA) diluted to a working concentration of 20 μM in a folding buffer (137 mM sodium chloride, 2.7 mM potassium chloride, 8 mM sodium phosphate dibasic, 2 mM potassium phosphate monobasic, pH 7.5) was added to the MIM-MS samples for 1 h. After washing in folding buffer, the target sequence (100 bp sequence purchased from Integrated DNA Technologies/full-length CD4 ssDNA synthesized through PCR/ CD4 mRNA from total RNA in lysate) in a probe hybridization buffer (Molecular Technologies, USA) was added to the MIM-MS. Hybridization buffer with 10% formamide was used for the 100 bp and full-length sequence while 15% formamide was used for the mRNA. The samples were incubated overnight (O/N) at 37 ^{o}C and 45 ^{o}C for the 100 bp/full-length sequence and the mRNA, respectively. Following washing with a probe wash buffer (Molecular Technologies, USA), the detection oligo (Integrated DNA Technologies, Inc., USA) diluted to a working concentration of 10 μM in hybridization buffer with 10% or 15% formamide depending upon the target sequence was added to the MIM-MS. The samples were then incubated O/N at 37 ^{o}C or 45 ^{o}C. Finally, excess detection probes were removed with wash buffer.

CD4 ssDNA synthesis

Full-length *CD4* ssDNA was generated by a two-step PCR protocol. For the first reaction, full-length *CD4* double-stranded cDNA (Accession NM_000616.4, NCBI) was amplified from the lentiviral plasmid Phage2-CMV-CD4 using *CD4* Fwd 5'-ATGAACCGGGGAGTCCCTTTTAG-3' and *CD4* Rev 5'-TCAAATGGGGCTACATGTCTTCTG-3' primers. The *CD4* cDNA product was purified by DNA agarose gel electrophoresis and was used as template for the second PCR reaction to generate *CD4* ssDNA. For this reaction, only the *CD4* Fwd primer was used to generate ssDNA copies of the coding strand of *CD4*. The final product was purified using a PCR purification kit (Qiagen, Germany) and subsequently concentrated using NanoSep centrifugal devices (Pall, USA). For chimeric *CCR5-CD4* ssDNA molecules, nucleotides 1-56 of *CD4* were replaced with nucleotides 1-56 of *CCR5*. *CCR5-CD4* ssDNA was generated with the above protocol using the *CCR5-CD4* Fwd primer 5'-

ATGGATTATCAAGTGTCAAGTCCAATCTATGACATCAATTATTATAC-ATCGGAGCCCCCAGCAGCCACTCAGG-3' for the second PCR reaction.

Total RNA extraction from Expi293 cells

Expi293 cells (ThermoFisher Scientific, USA) were transiently transfected with the Phage2-CMV-CD4 plasmid using the transfection reagent ExpiFectamine (ThermoFisher Scientific, USA) in accordance with the manufacturer's guidelines. The cells were incubated at 37 ^{o}C and 5% CO_2 under shaking conditions at 470 rpm. Control and transfected cells were harvested after 48 h incubation and centrifuged at 400g for 10 min. The supernatants were removed and the pellets were re-suspended in 10 mL TRIzol (ThermoFisher Scientific, USA) to lyse the cells. Total RNA was isolated from the cell lysate using Direct-zol RNA extraction kits (Zymo Research, USA) and concentrated using NanoSep centrifugal devices (Pall, USA).

CD4 quantification by flow cytometry

CD4 expression on transiently-transfected Expi293 cells was detected by flow cytometry (MACSQuant Analyzer 10, Miltenyi Biotec, Germany). Cells were stained using an APC-conjugated anti-CD4 antibody (Cat. no. MHCD0405, ThermoFisher Scientific, USA, 1:100 dilution) in PBS containing 2% fetal bovine serum (FBS) for 30 min at RT and washed twice before analysis.

Fluorescence microscopy and image processing

All fluorescence imaging was conducted using a Leica DMI 600 wide field microscope (Leica Camera AG, Germany) with a 100x objective (NA = 1.40, immersion medium - oil). For imaging AF555 and AF647, a Lumencor SPECTRA X (Lumencor, Inc., USA) illumination system was used while for AF750 and AF790, a separate LED for Cy7 excitation (ThorLabs, USA) was used. ImageJ was used to obtain the fluorescence enhancement factors. Selecting individual MIM scatterers from each image, the mean fluorescence intensity from a region of interest (ROI) spanning the 2D area of the ringshaped hotspot was computed. Using the same ROI area, the mean fluorescence from corresponding glass slide controls were obtained. Background signal was obtained using respective substrates with no added fluorophores and was subtracted from the images during fluorescence intensity analysis.

References

[1] Edward Mills Purcell. Spontaneous emission probabilities at radio frequencies. *Proceedings of the American Physical Society*, 69(11–12):681, 1946. doi: 10.1103/PhysRev.69.674.2.

[2] Philippe Goy, Jean-Michel Raimond, Michel Gross, and Serge Haroche. Observation of cavity-enhanced single-atom spontaneous emission. *Physical Review Letters*, 50(24):1903–1906, 1983. doi: 10.1103/PhysRevLett.50.1903.

[3] Daniel Kleppner. Inhibited spontaneous emission. *Physical Review Letters*, 47(4):233–236, 1981. doi: 10.1103/PhysRevLett.47.233.

[4] Sergei Kuhn, Ulf Hakanson, Lavinia Rogobete, and Vahid Sandoghdar. Enhancement of single-molecule fluorescence using a gold nanoparticle as an optical nanoantenna. *Physical Review Letters*, 97(1):017402–1–017402–4, 2006. doi: 10.1103/PhysRevLett.97.017402.

[5] Pascal Anger, Palash Bharadwaj, and Lukas Novotny. Enhancement and quenching of single-molecule fluorescence. *Physical Review Letters*, 96 (11):113002–1–113002–4, 2006. doi: 10.1103/PhysRevLett.96.113002.

[6] Erik Dulkeith, Arne C. Morteani, Thomas Niedereichholz, Thomas A. Klar, Jochen Feldmann, Stefano A. Levi, Frank C. J. M. van Veggel, David N. Reinhoudt, Michael Möller, and David I. Gittins. Fluorescence quenching of dye molecules near gold nanoparticles: Radiative and nonradiative effects. *Physical Review Letters*, 89(20):203002–1–203002–4, 2002. doi: 10.1103/PhysRevLett.89.203002.

[7] Remi Faggiani, Jianji Yang, and Philippe Lalanne. Quenching, plasmonic, and radiative decays in nanogap emitting devices. *ACS Photonics*, 2(12): 1739–1744, 2015. doi: 10.1021/acsphotonics.5b00424.

[8] Jianji Yang, Remi Faggiani, and Philippe Lalanne. Light emission in nanogaps: Overcoming quenching. *Nanoscale Horizons*, 1(1):11–13, 2016. doi: 10.1039/C5NH00059A.

[9] Nuttawut Kongsuwan, Angela Demetriadou, Rohit Chikkaraddy, Felix Benz, Vladimir A. Turek, Ulrich F. Keyser, Jeremy J. Baumberg, and Ortwin Hess. Suppressed quenching and strong-coupling of Purcell-enhanced single-molecule emission in plasmonic nanocavities. *ACS Photonics*, 5(1): 186–191, 2018. doi: 10.1021/acsphotonics.7b00668.

[10] Yun-Chorng Chang, Shih-Ming Wang, Hsin-Chan Chung, Chung-Bin Tseng, and Shih-Hui Chang. Observation of absorption-dominated bonding dark plasmon mode from metal–insulator–metal nanodisk arrays fabricated by nanospherical-lens lithography. *ACS Nano*, 6(4):3390–3396, 2012. doi: 10.1021/nn300420x.

[11] Valentin Flauraud, Raju Regmi, Pamina M. Winkler Duncan T. L. Alexander, Herve Rigneault, Niek F. van Hulst, Maria F. Garcia-Parajo, Jerome Wenger, and Jurgen Brugger. In-plane plasmonic antenna arrays with surface nanogaps for giant fluorescence enhancement. *Nano Letters*, 17(3):1703–1710, 2017. doi: 10.1021/acs.nanolett.6b04978.

[12] Shu Tian, Oara Neumann, Michael J. McClain, Xiao Yang, Linan Zhou, Chao Zhang, Peter Nordlander, and Naomi J. Halas. Aluminum nanocrystals: A sustainable substrate for quantitative SERS-based DNA detection. *Nano Letters*, 17(8):5071–5077, 2017. doi: 10.1021/acs.nanolett.7b02338.

[13] Annamaria Ruscito and Maria C. DeRosa. Small-molecule binding aptamers: Selection strategies, characterization, and applications. *Frontiers in Chemistry*, 4(14):1–14, 2016. doi: 10.3389/fchem.2016.00014.

[14] Franziska Pfeiffer and Gunter Mayer. Selection and biosensor application of aptamers for small molecules. *Frontiers in Chemistry*, 4(25):1–21, 2016. doi: 10.3389/fchem.2016.00025.

[15] David J. Javier, Nitin Nitin, Matthew Levy, Andrew Ellington, and Rebecca Richards-Kortum. Aptamer-targeted gold nanoparticles as molecular-specific contrast agents for reflectance imaging. *Bioconjugate Chemistry*, 19(6):1309–1312, 2008. doi: 10.1021/bc8001248.

[16] Qubit rna hs assay kit - thermo fisher scientific. `https://www.thermofisher.com/order/catalog/product/Q32852`, 2019 (Accessed: Dec 17, 2019).

[17] Vinodkumar Saranathan, Ainsley E. Seago, Alec Sandy, Suresh Narayanan, Simon G. J. Mochrie, Eric R. Dufresne, Hui Cao, Chinedum O. Osuji, and Richard O. Prum. Structural diversity of arthropod biophotonic nanostructures spans amphiphilic phase-space. *Nano Letters*, 15(6):3735–3742, 2015. doi: 10.1021/acs.nanolett.5b00201.

[18] Cheng Huang, Markus Moosmann, Jiehong Jin, Tobias Heiler, Stefan Walheim, and Thomas Schimmel. Polymer blend lithography: A versatile method to fabricate nanopatterned self-assembled monolayers. *Beilstein Journal of Nanotechnology*, 3(1):620–628, 2012. doi: 10.3762/bjnano.3.71.

[19] Vinayak Narasimhan, Radwanul Hasan Siddique, Jeong Oen Lee, Shailabh Kumar, Blaise Ndjamen, Juan Du, Natalie Wong, David Sretavan, and Hyuck Choo. Multifunctional biophotonic nanostructures inspired by the longtail glasswing butterfly for medical devices. *Nature Nanotechnology*, 13(6):512–519, 2018. doi: 10.1038/s41565-018-0111-5.

[20] Radwanul Hasan Siddique, Jan Mertens, Hendrik Holscher, and Silvia Vignolini. Scalable and controlled self-assembly of aluminum-based random plasmonic metasurfaces. *Light: Science and Applications*, 6(7):e17015, 2017. doi: 10.1038/lsa.2017.15.

[21] Emil Prodan, Corey Radloff, Naomi J. Halas, and Peter Norlander. A hybridization model for the plasmon response of complex nanostructures. *Science*, 302(5644):419–422, 2003. doi: 10.1126/science.1089171.

[22] Felicia Tam, Allen L. Chen, Janardan Kundu, Hui Wang, and Naomi J. Halas. Mesoscopic nanoshells: Geometry-dependent plasmon resonances beyond the quasistatic limit. *The Journal of Chemical Physics*, 127(20): 204703–1–204703–6, 2007. doi: 10.1063/1.2796169.

[23] Rizia Bardhan, Nathaniel K. Grady, Joseph R. Cole, Amit Joshi, and Naomi J. Halas. Fluorescence enhancement by Au nanostructures: nanoshells and nanorods. *ACS Nano*, 3(3):744–752, 2009. doi: 10.1021/nn900001q.

[24] Prashant K. Jain, Kyeong Seok Lee, Ivan H. El-Sayed, and Mostafa A. El-Sayed. Calculated absorption and scattering properties of gold nanoparticles of different size, shape, and composition: Applications in biological imaging and biomedicine. *The Journal of Physical Chemistry B*, 110(14): 7238–7248, 2006. doi: 10.1021/jp057170o.

[25] Christopher M. Dundas, Daniel Demonte, and Sheldon Park. Streptavidin–biotin technology: Improvements and innovations in chemical and biological applications. *Applied Microbiology and Biotechnology*, 97(21):9343–9353, 2013. doi: 10.1007/s00253-013-5232-z.

[26] Zhanjun Yang, Shufen Luo, Juan Li, Xin'an Jiao, and Xiaoya Hu. A biotin-streptavidin signal amplification strategy for a highly sensitive chemiluminescent immunoassay for chicken interferon-y. *RSC Advances*, 3(45):22868–22871, 2013. doi: 10.1039/C3RA44325F.

[27] Anne K. Kenworthy, Kalina Hristova, Dave Needham, and Thomas J. McIntosh. Range and magnitude of the steric pressure between bilayers containing phospholipids with covalently attached poly(ethylene glycol). *Biophysical Journal*, 68(5):1921–1936, 1995. doi: 10.1016/S0006-3495(95)80369-3.

[28] Wayne A. Hendrickson, Arno Pähler, Janet L. Smith, Yoshinori Satow, Ethan A. Merritt, and Richard P. Phizackerley. Crystal structure of core streptavidin determined from multiwavelength anomalous diffraction of synchrotron radiation. *Proceedings of the National Academy of Sciences*, 86(7):2190–2194, 1989. doi: 10.1073/pnas.86.7.2190.

[29] Philip B. Johnson and Robert W. Christy. Optical constants of the noble metals. *Physical Review B*, 6(12):4370–4379, 1972. doi: 10.1103/PhysRevB.6.4370.

[30] Neil M. Bell and Andrew M. L. Lever. HIV Gag polyprotein: Processing and early viral particle assembly. *Trends in Microbiology*, 21(3):136–144, 2013. doi: 10.1016/j.tim.2012.11.006.

[31] Matthew J. Pace, Erin H. Graf, Luis M. Agosto, Angela M. Mexas, Frances Male, Troy Brady, Frederic D. Bushman, and Una O'Doherty. Directly infected resting CD4+T cells can produce HIV Gag without spreading infection in a model of HIV latency. *PLOS Pathogens*, 8(7): e1002818, 2012. doi: 10.1371/journal.ppat.1002818.

[32] Kathy Wehrly and Bruce Chesebro. p24 antigen capture assay for quantification of human immunodeficiency virus using readily available inexpensive reagents. *Methods*, 12(4):288–293, 1997. doi: 10.1006/meth.1997.0481.

[33] Kenneth Murphy, Casey Weaver, and Casey Weaver. *Janeway's Immunobiology*. New York: Garland Science, ninth edition, 2017. doi: 10.1201/9781315533247.

[34] Jean-Charles Grivel, Robin J. Shattock, and Leonid B. Margolis. Selective transmission of R5 HIV-1 variants: Where is the gatekeeper? *Journal of Translational Medicine*, 9(1):S6, 2011. doi: 10.1186/1479-5876-9-S1-S6.

[35] Benhur Lee, Matthew Sharron, Luis J. Montaner, Drew Weissman, and Robert W. Doms. Quantification of CD4, CCR5, and CXCR4 levels on lymphocyte subsets, dendritic cells, and differentially conditioned monocyte-derived macrophages. *Proceedings of the National Academy of Sciences*, 96(9):5215–5220, 1999. doi: 10.1073/pnas.96.9.5215.

[36] Emily J. Platt, Kathy Wehrly, Shawn E. Kuhmann, Bruce Chesebro, and David Kabat. Effects of CCR5 and CD4 cell surface concentrations on infections by macrophagetropic isolates of human immunodeficiency virus type 1. *Journal of Virology*, 72(4):2855–2864, 1998. URL `https://jvi.asm.org/content/72/4/2855`.

[37] Jianbin Wang, Keith Crawford, Menglan Yuan, Hui Wang, Paul R. Gorry, and Dana Gabuzda. Regulation of CC chemokine receptor 5 and CD4 expression and human immunodeficiency virus type 1 replication in human macrophages and microglia by T helper type 2 cytokines. *The Journal of Infectious Diseases*, 185(7):885–897, 2002. doi: 10.1086/339522.

[38] Matthew J. Pace and Una O'Doherty. Hematopoietic stem cells and HIV infection. *The Journal of Infectious Diseases*, 207(12):1790–1792, 2013. doi: 10.1093/infdis/jit120.

[39] Joseph N. Zadeh, Conrad D. Steenberg, Justis S. Bois, Brain R. Wolfe, Marshall B. Pierce, Asif R. Khan, Robert M. Dirks, and Niles A. Pierce. Nupack: Analysis and design of nucleic acid systems. *Journal of Computational Chemistry*, 32(1):170–173, 2011. doi: 10.1002/jcc.21596.

[40] Harvey Lodish, Arnold Berk, Lawrence S. Zipursky, Paul Matsudaira, David Baltimore, and James Darnell. *Molecular Cell Biology*. New York: W. H. Freeman, fourth edition, 2000. URL `https:`

//www.macmillanlearning.com/college/us/product/Molecular-Cell-Biology/p/1464183392.

[41] Georgi K Marinov, Brain A. Williams, Ken McCue, Gary P. Schroth, Jason Gertz, Richard M. Myers, and Barbara J. Wold. From single-cell to cell-pool transcriptomes: Stochasticity in gene expression and RNA splicing. *Genome Research*, 24(3):496–510, 2014. doi: 10.1101/gr.161034.113.

Chapter 6

BIOINSPIRED NANOSTRUCTURES FOR SURFACE-ENHANCED RAMAN SPECTROSCOPY

This chapter was adapted from:

V. Narasimhan, R. H. Siddique, H. Park, and H. Choo (2020). "Bioinspired disordered flexible metasurfaces for human tear analysis using broadband surface-enhanced Raman scattering." In: *ACS Omega* 5.22, pp. 12915–12922. DOI: 10.1021/acsomega.0c00677.

Abstract

Flexible surface-enhanced Raman spectroscopy (SERS) has received attention as a means to move SERS-based broadband biosensing from bench to bedside. However, traditional flexible periodic nanoarrangements with sharp plasmonic resonances or their random counterparts with spatially varying uncontrollable enhancements are not reliable for practical broadband biosensing. Here, we report bioinspired quasi-(dis)ordered nanostructures presenting a broadband yet tunable application-specific SERS enhancement profile. Using simple, scalable biomimetic fabrication, we create a flexible metasurface (flex-MS) of quasi-(dis)ordered metal-insulator-metal (MIM) nanostructures with spectrally variable, yet spatially controlled electromagnetic hotspots. The MIM is designed to simultaneously localize electromagnetic signal and block background Raman signals from the underlying polymeric substrate – an inherent problem of flexible SERS. We elucidate the effect of quasi-(dis)ordering on broadband tunable SERS enhancement and employ the flex-MS in a practical broadband SERS demonstration to detect human tear uric acid within its physiological concentration range (25 – 150 μM). The performance of the flex-MS towards non-invasively detecting whole human tear uric acid levels *ex vivo* is in good agreement with a commercial enzyme-based assay.

6.1 Introduction

Surface-enhanced Raman scattering (SERS) has shown great promise as a technique for molecular fingerprinting due to its high sensitivity and selectivity along with its inherent simplicity [1–3]. In particular, SERS from flexible substrates has received great attention recently owing to its advantages over rigid substrates [4–6]. For instance, flexible SERS can be used on irregular surfaces for in situ biosensing thereby overcoming complex analyte extraction strategies and other sample preparation steps required while using conventional rigid substrates. However, the adoption of flexible SERS as a point-of-care diagnostic tool has been limited by a number of factors [6]. Firstly, most structures used for this application are designed either with periodic arrangements due to their highly predictable plasmonic resonances [7, 8] or with random arrangements due to their ease of fabrication [9, 10]. However, periodic structures with narrowband resonance profiles are not tunable for multiplexing [6–8]. Multiplexed in situ SERS for instance would require a broadband and tunable plasmonic resonance profile to provide uniform enhancement of various Raman modes occurring at greatly differing vibrational energy states [11–13]. In the same vein, random structures do not guarantee repeatable SERS performance for a given bandwidth due to spatially varying enhancements that are not tunable [14]. Secondly, flexible SERS platforms are usually made of polymers that generate a considerable Raman background signal [6]. Finally, challenges in obtaining reproducible signal can also be attributed to the difficulty in homogeneously, scalably and cost-effectively manufacturing SERS active sites or hotspots [15]. These issues necessitate the requirement for flexible SERS approaches with spatially uniform broadband, yet tunable plasmonic resonances that are scalably and reliably manufacturable.

Inspiration can be sought from nature which boasts a plethora of biophotonic nanostructures possessing quasi-(dis)order or controlled disorder where both structural dimensions and periodicity follow unique distributions [16, 17]. Such an amalgamation of short-range order (i.e. periodicity) with long-range disorder (i.e. randomization) along with variations in structure size leads to a host of useful omnidirectional broadband, yet tunable optical properties [18–20]. In this work, using a simple biomimetic fabrication process, we realize a highly scalable and flexible plasmonic metasurface-based (flex-MS) SERS platform. The flex-MS consists of a dense quasi-(dis)ordered ensemble of gold (Au) nanodisks on nanoholes separated by a sub-10 nm silicon dioxide (SiO_2) nanogap

in a metal-insulator-metal (MIM) configuration. The entire configuration is created at a wafer-scale over a 400 μm-thick silicone elastomer (PDMS) layer. The MIM is designed not only for light confinement and field enhancement, but is also responsible for blocking the Raman background signal from the underlying PDMS. The fabrication approach which is spin-coating-based allows for a short-range-ordered Gaussian-distribution of MIM nanostructure diameters resulting in a broadband, yet tunable plasmonic resonance and corresponding $|\frac{E}{E_o}|^2$ enhancement factor (EF). Through rigorous numerical simulations and comparative experimentation, we isolate the contributions of the bioinspired short-range periodicity (i.e. positional disorder) and the diameter distribution (i.e. size disorder) towards SERS EF. As a practical broadband SERS demonstration of the flex-MS, we perform the label-free detection of human tear uric acid (UA) towards the diagnosis various chronic pathologies. Our platform effectively tracks prominent peaks of UA at large Raman-shifts within its physiological concentration range (25 – 150 μM) in human tears. Finally, we show that the performance of the flex-MS in detecting UA levels in whole human tear samples from different subjects is in good agreement with a commercial enzyme-based assay.

6.2 Flex-MS fabrication and characterization

The flex-MS was fabricated using a simple process consisting of three steps, as shown in Figure 6.1a. On spin-coated PDMS thin-films, the first step involves a biomimetic technique that relies on nanostructuring through the lateral phase-separation of two synthetic polymers – polystyrene (PS) and polymethyl methacrylate (PMMA) co-dissolved in methyl ethyl ketone (MEK) [20, 21]. This approach is analogous to the formation of quasi-(dis)ordered biophotonic nanostructures on the wings and scales of birds and insects [22]. The lateral phase-separation of PS and PMMA occurs under spin-coating which results in densely-packed quasi-(dis)ordered distribution of circular hydrophobic PS islands in a matrix of hydrophilic PMMA (Figure 6.2). Furthermore, through the control of various parameters such as the spin-speed, relative humidity, polymer weight ratios, and molecular weights, the average diameter and short-range periodicity of the PS islands can be effectively tuned [23, 24]. Next, through selective dissolution of PMMA in acetic acid which leaves behind a nanopillar mask of PS, SiO_2 is directionally deposited through E-beam evaporation. Finally, Au of an appropriate thickness is directionally evap-

orated over the SiO_2 nanopillars to create a scalable flex-MS with uniform sub-10 nm-thick MIM nanogaps. A photograph and SEM image of the flex-MS are shown in Figures 6.1b and c. A 2D fast Fourier transform (FFT) of the top view SEM image as shown in the inset of Figure 6.1c reveals a ring-shape distribution in the spatial domain that is characteristic of quasi-(dis)order in nature [16, 17, 20]. The average short-range isotropic periodicity in this case is 318±45 nm. Additionally, the second inset in Fig. 1c shows a high-magnification SEM image of a single MIM structure confirming the sub-10 nm hotspot. Additionally, we have verified the existence of the sub-10 nm gap in our prior work [24]. Figure 6.1d shows a distribution of MIM structure diameters which can be estimated by a Gaussian profile fit with a mean and standard deviation (SD) of 101±49 nm.

6.3 Single MIM structure simulation

The aforementioned dimensions were chosen through rigorous finite-difference time-domain (FDTD) simulations. First, as shown in Figure 6.3a, a single MIM structure with a 5 nm insulator gap was simulated to obtain the extinction profile and electric-field distribution. The plasmonic behaviors of the two metal layers (Au nanohole and Au nanodisk) couple with each other leading to strong electric-field confinement at the MIM junction [24]. This effect has been demonstrated for different MIM combinations towards broadband SERS applications [25, 26]. Additionally, we have previously demonstrated the use of similar MIM structures with higher-order plasmonic gap modes towards plasmon-enhanced fluorescent detection of nucleic acids and suppression of fluorescence quenching [24]. A modal analysis reveals that in the Vis-NIR regime, this coupling results in the formation of a dipolar mode polarized along the MIM junction (Figure 6.3b). This in turn produces a very tunable and large extinction cross-section and a corresponding localized $|E|^2$ enhancement. Figure 6.3c presents the maximum normalized $|\frac{E}{E_o}|^2$ enhancement numerically obtained for single MIM structures ranging from 60 – 110 nm in diameter with a 5 nm gap. However, like most ordered plasmonic structures used for SERS, this mode is fairly narrowband.

6.4 Flex-MS ensemble simulation

To quantify the impact of quasi-(dis)ordering on the $|\frac{E}{E_o}|^2$ enhancement, we generated an ensemble of quasi-(dis)ordered MIM structures to simulate their

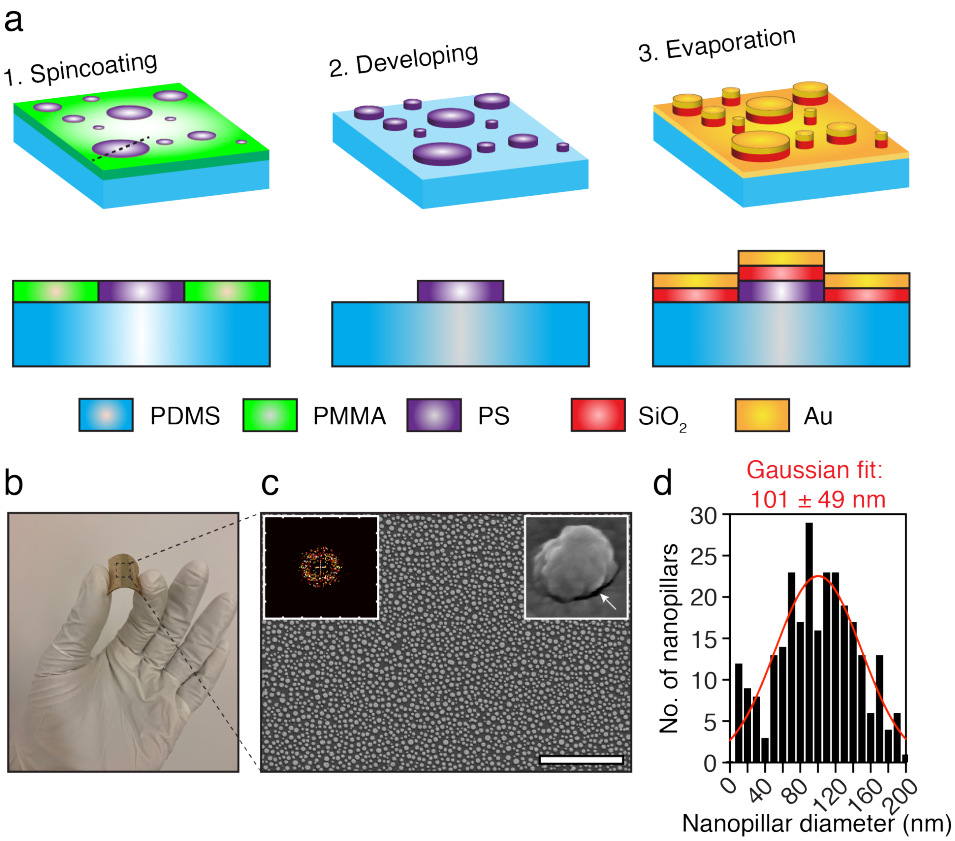

Figure 6.1: Fabrication and characterization of the flex-MS. (a) Simple and scalable three-step fabrication process of the flex-MS. (b) The fabricated flex-MS sample with (c) quasi-(dis)ordered MIM nanostructures. Insets correspond to the 2D FFT taken to determine a short-range periodicity of 318±45 nm (left) and a single MIM nanostructure of diameter 100 nm with the sub-10 nm insulator nanogap indicated by the white arrow (right). Scale bar: 2 μm. (d) MIM structure diameter distribution with a Gaussian mean and SD of 101±49 nm.

optical properties. Two aspects were studied: 1) short-range periodicity (i.e. positional disorder) and 2) diameter distribution (i.e. size disorder). Here, the diameters of the structures were made to obey a Gaussian distribution as with the flex-MS (diameter: 98±30 nm) with short-range periodicity (319±37 nm) (Figure 6.4).

To isolate the individual contributions of 1) and 2), periodic structures (diameter: 100 nm, periodicity: 320 nm) and short-range-ordered structures of the same diameter (diameter: 100 nm) were considered. For the three categories of structures, an insulator gap of 9 nm was chosen to tune the resonance close to the laser wavelength (λ_L = 785 nm) (Figure 6.5). The effective normal-

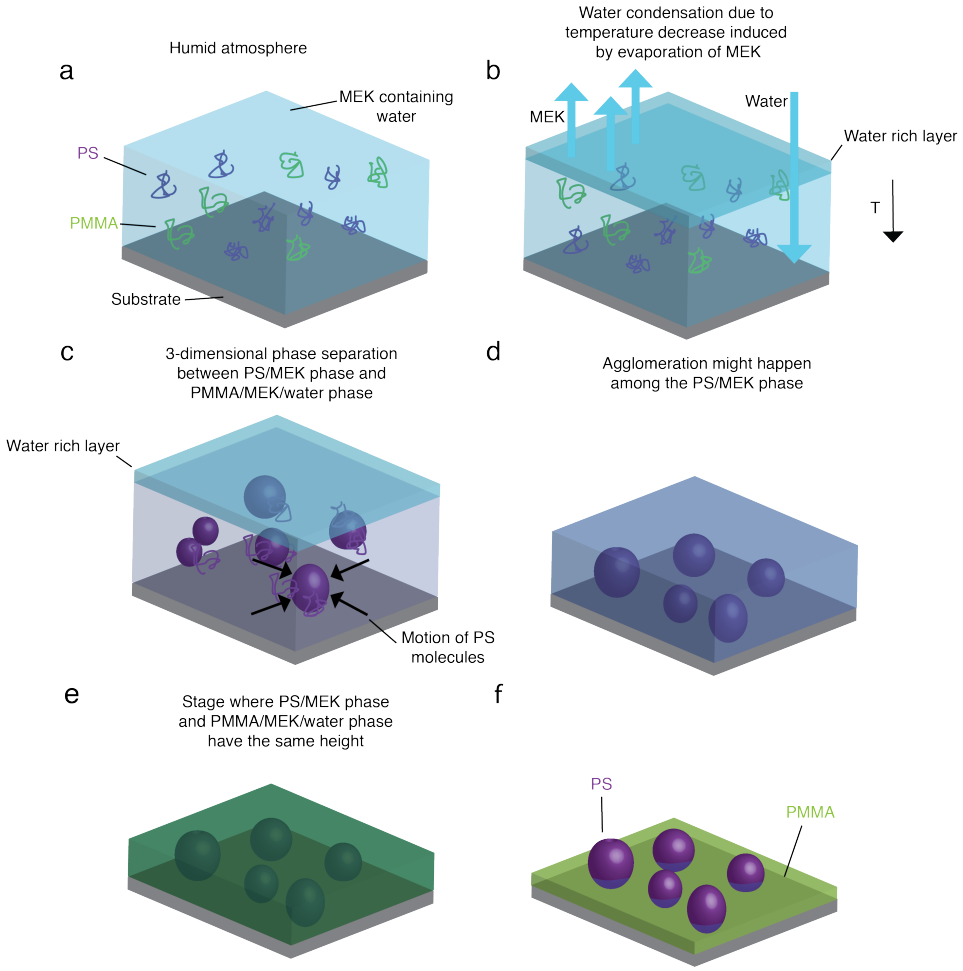

Figure 6.2: Schematic of the different stages of the 3-dimensional phase separation process.

ized $|\frac{E}{E_o}|^2$ enhancement in each case (averaged over 4000 individual hotspots) was computed not only at the laser wavelength (λ_L = 785 nm), but also the Raman-shifted wavelengths of relevance (λ_1, λ_2, and λ_3 = 827 nm, 861 nm, and 902 nm) for this work.

For periodic structures, the resonance profile is predictably governed by the collective out-of-plane resonance of individual MIM structures that dominate any weaker in-plane lattice effects [27]. This is evidenced by the fact that the periodic array resonance position and mode-shape is identical to that of a single MIM structure (diameter: 100 nm, gap: 9 nm) (Figures 6.6 and 6.7a). Next, quasi-(dis)ordered structures with the same diameter (i.e. positional disorder) were studied. The effect of pure positional disorder retains the collective out-of-plane resonance of individual MIM structures marked by the same res-

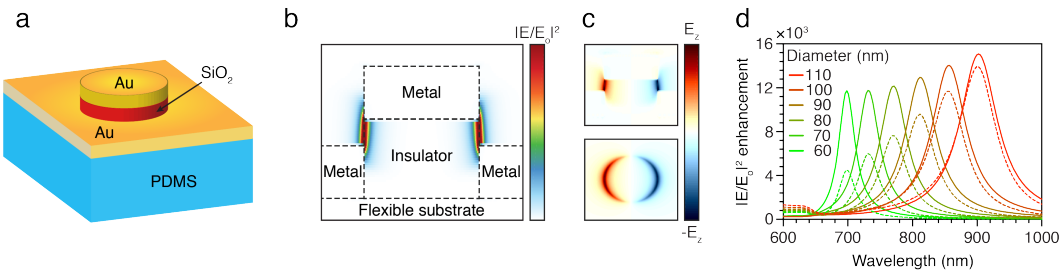

Figure 6.3: Single MIM structure simulations. (a) A schematic of a single MIM nanostructure on the flex-MS platform (b) The coupling of the Au nanodisk and Au nanohole across the SiO_2 nanogap results in greatly enhanced electric-field environments. (c) The field profile of the nanogap shows the presence of a vertically polarized dipolar mode. (d) The normalized maximum theoretical enhancement (solid curves) and extinction cross-section (dotted curves) of a single MIM nanostructure of varying diameter between 60 – 110 nm with a fixed gap size of 5 nm.

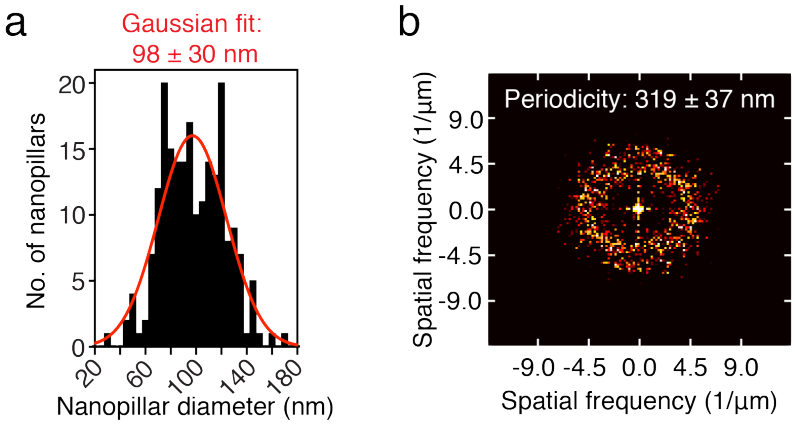

Figure 6.4: An ensemble with (a) diameter distribution of 98±30 nm and (g) a short-range ordered periodicity of 319±37 nm was simulated using FDTD

onance position and intensity as that of the periodic array given the same number of averaged hotspots (Figure 6.7b). In other words, for a periodicity that is large enough to ensure either weak or no coupling between adjacent nanostructures, the effect of short-range order (i.e. pure positional disorder) is negligible [28, 29]. Finally, the introduction of a Gaussian distribution of diameters along with the short-range order (i.e. size and positional disorder) produces a considerably more broadband $|\frac{E}{E_o}|^2$ enhancement compared to the periodic structures as shown in Figure 6.7c due to the resonance of subsets of MIM structures of a given diameter (Figures 6.7d and 6.8) [28]. The bandwidth of the $|\frac{E}{E_o}|^2$ enhancement of size-disordered structures ($\sim$ 219 nm) was

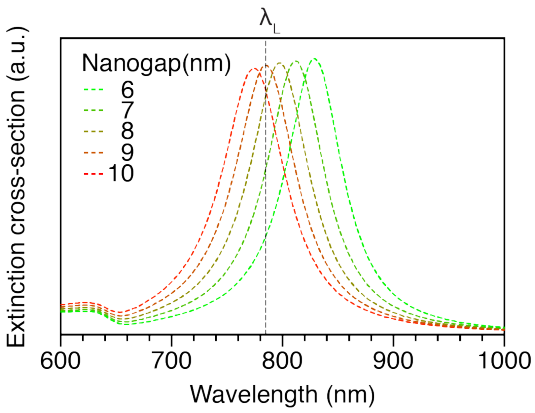

Figure 6.5: Extinction cross-section of a single MIM nanostructure as a function of nanogap size. A gap size of 9 nm is optimally tuned to match the laser wavelength

3.4 times larger than that of the periodic structures ($\sim$ 65 nm). The fractal, yet controllable nature of the MIM ensemble with size and positional disorder produces a broadband $|\frac{E}{E_o}|^2$ enhancement that encompasses λ_L and λ_{1-3}. While the periodic structures and those with pure positional disorder provide a high effective enhancement at λ_L (i.e. $|\frac{E}{E_o}|^2_{\lambda_L}$) of 3358 and 3430, respectively, their enhancements at λ_{1-3} is considerably lower (periodic: $|\frac{E}{E_o}|^2_{\lambda_1} \approx 1210$, $|\frac{E}{E_o}|^2_{\lambda_2} \approx 563$ and $|\frac{E}{E_o}|^2_{\lambda_3} \approx 285$; pure positional disorder: $|\frac{E}{E_o}|^2_{\lambda_1} \approx 1252$, $|\frac{E}{E_o}|^2_{\lambda_2} \approx 585$ and $|\frac{E}{E_o}|^2_{\lambda_3} \approx 292$). In comparison, the introduction of size disorder provides a more uniform enhancement with $|\frac{E}{E_o}|^2_{\lambda_L} \approx 1992$, $|\frac{E}{E_o}|^2_{\lambda_1} \approx 1748$, $|\frac{E}{E_o}|^2_{\lambda_2} \approx 1305$ and $|\frac{E}{E_o}|^2_{\lambda_3} \approx 921$.

The origin of this broadband effect can be of great benefit to SERS. As per the frequently-used $|E|^4$-approximation, SERS enhancement factor (EF) is typically expressed as,

$$EF\left(\omega_L, \mathbf{r_m}\right) = \left|\frac{E_{loc}\left(\omega_L, \mathbf{r_m}\right)}{E_{inc}\left(\omega_L, \mathbf{r_m}\right)}\right|^4 \tag{6.1}$$

where $E_{loc}\left(\omega_L, \mathbf{r_m}\right)$ and $E_{inc}\left(\omega_L, \mathbf{r_m}\right)$ are the localized and incident electric-fields at the laser excitation frequency of ω_L for a Raman dipole at position $\mathbf{r_m}$ [30]. Here, a significant contribution from the radiative enhancement M_{rad} is overlooked in favor of electric-field enhancement M_{loc} [30–33]. M_{rad} measures the enhancement of the power radiated by a dipole in the presence of a plasmonic nanostructure. Factoring in this contribution, the EF can be more precisely expressed as [30],

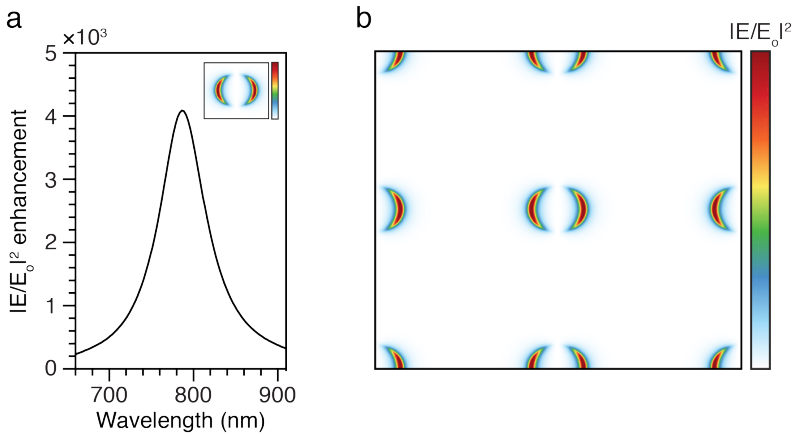

Figure 6.6: Origin of the flex-MS resonance. (a) The $|\frac{E}{E_o}|^2$ enhancement from a single MIM structure of diameter 100 nm and gap 9 nm. Inset shows the field profile of the single MIM structure. (b) The field-profile of a periodic distribution of MIM structures (diameter: 100 nm, gap: 9 nm, periodicity: 320 nm) showing no coupling between adjacent structures.

$$\begin{aligned} EF\left(\omega_L, \omega_R, \mathbf{r_m}\right) &= M_{loc}\left(\omega_L, \mathbf{r_m}\right) M_{rad}\left(\omega_R, \mathbf{r_m}\right) \\ &= \left|\frac{E_{loc}\left(\omega_L, \mathbf{r_m}\right)}{E_{inc}\left(\omega_L, \mathbf{r_m}\right)}\right|^2 \left|\frac{E_{loc}\left(\omega_R, \mathbf{r_m}\right)}{E_{inc}\left(\omega_R, \mathbf{r_m}\right)}\right|^2 \end{aligned} \tag{6.2}$$

where ω_R is the Stokes-shifted Raman scattering frequency. The $|E|^4$-approximation assumes that $\omega_R \approx \omega_L$ and as a result, $M_{\text{loc}} \approx M_{\text{rad}}$. While this approximation is accurate for ω_L in the blue and green regime, it is inaccurate in the red and NIR regime particularly within the fingerprint region (500 – 1500 cm^{-1}) [32, 34]. This is because for a given vibrational mode, the difference between the vibrational and excitation energies becomes more significant for lower energy excitations. In principle, for NIR-based SERS, broadband *EF*s are greatly desirable as they better account for M_{rad} [32]. Based on our ensemble simulations, the effective $EF\left(\omega_L, \omega_{1-3}\right)$ for the periodic structures ($EF\left(\omega_L, \omega_1\right) \approx$ 4.06e+06, $EF\left(\omega_L, \omega_2\right) \approx$ 1.89e+06, and $EF\left(\omega_L, \omega_3\right) \approx$ 0.96e+06) and those with purely positional disorder ($EF\left(\omega_L, \omega_1\right) \approx$ 4.29e+06, $EF\left(\omega_L, \omega_2\right) \approx$ 2.01e+06, and $EF\left(\omega_L, \omega_3\right) \approx$ 1.00e+06) are evidently lower for ω_2 and ω_3 than structures with size and positional disorder ($EF\left(\omega_L, \omega_1\right) \approx$ 3.48e+06, $EF\left(\omega_L, \omega_2\right) \approx$ 2.60e+06, and $EF\left(\omega_L, \omega_3\right) \approx$ 1.84e+06) (Figure 6.7e).

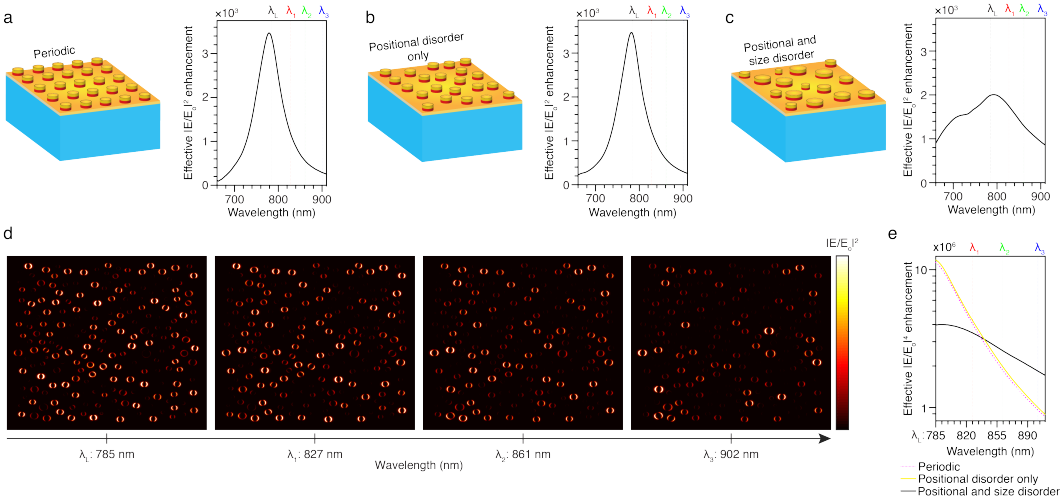

Figure 6.7: An ensemble of (a) periodic MIM nanostructures and (b) those with pure positional disorder demonstrating an identical narrowband effective normalized $|\frac{E}{E_o}|^2$ enhancement profile. (c) The effective normalized $|\frac{E}{E_o}|^2$ enhancement profile of a quasi-(dis)ordered MIM ensemble with both positional and size disorder is broadband compared to (a) and (b). The $|\frac{E}{E_o}|^2$ enhancement profile encompasses the excitation and the Raman-shifted wavelengths (λ_L, λ_1, λ_2 and λ_3) of relevance in this work. (d) The field-map spanning the 3.5 x 3.5 μm array at λ_L, λ_1, λ_2 and λ_3 shows the progressive excitation of first small and then larger MIM nanostructures with increasing wavelength. (e) The effective $|\frac{E}{E_o}|^2$ enhancement from periodic structures, structures with positional disorder only and those with both positional and size disorder. This effective enhancement was numerically computed as $EF\,(\omega_L, \omega_R)$.

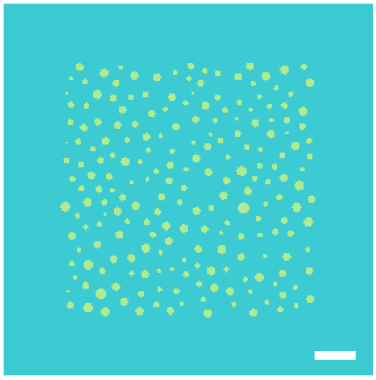

Figure 6.8: The 3.5 x 3.5 μm flex-MS ensemble simulated on FDTD. Scale bar: 600 nm.

6.5 Experimental demonstration of broadband SERS EF

The effect of bioinspired quasi-(dis)order was then experimentally verified by comparing the optical properties of the flex-MS with periodic MIM structures (diameter: 100 nm, periodicity: 320 nm, gap: 9 nm) fabricated via E-beam

lithography. Using a micro-spectroscopic setup in dark-field (DF) mode, the scattering cross-section of the two metasurfaces were measured in the NIR regime. This revealed the considerably more broadband scattering profile of the flex-MS compared to the periodic array (Figure 6.9a). Furthermore, the existence of the 9 nm gap was verified through simulation (Figure 6.10). The SERS performance of the two sets of structures was compared by detecting UA – a SERS-active molecule with prominent peaks at 640 cm^{-1}, 1134 cm^{-1}, and 1645 cm^{-1} which originate from skeletal ring and C–N bond deformations [35]. When excited with a 785 nm laser, these peaks appear at 827 nm, 861 nm, and 902 nm, respectively (i.e. $\omega_L \neq \omega_R$). For the same UA concentration in DI water (150 μM) and three different laser powers (0.32 mW, 0.62 mW, and 1.12 mW), the three peaks under consideration were uniformly enhanced by the flex-MS compared to the periodic MIM structures (Figures 6.9b and c). The 640 cm^{-1} peak was enhanced more significantly by the periodic structures compared to the flex-MS as this peak lies closest to ω_L where the sharp plasmonic resonance of the former is tuned. However, 1134 cm^{-1} and 1645 cm^{-1} peaks that were located further away from ω_L were enhanced more significantly by the flex-MS due to its broadband enhancement profile. This property is particularly useful for sensing with low power. In our case for instance, when using a power of 0.32 mW, the 1134 cm^{-1} and 1645 cm^{-1} peaks were enhanced 3.1- and 5.7-fold by the flex-MS compared to the periodic structures. Finally, the background suppression property of the flex-MS was also verified through comparative experimentation (Figure 6.11).

6.6 Broadband SERS-based biosensing

Finally, the broadband enhancement of the flex-MS platform was used to detect various concentrations of UA. Hyperuricemia (i.e. elevated levels of blood UA) has been identified as a biomarker of various diseases such as gout or gouty arthritis [36], diabetes [37], Parkinson's disease [38], renal disease [39], and cardiovascular disease [40], to name a few. While continual monitoring of UA in blood is hindered by the invasive nature of blood collection and sampling, human tears which are considerably less invasive to assay thereby proving to be an interesting alternative [41]. Tears are also far less complex in constituents compared to blood and have large average concentrations of UA (68$\pm$46 μM) [10]. Furthermore, a clear correlation between blood and tear UA levels has been established [10]. As a result, assaying tear UA levels non-

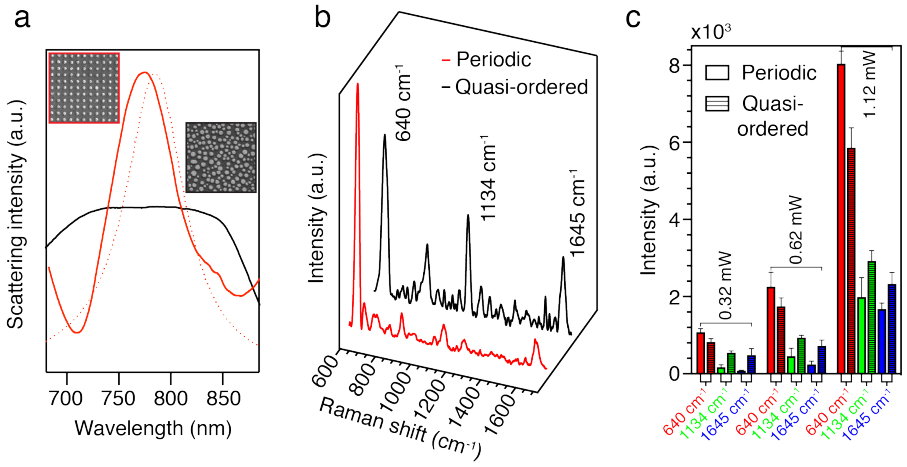

Figure 6.9: Experimental demonstration of broadband SERS *EF*. (a) Scattering intensity of the fabricated periodic and quasi-(dis)ordered array shown as solid lines measured using a micro-spectroscopic setup operating in DF mode. The simulated scattering profile of a single MIM structure (gap: 9 nm) which most closely matches the experimental result is also shown as a dotted line. The SEM images of the corresponding structures are shown in the inset. (b) SERS spectra of UA measured at 0.62 mW laser power. While the periodic MIM array enhances the 640 cm^{-1} peak considerably, the flex-MS offers a more broadband enhancement of all three peaks (c) The same analysis is performed for various laser powers.

invasively and in a label-free fashion via flexible SERS holds great promise. Using the flex-MS, we first tracked the 640 cm^{-1}, 1134 cm^{-1}, and 1645 cm^{-1} peaks for UA concentrations ranging from 25 – 150 μM in phosphate-buffered saline (PBS) (Figures 6.12a-c). Next, to better simulate the SERS profile of UA in whole tears, we prepared various concentrations of UA between 25 – 150 μM in an artificial tear buffer which consisted of various prominent tear proteins such as lysozyme, lactoferrin, albumin, and immunoglobulins, as well as electrolytes that maintain tear osmolarity such as Na^+, K^+, Cl^+, and HCO_3^- (see Methods Section 6.8: Artificial tear buffer preparation for additional details). As a practical demonstration of broadband SERS enhancement, the 640 cm^{-1}, 1134 cm^{-1}, and 1645 cm^{-1} peaks were tracked with excellent linearity being observed as shown in Figure 6.12d. These measurements from an artificial tear buffer were used as a characteristic curve to map measurements taken for whole tears. Finally, we analyzed the performance of the flex-MS towards the detection of UA levels in whole tears. Here, we tested pooled tears from eight different samples obtained from healthy subjects. As a comparison, the

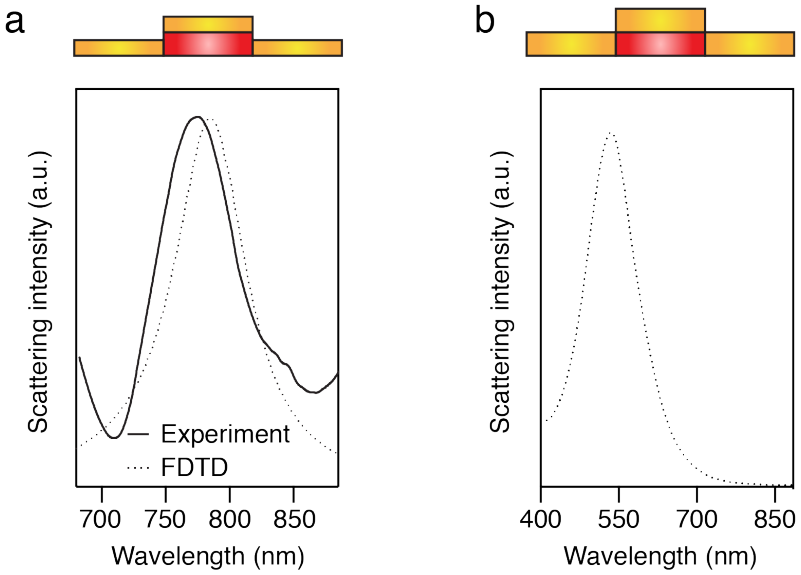

Figure 6.10: Verification of the sub-10 nm gap. (a) MIM structures with an open 9 nm gap where the experimentally observed scattering cross-section is in agreement with that computed through FDTD. The scattering peak is tuned close to the laser excitation wavelength λ_L of 785 nm. (b) The same structures with a covered nanogap demonstrating a resonance in the visible regime.

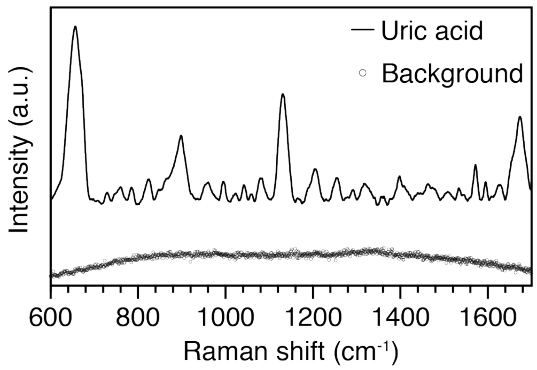

Figure 6.11: Effective suppression of background signal from the underlying polymer substrate by the flex-MS. In comparison, the SERS spectra of 150 μM uric acid on the flex-MS is shown.

same measurement was made using a commercial colorimetric enzyme-based assay. The average concentration from the flex-MS for the 640 $^{-1}$, 1134 $^{-1}$, and 1645 $^{-1}$ peaks (66 μM, 67 μM, and 67 μM, respectively) was in good agreement with that from the enzyme-based assay (76 μM) which demonstrates the potential of the flex-MS as an effective label-free SERS diagnostic platform (Figure 6.12e).

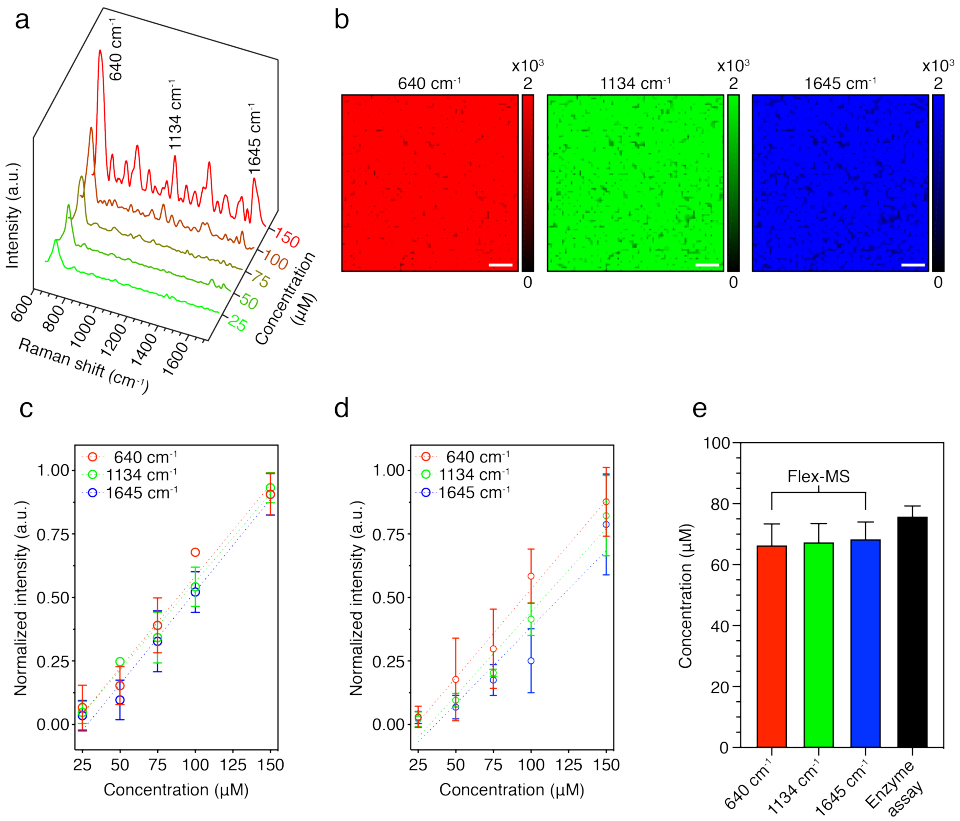

Figure 6.12: Practical biosensing using the flex-MS. (a) Peaks of UA at 640 cm^{-1}, 1134 cm^{-1}, and 1645 cm^{-1} tracked between 25 – 150 μM in PBS. (b) SERS surface mapping (UA concentration: 150 μM) over a 150 x 150 μm area at 640 cm^{-1}, 1134 cm^{-1}, and 1645 cm^{-1} showing spatial uniformity. Scale bars: 20 μm. (c) Normalized intensity of each peak shows excellent linearity. (d) The 640 cm^{-1}, 1134 cm^{-1}, and 1645 cm^{-1} peaks tracked between 25 – 150 μM in artificial tear buffer. (e) The SERS performance of the flex-MS using all three peaks is compared for pooled whole tears consisting of 8 individual tear samples with a commercial enzyme-based assay. The two results are in good agreement.

6.7 Conclusion

In summary, using a simple biomimetic fabrication process, we have developed a cost-effective, scalable and flexible plasmonic metasurface-based platform for label-free SERS. The flex-MS consists of a dense ensemble of closely-coupled Au nanodisks and Au nanoholes separated by sub-10 nm SiO_2 nanogaps in an MIM arrangement all on flexible PDMS thin films. The MIM provides a very tunable and large extinction cross-section and a corresponding localized $|E|^2$ enhancement. When considering an ensemble of such MIM structures exhibiting controlled disorder, the resonance profile of the entire system be-

comes broadband, thereby enabling the uniform enhancement of not just the excitation wavelength (λ_L), but also large Stokes-shifted Raman scattering wavelengths ($\lambda_R \neq \lambda L$). Finally, using flex-MS as a broadband diagnostic platform, we demonstrate the label-free detection of UA in both artificial tear buffer as well as whole human tear samples. Additionally, we compare the performance of the flex-MS with a commercial UA measurement assay and show that they are in good agreement. As a result, we envisage that through broadband SERS enhancement, the flex-MS can prove to be a reliable and scalable label-free diagnostic platform for a variety of SERS-active molecules.

6.8 Materials and methods

Biomimetic flex-MS fabrication

First, a 400 μm-thick PDMS layer (Sylgard 184 elastomer base mixed with curing agent in a ratio of 10:1, Dow Chemical Co., USA) was spin-coated on a 4 inch Si wafer and cured at 65^{o}C for 12 hours. Next, poly(methyl methacrylate) (PMMA, $M_w = 5090$, Polymer Standards Service GmbH, Germany) and polystyrene (PS, $M_w = 3250$, Polymer Standards Service GmbH, Germany) were co-dissolved in methyl ethyl ketone (MEK, Sigma-Aldrich, USA) with mass ratios of 70%:30%. The solution concentrations were 20 mg mL^{-1}. After exposing the PDMS substrate to O_2 plasma for 5 mins, the polymer blend solutions were spin-coated at a spin-speed of 3500 rpm and acceleration of 2000 rpm s^{-1} for 30 s. Relative humidity was maintained between 40–50% during the spin-coating. As shown in Figure 6.2, the de-mixing of the blend components occurs during spin-coating due to the difference in relative solubility of PS and PMMA in MEK. First, water condensation begins at humidity levels above 35% forming a water-rich layer at the air/solution interface due to the difference in evaporation rate between water and MEK. Water starts to condense from the air into the solution because of the evaporation of MEK decreasing the temperature on the top below the dew point. Due to the high water concentration, a 3D phase separation occurs between PS/MEK and PMMA/MEK/water. Upon drying, a purely lateral morphology was formed with ellipsoidal PS islands in a PMMA matrix. The samples were then rinsed in acetic acid for 60 s and dried in a stream of N_2 to remove the PMMA matrix leaving behind the PS islands. The resulting PS nanopillar mask then served as a template for the E-beam evaporation of a 100$\pm$0.5 nm-thick SiO_2 layer (CHA MK40 E-Beam Evaporation, CHA Industries, USA). Next, a 91$\pm$1.1

nm-thick Au layer was deposited (CHA MK40 E-Beam Evaporation, CHA Industries, USA) over the SiO_2 to generate the MIM layer with $\approx 9\pm1.6$ nm gap. Finally, the PDMS film was peeled off the Si wafer and served as a SERS substrate for biosensing experiments.

Periodic MIM array fabrication

PMMA950 A4 (MicroChem, USA) E-beam resist was spin-coated at 1500 rpm for 60 s onto an Si substrate cleaned with acetone and isopropyl alcohol prior to spin-coating. The sample was then exposed at a dosage of 800 μC cm^{-2} (Raith EBPG 5200, Raith Nanofabrication, Germany). Following exposure, development was carried out using a 1:1 ratio of IPA:MIBK for 1 min. Next, SiO_2 was directionally deposited via E-beam evaporation (CHA MK40 E-Beam Evaporation, CHA Industries, USA) after which lift-off was performed in Remover PG leaving behind SiO_2 nanopillars. Finally, Au of an appropriate thickness was deposited (CHA MK40 E-Beam Evaporation, CHA Industries, USA) over the SiO_2 to generate the MIM layer.

High-resolution imaging and statistical analyses of the flex-MS

SEM imaging was performed on the flex-MS using a Nova 200 Novalab Dual-beam microscope (FEI, USA) at 10 kV. ImageJ (National Institutes of Health, USA), a Java-based public-domain image processing tool was used to obtain the diameter distribution of the nanostructures. Every pixel in the acquired SEM images were converted to black or white based on a thresholding condition that was obtained by calculating the mean intensity value of all pixels of the image. Following this, the diameter distribution of the MIM scatterers was determined. Finally, the FFT analysis to determine short-range periodicity was performed using MATLAB (MathWorks, USA).

Optical simulations of the flex-MS

Optical simulations of a single MIM nanostructure as well as the quasi-ordered/-periodic ensemble as a whole were performed using a 3D finite-difference time-domain software (Lumerical Solutions, Canada). A combination of periodic and perfect matching layer (PML) boundary conditions along with a plane wave source was used. The absorption cross section was obtained in the total field region inside the source while the scattering cross-section was obtained in the scattered field region outside the source. The influence of the nanogap was

studied as shown in Figure 6.10. The $|\frac{E}{E_o}|^2$ enhancement was obtained by placing a frequency-domain field monitor at the MIM junction spanning the entire MIM nanostructure or the ensemble, respectively. The field-maps as well as the effective $|\frac{E}{E_o}|^2$ enhancement (averaged over 4000 individual hotspots or mesh cells) in the case of the ensemble were calculated using MATLAB (MathWorks, USA).

Spectroscopic analyses

An optical microscope operating in dark-field (DF) mode was used for the micro-spectroscopic investigation of the fabricated flex-MS and periodic MIM array samples. A halogen lamp was used as a light source using a 50x objective. The scattered light was collected in a confocal configuration and analyzed using a spectrometer (AvaSpec-ULS2048x64-USB2). A 400 μm core optical fiber was used to obtain a spatial resolution of 20 μm to characterize the scattering of the samples.

SERS measurements

All SERS measurements were performed by incubating a 30 μL droplet of reagent on the flex-MS for 30 min. Following this, the drop was dislodged from the sample surface using a stream of N_2. The sample was then measured dry using a Raman microscope (inVia, Renishaw, United Kingdom) with a 50x objective lens. A 785 nm laser operated at 0.32, 0.62, or 1.12 mW for a duration of 60 s was used to take the measurements.

Artificial tear buffer preparation

Artificial tear buffer was prepared using previously reported methods [10, 42]. Briefly, electrolytes K^+, HCO_3^-, Na^+, and Cl^- were added to DI water at concentrations of 24 mM, 24 mM, 130 mM, and 130 mM, respectively. Following this, representative tear proteins such as lysozyme, lactoferrin, albumin, and IgG were added at concentrations of 2 mg mL^{-1}, 2 mg mL^{-1}, 0.02 mg mL^{-1} and 3 μg mL^{-1}, respectively.

Whole tear assay

Eight individual tear samples were collected from healthy subjects and pooled for the experiment. For a comparative study, a commercial enzyme-based colorimetric uric acid detection kit (Sigma-Aldrich, USA) was used. The assay was performed following the manufacturer's protocol.

References

[1] Shuming Nie and Steven R. Emory. Probing single molecules and single nanoparticles by surface-enhanced Raman scattering. *Science*, 275(5303): 1102–1106, 1997. ISSN 0036-8075. doi: 10.1126/science.275.5303.1102.

[2] Bhavya Sharma, Renee R. Frontiera, Anne-Isabelle Henry, Emilie Ringe, and Richard P. Van Duyne. SERS: Materials, applications, and the future. *Materials Today*, 15(1):16 – 25, 2012. ISSN 1369-7021. doi: https://doi.org/10.1016/S1369-7021(12)70017-2.

[3] Judith Langer, Dorleta Jimenez de Aberasturi, Javier Aizpurua, Ramon A. Alvarez-Puebla, Baptiste Auguié, Jeremy J. Baumberg, Guillermo C. Bazan, Steven E. J. Bell, Anja Boisen, Alexandre G. Brolo, Jaebum Choo, Dana Cialla-May, Volker Deckert, Laura Fabris, Karen Faulds, F. Javier García de Abajo, Royston Goodacre, Duncan Graham, Amanda J. Haes, Christy L. Haynes, Christian Huck, Tamitake Itoh, Mikael Käll, Janina Kneipp, Nicholas A. Kotov, Hua Kuang, Eric C. Le Ru, Hiang Kwee Lee, Jian-Feng Li, Xing Yi Ling, Stefan A. Maier, Thomas Mayerhöfer, Martin Moskovits, Kei Murakoshi, Jwa-Min Nam, Shuming Nie, Yukihiro Ozaki, Isabel Pastoriza-Santos, Jorge Perez-Juste, Juergen Popp, Annemarie Pucci, Stephanie Reich, Bin Ren, George C. Schatz, Timur Shegai, Sebastian Schlücker, Li-Lin Tay, K. George Thomas, Zhong-Qun Tian, Richard P. Van Duyne, Tuan Vo-Dinh, Yue Wang, Katherine A. Willets, Chuanlai Xu, Hongxing Xu, Yikai Xu, Yuko S. Yamamoto, Bing Zhao, and Luis M. Liz-Marzán. Present and future of surface-enhanced Raman scattering. *ACS Nano*, 14(1):28–117, 01 2020. doi: 10.1021/acsnano.9b04224.

[4] Kaichen Xu, Zuyong Wang, Chuan Fu Tan, Ning Kang, Lianwei Chen, Lei Ren, Eng San Thian, Ghim Wei Ho, Rong Ji, and Minghui Hong. Uniaxially stretched flexible surface plasmon resonance film for versatile surface enhanced Raman scattering diagnostics. *ACS Applied Materials & Interfaces*, 9(31):26341–26349, 08 2017. doi: 10.1021/acsami.7b06669.

[5] Hao Cui, Shuoyu Li, Shaozhi Deng, Huanjun Chen, and Chengxin Wang. Flexible, transparent, and free-standing silicon nanowire SERS platform for in situ food inspection. *ACS Sensors*, 2(3):386–393, 03 2017. doi: 10.1021/acssensors.6b00712.

[6] Kaichen Xu, Rui Zhou, Kuniharu Takei, and Minghui Hong. Toward flexible surface-enhanced Raman scattering (SERS) sensors for point-of-care diagnostics. *Advanced Science*, 6(16):1900925, 2019. doi: 10.1002/advs.201900925.

[7] Hyelim Kang, Chul-Joon Heo, Hwan Chul Jeon, Su Yeon Lee, and Seung-Man Yang. Durable plasmonic cap arrays on flexible substrate with real-

time optical tunability for high-fidelity SERS devices. *ACS Applied Materials & Interfaces*, 5(11):4569–4574, 06 2013. doi: 10.1021/am400019v.

[8] Jae Won Jeong, Se Ryeun Yang, Yoon Hyung Hur, Seong Wan Kim, Kwang Min Baek, Soonmin Yim, Hyun-Ik Jang, Jae Hong Park, Seung Yong Lee, Chong-Ook Park, and Yeon Sik Jung. High-resolution nanotransfer printing applicable to diverse surfaces via interface-targeted adhesion switching. *Nature Communications*, 5(1):5387, 2014. doi: 10.1038/ncomms6387.

[9] Limei Tian, Qisheng Jiang, Keng-Ku Liu, Jingyi Luan, Rajesh R. Naik, and Srikanth Singamaneni. Bacterial nanocellulose-based flexible surface enhanced Raman scattering substrate. *Advanced Materials Interfaces*, 3 (15):1600214, 2016. doi: 10.1002/admi.201600214.

[10] Moonseong Park, Hyukjin Jung, Yong Jeong, and Ki-Hun Jeong. Plasmonic Schirmer strip for human tear-based gouty arthritis diagnosis using surface-enhanced Raman scattering. *ACS Nano*, 11(1):438–443, 01 2017. doi: 10.1021/acsnano.6b06196.

[11] Gabriele C. Messina, Mario Malerba, Pierfrancesco Zilio, Ermanno Miele, Michele Dipalo, Lorenzo Ferrara, and Francesco De Angelis. Hollow plasmonic antennas for broadband SERS spectroscopy. *Beilstein Journal of Nanotechnology*, 6:492–498, 2015. ISSN 2190-4286. doi: 10.3762/bjnano.6.50.

[12] Mengqiu Li, Jian Xu, Maria Romero-Gonzalez, Steve A Banwart, and Wei E Huang. Single cell Raman spectroscopy for cell sorting and imaging. *Current Opinion in Biotechnology*, 23(1):56 – 63, 2012. ISSN 0958-1669. doi: https://doi.org/10.1016/j.copbio.2011.11.019.

[13] Francesco De Angelis, Mario Malerba, Maddalena Patrini, Ermanno Miele, Gobind Das, Andrea Toma, Remo Proietti Zaccaria, and Enzo Di Fabrizio. 3D hollow nanostructures as building blocks for multifunctional plasmonics. *Nano Letters*, 13(8):3553–3558, 08 2013. doi: 10.1021/nl401100x.

[14] Xiu-Mei Lin, Yan Cui, Yan-Hui Xu, Bin Ren, and Zhong-Qun Tian. Surface-enhanced Raman spectroscopy: Substrate-related issues. *Analytical and Bioanalytical Chemistry*, 394(7):1729–1745, Aug 2009. ISSN 1618-2650. doi: 10.1007/s00216-009-2761-5.

[15] Liping Wu, Wanlin Wang, Wang Zhang, Huilan Su, Qinglei Liu, Jiajun Gu, Tao Deng, and Di Zhang. Highly sensitive, reproducible and uniform SERS substrates with a high density of three-dimensionally distributed hotspots: Gyroid-structured Au periodic metallic materials. *NPG Asia Materials*, 10(1):e462–e462, 2018. doi: 10.1038/am.2017.230.

[16] Villads Egede Johansen, Olimpia Domitilla Onelli, Lisa Maria Steiner, and Silvia Vignolini. *Photonics in Nature: From Order to Disorder*, pages 53–89. Springer International Publishing, Cham, 2017. ISBN 978-3-319-74144-4. doi: 10.1007/978-3-319-74144-4_3.

[17] Mathias Kolle and Seungwoo Lee. Progress and opportunities in soft photonics and biologically inspired optics. *Advanced Materials*, 30(2): 1702669, 2018. doi: 10.1002/adma.201702669.

[18] Diederik S. Wiersma. Disordered photonics. *Nature Photonics*, 7(3):188–196, 2013. doi: 10.1038/nphoton.2013.29.

[19] Marian Florescu, Salvatore Torquato, and Paul J. Steinhardt. Designer disordered materials with large, complete photonic band gaps. *Proceedings of the National Academy of Sciences*, 106(49):20658–20663, 2009. ISSN 0027-8424. doi: 10.1073/pnas.0907744106.

[20] Vinayak Narasimhan, Radwanul Hasan Siddique, Jeong Oen Lee, Shailabh Kumar, Blaise Ndjamen, Juan Du, Natalie Hong, David Sretavan, and Hyuck Choo. Multifunctional biophotonic nanostructures inspired by the longtail glasswing butterfly for medical devices. *Nature Nanotechnology*, 13(6):512–519, 2018. doi: 10.1038/s41565-018-0111-5.

[21] Radwanul H. Siddique, Yidenekachew J. Donie, Guillaume Gomard, Sisir Yalamanchili, Tsvetelina Merdzhanova, Uli Lemmer, and Hendrik Hölscher. Bioinspired phase-separated disordered nanostructures for thin photovoltaic absorbers. *Science Advances*, 3(10), 2017. doi: 10.1126/sciadv.1700232.

[22] Vinodkumar Saranathan, Ainsley E. Seago, Alec Sandy, Suresh Narayanan, Simon G. J. Mochrie, Eric R. Dufresne, Hui Cao, Chinedum O. Osuji, and Richard O. Prum. Structural diversity of arthropod biophotonic nanostructures spans amphiphilic phase-space. *Nano Letters*, 15(6):3735–3742, 06 2015. doi: 10.1021/acs.nanolett.5b00201.

[23] Radwanul Hasan Siddique, Shailabh Kumar, Vinayak Narasimhan, Hyounghan Kwon, and Hyuck Choo. Aluminum metasurface with hybrid multipolar plasmons for 1000-fold broadband visible fluorescence enhancement and multiplexed biosensing. *ACS Nano*, 13(12):13775–13783, 12 2019. doi: 10.1021/acsnano.9b02926.

[24] Vinayak Narasimhan, Radwanul Hasan Siddique, Magnus Hoffmann, Shailabh Kumar, and Hyuck Choo. Enhanced broadband fluorescence detection of nucleic acids using multipolar gap-plasmons on biomimetic Au metasurfaces. *Nanoscale*, 11:13750–13757, 2019. doi: 10.1039/C9NR03178B.

[25] Yang Yang, Zhipeng Hu, Yin Wang, Baoju Wang, Qiuqiang Zhan, Yuan Zhang, and Xianyu Ao. Broadband SERS substrates by oblique angle deposition method. *Optical Materials Express*, 6(8):2644–2654, Aug 2016. doi: 10.1364/OME.6.002644. URL `http://www.osapublishing.org/ome/abstract.cfm?URI=ome-6-8-2644`.

[26] Dongxing Wang, Wenqi Zhu, Michael D. Best, Jon P. Camden, and Kenneth B. Crozier. Wafer-scale metasurface for total power absorption, local field enhancement and single molecule Raman spectroscopy. *Scientific Reports*, 3(1):2867, 2013. doi: 10.1038/srep02867. URL `https://doi.org/10.1038/srep02867`.

[27] V. G. Kravets, A. V. Kabashin, W. L. Barnes, and A. N. Grigorenko. Plasmonic surface lattice resonances: A review of properties and applications. *Chemical Reviews*, 118(12):5912–5951, 06 2018. doi: 10.1021/acs.chemrev.8b00243.

[28] Baptiste Auguié and William L. Barnes. Diffractive coupling in gold nanoparticle arrays and the effect of disorder. *Opt. Lett.*, 34(4):401–403, Feb 2009. doi: 10.1364/OL.34.000401.

[29] Herve Bertin, Yoann Brûlé, Giovanni Magno, Thomas Lopez, Philippe Gogol, Laetitia Pradere, Boris Gralak, David Barat, Guillaume Demésy, and Beatrice Dagens. Correlated disordered plasmonic nanostructures arrays for augmented reality. *ACS Photonics*, 5(7):2661–2668, 07 2018. doi: 10.1021/acsphotonics.8b00168.

[30] Song-Yuan Ding, En-Ming You, Zhong-Qun Tian, and Martin Moskovits. Electromagnetic theories of surface-enhanced Raman spectroscopy. *Chem. Soc. Rev.*, 46:4042–4076, 2017. doi: 10.1039/C7CS00238F.

[31] Eric C. Le Ru and Pablo G. Etchegoin. *SERS enhancement factors and related topics*, pages 185 – 264. Elsevier, Amsterdam, 2009. ISBN 978-0-444-52779-0. doi: https://doi.org/10.1016/B978-0-444-52779-0.00010-6.

[32] Paul L. Stiles, Jon A. Dieringer, Nilam C. Shah, and Richard P. Van Duyne. Surface-enhanced Raman spectroscopy. *Annual Review of Analytical Chemistry*, 1(1):601–626, 2008. doi: 10.1146/annurev.anchem.1.031207.112814. PMID: 20636091.

[33] Adam D. McFarland, Matthew A. Young, Jon A. Dieringer, and Richard P. Van Duyne. Wavelength-scanned surface-enhanced Raman excitation spectroscopy. *The Journal of Physical Chemistry B*, 109(22):11279–11285, 06 2005. doi: 10.1021/jp050508u.

[34] Sebastian Schlücker. Surface-enhanced Raman spectroscopy: Concepts and chemical applications. *Angewandte Chemie International Edition*, 53(19):4756–4795, 2014. doi: 10.1002/anie.201205748.

[35] Chloe Westley, Yun Xu, Baskaran Thilaganathan, Andrew J. Carnell, Nicholas J. Turner, and Royston Goodacre. Absolute quantification of uric acid in human urine using surface enhanced Raman scattering with the standard addition method. *Analytical Chemistry*, 89(4):2472–2477, 02 2017. doi: 10.1021/acs.analchem.6b04588.

[36] Anthony M. Reginato, David B. Mount, Irene Yang, and Hyon K. Choi. The genetics of hyperuricaemia and gout. *Nature Reviews Rheumatology*, 8(10):610–621, 2012. doi: 10.1038/nrrheum.2012.144.

[37] Vidula Bhole, Jee Woong J. Choi, Sung Woo Kim, Mary de Vera, and Hyon Choi. Serum uric acid levels and the risk of type 2 diabetes: A prospective study. *The American Journal of Medicine*, 123(10):957 – 961, 2010. ISSN 0002-9343. doi: https://doi.org/10.1016/j.amjmed.2010.03.027.

[38] Min Wen, Bo Zhou, Yun-Hua Chen, Zhao-Lei Ma, Yun Gou, Chun-Lin Zhang, Wen-Feng Yu, and Ling Jiao. Serum uric acid levels in patients with Parkinson's disease: A meta-analysis. *PLOS ONE*, 12(3):1–13, 03 2017. doi: 10.1371/journal.pone.0173731.

[39] Kentaro Kohagura, Masako Kochi, Tsuyoshi Miyagi, Takanori Kinjyo, Yuichi Maehara, Kazufumi Nagahama, Atsushi Sakima, Kunitoshi Iseki, and Yusuke Ohya. An association between uric acid levels and renal arteriolopathy in chronic kidney disease: A biopsy-based study. *Hypertension Research*, 36(1):43–49, 2013. doi: 10.1038/hr.2012.135.

[40] Daniel I. Feig, Duk-Hee Kang, and Richard J. Johnson. Uric acid and cardiovascular risk. *New England Journal of Medicine*, 359(17):1811–1821, 2008. doi: 10.1056/NEJMra0800885. PMID: 18946066.

[41] Suzanne Hagan, Eilidh Martin, and Amalia Enríquez-de Salamanca. Tear fluid biomarkers in ocular and systemic disease: Potential use for predictive, preventive and personalised medicine. *The EPMA journal*, 7(1): 15–15, 07 2016. doi: 10.1186/s13167-016-0065-3.

[42] Heidi R. Culver, Marissa E. Wechsler, and Nicholas A. Peppas. Label-free detection of tear biomarkers using hydrogel-coated gold nanoshells in a localized surface plasmon resonance-based biosensor. *ACS Nano*, 12(9): 9342–9354, 09 2018. doi: 10.1021/acsnano.8b04348.

Chapter 7

CONCLUSION AND FUTURE DIRECTION

This thesis documents various examples of the effective utilization of multifunctional nanostructures inspired by biophotonic counterparts for medical applications. More specifically, the first half of the work is dedicated towards multifunctional bioinspired nanostructures for an implantable technology while the second half discusses their use in plasmonic biosensing.

7.1 Bioinspired nanostructures for optical implants

Chapters 2 – 4 describe a highly-miniaturized MEMS-based passive intraocular pressure (IOP) sensor implant along with various issues faced during implant design and *in vivo* implementation. These issues pertain to optical stability and background bias generation, novel detector integration, and biocompatibility. Through the incorporation of multifunctional bioinspired nanostructures to different aspects of the sensor's layout, the aforementioned issues are mitigated. In Chapter 3, the integration of black-silicon (b-Si) nanostructures inspired by light-trapping flower petal epidermal micro-/nanostructures onto the IOP sensor platform is covered. These nanostructures produce an absolute NIR reflectivity as low as 3.5%, improving the optical signal-to-noise ratio (SNR) of the device resulting in a 3.4-fold reduction in IOP readout error measured on bench. This enables *in vivo* monitoring of IOP using a slit-lamp (a ubiquitous ophthalmic microscope) as a detector at a large readout distance of 12 cm thereby increasing the clinical viability of this technology. Furthermore, through confocal immunofluorescence microscopy, the integration of the b-Si nanostrutures is shown to greatly improve sensor biocompatibility after 6 months. Figure 7.1 presents an illustrative summary of Chapter 3.

Next, in Chapter 4, nanostructures inspired by the omnidirectional light-scattering nanostructures on *Chorinea faunus* butterfly wings are integrated onto the freestanding silicon nitride (Si_3N_4) membrane of the IOP sensor. These nanostructures improve the optical acceptance angle of the sensor by 3-fold on bench. Furthermore, they reduce the angle-dependent IOP error of the device from 4.59 mmHg to 0.07 mmHg at an oblique incident angle of 12°. In various *in vitro* tests, the nanostructures inhibit the adhesion and prolif-

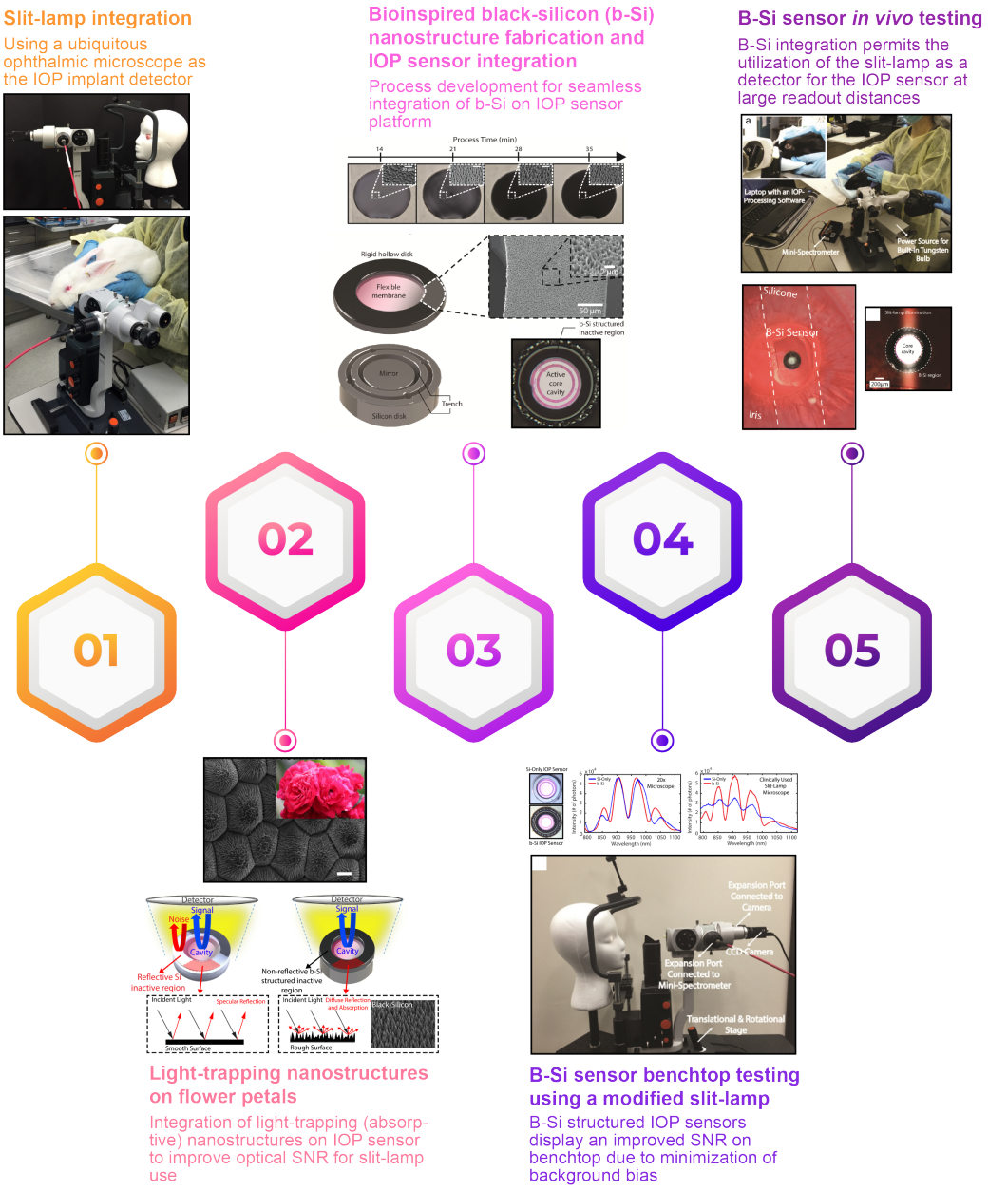

Figure 7.1: Illustrative summary of Chapter 3.

eration of representative proteins, bacteria and eukaryotic cells. Finally, in a month-long successful *in vivo* study, they improve the optical stability of the sensor by lowering the IOP error by 3-fold compared to the previous generation of devices. This enables the use of a custom-built portable hand-held IOP detector paving the way for future point-of-care self-monitoring applications. After the study, the harvested sensor when examined through confocal immunofluorescence microscopy, demonstrated considerable improvement in

biocompatibility over the previous generation of devices. Figure 7.2 presents an illustrative summary of Chapter 4.

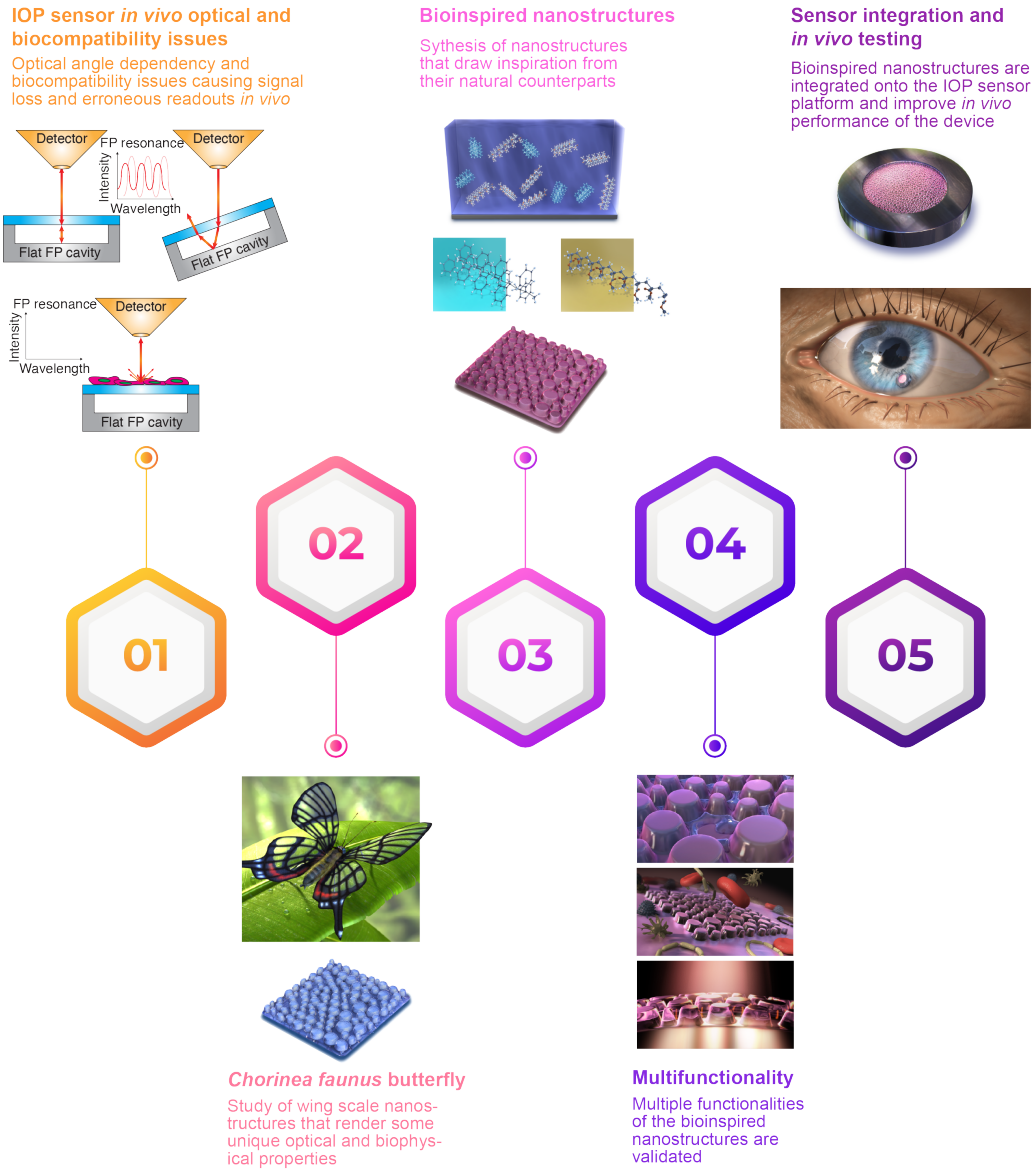

Figure 7.2: Illustrative summary of Chapter 4.

7.2 Bioinspired nanostructures for plasmonic biosensors

Chapters 5 and 6 describe the development of bioinspired metal-insulator-metal (MIM) metasurfaces for two different plasmonic biosensing applications – plasmon-enhanced fluorescence and surface-enhanced Raman spectroscopy (SERS), respectively. In both cases, the metasurface is fabricated through a simple and highly scalable biomimetic fabrication process. In Chapter 5,

the higher-order quadrupolar mode of MIM metasurface (MIM-MS) exhibits strong broadband resonance in the visible-near-infrared regime with minimal absorptive losses. Furthermore, it effectively suppresses quenching, making it highly suitable for broadband plasmon-enhanced fluorescence. Through simple functionalization, the effects of fluorescence enhancement and the suppression of quenching are demonstrated by sensing the streptavidin-biotin complex. Here, a 91-, 288-, 403-, and 501-fold fluorescence enhancement is observed for Alexa Fluor 555, 647, 750, and 790, respectively. Finally, the multiplexed detection of single-stranded DNA (*gag*, *CD4* and *CCR5*) analogues of genes studied in the pathogenesis of HIV-1 between 10 pM–10 μM concentrations and then *CD4* mRNA in the lysate of transiently-transfected cells with a 5.4-fold increase in fluorescence intensity relative to an untransfected control is demonstrated. As a result, the utilization of this bioinspired MIM-MS promises to be a versatile technique for the multiplexed detection of various nucleic acid sequences at low concentrations using plasmon-enhanced fluorescence. Figure 7.3 presents an illustrative summary of Chapter 5.

Finally, Chapter 6 discusses the utilization of flexible versions of the MIM metasurface (flex-MS) for label-free broadband SERS biosensing. By leveraging nature-inspired structural size and positional disorder, broadband SERS enhancement factors (*EF*s) are engineered. This enables the uniform enhancement of various Raman peaks of Raman-active biomolecules specifically for NIR-SERS where energy differences between the vibrational modes and the excitation tend to be significant. The origins of broadband SERS *EF* due to size and positional disorder is explained through rigorous FDTD simulations following which, an experimental verification of the same is conducted through the broadband SERS detection of uric acid (UA). More specifically, through comparative experimentation, the 1134 cm^{-1} and 1645 cm^{-1} peaks of UA are shown to be enhanced 3.1- and 5.7-fold at a low laser power of 0.32 mW by the flex-MS compared to traditional substrates with periodically-arranged nanostructures. The flex-MS is then employed as a SERS biosensor to detect UA label-free in whole human tears within a physiologically relevant concentration range (25–150 μM). The approach is in good agreement with results taken concurrently from traditional enzyme-based assays for UA. Figure 7.4 presents an illustrative summary of Chapter 6.

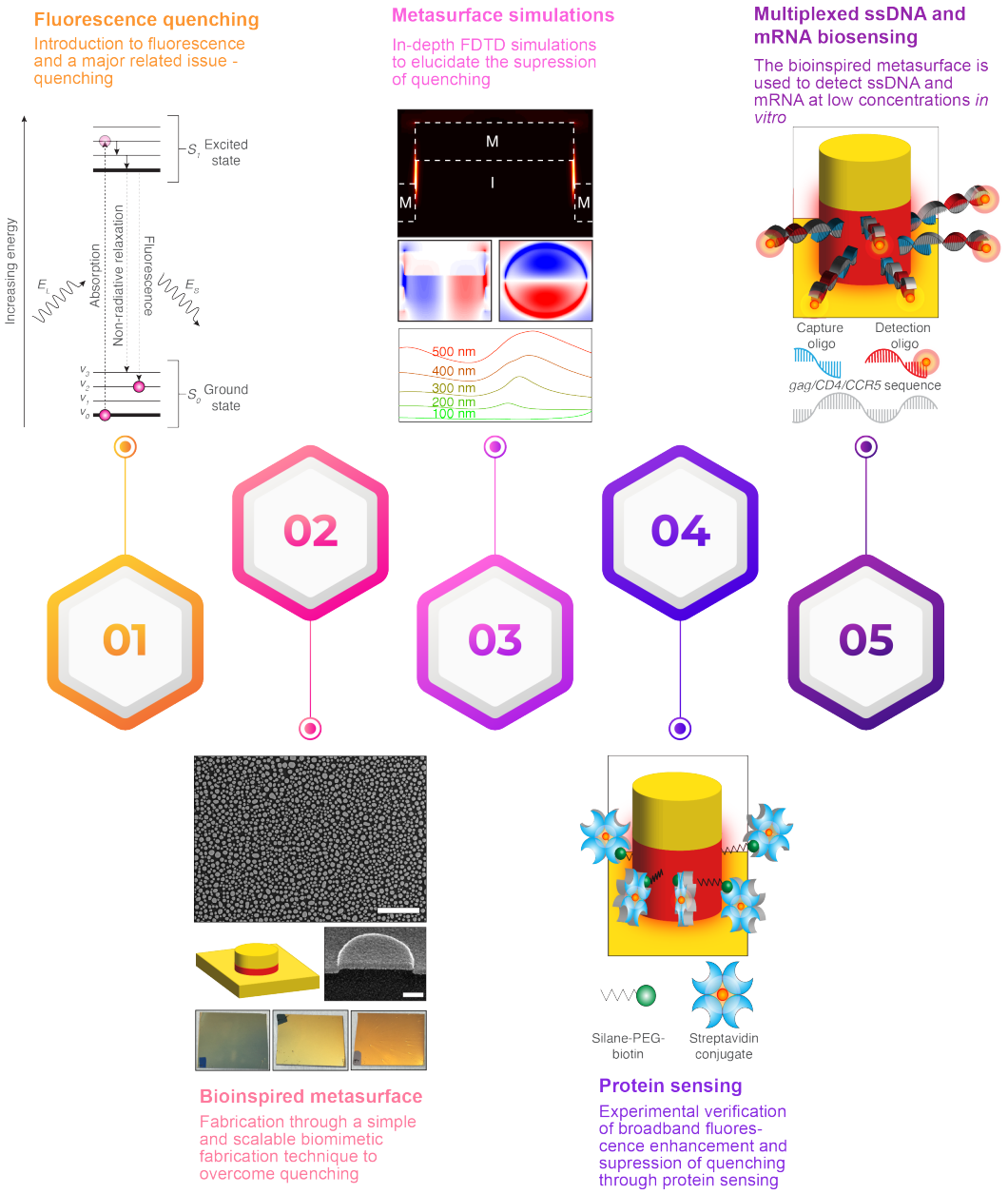

Figure 7.3: Illustrative summary of Chapter 5.

7.3 Future direction

Within the scope of this work, potential future directions could involve the simultaneous incorporation of various multifunctional bioinspired nanostructures on the same medical platform. For instance, as shown in Figure 7.5, an ophthalmic implant package can contain: 1) a Fabry-Pérot-based IOP sensor integrated with light trapping b-Si nanostructures and omnidirectionally-scattering nanostructures on the Si_3N_4 membrane and 2) a plasmonic biosen-

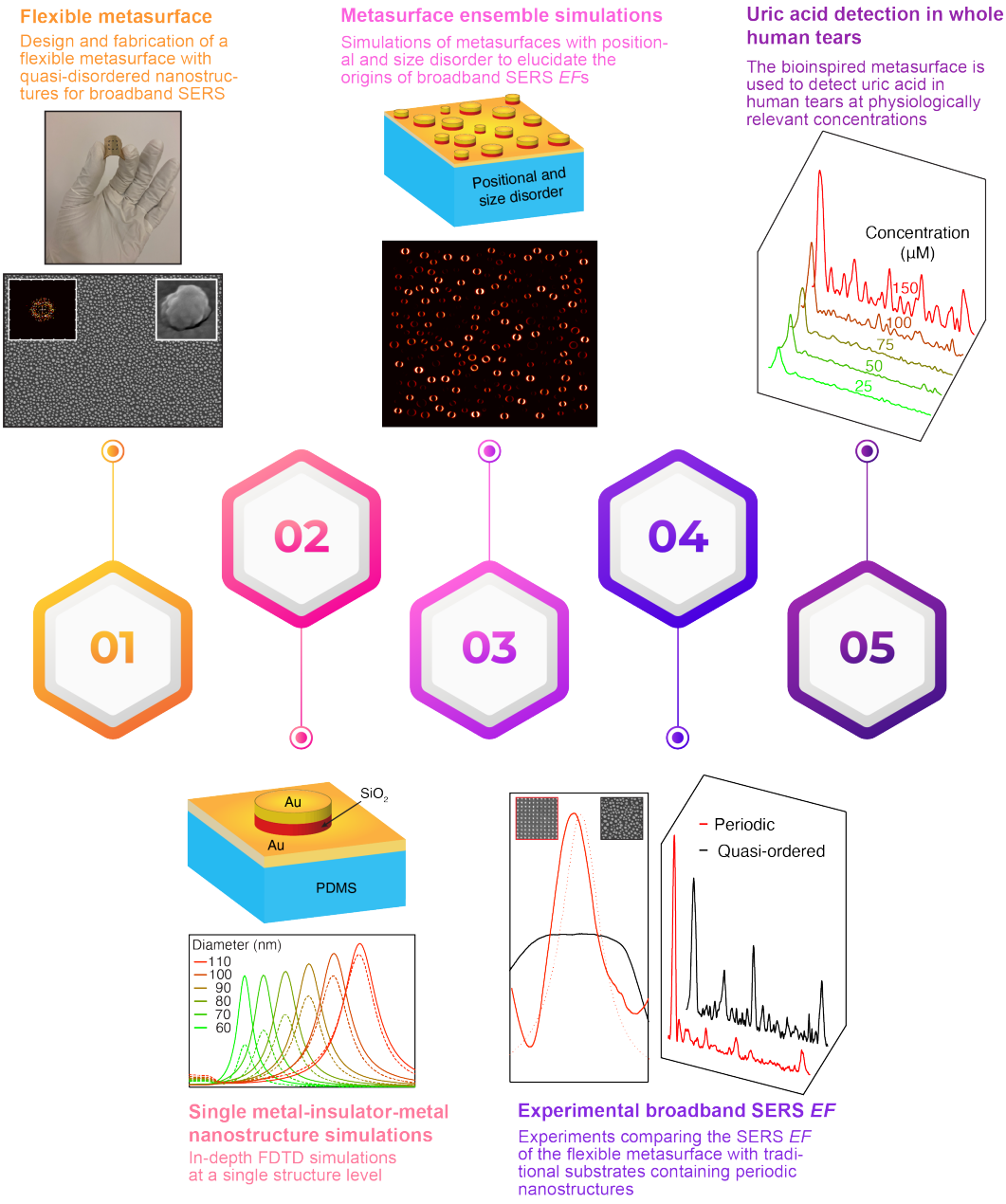

Figure 7.4: Illustrative summary of Chapter 6.

sor with quasi-(dis)ordered MIM nanostructures. Furthermore, given advancements in fields such as internet of things (IoT), particularly in healthcare technology, smartphones with onboard photonic modules like near-infrared (NIR) and Raman spectrometers, light-emitting diodes (LEDs) and optical filters can be used for detection/monitoring purposes. Therefore, a medical platform with multi-parametric sensing/monitoring capabilities for point-of-care self-monitoring purposes can be envisaged through bioinspired nanostructure

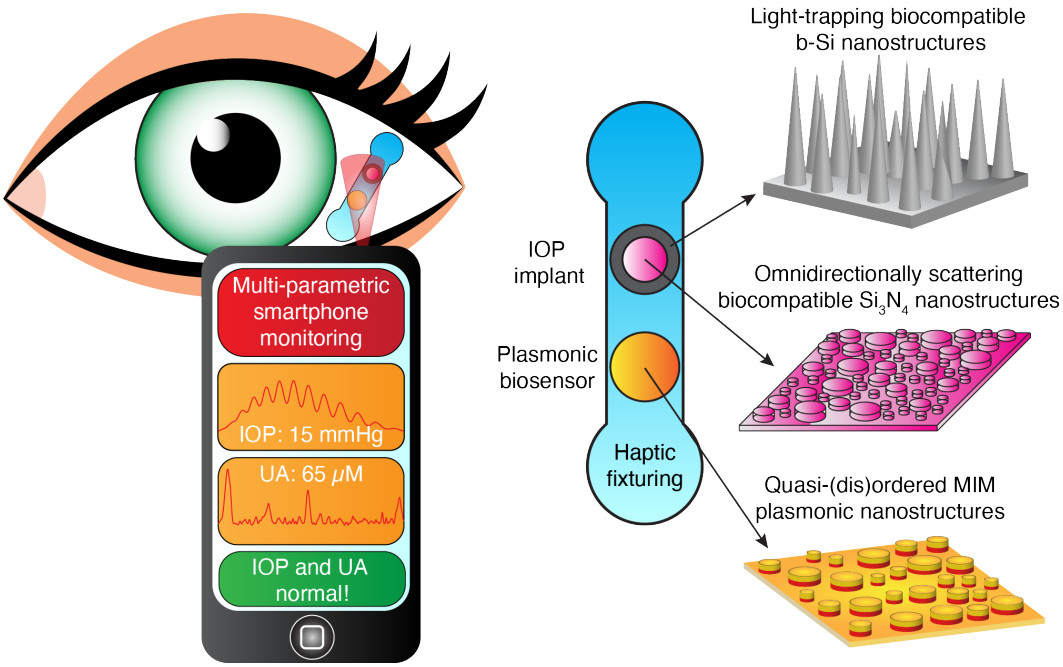

Figure 7.5: Possible future direction of this work. An ophthalmic implant package containing an IOP sensor implant integrated with light trapping b-Si nanostructures and omnidirectionally-scattering Si_3N_4 membrane nanostructures as well as a plasmonic biosensor with quasi-(dis)ordered MIM nanostructures can be envisioned. Detection is performed using a smartphone.

integration.

In closing, nature offers a boundless reservoir of blueprints for multifunctional nanostructure design and fabrication. The utilization of nanostructures inspired from nature in biomedicine is certainly a nascent field making the scope of possibilities and applications in this space limitless. As a result, such an approach can plausibly lead to multifunctional next-generation solutions to highly complex interdisciplinary medical problems.